LANCASTER UNIVERSITY

DOCTORAL THESIS

Discerning nonlinear brain dynamics from EEG: An application to autistic spectrum disorder in young children

---

Supervisors:

Aneta Stefanovska

Peter V.E. McClintock

Author:

Valentina Ticcinelli

A thesis submitted in fulfilment of the requirements

for the degree of Doctor of Philosophy

in the

Nonlinear Biomedical Physics Group

Physics Department

February 23, 2018

To my friends.

Acknowledgements

First and foremost, I will never be grateful enough to Prof. Aneta Stefanovska for giving me the opportunity to be part of her group. This PhD experience shook my life from its very roots and turned myself in such a stronger and wiser person. Her patient and uninterrupted guidance accompanied me through the life obstacles and scientific challenges faced during these years, and was of constant inspiration.

Then, the most sincere thanks go to Prof. Peter Vaughan Elsmere McClintock, whose limitless kindness and wisdom I could always could count on. Also, I am extremely grateful for his patience and magical skills in turning my writings into English.

It was also an honour to collaborate with Dr. Megan Thomas and her Blackpool Teaching Hospitals team, whose expertise on EEG and children on the autistic spectrum made this project possible.

I also have to express my gratitude to Dr. Tomislav Stankovski. I most likely wouldn't have made it through without the countless Viber calls he made to check on me. His empathic support pushed trust in myself especially in the hardest moments.

Next in line there is all the UK company: Elaine, who welcomed me to her home before I built one of my own. Kate, for all the hugs, climbs, and boat chats. Dima Z., for being such a sweet, reliable friend and for having bought a house so that we all can come back and visit.

Then, thanks to my officemates for making our office(s) such a nice place to be: Phil, who was patient enough to initiate me to the groups' topics. Spase, who forcefully convinced me to buy a bike and go bouldering: thanks to that I will never again underestimate the impact of the highly improbable. Dima I., whose code just rocks. Gemma, who is always

so ready to help despite being involved in thousand of things. Will, Zhenia, Miroslav, Yunus, Ola, Max, Fede, Basti, Mahmoud, Vamsi, Julian and all the others whom I was lucky enough to meet: thanks for all the fruitful discussions, the sports and the pub time. Then the other friends I met in the Physics corridor and/or hanging from the climbing wall, among whom Mike, Veronica, Seriozha, Klen, Rob, Han and Paul. Thanks for sharing so many happy moments with me, and for forming a stable community core in this shape-shifter of a town. Thanks Sora for all the laughter and our developed expertise in randomly bumping into each others. And thanks to Moniek, for proving me that a disciplined lifestyle could be enjoyable, for future references.

A lot of affection goes to Maja, who holds a special place in my heart. Thanks for being reckless enough to be by my side on the improbable paths we tread around Europe.

To conclude with the Lancastrian family, a huge thanks goes to Jakub. Our little universe kept me kind-of sane during these four years: knowing that it is still accessible within Switzerland makes also the future look way less scary.

Finally, the Italian front. Thanks to my fantastic siblings: I might be the big sister, but more and more often I find myself looking up on them. Thanks to Elena Zorzi, who has always been such a drive and inspiration and is to me an unmovable reference point.

To conclude, the final thanks go to my parents, who always encouraged me to be myself and follow my aspirations, and gave me unconditional, constant support. Only as an adult I could understand how much sacrifice it required from them, and I am fully and knowingly grateful for every drop of it.

Declaration

This thesis is my original work and has not been submitted, in whole or in part, for a degree at this or any other university. Nor does it contain, to the best of my knowledge and belief, any material published or written by another person, except as acknowledged in the text.

Abstract

A challenging goal in neuroscience is that of identifying specific brain patterns characterising autistic spectrum disorder (ASD). Genetic studies, together with investigations based on magnetic resonance imaging (MRI) and functional MRI, support the idea that distinctive structural features could exist in the ASD brain. In the developing brains of babies and small children, structural differences could provide the basis for different brain connectivity, giving rise to macroscopic effects detectable by e.g. electroencephalography (EEG). A significant body of research has already been conducted in this direction, mainly computing spectral power and coherence. Perhaps due to methodological limitations, together with high variability within and between the cohorts investigated, results have not been in complete agreement, and it is therefore still the case that the diagnosis of ASD is based on behavioural tests and interviews.

This thesis describes a step-by-step characterisation and comparison of brain dynamics from ASD and neurotypical subjects, based on the analysis of multi-probe EEG time-series from male children aged 3-5 years. The methods applied are all ones that take explicit account of the intrinsically non-linear, open, and time-variable nature of the system.

Time-frequency representations were first computed from the time-series to evaluate the spectral power and to categorise the ranges encompassing different activities as low-frequency (LF, 0.8-3.5 Hz), mid-range-frequency (MF, 3.5-12 Hz) or high-frequency (HF, 12-48 Hz). The spatial pathways for the propagation of neuronal activity were then investigated by calculation of wavelet phase coherence. Finally, deeper insight into brain connectivity was achieved by computation of the dynamical cross-frequency coupling between triplets of spatially distributed phases. In doing so, dynamical Bayesian inference was used to find the coupling parameters between the oscillators in the spatially-distributed network. The sets of parameters extracted by this means allowed evaluation of the strength of particular coupling components of the triplet LF, MF→HF, and enabled reconstruction of the coupling functions. By investigation of the form of the coupling functions, the thesis goes beyond conventional measures like the directionality and strength of an interaction, and reveals subtler features of the underlying mechanism.

The measured power distributions highlight differences between ASD and typically developing children in the preferential frequency range for local synchronisation of neuronal activity: the relative power is generally higher at LF and HF, and lower at MF, in the ASD case. The phase coherence maps from ASD subjects also exhibited differences, with lower connectivity at LF and MF in the frontal and fronto-occipital pairs, and higher coherence at high frequencies for central links. There was higher inter-subject variability in a comparison of the forms of coupling functions in the ASD group; and a weaker coupling in their theta-gamma range, which can be linked with the cognitive features of the disorder.

In conclusion, the approach developed in this thesis gave promising preliminary results, suggesting that a biomarker for ASD could be defined in terms of the described patterns of functional and effective connectivity computed from EEG measurements.

List of publications

Journal articles

Part of the work presented in this thesis has been published in the following papers:

- V. Ticcinelli, T. Stankovski, D. Iatsenko, A. Bernjak, A. E. Bradbury, A. R. Gallagher, P. Clarkson, P. V. McClintock, and A. Stefanovska, "Coherence and coupling functions reveal microvascular impairment in treated hypertension," *Frontiers in Physiology*, vol. 8, p. 749, 2017.
- T. Stankovski*, V. Ticcinelli*, P. V. E. McClintock, and A. Stefanovska, "Neural cross-frequency coupling functions," *Frontiers in Systems Neuroscience*, vol. 11, no. 33, p. 10.3389, 2017. * The authors contributed equally to the work
- T. Stankovski, V. Ticcinelli, P. V. E. McClintock, and A. Stefanovska, "Coupling functions in networks of oscillators," *New Journal of Physics*, vol. 17, no. 3, p. 035002, 2015.

In addition, the following manuscripts are currently in preparation:

- G. Lancaster, D. Iatsenko, V. Ticcinelli, A. Pidde, A. Stefanovska, "Surrogate data for hypothesis testing of dynamical systems", Article.
- V. Ticcinelli, T. Stankovski, M. Thomas, J. Bradley, P. V. E. McClintock, and A. Stefanovska, "Characterisation of autistic brain dynamics from EEG of young children", Article.

Patent pending

Part of the methods presented in this thesis have been applied for the following scope:

- V. Ticcinelli, A. Stefanovska, M. Thomas, and P.V.E. McClintock, "EEG-based marker for autistic spectrum disorder," *GB1620926.4*

Conference contributions

Part of the work presented in this thesis has also been presented at the following events:

Conference paper and invited talk

- V. Ticcinelli, T. Stankovski, P.V.E. McClintock, and A. Stefanovska, "Ageing of the couplings between cardiac, respiratory and myogenic activity in humans," *Proceedings of the 37th Annual International Conference of the IEEE (Engineering in Medicine and Biology Society)*, Milan, Italy, August 25-29 2015

Contributed talk

- "Coupling functions between cardiac and myogenic activity in microvascular flow of aged and hypertensive subjects," *9th meeting of ESGCO, international conference on biological oscillations*, Lancaster University, United Kingdom, 10-14 April 2016.

Poster presentations

- "Coupling functions for network of oscillators – coupling decomposition", *9th International Summer School/Conference "Let's face chaos through nonlinear dynamics"*, University of Maribor, Slovenia, 22 June - 6 July 2014.

- "Coupling functions for network of oscillators – Form characterisation", *6th International Workshop on Set-Oriented Numerics*, Imperial College (London), United Kingdom, 28th September – 1st October 2015.

- "Coupling functions for networks of oscillators – Eyes open / eyes closed", *Brain-Modes 2016*, University of Bruxelles, 30th November- 2nd December 2016.

- "Neural cross-frequency coupling functions", *26th Annual Computational Neuroscience Meeting*, University of Antwerp, Belgium, July 15-20 2017.

Contents

List of Figures

List of Tables

Chapter 1

Introduction

Networks of interacting oscillators abound in nature (Strogatz, 2001), ranging from large-scale climatic interactions (Donges et al., 2009), to small-scale coupled molecular systems (Dolmetsch et al., 1997). The firing of ensembles of neurons in the brain is also regulated by network dynamics (Achard et al., 2006). Measures like electroencephalography (EEG) provide a mean-field global observable that describes their synchronous oscillating dynamics (Deco et al., 2008) by picking up the activity underneath individual probes on the scalp. The macroscopic behaviour of these synchronised oscillators has been observed ever since the very first EEG recordings (Berger, 1929), with the brain's electrical activity emerging in waves (Buzsáki and Draguhn, 2004).

A diversity of signal processing methods has been applied over the years to characterise the features of these brain waves in terms of their frequency range and amplitude, with different brain states and functions being associated with EEG waves having specific frequencies and emerging at particular locations (Buzsáki, 2006). One of the current challenges for the applications of nonlinear methods of analysis to EEG is to detect specific brain patterns characterising autistic spectrum disorder (ASD).

Historically, the high occurrence of multiple cases of ASD among siblings resulted in the disorder being attributed to bad parenting. Thanks to the advent of genetic studies this view was subsequently rejected (Bailey et al., 1995, Fatemi et al., 2005). In particular, it was found that genes associated with ASD are preferentially expressed in brain synapse proteins (Berkel et al., 2010, Durand et al., 2007, Gilman et al., 2011). This fact, together with MRI (Hazlett et al., 2017) and fMRI-based investigations (Just et al., 2004), suggested a genetic predisposition for ASD that could result in an altered anatomical and functional development of the brain (Belmonte et al., 2004). The correspondingly different "wiring" of the brain is likely to give rise to specific brain dynamics.

A considerable body of research has already been conducted in this direction. In particular, the EEG signal has been analysed with the aim of identifying ASD signatures, especially in the distribution of spectral power and in coherence measures (Belmonte et al., 2004, Bosl et al., 2011, Coben et al., 2008, Duffy and Als, 2012, Khan et al., 2013, Murias et al., 2007). The results in the literature are not in complete agreement as to what best describes the EEG of an autistic child. There are many factors that may have played roles in generating the mixed outcomes, for example the ages of the subjects, the reference channel used, and the type of activity or resting state used. It could also be the case that the signal processing tools used were unable to describe the system at a level deep enough to disclose the fundamental differences between the groups.

These could be some of the reasons why, despite much scientific effort, the diagnosis of ASD still rests solely on behavioural tests and interviews with the children's families (Gotham et al., 2009). The diagnostic process can take years, thereby preventing early intervention in cases where the presence of ASD has not been obvious from an early age. Finding specific signatures of ASD in a test as clinically common and globally widespread as EEG could therefore help physicians in the diagnostic process, thereby improving both the efficacy of intervention strategy and the quality of life for both the children and their families.

In the work described below, EEG time-series from a cohort of male children aged 3-5 years have been studied. The 10-20 multi-probe montage was used. Because biological processes are intrinsically nonlinear, open, and time-variable (Suprunenko et al., 2013), all of the methods applied here for characterisation of EEG time-series took these features explicitly into account. The brain dynamics was characterised systematically, step-by-step, by tackling the problem through sequential levels of analysis (Clemson et al., 2016).

First, time-frequency representations were obtained by the mean of the wavelet transform (Daubechies, 1990), in order to evaluate how the overall spectral content was generated by non-stationary processes happening at different frequencies. The ranges encompassing different activities were categorised as low frequency (LF, 0.8-3.5 Hz), mid-range frequency (MF, 3.5-12 Hz) or high frequency (HF, 12-48 Hz).

The spatial pathways for the propagation of neuronal activity were then investigated. This was achieved by computing the wavelet phase coherence (Sheppard et al., 2011, 2012), allowing us to detect matching phase dynamics in pairs of probes. This measure of coherence provides a value at each frequency. It is important to stress that phase coherence is a state of the system which does not necessarily imply any underlying coupling.

A detailed study of the coupling means going beyond the conventional description in terms of phase and amplitude values. It requires reconstruction of the nonlinear dynamics of the system, with the goal of revealing the underlying neuronal mechanisms generating the measured EEG data. This kind of knowledge can be achieved by considering the brain as a collection of oscillators whose activities project on space, i.e. on various parts of the scalp, and whose phase and amplitude can be extracted from the EEG at certain points (i.e. probe locations) and for certain frequency ranges. The interactions between the oscillators can be inferred by coupling the time evolution of their spatially-distributed activity according to a certain model. This approach has been already applied to study some cases of amplitude-to-amplitude (Bruns et al., 2000, De Lange et al., 2008), phase-to-phase (Jirsa and Müller, 2013, Stankovski et al., 2015, 2017b) and phase-amplitude (Axmacher et al., 2010, Jensen and Colgin, 2007, Schack et al., 2002, Tort et al., 2010, Voytek et al., 2010) coupling.

In this thesis, the focus has been placed on phase-to-phase interactions and, for the first time, cross-frequency phase coupling functions have been inferred from the multidimensional EEG data of neurotypical and ASD children, going beyond *functional* brain connectivity and describing the underlying *effective* connectivity. In order to do so, the time evolutions of the collective LF, MF and HF phases were extracted from each time-series by Butterworth filtering and Hilbert transformation. Then, for each pair of probes, a triplet of phases was built by taking the LF and MF phases from one source and the HF from the other. This design of the coupling network allowed the study of the spatial propagation of the phenomena regulating the low-to-high phase-to-phase coupling, which had already been found to be of central importance for the eyes-open eyes-closed brain states (Jirsa and Müller, 2013, Stankovski et al., 2017b), as well as for cardio-vascular regulation (Iatsenko et al., 2013, Rosenblum et al., 2002, Ticcinelli et al., 2017). Each triplet was treated as a system of coupled phase oscillators subject to noise, and the time-variable coupling parameters were inferred by dynamical Bayesian inference (Smelyanskiy et al., 2005, Stankovski et al., 2012, 2017b). The strength of specific coupling components was calculated from the inferred parameters (Rosenblum and Pikovsky, 2001). Moreover, the latter allowed reconstruction of the coupling functions describing the interactions (Stankovski et al., 2017a). By mapping the value of the coupling as a function of the two phases involved, coupling functions go beyond the directionality and strength of an interaction, to describe in more subtle detail the mechanism underlying it. In order to quantify such morphological features, the form of the coupling functions LF, MF$\rightarrow$HF from the ASD and control group were compared by computation of indices like polar similarity (Stankovski et al., 2017a, Ticcinelli et al., 2017), or similarity with average functions (Kralemann et al., 2013, Stankovski et al., 2017a).

Thesis structure

In order to define the context and describe the background, current knowledge of brain dynamics is briefly reviewed (Chapter 2). The commonest approaches undertaken to describe connectivity and causality are also described (Section 2.2). The methods of analysis that will be applied to the dataset are then presented, together with their applications to simulated data (Chapter 3). To set the background for applications to the autistic case, the outcomes of recent studies of ASD signatures in children EEG are reviewed (Chapter 4). Nonlinear methods are then discussed in Chapter 3. They are then applied to multidimensional EEG data recorded from ASD and non-ASD children, and the results are presented (Chapter 5). The potential significance of the results as a biomarker for ASD is finally discussed (Chapter 6). In conclusion, limitations due to the specific set of data used, and to EEG measures in general, are listed together with suggestions for possible improvements and future developments (Chapter 7). In Appendix A, a brief description of the anatomo-physiology of the brain is provided to explain the cellular and anatomical terms used in the thesis.

Chapter 2

Brain dynamics

2.1 Neuronal oscillations

The human brain is composed by about 100 billion neuronal cells connected in a complex network, with an estimated number of 200 trillion connections between them (Buzsáki, 2006).

Neurons are electrically excitable cells. They maintain cross-membrane voltage by means of ion pumps and channels placed within their membranes. If the cross-membrane voltage reaches a specific threshold, an electrochemical pulse is generated and travels along the neuron and propagates to downstream neurons via synaptic interactions (Kandel et al., 2000).

Single neurons can also display self-paced electrical oscillatory properties as a further developed form of ionic conductance (Buzsáki and Draguhn, 2004). These autorhythmic neurons may act as pacemakers (by firing with a specific frequency) or as resonators (by having a preferential response to certain firing frequencies) (Llinás, 1988). Within a network of neurons, such cells can give rise to coherent network oscillations. Such waves propagating in the network are believed to be the mechanism by which information is represented in the brain (Wang, 2010).

Specific patterns of synchronisation in the neuronal networks can achieve complex brain functions such as perception, memory and consciousness (Engel et al., 2001, Varela et al., 2001). Those are not only responses to incoming stimuli (bottom-up mechanism), but are also based on the memory of previous experience, stored in the architecture of cortical and subcortical networks (top-down mechanism) (Engel et al., 2001). Bottom-up and top-down mechanism are simultaneously implemented by large-scale networks that integrate both incoming and endogenous activity (Varela et al., 2001).

The most efficient way to achieve synchronous firing of ensembles of neurons is to have them temporally coordinated so that their membrane potential reaches a value close to threshold in a specific time-window (Mirollo and Strogatz, 1990). In such a setting, an input that is not timed with the basic rhythm is less likely to cause a response. Moreover, the energetic cost of propagating the action potential is lower if contiguous neurons are regulated by oscillating membrane potential with similar frequencies (Mirollo and Strogatz, 1990).

Rhythms with different frequencies can not only exist simultaneously on the same network, but also interact with each other (Klimesch, 1999), giving rise to the extremely complex, powerful and plastic brain networks, and networks of networks.

2.1.1 Electroencephalogram

In summary, within the cortex, neurons are interconnected and organised in specialised networks, and in networks of networks. The collective, timed behaviour of ensembles of neurons generates waves of electrical activity travelling within the system: bodies of single units firing in a synchronised or unsynchronised fashion lead to the emergency or disappearance of rhythms in the sum of action potentials, centred around specific frequencies.

The portion of this electrical activity which reaches the surface of the brain can be picked up from the scalp by means of electroencephalographic (EEG) probes. Since the very early days of neuroscience, it has been clear that different states and functions of the brain are associated with the presence- or the absence- of specific frequency contents in the EEG signal, and a lot has been done in order to characterise these correspondences. In the following section, the origin and characterisation of EEG signal will be briefly introduced.

2.1.1.1 Origin of EEG

It was 1875 when Richard Caton published in the British Medical Journal a paper in which he described how he observed and measured specific electrical activities on the cerebral cortex of dogs and apes by using unipolar electrodes and a galvanometer (Caton, 1875).

Nevertheless, it took almost 45 years from then to get the first human electroencephalographic recording, obtained by the German psychiatrist Hans Berger in 1929. Berger was profoundly convinced that human beings are the source and means of propagation of what he called 'psychische energie', some kind of mental energy that was, according to him, ubiquitous within the human body, and even able to travel between individuals, allowing non-verbal, telepathic communication. Inspired by Caton's work, he put together the EEG machinery with the goal to find a signature of this energy, and prove his theories (Niedermeyer and da Silva, 2005).

2.1.2 First band separations of EEG

It was Berger himself to identify and name the alpha (α) and beta (β) rhythms in his first EEG studies. In his first report he wrote: *"The electroencephalogram represents a continuous curve with continuous oscillations in which... one can distinguish larger first order waves with an average duration of 90 milliseconds and smaller second order waves of an average duration of 35 milliseconds."* (Berger, 1929). He then named both rhythms in his second report: *"For the sake of brevity I shall subsequently designate the waves of first order as alpha waves = α-w, the waves of second order as beta waves = β-w, just as I shall use "E. E. G." as the abbreviation for the electroencephalogram."*(Berger, 1931). The alpha-blocking response caused by eyes-opening was described in the second report too, with beta activity becoming observable in the time domain when alpha wave disappeared.

The gamma (γ) frequency range was introduced by Jasper and Andrews (Jasper and Andrews, 1938), observed as superimposed to occipital alpha activity. However, it was kept unified with the beta range till the 90s, when the sampling frequencies of EEG instrumentation improved and the gamma band became the centre of many studies about cognition (Llinas et al., 1991).

The delta (δ) band was named in 1936 by Grey Walter (Walter, 1936), and included all the frequencies slower than alpha range.

The theta (θ) band was the last one to be introduced, and named after the hypothesis of its thalamic origin (Walter, 1936).

2.1.3 Functional meaning and spatial location

Many studies along the years went beyond the definition of bands, and tried to characterise more deeply their connection with brain states.

2.1.3.1 Alpha band

As previously mentioned, alpha wave has been the first to be discovered (Berger, 1929) and has been intensively studied ever since. It is the most easily observable oscillatory component of the EEG, and its strength adjusts sensibly when the subject's state changes: the most evident drop of alpha wave amplitude is observed when the subject opens their eyes after a period with eyes closed. Because this phenomenon was already described in Berger's second EEG report (Berger, 1931), it is often refereed to as 'Berger effect'.

It has been also observed that engaging into a task causes a further drop of alpha activity (Klimesch, 1999). Therefore, alpha oscillation has been targeted as 'idling' rhythm (Pfurtscheller and Aranibar, 1977), and its disappearance in the EEG has been associated with some form of brain activation. Recently, it has been suggested that the emergence of alpha oscillation could not only indicate a state of inactivity, but on the contrary it could actively perform a selective inhibitory action over some cognitive and motor tasks, especially when they involve a top-down control. Under this interesting perspective, the disappearance of the wave indicates the release of the inhibition allowing for the emergency of other activities (Klimesch et al., 2007).

Since Berger's studies, it has been clear that the highest alpha rhythm is picked up over the occipital cortex: combined fMRI/EEG studies have deepened the picture of the occipital prevalence of this rhythm, and indicated the thalamus as the main subcortical generator of alpha rhythm (Feige et al., 2004), through thalamo-cortical loops with the visual cortex. The inverse proportionality of alpha power and brain activity was also observed by other fMRI-EEG combined studies (Goldman et al., 2002, Laufs et al., 2003).

2.1.3.2 Beta band

The beta band was identified in Berger's first report and named in the second (Berger, 1931). The smaller amplitude wave within the beta frequency range could be observed with eyes open, when alpha activity diminished. Berger hypothesised that is could be beta and not alpha wave to be the expression of mental activity (Berger, 1938), and in the same year Jasper and Andrews disclosed the different nature of alpha and beta rhythms (Jasper and Andrews, 1938) documenting their distinct emergence, spatial distribution and independent frequency patterns. In this work, they also first identified the need to put a higher limit to the beta band, and called 'gamma' the range above 30-35Hz.

In 1985, a study by Cole isolated attentional from cognitive tasks, and observed how the drop of alpha activity reflected attentional demands toward the environment, while the emergence of beta activity reflected the initiation of emotional and cognitive processes (Cole and Ray, 1985).

The beta rhythm has been intensively studied even in relation to movement: a consistent pool of research agreed in detecting the de-synchronisation of firing at beta range during the action, with consequential re-synchronisation after the completion of the task (McFarland et al., 2000). It has therefore been proposed that the beta oscillation could have the functional role to maintain the motor-sensorial feedback loop (Engel and Fries, 2010).

2.1.3.3 Gamma band

The gamma activity was first identified and named by Jasper and Andrews in their work dated 1938 (Jasper and Andrews, 1938). However, the term 'beta' encompassed all the frequencies above 40Hz till the 90s. Just then, when many studies focused on high-frequency waves induced by mental and motor tasks, the term 'gamma' was brought back under the spotlight (Llinas et al., 1991).

The emergence of gamma activity in temporal-occipital sites during visual perception and object representation has been identified in the '90s (Tallon-Baudry and Bertrand, 1999). Later on, deep-EEG studies allowed to precisely identify that gamma activity as response to a visual stimulus firstly appears in specific cortex gyri within the occipito-temporal sites and then propagates to parietal locations (Lachaux et al., 2005). The emergence of gamma oscillations during cognitive tasks such as object recognition (Rodriguez et al., 1999), learning (Miltner et al., 1999) and emotional evaluation (Müller et al., 2000) has been detected by numerous studies.

Several biochemical time-constant processes involved in the interaction of an ensemble of neurons manifest with time-constants falling into the gamma band. These parameters determine if the inputs from multiple upstream sources can be integrated as a single event (Buzsáki, 2010), suggesting that the dynamics of ensembles of cells can be organised in gamma cycles (Buzsáki and Wang, 2012). As the regions of the brain in which gamma activity is detected are characterised by the presence of inhibitory interneurons with GABA synapses, is has been suggested that the synchronisation in gamma band could be achieved by summing inhibitory more than excitatory potentials (Buzsáki and Wang, 2012).

This description pictures gamma oscillation like a local phenomenon, but spatially separated patches of synchronised gamma activity can interact with each other through direct neuronal connections like interneurons (Buzsáki and Draguhn, 2004). Also, slower temporal coordination among oscillators at gamma frequencies may be achieved by modulation from the phase of slower rhythms (Canolty et al., 2006, Jensen and Colgin, 2007).

2.1.3.4 Theta band

In the years, the term 'theta rhythms' has been referring to two different phenomena sharing similar frequency range. On one hand, it defined a strong regular oscillation of 4-6 Hz which has been detected from the hippocampus of several mammals. It has been hypothesised that the rhythm could reflect the readiness of the hippocampus to process external inputs, especially during exploration and state of alert (Buzsáki, 2005). On the other hand, in humans, the term 'theta' usually refers to EEG oscillations in the 4–7 Hz frequency range, regardless of the location. The functional significance of this rhythm is mainly associated with memory tasks (Jensen and Tesche, 2002) and cognition (Klimesch, 1999).

It has not been fully established if there is a direct link between the hippocampal and the cortical theta activity in humans. A study with EEG and MEG observed the emergence of the theta rhythm in the hippocampus before the presentation of a memory task (Tesche and Karhu, 2000), confirming the founding of animal studies (Buzsáki, 2005).

2.1.3.5 Delta band

The delta wave has been observed since its discovery in the EEG during deep sleep. It has been later found that within the delta frequency band there are at least 3 oscillations with distinct mechanisms and sites of origin: the slower <1 Hz cortical oscillation, a thalamic oscillation (1–4 Hz), and a faster cortical oscillation (1–4 Hz).

A study conducted on both anaesthetised animals and in naturally sleeping humans disclosed how spatially distributed synchronization of the slow oscillation can modulate the phase of thalamic and cortical faster delta (1–4 Hz) oscillations (Amzica and Steriade,

	Age (years)	δ band (Hz)	θ band (Hz)	α band (Hz)	β band (Hz)	γ band (Hz)
Standard	Adults	4	8	13	40	40+
Stroganova et al. (1999)	0.5-1		5.2	9.6		
Marshall et al. (2002)	1-4		6	9		
Boersma et al. (2011)	5-7	4	6	11	25	
Boersma et al. (2013)	2-5	4	10		25	
Orekhova et al. (2007)	3-8			13.2	24	70
Clarke et al. (2016)	8-12	3.5	7.5	12.5	25	
Duffy and Als (2012)	2-12	2	8	12	30	
Cantor et al. (1986)	4-12	3.5	7.5	12	30	
Coben et al. (2008)	6-11	3.5	7.5	12.5		

TABLE 2.1: Upper limits of EEG bands standards for adults and as adjusted for children studies

1998). Other studies focusing on the lower-amplitude delta wave still observable in awake subjects identified its possible rule in governing cognitive processes (Başar et al., 2001).

2.1.4 Children EEG

When dealing with children, the traditional limits of EEG bands have to be re-discussed. It has been found that during the development years brain activity undergoes changes together with the maturation of cellular substrates (Hudspeth and Pribram, 1992). In particular, it seems like the alpha wave spectral peak occurs at slower frequencies (8 Hz instead of 10 Hz) in younger children (Boersma et al., 2011, Marshall et al., 2002, Stroganova et al., 1999).

Considering the maturation of EEG in early childhood, in order to prevent splitting the same activity in different bands across the groups, authors adapted the limits of the bands according to the spectral content of the time-series they analysed (Table 2.1 shows some examples). Some studies joined consecutive bands for spectral investigations (Boersma et al., 2013).

2.1.5 The reference probe

When analysing EEG recordings, it must be bared in mind that what is measured by each probe is a voltage, i.e. a difference of electric potential energy between two probes.

With a bipolar setting, pairs of electrodes share the same amplifiers, and each pair records the corresponding voltage within the locations where the two poles are placed. For unipolar settings, every electrode has an amplifier, and the voltage is measured between each active probe and a reference, which is common to all active electrodes. In other words, if the reference is the probe X, the times series V_A of the probe A is a voltage derived from the difference of electric potential energy E_A and E_X.

Common choices for the on-line reference probe are the apex of the head (probe Cz), linked or single earlobes (Mantini et al., 2007), the electric potential energy from one mastoid (Delorme and Makeig, 2004, Marinazzo et al., 2011), and linked mastoids (Faes et al., 2015).

For EEG measures, the choice of the reference is a procedure that can be performed off-line. For example, in the case of the off-line common average (CA) (Andrzejak et al., 2001, Lehnertz and Elger, 1995), the idea is to generate for every probe A_i a new voltage time-series V'_{A_i} by subtracting the average time-series V_{CA} from each original V_{A_i}. This linear transformation should reduce the bias in the spatial distribution of the voltages coming from the position of the reference probe during the recording. For example, for the probe A_1 the transformation acts as follows:

$$\begin{aligned} V_{A_1} &= E_1 - E_x \\ V_{CA} &= 1/N \sum_i V_{A_i} = 1/N \sum_i (E_i - E_x) \\ &= 1/N \sum_i E_i \ - E_x \\ V'_{A_1} &= V_{A_1} - V_{CA} = E_1 - E_x - (1/N \sum_i E_i \ - E_x) \\ &= E_1 - 1/N \sum_i E_i \ , \end{aligned} \tag{2.1}$$

which is not dependent on E_x.

In the case of re-referencing to one of the active probes (named here B), or to 2 linked probes, an analogue transformation removes the dependence on the original reference and shifts it to the new one:

$$
\begin{aligned}
V_{A_1} &= E_1 - E_x \\
V_B &= E_b - E_x \\
V'_{A_1} &= V_{A_1} - V_B = E_1 - E_x - (E_B - E_x) = E_1 - E_B \ . \qquad (2.2)
\end{aligned}
$$

Arguably, every choice of reference has its implication on the analysis, and defining which is the best choice for each investigation is not a trivial problem (Hagemann et al., 2001, Hu et al., 2010, Yao et al., 2005). In order to overcome this limitation, several transformations involving realistic head models have been implemented in order to reconstruct the topographic map of the electric field potential at its sources starting from the scalp EEG (Michel and Murray, 2012).

2.1.6 Types of connectivity

Connectivity can be investigated under a *structural*, *functional* and *effective* point of view (Friston, 2011). The first provides information on the actual anatomical connections running between different areas of the brain, and can be investigated with great space-resolution by MRI studies. In the recent years a global project has started with the aim to map the human connectome via MRI imaging (Van Essen et al., 2012). The second provides information about timed patterns of brain activation emerging in resting state or triggered by a task. It can be investigated with fMRI (Friston et al., 1999), fNIRS (Ferrari and Quaresima, 2012), or EEG techniques (Varela et al., 2001) by detecting simultaneous brain activation on different areas of the brain. The third aims to provide insight on the mechanism generating the connection, going beyond the structural and functional description of it. It requires the application of a model and the characterisation of its parameters (Aertsen et al., 1989, Friston, 2011).

While MRI and fMRI based studies can disclose with great space-resolution differences in the structural and low-frequency functional connectivity, EEG is the optimal method to investigate higher frequency *functional* and *effective* connectivity.

2.1.7 Cross-frequency interactions

As already mentioned in the description of gamma oscillation, it has been shown that interactions can occur in the brain network between oscillations with different frequencies (Canolty et al., 2006).

The speed of neuronal communication is limited by the physical time needed for the action potential to travel through the axon, and by synaptic delays. The period of an oscillation is therefore proportional to the number of neurons engaged in series in the transmission. Because most neuronal connections are local, higher frequency oscillations can happen in small groups of neurons, while slower oscillations propagate on a longer neuronal chain (Buzsáki and Draguhn, 2004, Steriade, 2001). To integrate these phenomena happening at different scales, it has been suggested that slower oscillations that can propagate on longer distances could function as a means to synchronise faster oscillations emerging in spatially separated networks (von Stein et al., 2000).

For instance, slower cross-frequency couplings were investigated during auditory novelty oddball task, with increased bi-coherence coupling for delta-theta bands and delta-alpha bands over several areas of the cortex (Isler et al., 2008). The delta-alpha coupling was also compared in eyes-open and eyes-closed EEG with bispectra and bicoherence (Jirsa and Müller, 2013) and with coupling functions (Stankovski et al., 2017b), showing a prominent delta-alpha coupling in eyes closed.

2.2 Coupling and causality in the neuronal network

One of the aims of estimating brain interactions is to investigate the connectivity pathways of the information flow among cortical area. The coupling among brain waves responsible for such interactions can be described with its strength and directionality. Estimating the directionality of coupling introduces the concept of causality: by abstracting from the physical mechanism underlying the connection, methods like Granger causality (Granger, 1969) have been applied very popularly in applications to biophysics and neuroscience.

According to this approach, a time series X is causal to another time series Y if the past values of X can be useful to predict the future values of Y. This method can be very powerful to detect a linear statistical relationship between time series. Several extensions of Granger causality have been proposed in order to encompass the presence of nonlinear relationships within the time-series (Marinazzo et al., 2011), including the possibility to detect causality between time-series by using any polynomial kernel function (Marinazzo et al., 2008). The major limitation of this approach is the assumption that temporal sequence implies causality, which may or may not be correct.

A similar approach to detect causality relies on entropy-based measures of information Information stored in a time series is quantified by its own entropy. Causality in this framework is seen as joint transfer entropy, or information transfer, obtained with Granger causality applied in a probabilistic framework (Vicente et al., 2011). However, this approach does not allow one to draw any conclusion on how the observed activity is generated at a network level.

A different approach in the determination of causality within neural networks consists in the application of dynamical causal modelling. The central idea behind dynamic causal modelling is to treat the brain as a deterministic nonlinear dynamical system that is subject to inputs and produces outputs (Friston et al., 2013). The inputs are given to the system in form of perturbations, and the outputs are the measured responses. The coupled - unobserved - brain states responsible for this mechanism constitute the model for the detected brain connectivity. The objective of the analysis is to estimate the parameters of the coupling by perturbing the system and measuring the response. Bayesian inference of connections is made using the posterior density, computed using the likelihood and prior densities.

As discussed in a recent comparative review (Friston et al., 2003), Granger causality and dynamical causal modelling complement each other in the framework of detecting causation as time- dependence. If the first can be applied empirically to detect the coupling strength and directionality in time series from resting states or in comparing different conditions, the latter, on the contrary, requires specific tailor-made models of the system as hypotheses to be tested. However, also Granger causality is not completely model-free, as the model selection is implicit for its application (linear time dependence) and also explicit in the selection of the differential equations' order. Granger causality and dynamical causal modelling as described above can be applied to detect amplitude relationship between time-series. Generalisations of the methods have been developed in order to investigate phase dynamics, by applying the first to spectra (Brovelli et al., 2004), and the latter to phase-time series (Penny et al., 2009).

Coupling as a form of interaction has been also formalised and studied in a more physical sense. Back to 1673, Huygens first observed that two pendulum clocks sharing a beam as support would synchronise their rhythms (Huygens, 1673). The coupling in this case was represented by the nature of the beam, whose elastic behaviour functioned as a means of interaction between the movements of the pendula, allowing mutual adjustments between their phases. However, a theoretical definition of phase coupling was first introduced a couple of centuries later by Winfree, in the context of population dynamics as interacting phase oscillators (Winfree, 1967). He defined the coupling function between the phases as the product of influence and sensitivity functions.

Later on, in a famous work by Kuramoto, the synchronisation phenomena in a large population of oscillators was fully described by reducing the complex multivariate oscillatory dynamics to phase dynamics (Kuramoto, 1984). Rather than local coupling, Kuramoto built his model by introducing an all-to-all coupling in the system. The coupling was modelled as a sinusoidal function of the phase difference i.e. diffusive coupling. The phase difference is particularly convenient in studying synchronisation, as it reduces the dimensionality of the problem.

It was only with the new millennium that computational power became strong enough to allow coupling functions to be inferred from data. Based on Kuramoto's theoretical model, reconstructed coupling functions can allow one to detect the directionality, strength and mechanism of each interaction (Rosenblum and Pikovsky, 2001). In the following years, different methods for the inference of coupling functions from data were developed. Phase dynamics were investigated in chemical oscillators and it was demonstrated that a model obtained from experiments on a single oscillator can predict synchronisation in large populations of interacting oscillators (Kiss et al., 2005). The inference was later extended within a Bayesian framework, in order to propagate the information on estimated coupling parameters between consecutive windows, and therefore follow time-variability both in the coupling rule and in the oscillators dynamics (Stankovski et al., 2012).

Chapter 3

Materials and methods

3.1 Spectral analysis

In order to introduce the bases of spectral analysis, the concept of analytic decomposition of a time series is briefly introduced, together with some terminology.

3.1.1 Analytic decomposition

A real signal $s(t)$ can be approximated by braking it down into a sum of sinusoidal *components* $\hat{s}(t)$, of the form

$$\begin{aligned} \hat{s}(t) &= A(t)\ \cos\big(\omega(t)\cdot t+\theta\big) \\ &= A(t)\ \cos\big(2\pi f(t)\cdot t+\theta\big) \\ &= A(t)\ \cos\ \phi(t)\ , \end{aligned} \tag{3.1}$$

where $A(t)$ is the *instantaneous amplitude*, θ the initial phase shift, and $\omega(t) = 2\pi f(t)$ the *instantaneous frequency*, in rad/s or Hz, respectively. The cosine argument $\omega(t)\cdot t+\theta$ forms the *instantaneous phase* $\phi(t)$, therefore $\omega(t) = \dot{\phi}(t)$.

Each component can be also analytically expressed as a time-series of complex numbers $u(t) = \Re[u(t)] + Im[u(t)]$, or $u(t) = A(t)e^{i\phi(t)}$, where

$$\begin{aligned} A(t) &= |u(t)| = \sqrt{\Re[u(t)]^2 + \Im[u(t)]^2} \\ \phi(t) &= \langle u(t) \rangle = \arctan\big(\frac{\Im[u(t)]}{\Re[u(t)]}\big) \ . \end{aligned} \tag{3.2}$$

The EEG signal, for example, generates from the superposition of components having different frequencies. The components are affected by noise and their frequencies and amplitudes are time-variable. Therefore, trying to characterise features and dynamics of such signals by observing their time-domain can be an arduous task. In this case, transforming to the frequency domain can lead to a simpler representation of the information contained in the signal.

Historically, the most wide-spread tool to perform this task is the Fourier transform (FT) (Fourier, 1822), along with its time-localised version, the windowed-Fourier transform (WFT) (Gabor, 1946). Another tool to expand a signal into its time-frequency domain is the Wavelet transform (Daubechies, 1990, Stefanovska et al., 1999). In the next section the performance of the 3 methods will be compared on numerically simulated EEG signals (Clemson et al., 2016). The most suitable method will then be applied on the real data.

3.1.2 Fourier transform

The FT dates back to 1822, when Joseph Fourier proved how some functions could be decomposed into an infinite sum of harmonics (Fourier, 1822). Each point- in frequency- of the FT is proportional to the amplitude of the corresponding frequency component, and is given by the following integral:

$$FT(f) = \int_{-\infty}^{+\infty} s(t)e^{-i2\pi ft}dt \ . \tag{3.3}$$

The FT does not take into account time-variability, and it is reliably applicable only under the assumption of infinite and stationary signals. In real life, this is never the case. Therefore, even if the FT can give an initial glance to the spectral content of a time-series, artefacts due to non-infinity and non-stationarity are likely to mask the real spectral information.

The transformation from time to frequency domain in the FT preserves the number of points in the signal, so that a time-series $s(t_{1:N})$ with N samples is converted into a $FT(f_{1:N})$, with also N samples. For real signals, $FT(f_n)$ is symmetric, hence the informative samples are $n = 1 : N/2$. In summary, the frequency axes of FT is linearly divided in bins with width $\Delta f = F_s/N$, and ranges from the slower detectable component having $f_{min} = F_s/N$ to the highest with $f_{max} = F_s/2$.

3.1.3 Windowed Fourier transform

An extension of the FT is the Windowed Fourier transform (WFT) (Gabor, 1946). By computing the FT on consecutive epochs of the time-series, it allows one to expand the signal in both time and frequency domain. It is defined as:

$$WFT(f,t) = \int_0^{+\infty} s(u)g(u-t)e^{-i2\pi fu}du \; , \tag{3.4}$$

and it consists, for every frequency step, in the FT of the convolution of the signal $s(t)$ with a windowing function $g(t)$.

A common choice for $g(t)$ is a Gaussian function:

$$g(t) = \frac{1}{\sqrt{2\pi}f_0} e^{\frac{-t^2}{2f_0^2}} \; , \tag{3.5}$$

where the adimensional parameter f_0, called *resolution parameter*, defines the width of the window, and therefore tunes the ratio between time and frequency resolution.

Fig. 3.1 shows how the parameter f_0 acts over the extension of the Gaussian windowing function, which is independent of the investigated frequency f. The frequency step

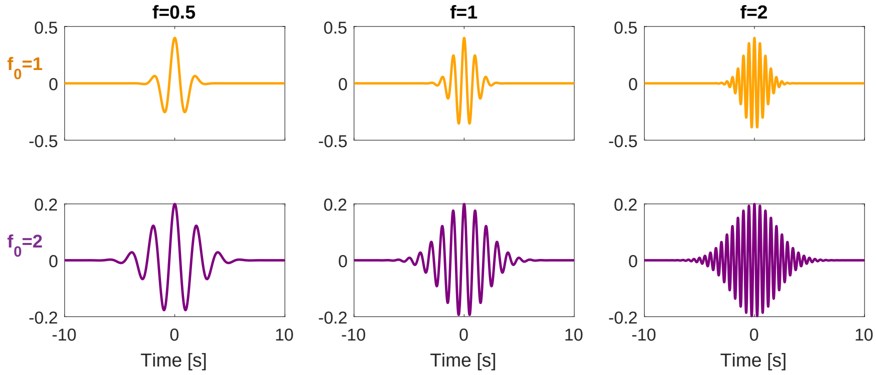

FIGURE 3.1: Effect of the f_0 parameter in the construction of the windowing function of the WFT for different frequencies f. Note the length of the window does not depends on the investigated frequency f. Vertical axes are adimensional.

is linear, therefore every frequency step is equal to the previous step $+\Delta f_w$. The frequency discretisation is obtained by choosing $\Delta f_w = F_s/N_w$, where N_w is the number of samples included in the windowing function.

Time-frequency resolution is a crucial in time-frequency analysis. As a matter of fact, the indetermination principle puts a limit on how precisely the frequency and time-localisation of a specific component can be detected. This is due to the need of using a higher number of samples N to achieve a smaller Δf (as $\Delta f = F_s/N$). At the same time, a longer window will insert uncertainty on where exactly –in time– the oscillation is placed. The lower frequency limit is also affected by the length of the chosen windowing function, as $f_{min} = F_s/N$.

3.1.4 Continuous Wavelet transform

The last method for time-frequency representation presented here is the continuous Wavelet transform (WT). Similarly to the WFT, it involves a windowing function (in this case called wavelet function, $\psi(u)$), and allows one to investigate the components of a time series in the time-frequency domain. The main difference between the two methods is the presence of a scaling factor of the wavelet which allows one to adjust the length of the window (i.e. the time/frequency resolution) to each investigated frequency, with logarithmic spacing. In this work, the fineness of the frequency discretisation is determined by the *number-of-voices* parameter μ, so that the next frequency equals the previous one multiplied by $2^{1/\mu}$. The choice of μ is linked with the analytical limit of frequency resolution depending on the length of the wavelet function (Iatsenko et al., 2015).

The WT is defined as

$$WT(a,t) = \int_0^\infty s(u)\psi\Big(\frac{u-t}{a}\Big)\frac{du}{a}\;, \tag{3.6}$$

where the scale a is inversely proportional to the investigated frequency f, with a relationship depending on the specific ψ. A common choice for ψ is the complex Morlet wavelet, defined as:

$$\psi_M(x) = \frac{1}{\sqrt{2\pi}}(e^{i2\pi f_0 x} - e^{-\frac{(2\pi f_0)^2}{2}})e^{\frac{-x^2}{2}}\;, \tag{3.7}$$

where f_0 is the *resolution parameter* and x is the adimensional quantity $(u-t)/a$ of Equation 3.6. Similiarly to the WFT, f_0 it adjusts the time/frequency resolution. A convenient feature of the complex Morlet wavelet is that there is a direct relationship between scale and frequency, being $a = f_0/f$. Considering this, the equation for the WT becomes

$$WT_M(f,t) = \int_0^\infty s(u)\psi_M\Big(\frac{f(u-t)}{f_0}\Big)\frac{f}{f_0}du\;. \tag{3.8}$$

Figure 3.2 shows how the parameter f_0 determines the number of oscillations embedded underneath the Gaussian window. Note that, regardless of f_0, the same number of periods of the oscillation with frequency f are included in the wavelet, therefore a higher f_0 generates a longer wavelet function. This was not the case for the WFT (Figure 3.1).

3.1.5 Simulated EEG to compare time-frequency representations

A synthetic signal $s(t)$ has been generated by simulating the EEG frequency content, i.e. by the overlapping of 5 oscillations having time-variable frequencies centred around $F_i = [2,5,10,20,40]$ Hz and amplitude $A_i = [6,5,4,3,2]\ \mu V$. For simplicity, no coupling

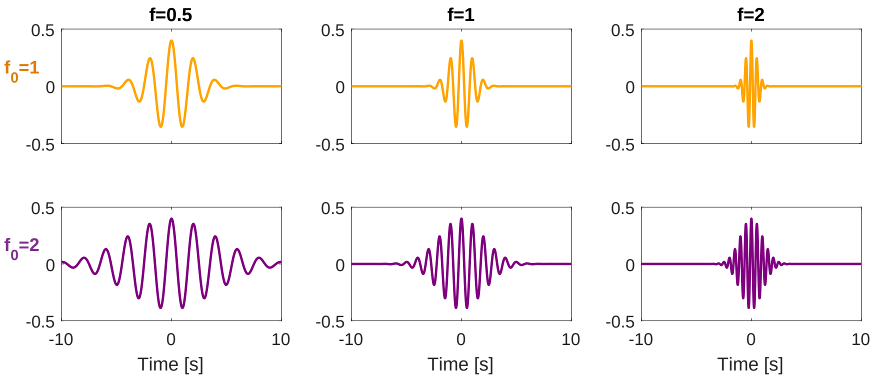

FIGURE 3.2: Effect of the f_0 parameter in the construction of the wavelet function of the WT for different frequencies f. Note that the length of the window depends on the investigated frequency f. Vertical axes are adimensional.

has been set between them. To simulate the dataset analysed in this work, the length of the signal was 60s, and the sample frequency $F_s = 256$ Hz. Each component $x_i(t)$, with $i = 1 : 5$, was generated so that both the speed and amount of the variability, were proportional to the average frequency F_i with $f_i(t) = F_i - 0.2F_i\ \sin(2\pi\, 0.025\, F_i\, t)$. The phase of each component was computed by adding noise to the time variable frequency, by the relation

$$\phi_i(t) \quad = \big(2\pi f_i(t) + \xi(t)\big) \cdot t\ , \tag{3.9}$$

including the noise $\xi(t)$ modelled as white Gaussian $\langle \xi(t)\xi(\tau)\rangle = \delta(t-\tau)D$. The simulation was run twice: (i) with no noise ($D = 0$) and (ii) with noise intensity $D = 5$. Finally the simulated signal was reconstructed as

$$s(t) \quad = \textstyle\sum_{i=1}^{5} A_i\ \cos(\phi_i(t) + \theta_i)\ , \tag{3.10}$$

with θ_i random initial phase shifts.

The capability of the methods to correctly resolve the different components of $s(t)$ have been tested for the classical FT and for both WFT and WT (with resolution parameters $f_0 = [1, 2, 3]$). Power spectra from WFT and WT are calculated by time-averaging the square of the absolute values of the time-frequency representation, i.e. by $\langle |WFT(f,t)|^2\rangle_t$

and $\langle |WT(f,t)|^2 \rangle_t$.

A window of 2s of each x_i is plotted in the first panel of Figure 3.3, with the corresponding simulated EEG obtained by their summation (in the second panel). The FT power of the full signal is shown in the third panel, where the groups of spikes corresponding to each component are still recognisable.

Middle panels in Figure 3.3 show the performance of WFT. It can be seen how, with the increasing of f_0, the time resolution becomes more blurred. Especially for the higher frequency component, the average spectra resemble the spikes in the FT.

Bottom panels in Figure 3.3 show the performance of WT. The effect of f_0 is more evident here, with the ridges being better resolved in the time-frequency domain for higher values of f_0. However, in the time-averaged domain the higher frequency resolution leads to the emergence of 'double-bumps' in the spectra, which could trick the observer in splitting a single mode into two.

The effect of noise is evident in the time-evolution of the single components in the first panel of Figure 3.4, and not so clear in the time-evolution of the signal $s(t)$ in the second panel. In the FT of the whole signal, the presence of specific components is barely distinguishable underneath the noise.

The time-frequency representations give a better insight into the power distribution. Even if the evolution of the ridges is less clear in presence of noise, the time-average spectra are all able to isolate the single components. For the WFT, the main effect of increasing the resolution parameter is a more spike-like frequency resolution. For the WT, increasing f_0 gives two-fold effects: it improves the resolution of the individual components, and at the same time amplifies the 'double bump' effect for each of them.

3.1.6 Conclusions about the time-frequency representation

An important consideration on the choice between WT and WFT regards the number of points included in each frequency band. In the case of EEG, the frequency range 0.8-48

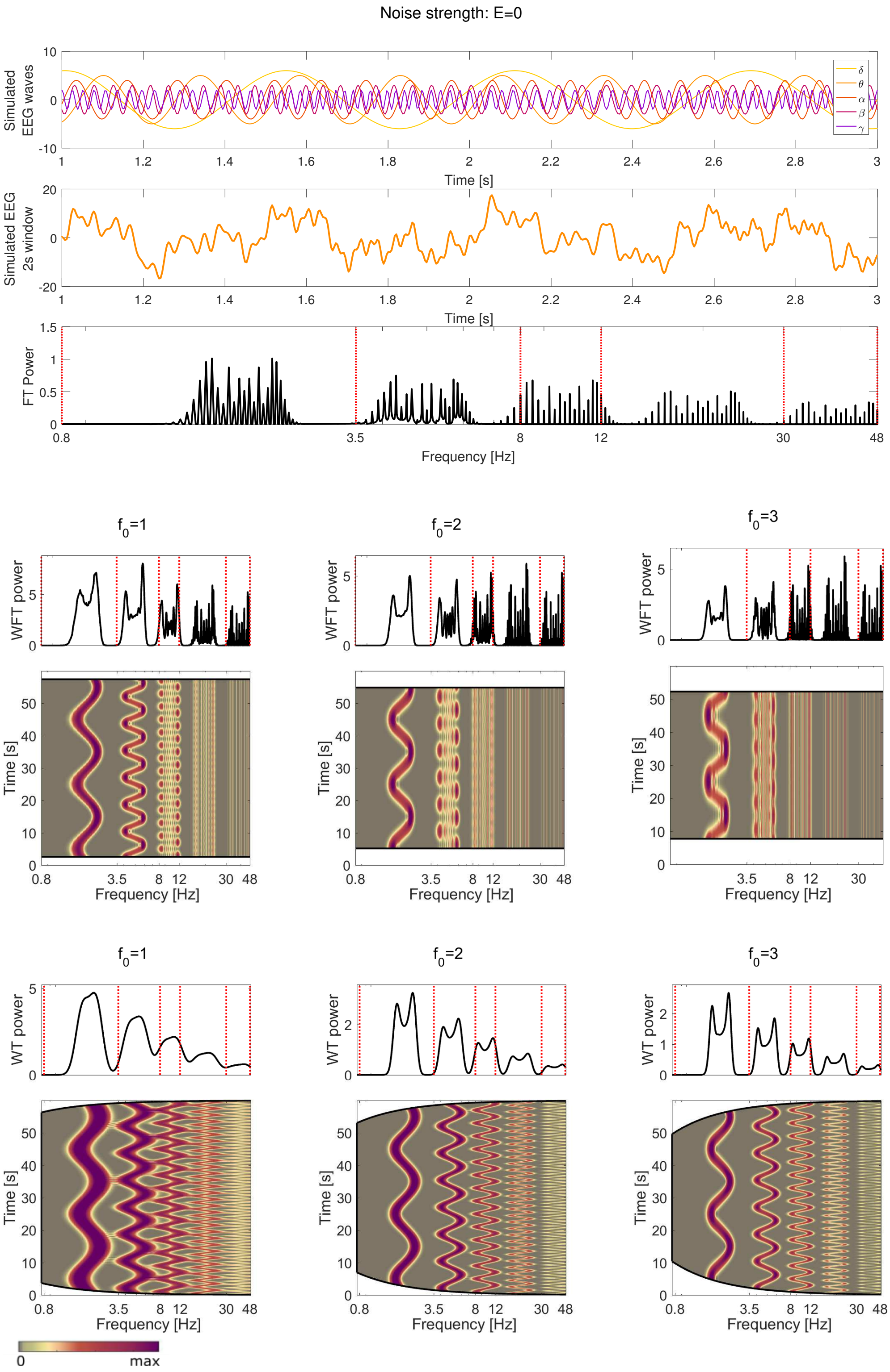

FIGURE 3.3: Simulation of EEG signal from Equation 3.10 with time-variable frequencies and no noise. Individual bands, summed time series and FT power spectra (on a logarithmic frequency scale) are shown on the top panels. To compare the performance of the two methods, WFT and WT are computed for different values of the resolution parameter f_0. Note how f_0 modulates the compromise between time and frequency resolution of the ridges.

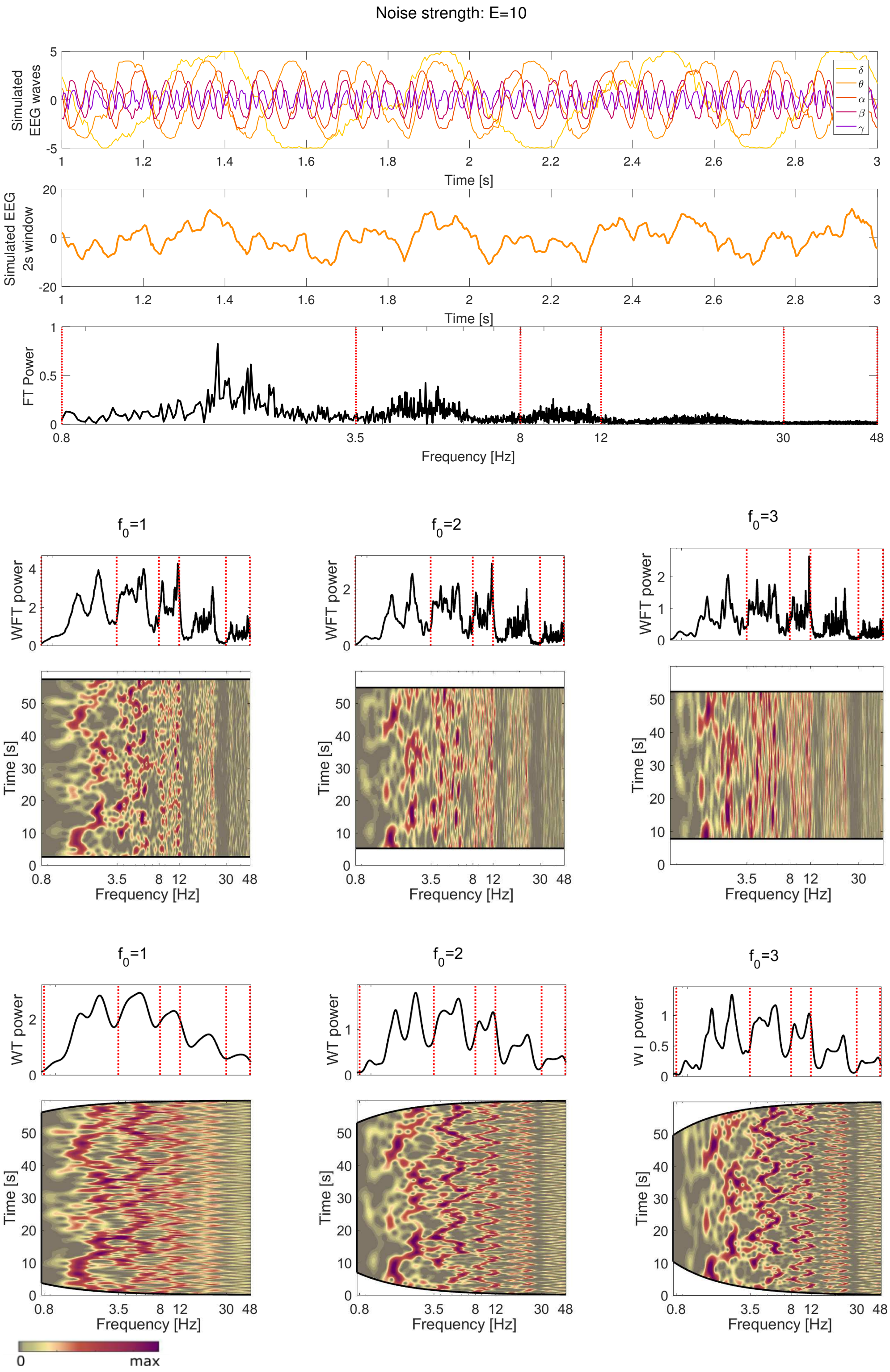

FIGURE 3.4: Simulation of EEG signal from Equation 3.10 with time-variable frequencies and noise intensity $E = 10$. Individual bands, summed time series and FT power spectra (on a logarithmic frequency scale) are shown on the top panels. To compare the performance of the two methods, WFT and WT are computed for different values of the resolution parameter f_0. Note how f_0 modulates the compromise between time and frequency resolution of the ridges.

Hz is conventionally divided in 5 intervals: delta (0.8-3.5 Hz), theta (3.5-8 Hz), alpha (8-13 Hz), beta (13-30 Hz) and gamma (30-48 Hz) bands, which are respectively 2.7, 4.5, 5, 17, 18 Hz wide. In the case of the WFT, as the frequency resolution is linear, the delta interval contains about 1/7 of the samples contained in gamma band. For the WT, with the number-of-voices parameter $\mu = 33$, the number of point for each interval are respectively 70, 39, 23, 40, 22. Therefore, for this case, the logarithmic resolution allows for a more uniform distribution of the information between the intervals of interest.

For this reason, and for its capability of better resolving closer components at mid-high frequency, the further analysis will be performed with WT and $f_0 = 2$.

For the real data, the relative power is also computed in order to investigate how spectral content is distributed, regardless of its amplitude. Relative power is computed by dividing each frequency sample by the sum of the total spectra, and therefore has unitary area. It is better to talk about *area* instead of *integral* because the logarithmic spacing of the frequency axes could lead to a misleading interpretation. As a matter of fact, the WT is defined on the logarithmic scale, therefore bins on the lower part of the spectra have a narrower base than the ones on the higher counterpart. This effect is counterbalanced by the stretch due to the logarithmic representation. Talking about 'integral' would imply weighting each bin by the absolute extension of its base, which in this case is non correct.

3.2 Wavelet phase coherence

Defining the phases ϕ as the angle of the WT coefficient, i.e. $\phi(f,t) = \arctan(\frac{\Im(WT(f,t))}{\Re(WT(f,t)})$, the Wavelet phase coherence (WPC) between two signals was determined as

$$WPC(f) = \frac{1}{N}|\sum_{n=1}^{N} e^{i(\phi_1(f,t_n)-\phi_2(f,t_n))}| \,, \tag{3.11}$$

which is equivalent to

$$WPC(f) = \sqrt{\left(\frac{1}{N}\sum_{n=1}^{N}\sin\left(\Delta_\phi(f,t_n)\right)\right)^2 + \left(\frac{1}{N}\sum_{n=1}^{N}\cos\left(\Delta_\phi(f,t_n)\right)\right)^2} \,, \tag{3.12}$$

where Δ_ϕ is equal to $\phi_1 - \phi_2$ (Sheppard et al., 2012).

For signals which perfectly preserve the phase difference in time, i.e. $\Delta_\phi(f, t_n) = \delta_{const}(f)$, the value of WPC will be

$$\begin{aligned} WPC_{const}(f) =& \sqrt{\langle \sin(\delta_{const}(f)) \,\rangle_t^2 + \langle \cos(\delta_{const}(f)) \,\rangle_t^2} \\ =& \sqrt{\sin(\delta_{const}(f))^2 + \cos(\delta_{const}(f))^2} = 1 \,. \end{aligned} \tag{3.13}$$

On the contrary, for signals with perfectly random phase difference in time, i.e. $\Delta_\phi(f, t_n) = rand[0\ 2\pi] = \delta_{rand}(f, t)$, WPC will assume the value of

$$\begin{aligned} WPC_{rand}(f) &= \sqrt{\langle \sin(\delta_{rand}(f,t)) \,\rangle_t^2 + \langle \cos(\delta_{rand}(f,t)) \,\rangle_t^2} \\ &= \sqrt{0 + 0} = 0 \,. \end{aligned} \tag{3.14}$$

More complicated relationships give intermediate coherence between 1 and 0.

By definition, WPC depends strictly only on the phases, and is therefore independent of the amplitude of the signals.

Time-localised Wavelet phase coherence WPC$_{TL}$ (Sheppard et al., 2012) was computed for simulated time-series as well, by applying equation 3.11 to windows of the signals containing 10 periods of the corresponding frequency. This computation, albeit having the advantage of making time-localisation of coherent epochs possible, is based on a lower number of samples than the non-time-localised one, and therefore produces values of coherence which are more susceptible to the effect of random phenomena.

3.2.1 Simulated EEG to test coherence analysis

Two synthetic signals $s_1(t), s_2(t)$ have been generated, characterised by central frequencies of $f_1 = 10$ Hz and $f_2 = 11$ Hz. This time, the signals were coupled with a diffusive coupling acting from s_1 to s_2, which by construction increases in strength the more the phases of the two oscillators differ. In other words, the diffusive coupling acts to synchronise the two oscillators by making their phases more coherent against the difference in the oscillators' natural frequencies. This type of coupling has been extensively studied, and it is the base of the Kuramoto model for coupled phase oscillators (Kuramoto, 1984). The described system was constructed as:

$$\begin{cases} \dot{\phi}_1(t) & = 2\pi f_1(t) + \xi_1(t), \\ \dot{\phi}_2(t) & = 2\pi f_2(t) + C(t) \sin\big(\phi_1(t) - \phi_2(t)\big) + \xi_2(t) \ , \end{cases} \tag{3.15}$$

where the dynamical noise $\xi(t)$ was again modelled as white Gaussian $\langle \xi(t)\xi(\tau)\rangle = \delta(t-\tau)D$ (Stankovski et al., 2012).

Here and in what follows, the differential equations are integrated by applying the Heun method: calling $\dot{\phi}(t) = f(t, \phi(t))$, h the time sampling and $t_{i+1} = t_i + h$, the algorithm calculates at each integration step a temporary value $\tilde{\phi}_{i+1} = \phi_i + hf(t_i, \phi_i)$ and then the final approximation $\phi_{i+1} = \phi_i + \frac{h}{2}[f(t_i, \phi_i) + f(t_{i+1}, \tilde{\phi}_{i+1})]$ at the next step.

The simulation was run twice: (i) with time-constant coupling strength $C(t) = 6$ Hz, and (ii) with time variable strength $C(t) = 6 + 6 \cdot \sin(0.2\ t)$ Hz (which has time average $\langle C(t)\rangle = 6$ Hz). The noise was set low, for simplicity, with strength $D = 0.0002$. Finally the simulated signals were reconstructed with time variable amplitudes $A_1(t), A_2(t)$, so that the envelope of the signal was uniformly and randomly varying at 10 and 11 Hz respectively. This was achieved by linearly interpolating a random sequence of amplitude values (between 0 and 1, 10 and 11 values for every second of the time series s_1 and s_2 respectively) with the Matlab function `spline` to match the signal sampling and by multiplying them to the sinusoidal, i.e.

$$\begin{cases} s_1(t) & = 2A_1(t)\ \cos(\phi_1(t)) \\ s_2(t) & = A_2(t)\ \cos(\phi_2(t)) \ . \end{cases} \tag{3.16}$$

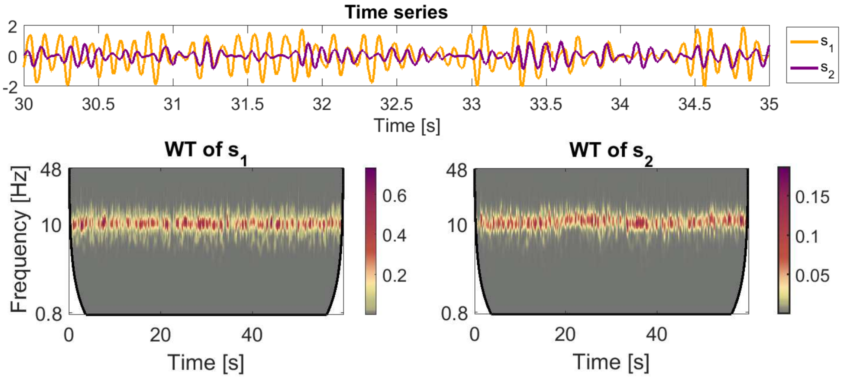

FIGURE 3.5: A 5s window of the simulated time-series of Equation 3.16, and their full-length wavelet transform. Note the uncorrelated amplitude of the signals, and the effect of the coupling in the frequency variability of the ridge in the WT of s_2

A window of 5s of the time-series is plotted in Figure 3.5, together with the WT, for the time-variable coupling case (with resolution parameter $f_0 = 1$). Note how, in the top panel, the amplitude of the signals is uncorrelated, and the phases are transitioning from a state of incoherence to a state of coherence. This happened because the time-window corresponds to the ascending part of the coupling strength, as will be discussed in Figure 3.8. Also note how the ridge in the Wavelet transform of s_1 was stable in time around 10Hz, while for s_2 the frequency slightly varied in time because of the variable strength of the coupling.

The case with constant coupling $C(t) = 6$ Hz is analysed first. Figure 3.6 shows the time series, the value of the coupling, and the time-localised plots of WPC$_{TL}$, with the coherent ridge correctly centred around 10 Hz.

The time average of WPC$_{TL}$ (in purple) is presented on the top left panel in Figure 3.7. The results for the non-time-localised computation are reported on the right-side panel. The threshold generated by 100 Fourier transform surrogates (as explained in Section 3.5) is shaded in corresponding colours. The bottom panels show the *effective coherence*, i.e. the positive results of the subtraction between a coherence plot and the corresponding surrogates. It can be noted how both time-localised and non time-localised computations correctly isolated the coherent frequency band centred around 10 Hz. However, the time-localised computation produced both higher spurious coherence outside the relevant

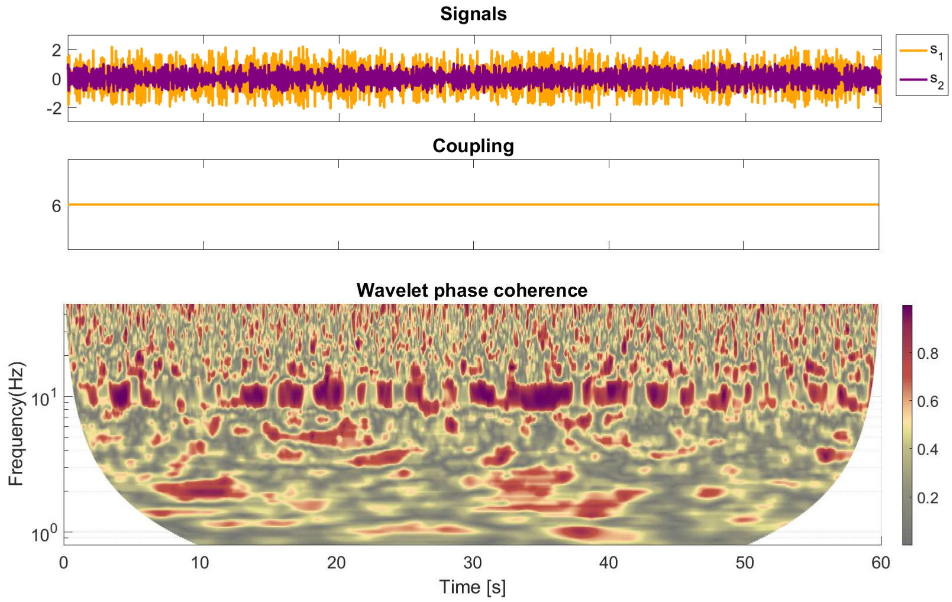

FIGURE 3.6: Simulation of time series of Equation 3.16 with constant coupling. Note that the ridge around 10 Hz in the time-localised Wavelet phase coherence corresponds to the frequency of the coupled oscillators.

frequency interval and a higher surrogate threshold within the coherent frequency band. This led to a less pronounced effective coherence for the time-localised case.

For the time-variable coupling ($C(t) = 6 + 6\sin(0.2\,t)$ Hz), results were similar. Figure 3.8 illustrates the time series, the time-evolution of the variable coupling and WPC$_{TL}$. The latter shows how the coherent ridge centred around 10 Hz was not maintained in

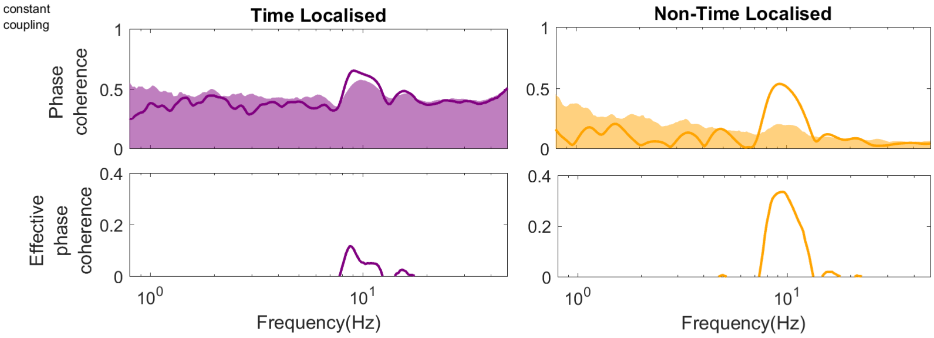

FIGURE 3.7: Comparison between time-localised (in purple) and non-time-localised Wavelet phase coherence (in orange) for a time-constant coupling. On the top, the surrogate level is shaded in same colours. On the bottom panels, the surrogate level is subtracted from the coherence, and only the positive parts (effective coherence) are shown. Note that the peak at 10 Hz is higher for the non time-localised version.

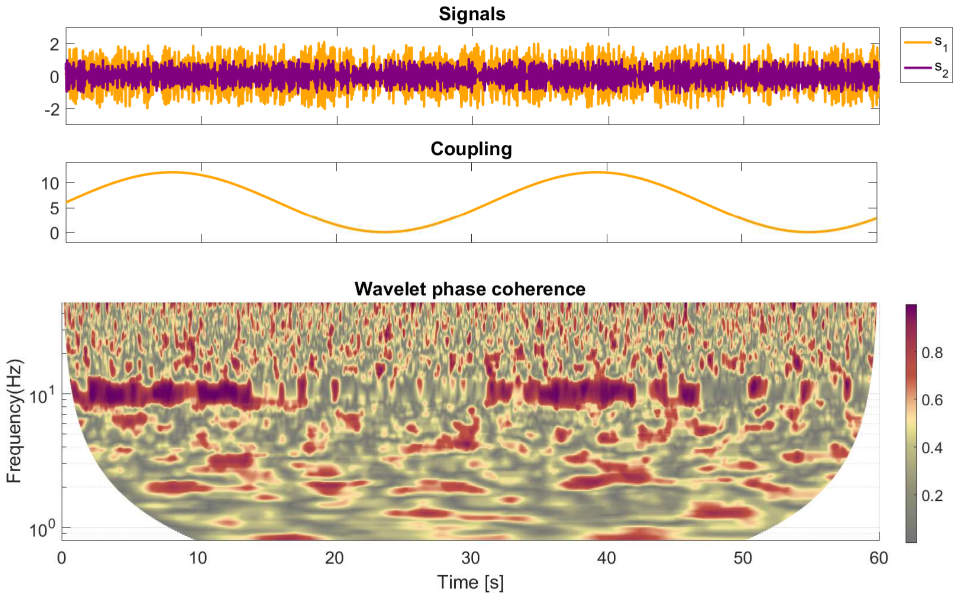

FIGURE 3.8: Simulation of time series of Equation 3.10 with time-variable coupling. The ridge around 10 Hz in the time-localised Wavelet phase coherence corresponds to the frequency of the coupled oscillators, and appears in correspondence of the time-windows with higher coupling.

time, like in the case of constant coupling, but appeared when the coupling strength went above ∼5 Hz. Being the average value of the time-variable coupling strength equal to the previously discussed case of constant coupling strength, the time-average values of Figure 3.9 are comparable to the values shown in Figure 3.7. The non-time localised case produced lower coherence in the band of interest when compared to the constant-coupling

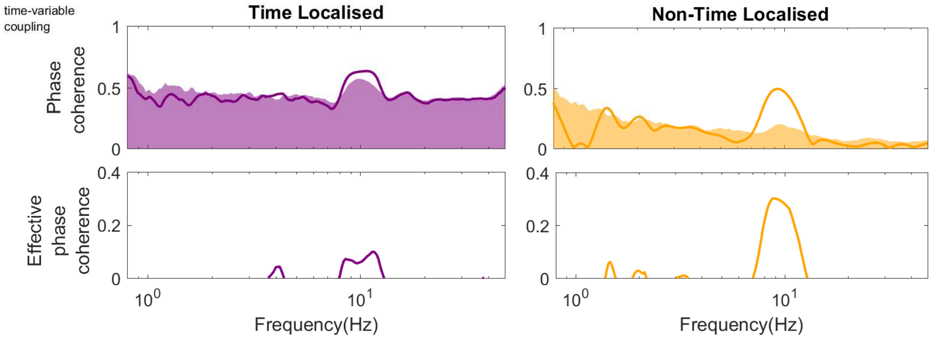

FIGURE 3.9: Comparison between time-localised (in purple) and non-time-localised Wavelet phase coherence (in orange) for a time-variable coupling. On the top, the surrogate level is shaded in same colours. On the bottom panels, the surrogate level is subtracted from the coherence, and only the positive parts (effective coherence) are shown. Note that the peak at 10 Hz is higher for the non time-localised version.

case, together with some spurious effective coherence at lower frequencies.

3.2.2 Conclusions about the coherence investigations

The numerical simulation highlighted the loss of effective coherence when the time-localisation is requested. This effect is probably due to the reduced number of periods of the oscillations included in each time-window. Because the EEG signals involved in this study are recorded in resting state, and there is no time-correspondence between data obtained from different subjects, coherence computation will be performed with non-time localised wavelet phase coherence. In order to compare the results, the values of coherence reported in this work correspond to the average value of WPC both in time and within each investigated frequency interval.

3.3 Cross-frequency coupling

As introduced in Section 3.2, the mutual adjustments of oscillating rhythms can be expressed as an inter-dependence between the phases and frequency of the oscillators involved. However, albeit the coherence analysis can detect the *presence* and *strength* of same-frequencies relationship (Sheppard et al., 2012, Varela et al., 2001), it can not provide any information about the *mechanism* of the coupling. As a matter of fact, two oscillators can be highly coherent, i.e. evolving with the same frequency, without being actually coupled.

In what follows, the focus will be directed on coupling existing between different frequencies (cross-frequency coupling) by modelling the data as systems of interacting phase oscillators (Kuramoto, 1984, Stankovski et al., 2015). The coupling information from such systems can be expressed in the form of a coupling function (Rosenblum and Pikovsky, 2001, Stankovski et al., 2012).

The coupling function's decomposition enables one to isolate the functional contribution of each component of the system to the overall coupling relationship (Iatsenko et al., 2013, Stankovski et al., 2015). Therefore, the study of coupling functions not only provides information of existence and strength of the coupling, but also enables one to go deeper in the characterisation of an interaction by describing the *mechanisms* underlying the functional connectivity of a network.

For these reasons, extraction and reconstruction of coupling functions between interacting oscillatory processes has been recently performed on multiple fields of science, including brain dynamics (Stankovski, 2017), cardiorespiratory interactions (Iatsenko et al., 2013, Kralemann et al., 2013, Stankovski et al., 2012, Ticcinelli et al., 2017), chemistry (Kiss et al., 2005, Miyazaki and Kinoshita, 2006, Tokuda et al., 2007), and secure communications (Stankovski et al., 2014b).

In this section it will be also shown how, by the means of the Dynamical Bayesian Inference, it is possible to infer the coupling parameters characterising the existent interactions from the data (Duggento et al., 2012, Stankovski et al., 2012).

3.3.1 Coupling decomposition

The diffusive coupling applied in Section 3.2 is one of the possible types of cross-frequency phase interaction. As a matter of fact, the same mathematical framework can be extended to a network of N interacting units subject to dynamical noise and governed by different time-varying relationships.

Assuming that the coupling is weak enough, such systems can be investigated by studying their phase dynamics (Kuramoto, 1984, Pikovsky et al., 2001). To do so, a system of N stochastic differential equations with time varying parameters can be built as

$$\dot{\phi}_i(t) = \omega_i(t) + q_i(\phi_1, \ldots, \phi_N, t) + \xi_i(t) \ , \tag{3.17}$$

with $i = 1, \ldots, N$. The equation shows how the instantaneous frequency of each oscillator $\dot{\phi}_i(t)$ is generated by the sum of a deterministic part, composed by the natural frequency ω_i and the coupling function q_i, and a stochastic part represented by ξ_i, which is modelled as Gaussian white noise such that $\langle \xi_r(t)\xi_s(\tau)\rangle = \delta(t-\tau)D_{r,s}$ (Stankovski et al., 2015).

By focusing on the deterministic part, it is evident how the natural frequency ω_i undergoes an additive modulation by the means of the coupling function q_i. Note that this form of coupling has been used in Equation 3.15 to model the diffusive coupling. The difference is that, this time, the coupling function q_i is general, and depends both on time and on the phases $\phi_{1,\ldots,N}$ of the oscillators composing the network – including the self-dynamics. In this configuration, the diffusive pairwise coupling previously discussed is one of the several interactions inferred from the network.

3.3.1.1 Decomposition according to the coupling order

The coupling function q_i in Equation 3.17 encompasses all the frequency-modulation acting on the oscillator i. One of the possibilities to gain detailed insights into the mechanism of the interaction is to decompose q_i into the sum of partial contributions. This can be done according to the different *order* of coupling (Iatsenko et al., 2013, Stankovski et al., 2014a), where the coupling of order k depends on the phases of k oscillator, i.e.

$$\begin{aligned}\dot{\phi_i}(t) = \omega_i(t) + \sum_l q_i'(\phi_l, t) + \sum_{lm} q_i''(\phi_l, \phi_m, t) + \\ + \sum_{lmn} q_i'''(\phi_l, \phi_m, \phi_n, t) + \ldots + \xi_i(t)\ .\end{aligned} \tag{3.18}$$

In Equation 3.18, q_i' represents the coupling from one oscillator, q_i'' the coupling from two oscillators, and so on.

Under the assumption that the deterministic part of the differential Equation 3.17 is quasiperiodic, it can be decomposed by the means of Fourier approximation into a sum of base functions $\Phi_k = \exp[\imath(k_1\phi_1 + k_2\phi_2 + \ldots + k_N\phi_N)]$ (Duggento et al., 2012, Kralemann et al., 2011), where $k_{1:N}$ can assume the value from -K to K, where K is the order to which the Fourier approximation is stopped.

The base functions are modulated by the set of time-varying parameters $\mathbf{c}_k^{(i)}$

$$\dot{\phi}_i(t) = \sum_{k=-K}^{K} \mathbf{c}_k^{(i)} \mathbf{\Phi}_k(\phi_1, \phi_2, \ldots, \phi_n) + \xi_i(t) \; . \tag{3.19}$$

By decomposing Equation 3.19 in the same way as in in Equation 3.18, it is possible to isolate the different orders of the network coupling:

$$\begin{aligned}\dot{\phi}_i(t) = \mathbf{c}_0^{(i)} &+ \sum_{k=-K}^{K} \mathbf{c}'^{(i:l)}_k \mathbf{\Phi}_k(\phi_l) + \sum_{k=-K}^{K} \mathbf{c}''^{(i:l,m)}_k \mathbf{\Phi}_k(\phi_l, \phi_m) \\ &+ \sum_{k=-K}^{K} \mathbf{c}'''^{(i:l,m,n)}_k \mathbf{\Phi}_k(\phi_l, \phi_m, \phi_n) + \ldots + \xi_i(t) \; ,\end{aligned} \tag{3.20}$$

where $k \neq 0$ and the sums over $l, m, n = 1, \ldots, N$ with $l \neq m \neq n$ are implicit.

In this configuration, for each oscillator i the vector of coefficients $\mathbf{c}^{(i)}$ assumes different functional meanings with the different superscripts:

- $\mathbf{c}_0^{(i)}$ represents the natural frequency ω_i of the oscillator (one element)
- $\mathbf{c}'^{(i)}$ groups the coefficients of all the couplings coming from one oscillator, of the type $\substack{\sin \\ \cos}(k_1\phi_l)$. It defines $2 \cdot K \cdot N$ elements
- $\mathbf{c}''^{(i)}$ contains the coefficients of all the combinations of couplings from two oscillators, of the type $\substack{\sin \\ \cos}(k_1\phi_l \pm k_2\phi_m)$. It defines $2^2 \cdot K^2 \cdot \binom{N}{2}$ elements
- $\mathbf{c}'''^{(i)}$ contains the coefficients of all the combinations of couplings from three oscillators, of the type $\substack{\sin \\ \cos}(k_1\phi_l \pm k_2\phi_m \pm k_3\phi_n)$. It defines $2^3 \cdot K^3 \cdot \binom{N}{3}$ elements.

The maximum values of the superscript that $\mathbf{c}^{(i)}$ assumes indicates the order of coupling assumed for the network, i.e. the maximum number of oscillators involved into a coupling action. Considering this, the overall number ν of elements for the matrix $\mathbf{c}$ characterising a coupled network where the coupling order is stopped at the value Λ is given by

$$\nu = N \cdot \sum_{\lambda=0}^{\Lambda} 2^{\lambda} \cdot K^{\lambda} \cdot \begin{pmatrix} N \\ \lambda \end{pmatrix} . \tag{3.21}$$

3.3.1.2 Decomposition according to the oscillators involved

A further coupling classification could be performed based on the distinction between couplings coming from a group of oscillators which includes - or does not include- the one on which the coupling is acting on (Stankovski et al., 2015). The following terminology will be used:

- In the case of coupling coming from a single oscillator
    - if the source and the target of coupling are the same $q_A(\phi_A) \rightarrow$ *self-coupling*
    - If the source and the target of coupling are different $q_B(\phi_A) \rightarrow$ *direct-coupling*
- When the coupling comes from two (or more) oscillators:
    - If the target oscillator is among the sources $q_B(\phi_A, \phi_B) \rightarrow$ *common from two (or more)*
    - If the target oscillator is not among the sources $q_B(\phi_A, \phi_C) \rightarrow$ *direct from two (or more)*

In order to appreciate the physical meaning of the different coupling components, in what follows some examples of time series coupled uniquely by self and direct coupling will be presented. The time series are reconstructed from the phases simply by the relations: $s_1(t) = \sin\big(\phi_1(t)\big)$ and $s_2(t) = \sin\big(\phi_2(t)\big)$.

In the following examples, the $c_{i:\sigma}\sin(\phi_\sigma + 0.3\pi)$ coupling to the oscillator i from the group of oscillators σ will be introduced in the differential equations. The choice of $\sin$ over $\cos$, and the phase shift $+0.3\pi$ are purely arbitrary. Intuitively, one could be tricked in thinking that the effects of sin coupling and cos would cancel out each other, but this is not true. The presence of the $c_{i:\sigma}\cos(\phi_\sigma)$ would produce analogue effect on the time series, 0.5π-shifted in the evolution of the driving wave. The simultaneous presence of both would result into a superimposed effect, by affecting the instantaneous frequency of driven oscillator both at the $\pm 0.5\pi$ (for $c_{i:\sigma}\sin(\phi_\sigma)$ coupling) and $0,\ 2\pi$ (when $c_{i:\sigma}\cos(\phi_\sigma)$ coupling is present) phase of the driver.

Self-coupling

In this section, the physical meaning of *self coupling* in the case of coupled phase oscillators will be discussed. In order to appreciate the effect of this specific component, a system is constructed as

$$\begin{cases} \dot{\phi}_1(t) & = 2\pi f_1(t) + c_{1:1}\sin\left(\phi_1(t) + 0.3\pi\right) + \xi_1(t) \\ \dot{\phi}_2(t) & = 2\pi f_2(t) + \xi_2(t)\ , \end{cases} \tag{3.22}$$

with $f_1 = 1\,\text{Hz}$, $f_2 = 4$ Hz, and $c_{1:1}$ assuming iteratively the values [0, 1, 2, 3, 4, 5]. For simplicity, the Gaussian noise $\xi_1 = \xi_2$ was kept very low with noise strength $D = 0.0002$.

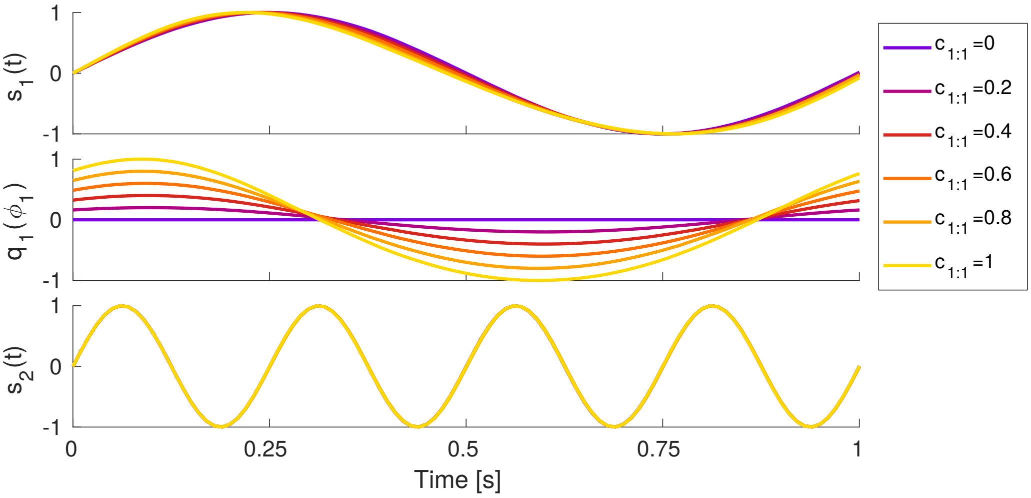

FIGURE 3.10: Effect of self-coupling function $q_1(\phi_1) = c_{1:1}\sin\left(\phi_1(t) + 0.3\pi\right)$ in the time domain. Different strength of the coupling parameter $c_{1:1}$ are colour-coded from blue $c_{1:1} = 0$ to yellow $c_{1:1} = 1$. Note how a higher self-coupling increases the nonlinearity of s_1, while s_2 is not affected by the different coupling strengths.

Figure 3.10 illustrates the time evolution of the time series $s_1,\ s_2$ and of the coupling function $q_1(\phi_1)$. Note how the amplitude of the coupling function increases with the strength of $c_{1:1}$.

It can be seen in Figure 3.10 how the increasing of the self-coupling component acts on the time series by making it less 'linear', i.e. by deforming the purely sinusoidal shape of the oscillation. Note how, for purely explanatory reasons, the value of the self-coupling is pushed to 100% of the corresponding natural frequency in order to achieve a visible effect. The self-coupling part of the phase interactions carries limited physical meaning when looking for cross-frequency couplings.

Direct coupling

This section investigates the effect of unidirectional *direct coupling*. Both the cases of low-to-high frequency coupling and high-to-low will be generated with $f_1 = 1$ Hz, $f_2 = 4$ Hz, and $c_{1:2}$ and $c_{2:1}$ assuming iteratively the values [0, 2, 4, 6, 8, 10]. For simplicity, the Gausian noise $\xi_1 = \xi_2$ was again kept very low with noise strength $D = 0.0002$.

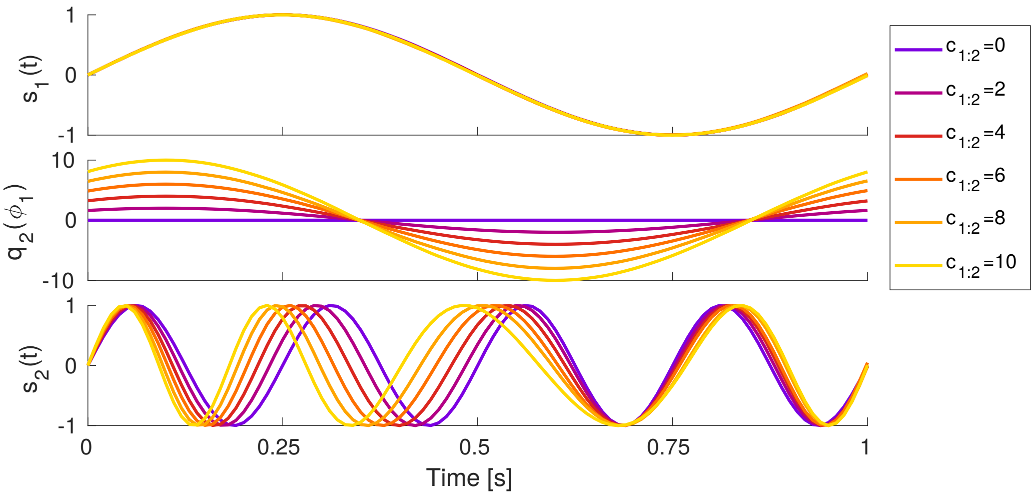

FIGURE 3.11: Effect of direct low-to-high coupling function $q_2(\phi_1) = c_{1:2} \sin\big(\phi_1(t) + 0.3\pi\big)$ in the time domain. Different strength of the coupling parameter $c_{1:2}$ are colour-coded from blue $c_{1:2} = 0$ to yellow $c_{1:2} = 10$. Note how higher direct-coupling increases the instantaneous frequency of s_2, while s_1 is not affected by the different coupling strengths.

In order to appreciate the effect of the low-to-high direct coupling, the system is constructed as

$$\begin{cases} \dot{\phi}_1(t) & = 2\pi f_1(t) + \xi_1(t) \\ \dot{\phi}_2(t) & = 2\pi f_2(t) + c_{2:1} \sin\big(\phi_1(t) + 0.3\pi\big) + \xi_2(t) \ , \end{cases} \tag{3.23}$$

with $c_{2:1}$ as the only non-zero coupling coefficient. Figure 3.11 shows the effect of this coupling on the time series. In the plot, $s_1(t)$ results are unaffected by the different coupling strength and the coupling function $q_2(\phi_1)$ corresponds to $q_1(\phi_1)$ of Figure 3.10. The analysis of the coupling function's effects on s_2, however, brings more interesting observations, as it is more clear how the position of the ridge and valley of $q_2(\phi_1) = c_{2:1} \sin\big(\phi_1(t) + 0.3\pi\big)$ are reflected on the time-evolution of the driven signal.

In Figure 3.11, the time-series s_2 evidently changes according to the value of the parameter $c_{2:1}$. The mechanism of this change can be understood by bearing in mind that the coupling function is added to the frequency of ϕ_1, and by following the time evolution of the two plots. In the first part of the plot, when $q_2(\phi_1)$ increases, the coupling accelerates the oscillation s_2, making it reach its maximum frequency when $q_2(\phi_1)$ has a maximum (which is at $0.5\pi - 0.3\pi$) in terms of phase evolution of ϕ_1). Then, $q_2(\phi_1)$ start decreasing, and as a consequence the frequency of s_2 decreases too, reaching its minimum at the minimum of $q_2(\phi_1)$ (or $1.75\pi - 0.3\pi$ in terms of phase evolution of ϕ_1). When $q_2(\phi_1) = 0$, the coupling has no effect on the instantaneous frequency of s_2: the curves corresponding to different values of $c_{2:1}$ are parallel around these time values. This type of coupling has a crucial physical meaning, as it is at the core of the cross-frequency phase modulation.

Very different scenario emerges when the direction of the direct coupling is inverted, i.e. when the high-to-low phase coupling is introduced into the system. To do so, the equations become:

$$\begin{cases} \dot{\phi}_1(t) & = 2\pi f_1(t) + c_{1:2} \sin\big(\phi_2(t) + 0.3\pi\big) + \xi_1(t) \\ \dot{\phi}_2(t) & = 2\pi f_2(t) + \xi_2(t) \ , \end{cases} \tag{3.24}$$

with $c_{1:2}$ the only coupling coefficient present in the system.

By examining Figure 3.12, it can be seen how in this case s_2 is not influenced by the different coupling strength, while the effect of the coupling is reflected on s_1. The physical nature of this coupling corresponds to the previously investigated case, with the instantaneous frequency of s_1 being increased and decreased according to the value of $c_{1:2} \sin\big(\phi_2(t) + 0.3\pi\big)$. However, in this case several periods of s_2 are contained within one full oscillation of s_1, and therefore the effect of this coupling exhausts itself within single periods of the slower oscillation. This mean that this type of coupling is not able to affect the *fundamental* frequency of the driven oscillator. Its effect on the time-evolution of s_1 is comparable to adding to the pure sinusoidal with frequency f_1 a higher frequency component (with frequency f_2).

The physical meaning of this type of phase coupling is therefore more limited than its corresponding counterpart. This is especially true when oscillations with very different fundamental frequencies need to be filtered out from a time series: in this case, the high-to-low coupling, even if present, is very likely to get filtered out.

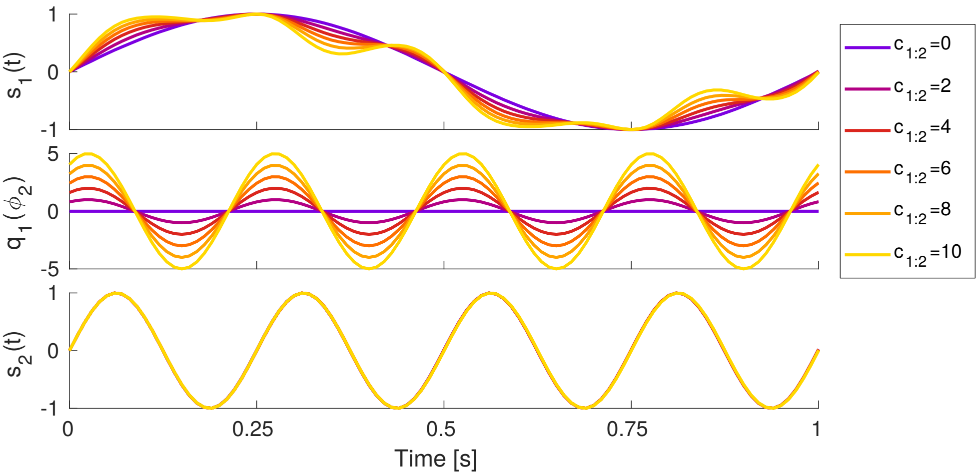

FIGURE 3.12: Effect of direct high-to-low coupling function $q_1(\phi_2) = c_{2:1} \sin\big(\phi_1(t) + 0.3\pi\big)$ in the time domain. Different strength of the coupling parameter $c_{2:1}$ are colour-coded from blue $c_{2:1} = 0$ to yellow $c_{2:1} = 10$. Note how higher direct-coupling increases the instantaneous frequency of s_1, while s_2 is not affected by the different coupling strengths.

3.3.2 Form of the coupling function

The coupling functions described above depended on only one phase, and therefore were fully representable on a 2-dimensional plot as function of time. But what if the coupling function is of the type $q_A(\phi_B, \phi_C)$? In this case, a 3-dimensional plot is needed to encompass the information carried out by the *form* of the coupling function (Rosenblum and Pikovsky, 2001, Stankovski et al., 2012). Moreover, as the coupling is a periodic function of the phases, its plot could be limited to the $0 - 2\pi$ evolution of the involved phases without loss of information.

In Figure 3.13, examples of form of the coupling function for $q_A = sin(\phi_B, \phi_C)$ will be shown for different types and order of coupling. The analytical form of the coupling function is general, and can therefore be a function of $N > 2$ phases. The reason why coupling functions of order higher than 2 are not shown is that they would need a 4-(or higher)-dimensional representation, not easy to achieve on paper.

The form of the self coupling $q_A(\phi_A, \phi_X)$ shown in Figure 3.13-a corresponds to the case discussed in Figure 3.10. The dimension of ϕ_X does not take part into the coupling mechanism, and therefore the form of the function is a purely sinusoidal wave propagating along the ϕ_A dimension.

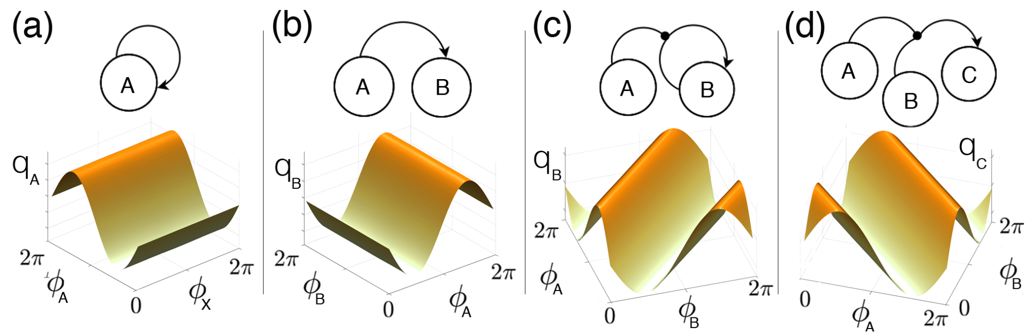

FIGURE 3.13: Schemes and forms of coupling components: (a) self-coupling; (b) direct coupling – from one oscillator; (c) common coupling – from two oscillators; (d) direct coupling – from two oscillators. Note that the labels on the horizontal axes of graphs indicate the sources of coupling, while the vertical axis label indicates the target oscillator in each case.

The form of the direct coupling $q_B(\phi_A, \phi_B)$ shown in Figure 3.13-b corresponds to the case discussed in Figures 3.12 and 3.11. There is no self-coupling in the system, therefore the dimension of ϕ_B does not add any information to the function. The form is again a purely sinusoidal wave propagating along the ϕ_A dimension.

The form of the common coupling $q_B(\phi_A, \phi_B)$ shown in Figure 3.13-c represents the first case of bivariate coupling function. The diagonal form of the function mirrors the dependence of the coupling on both phases, and originates from a function of the type $q_B = sin(\phi_A - \phi_B)$.

In Figure 3.13-d the form corresponding to a direct-from-two type of coupling is shown, i.e. $q_C(\phi_A, \phi_B)$. In this case, the diagonal form emerges from a coupling of the type $q_C = sin(\phi_A + \phi_B)$. Note how this produces a diagonal oriented in the opposite direction than in Figure 3.13-c.

Even if higher orders of coupling cannot be plotted because they have dimensionality higher than 3, the nomenclature for classification can be analogously extended, so that $q_C(\phi_A, \phi_B, \phi_C)$ is called *common from three* and $q_D(\phi_A, \phi_B, \phi_C)$ *direct from three*, and so on.

Such simple and deterministic cases of coupling are unlikely to be found in real data, but it is useful to bare in mind their form, as a more complex coupling interaction can be described qualitatively by similarity with them. For example, a coupling function which *resembles* the form of Figure 3.13-b could describe a situation where the direct coupling is the prevalent source of interaction.

3.3.3 Dynamical Bayesian inference

Till this point, it has been shown how the phase dynamics of a network of coupled phase oscillators can be decomposed and investigated. Equations 3.17 and 3.19 describing such a system and a possible parametrisation are reported here for convenience:

$$\begin{aligned} \dot{\phi}_i(t) &= 2\pi f_i(t) + q_i(\phi_i, \phi_j, \phi_k, \ldots, \phi_N, t) + \xi_i(t) \\ &= \textstyle\sum_{k=-K}^{K} \mathbf{c}_k^{(i)} \mathbf{\Phi}_k(\phi_1, \phi_2, \ldots, \phi_n) + \xi_i(t) \; . \end{aligned} \tag{3.25}$$

Characterising such a network, starting from data, means to infer for each oscillator the coupling parameters $\mathbf{c}^{(i)}$ of Equation 3.25. Also, the noise ξ_i, which is modelled as white Gaussian $\langle \xi(t)\xi(\tau) \rangle = \delta(t-\tau)D$, must be characterised and extracted. In what follows, it will be explained how this problem can be tackled by applying the dynamical Bayesian approach (Smelyanskiy et al., 2005, Stankovski et al., 2012), with the Fourier components $\mathbf{\Phi}$ of the model Equation 3.25 constituting the base functions for the inference.

3.3.3.1 The Bayesian theorem

In order to understand the mechanism of the inference, one should remember a few concepts of the Bayesian probability. Quite generally, the Bayesian statistics expresses the state of a system in terms of 'degrees of belief': in other words, the estimation of the probability of an hypothesis H includes a term which reflects the influence of *prior* beliefs, or evidences, E.

In its most classical form (Bayes, 1763), the Bayesian theorem can be expressed as

$$P(H|E) = \frac{P(E|H)\, P(H)}{P(E)} \; . \tag{3.26}$$

This famous equation allows one to evaluate $P(H|E)$, the *posterior* probability of H, given E. In the equation, the 'degrees of belief' is introduced by multiplying the probability of the hypothesis $P(H)$ (called *prior* probability), by a term which takes into account the impact of E. This term if formed by the nominator $P(E|H)$, which is the probability of the evidence given the hypothesis (called *likelihood* function), over the probability of the evidence regardless of the hypothesis, $P(E)$.

By applying the law of total probability, $P(E)$ can be expressed as the sum over all possible j hypothesis, i.e. $P(E) = \sum_j P(E \mid H_j)P(H_j))$. In the case of a continuous distribution, the theorem can be expressed as

$$p_E(H|E) = \frac{\ell(E|H)\, p_{\text{prior}}(H)}{\int \ell(E|H)\, p_{\text{prior}}(H) dH}\ , \tag{3.27}$$

where ℓ stands for *likelihood* and represents the $p_E(E|H)$, i.e. the probability density to observe the evidence given the hypothesis.

3.3.3.2 The inference algorithm

The output of the inference is a set of parameters $\mathcal{M} = \{\mathbf{c}, \mathbf{D}\}$ which describe the couplings (with $\mathbf{c}$) and noise (with $\mathbf{D}$) characterising the network of Equation 3.25. $\mathbf{c}$ is a group of matrices having ν elements (as from Equation 3.21): one for every time-window considered. $\mathbf{D}$ also is a group of matrices, one for each time-window: they are square matrices having $N \cdot N$ elements. The diagonal of each matrix expresses the noise strength extracted for each oscillator, while the other elements determine how much the noise from pairs of different oscillators is correlated (Duggento et al., 2012). The input of the process are the phase time series related to the data $\mathcal{X} = \{\mathbf{x}_l \equiv \mathbf{x}(t_l)\}$ $(t_l = lh)$, with $l = 1, \ldots, L$ and h sampling step.

With hypothesis $\mathcal{M}$ and evidence $\mathcal{X}$, The Bayes' theorem of Equation 3.27 would assume the form

$$p_{\mathcal{X}}(\mathcal{M}|\mathcal{X}) = \frac{\ell(\mathcal{X}|\mathcal{M})\, p_{\text{prior}}(\mathcal{M})}{\int \ell(\mathcal{X}|\mathcal{M})\, p_{\text{prior}}(\mathcal{M}) d\mathcal{M}}\ . \tag{3.28}$$

This allows one to obtain the *posterior* density $p_{\mathcal{X}}(\mathcal{M}|\mathcal{X})$ of the unknown $\mathcal{M}$ starting from the information contained in $\mathcal{X}$ and from the *prior* knowledge that one has on the parameters $p_{\text{prior}}(\mathcal{M})$. The process also need to reconstruct the likelihood function $\ell(\mathcal{X}|\mathcal{M})$, which is the probability density to observe $\mathcal{X}$ given the current choice of $\mathcal{X}$. As consecutive samples of white Gaussian noise are statistically independent events, the likelihood at each time can be considered as the probability of observing $\phi_{i,l+1}$ times the number of samples l.

In order to reconstruct the likelihood function, the noise term for each time sample for the oscillator i is quantified with the integral $\xi_i(t_l) \equiv \int_{t_l}^{t_{l+1}} \xi_i(t)\, dt$. By expressing the matrix D (describing the noise strength) with its Cholesky decomposition H^1, the noise at each sample can be calculated as $\xi_i(t_l) = \sqrt{h}\, H\, z_i$, and z_i is a vector of random variables (normally distributed) (Duggento et al., 2012).

The likelihood function, for a series of independent samples, can be written as $\ell(\mathcal{X}|\mathcal{M}) = \prod_l \ell(x_l|\mathcal{M})$. Passing to the logarithm of such quantity turns the product into a sum, so that $\ln \ell(\mathcal{X}|\mathcal{M}) = \sum_l \log \ell(x_l|\mathcal{M})$. Assuming normal distribution, the likelihood assumes the form

$$\ell(x|\mathcal{M}) = \frac{1}{(\sqrt{2\pi})\sqrt{\det \mathbf{D}}} e^{-\frac{1}{2}(x-\mu)^T \mathbf{D}^{-1}(x-\mu)}, \tag{3.29}$$

with μ being the vector of means and $\mathbf{D}$ being the covariance matrix. The logarithmic transformation allows one to avoid the computation of the exponential in Equation 3.29, i.e.

$$\ln \ell(x|\mathcal{M}) = -\frac{1}{2}\ln(2\pi) - \frac{1}{2}\ln\det \mathbf{D} - \frac{1}{2}(x-\mu)^T \mathbf{D}^{-1}(x-\mu) \tag{3.30}$$

(Smelyanskiy et al., 2005).

Assuming that h is small enough to follow the dynamical evolution of the time-series, the Euler midpoint discretisation can be used to approximate the phase dynamics using $\phi^*_{i,l} = (\phi_{i,l} + \phi_{i,l+1})/2$ as midpoint and $\dot{\phi}_{i,l} = (\phi_{i,l+1} - \phi_{i,l})/h$ as derivative.

The joint probability density of the phase dynamics $\dot{\phi}_{i,l}$ in respect of $[\phi_i(t_{l+1}) - \phi_i(t_l)]$ is calculated from the joint probability density of z_i. This is possible by imposing $P[\phi_i(t_{l+1})] = \det(J^\phi_\xi)P(\xi)$, where J^ϕ_ξ is the Jacobian term of the transformation of variables that can be calculated from the base functions $\Phi_{i,k}$. In particular, J^ϕ_ξ will have $\frac{\partial \Phi_{i,k}(\phi_{\cdot,l})}{\partial \phi_i}$ on the diagonal, and under the assumption that h is small, the determinant can be approximated with the product of such terms (Duggento et al., 2012).

---

[1] The Cholesky decomposition of the matrix D is the upper triangular matrix H so that $D = HH^T$.

This transformation adds one term to the log-likelihood function $\ln \ell(\mathcal{X}|\mathcal{M})$, which, minus the un-relevant term $\frac{1}{2}\ln(2\pi)$ becomes for each oscillator

$$\begin{aligned} S = \frac{L}{2}\ln|\mathbf{D}| + \frac{h}{2}\sum_{l=0}^{L-1}\Big(\mathbf{c}_k\frac{\partial\mathbf{\Phi}_k(\phi_{\cdot,l})}{\partial\phi}+ \\ + [\dot{\phi}_l - \mathbf{c}_k\mathbf{\Phi}_k(\phi^*_{\cdot,l})]^T(\mathbf{D}^{-1})[\dot{\phi}_l - \mathbf{c}_k\mathbf{\Phi}_k(\phi^*_{\cdot,l})]\Big)\ , \end{aligned} \tag{3.31}$$

where summation over the repeated indices k is implicit, and the dot index in $\phi.$ is substituted with the relevant index.

Assuming the normality of the prior probability $p_{\text{prior}}(\mathcal{M})$, and considering that the minus-log-likelihood of 3.31 is a quadratic form, the posterior probability $p_{\mathcal{X}}(\mathcal{M}|\mathcal{X})$ will also be normally distributed. The pair $\mathcal{M} = \{\mathbf{c}, \mathbf{D}\}$ constituting the stationary point of S, is calculated recursively from Equation 3.28 (Duggento et al., 2012), by splitting it into the Equations

$$\begin{aligned} \mathbf{D} &= \frac{h}{L}\left(\dot{\phi}_l - \mathbf{c}_k\mathbf{\Phi}_k(\phi^*_{\cdot,l})\right)^T\left(\dot{\phi}_l - \mathbf{c}_k\mathbf{\Phi}_k(\phi^*_{\cdot,l})\right) \\ \mathbf{r}_w &= (\mathbf{\Xi}_{\text{prior}})_{kw}\,\mathbf{c}_w + h\,\mathbf{\Phi}_k(\phi^*_{\cdot,l})\,(\mathbf{D}^{-1})\,\dot{\phi}_l + \\ &\quad - \frac{h}{2}\frac{\partial\mathbf{\Phi}_k(\phi_{\cdot,l})}{\partial\phi} \\ \mathbf{\Xi}_{kw} &= (\mathbf{\Xi}_{\text{prior}})_{kw} + h\,\mathbf{\Phi}_k(\phi^*_{\cdot,l})\ ,(\mathbf{D}^{-1})\,\mathbf{\Phi}_w(\phi^*_{\cdot,l}) \\ \mathbf{c}_k &= (\mathbf{\Xi}^{-1})_{kw}\,\mathbf{r}_w\ , \end{aligned} \tag{3.32}$$

where $\mathbf{\Sigma}_{\text{prior}} \equiv \mathbf{\Xi}^{-1}{}_{\text{prior}}$ is the covariance matrix of $\mathbf{c}$ and the summations over $l = 1, \ldots, L$ and over the repeated indices k and w, is implicit. The recursion is stopped then the current estimation of the parameters differs from the prior by a value higher than a set threshold.

This procedure is applied to sequential time-windows of the data, so that the computation of the current probability distribution of the parameters is based on the informative *priors* coming from the previous block of data, i.e. at each iteration the current *prior* depends on the previous *posterior*. For the first time window, the *prior* is set to a flat normal distribution with $\Xi_{\text{prior}} = 0$ and $\bar{\mathbf{c}}_{\text{prior}} = 0$.

The propagation of information between consecutive blocks of data must take into account the possible time-variability of the interacting dynamics (Stankovski, 2017, Stankovski et al., 2012). This is achieved by convolving the current *posterior* distribution with a *diffusion* normal distribution having covariance matrix Σ^{l}_{diff}. This measure adjusts how much the parameters can change between consecutive windows, and results in a *prior* distribution having covariance matrix $\Sigma^{l+1}_{\text{prior}} = \Sigma^{l}_{\text{post}} + \Sigma^{l}_{\text{diff}}$.

3.3.4 Quantitative measures

Once the matrix of parameters describing the network coupling $\mathbf{c}$ is inferred, it can be used to quantify –and compare– the characteristics of the specific coupling relations within the network. Those measures can be either based on the numerical values of subsets of the $\mathbf{c}$, or on morphological features of the coupling functions.

3.3.4.1 Coupling strength

The coupling strength quantifies the amplitude of the coupling coefficients. It is defined as the Euclidean norm of the inferred parameters corresponding to the Fourier components of a specific link –or ensembles of links– within the network (Rosenblum and Pikovsky, 2001). To quantify the coupling acting on the oscillator i from the combination of oscillators σ, the coupling strength $||q_{i:\sigma}||$ would be:

$$||q_{i:\sigma}|| = \sqrt{\sum_{k=-K}^{K} (c_k^{(i:\sigma)})^2}\,, \tag{3.33}$$

with K limit of the Fourier decomposition. One can think that each row of $\mathbf{c}$ corresponds to the coupling coefficients relative to the coupling acting on the oscillator i. With this configuration, for a network of N oscillators, in each row the indices relative to the coupling from links of order 1 ($\mathbf{c}'$ part of the $\mathbf{c}^{(i)}$ vector) is composed of $2 \cdot K \cdot N$ elements;

the strength of coupling of order 2 (from two oscillators) is indexed into the $\mathbf{c}''^{(i)}$ part of the vector, and it is composed of $2^2 \cdot K^2 \cdot N$ elements; the strength of the coupling of order 3 (from three oscillators) is indexed into the $\mathbf{c}'''^{(i)}$ part of the vector, and is composed by $2^3 \cdot K^3 \cdot N$ elements, and so on (Stankovski et al., 2015).

Within each row, one could be for example interested in quantifying the strength of the direct coupling acting on i from j. In this case the norm $||q_{i:j}||$ would include $2 \cdot K$ elements. Instead, the overall network strength of the coupling acting on i, $||q_i||$, would encompass the whole row of coefficients.

3.3.4.2 Similarity of the form

The coupling strength is enough to detect the presence and amount of coupling characterising an interaction. However, by observing the form of the coupling function, one can go beyond this and extract information about the *mechanism* of the interaction.

Starting by calculating the two-dimensional correlation between two coupling functions, it is possible to evaluate the similarity of their forms, irrespective of their amplitudes (Kralemann et al., 2013). This way it can be quantified how close the form of the coupling functions are to one another.

The similarity index is defined as

$$\rho_{i,j} = \frac{\langle \tilde{q}_i \, \tilde{q}_j \rangle}{||\tilde{q}_i|| \; ||\tilde{q}_j||} \, , \tag{3.34}$$

where $\langle \cdot \rangle$ denotes averaging over the $2\pi \cdot 2\pi$ phase grid, and $\tilde{q}_i$ is the deviation from the mean $\tilde{q}_i = q_i - \langle q_i \rangle$ (Kralemann et al., 2013).

The correlation ρ can be applied to quantify the similarity between:

- Two inferred coupling functions

- An inferred coupling function, and the average of an ensemble of coupling functions to which it belongs. This way it is possible to quantify for example inter-subject variability of a form, or the intra-subject variability of coupling functions quantified on different anatomical locations
- A coupling function inferred from a single time-window, and the time-average. This allows one to quantify the time-variability of the coupling function
- One inferred coupling function, and a coupling function having some numerically generated features (like the ones in Figure 3.13). This comparison allows one to quantify the prevalence of a specific type of coupling (e.g. direct, self, common) within a coupling function

The first three points are self explanatory. The latter is further explained in what follows.

3.3.4.3 Polar similarity

The concept of similarity has been extended from its original version (Kralemann et al., 2013) to extract information about the predominant functional source of the coupling (Stankovski et al., 2017b, Ticcinelli et al., 2017) within an inferred function q.

This can be achieved by numerically generating a coupling function Q resembling a specific partial coupling component, like in the examples shown in Figure 3.13. Possible phase-shift of the coupling functions is taken into account by generating a set of phase-shifted versions of Q. This similarity value is calculated as

$$\rho_{q,Q} = \max_{\vartheta} \left(\frac{\langle \tilde{q} \, \tilde{Q}_{\vartheta} \rangle}{\|\tilde{q}\| \, \|\tilde{Q}_{\vartheta}\|} \right) , \tag{3.35}$$

where the correlation in Equation 3.34 is computed iteratively between the coupling function q and a series of phase-shifted versions of Q, characterised by their phase shift ϑ ranging between $[0 - 2\pi]$.

Also, the numerical form Q_ϑ generating the highest ρ carries dual information: the extent of the similarity (described by ρ itself) and the corresponding phase shift, given by ϑ. The value of ϑ in this case indicates on which point of the phase evolution of the driving oscillator the driven oscillator undergoes the strongest acceleration. In the case of the coupling discussed in Figure 3.11, ϑ would have been 0.3π.

A natural way of presenting this information is by unifying the value of the similarity index ρ and the similarity phase ϑ into a complex number $P = \rho e^{i}\vartheta$. This number, called *polar similarity index* can then be plotted on the complex plane to provide a polar representation of the quantity.

Figure 3.14 illustrates the concept: two coupling functions extracted from real data (corresponding to delta→alpha coupling in brain waves (Stankovski et al., 2017b)) are shown in purple, with the small squares providing a top-view. They have been selected as examples for being very similar (in A) and very dissimilar (in B) to the form of a perfectly direct coupling. The numerical forms generating the highest values of ρ are overlapped with an orange grid. Note how in 3.14-A the real and the numerical functions better overlap than in 3.14-B, generating a similarity index with bigger module. The dashed lines

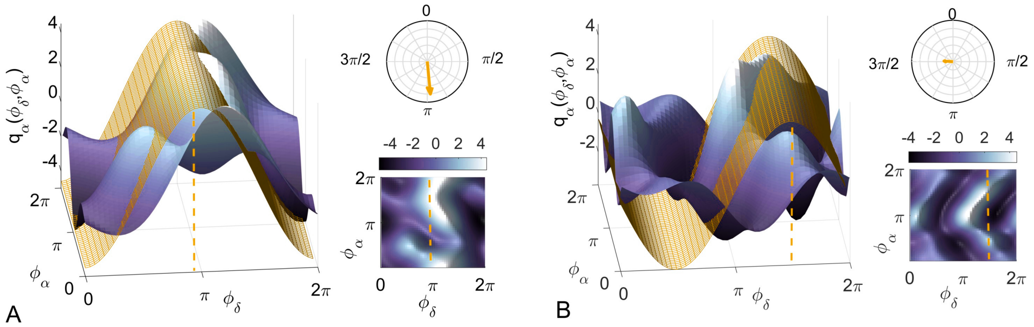

FIGURE 3.14: The meaning of the polar similarity index. Two examples of coupling functions, plotted in purple, are compared with numerically-generated sinusoidal functions, plotted in orange. The latter have been selected for being as similar as possible to the coupling functions: the only degree of freedom in the selection was the shift in phase (marked by the orange dashed lines). The arrows in the polar planes in the top right corners are the similarity indices, and point to the corresponding phase values for: (A) a coupling function with high similarity ($\rho = 0.82$) and (B) one with a low value ($\rho = 0.23$). A complementary 2D colour-contour plot of the coupling function is given in the bottom right-hand corner of each panel (figure modified from (Stankovski et al., 2017b)).

indicate the corresponding phase-shifts ϑ_M and ϑ_m, which are close to π for the form A and to $3/2\pi$ for B. The polar similarity indices are represented in the polar planes, with arrows having module equal to ρ and phase equal to ϑ.

3.3.5 Simulated EEG to test cross-frequency coupling analysis

In this section, the method is applied to a numerically simulated system with time-varying parameters in order to evaluate the accuracy of the inference procedure. In what follows, a single-source coupling from ϕ_1 to ϕ_X will be indicated by $\phi_1 \to \phi_X$. To indicate a coupling link originating from a specific subset of sources, the notation ϕ_1, ϕ_2, …, $\phi_N \to \phi_X$ will be used.

The simulated network of coupled phase oscillators is composed of five units, coupled as illustrated in Figure 3.15(a):

- X_1 oscillates without being influenced by any other, and with a time-varying natural frequency (dashed circle).
- X_2 is driven by the *direct from two* coupling X_1, $X_3 \to X_2$ (pink link)
- X_3 is driven by the *direct from three* coupling X_1, X_4, $X_5 \to X_3$ (purple link)
- X_4 is driven by the *common from three* coupling X_1, X_2, $X_4 \to X_4$ (orange link)
- X_5 is driven by the *common from two* coupling X_3, $X_5 \to X_5$ (yellow link).

The system of stochastic differential equations associated with the network is

$$\begin{cases} \dot{\phi}_1 &= \omega_1(t) + \xi_1(t) \\ \dot{\phi}_2 &= \omega_2 + c_{2:1,3}(t) \cdot \sin(\phi_1 + \phi_3) + \xi_2(t) \\ \dot{\phi}_3 &= \omega_3 + c_{3:1,4,5}(t) \cdot \sin(\phi_1 + \phi_4 + \phi_5) + \xi_3(t) \\ \dot{\phi}_4 &= \omega_4 + c_{4:1,2,4}(t) \cdot \sin(\phi_1 + \phi_2 + \phi_4) + \xi_4(t) \\ \dot{\phi}_5 &= \omega_5 + c_{5:3,5}(t) \cdot \sin(\phi_5 + \phi_3) + \xi_5(t) \ , \end{cases} \tag{3.36}$$

where ξ_i represents addictive white Gaussian noise. the length of the time-series is 2000s and the sampling step is set as $h = 0.01$. All the coupling coefficients $c_{i:\sigma}$, plus the natural frequency ω_1, are built as time-varying and are defined by

$$\begin{aligned} \omega_1(t) &= 2\pi f_1 + \sin(2\pi \cdot 0.03 \cdot t) \\ c_{2:1,3}(t) &= 1 + \sin(2\pi \cdot 0.0008 \cdot t) \\ c_{3:1,4,5}(t) &= 1.8 - 0.001 \cdot t \\ c_{4:1,2,4}(t) &= 0.5 + 0.001 \cdot t \\ c_{5:3,5}(t) &= 1.2 + 1.2 \cdot \cos(2\pi \cdot 0.001 \cdot t)\ , \end{aligned} \tag{3.37}$$

with $f_1 = 2.4$. The natural frequencies of the other oscillators were set as constant, i.e. $\omega_i = 2\pi f_i$ with $f_i = [5, 10, 20, 40]$. The time window for the dynamical Bayesian inference is set equal to 50 s. Such length ensure to include in each window enough

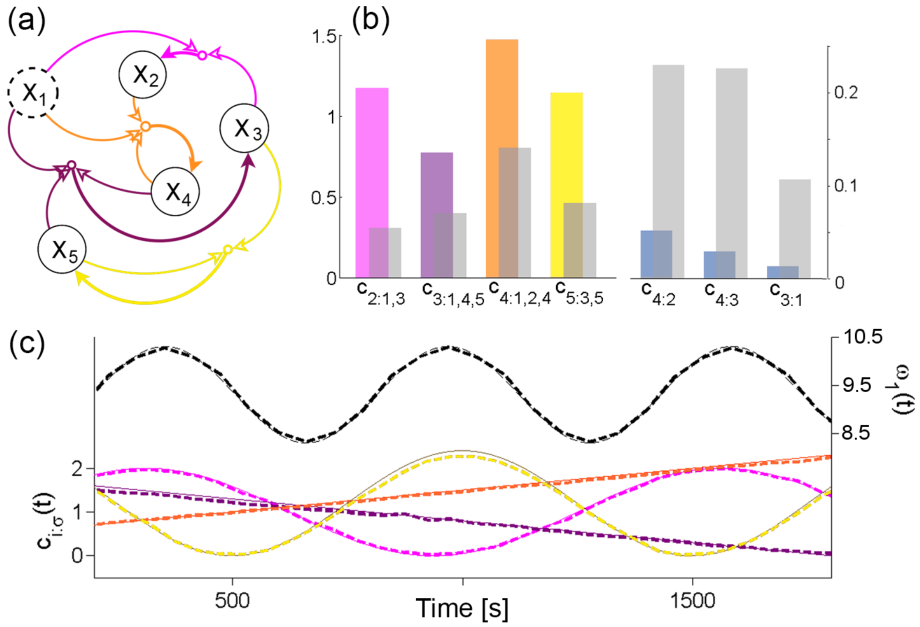

FIGURE 3.15: (a) The network scheme simulated. (b) Coupling strength of the inferred parameters for existing connections (on the left, bars coloured as in (a)) and non-existing connections (on the right, blue bars) compared with surrogates (grey bars).Note that the grey bars validate the numerical links and invalidate others non present. (c) The inferred time-varying parameters (dashed lines) compared with their numerically determined values (solid lines), coloured as in (a) and (b). Note how well the inferred set follows the numerical time-evolution (Figure modified from (Stankovski et al., 2017b)).

information about the dynamics of the system (i.e. 75 periods of the slower oscillation – 5000 samples), while allowing high-enough resolution to follow the time variability of the parameters (i.e. 40 windows are inferred).

In order to validate the results for the time-average coupling strength, a set of 100 surrogates of the original network was generated by randomly shuffling the phases of the time-series ϕ_i (Schreiber and Schmitz, 2000). This technique allows one to destroy phase-to-phase correlation within the network, without altering too much the statistical properties of the time-series. For each link, the 95% higher values from each distribution of 100 strengths is chosen as surrogate threshold.

Figure 3.15(b), on the left, shows the time-average coupling strength of the links effectively present in the net (with same colours as in the network scheme of panel (a)). It can be seen that the surrogates (grey bars) validate the coupling strengths of the links present in the network, by being lower than the inferred values with coloured bars. On the right, the coupling strengths computed for 3 links not present in the network ($X_4 \rightarrow X_2$, $X_4 \rightarrow X_3$, $X_3 \rightarrow X_1$), overlapped with grey bars for corresponding surrogates are shown on a lower scale. It can be seen that, in this case, the surrogates reach significantly higher values than the calculated couplings, implying that a coupling is (correctly) inferred to be below the significance level in cases when it is actually absent.

But how well does the inference follow the time varying dynamics of the system? The numerically set time-evolution of the coupling parameters, and of the natural frequency of X_1, are shown in Figure 3.15(c)), with solid thin lines colour-coded as before. The corresponding time evolution – sampled each 50 s – of the parameters provided by the dynamical Bayesian inference is plotted with dashed lines (and same colours). It can be deduced by the close overlapping of the curves that the method is also able to follow very well the time evolution of the parameters, besides being able to detect correctly the presence and strength of the links characterising the topology of the network (as indicated by the bars in Figure 3.15(b)).

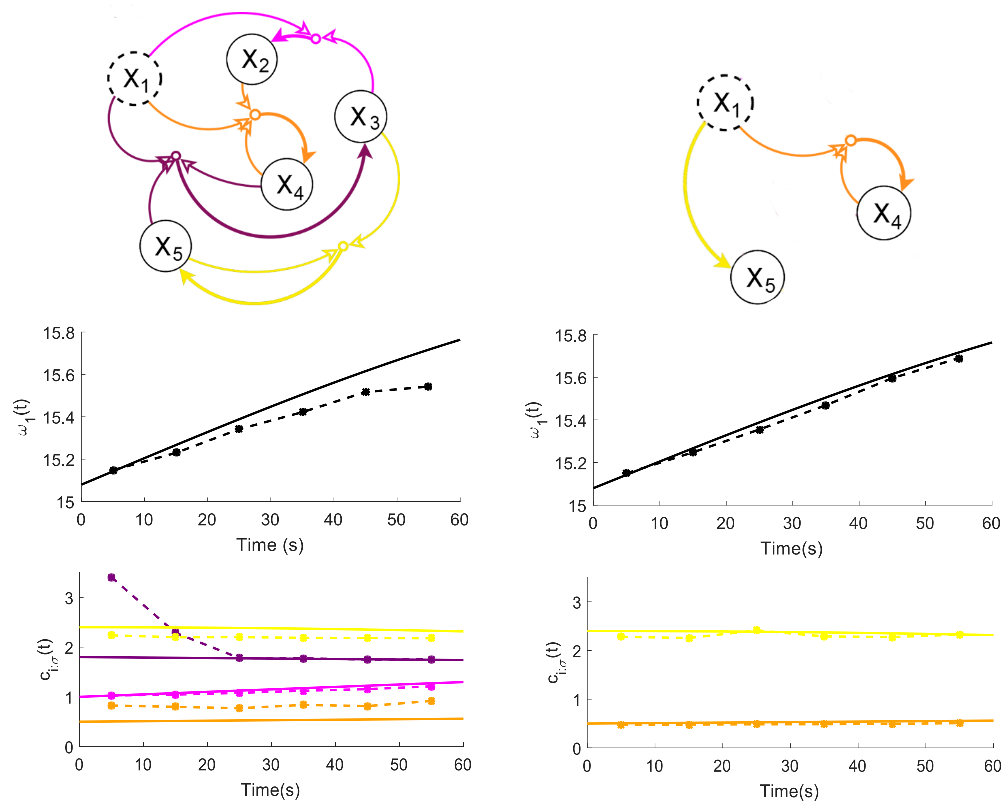

FIGURE 3.16: On the left column, inference performance for the coupling parameter of network of Equation 3.36 when 60 s of data are provided and the time window is reduced to 10 s. On the right column, inference performance on the same length of data, but with a simplified network. Note how the performance improves in the latter case.

It must be taken into account that in the case of shorter recordings, the performance of the inference is worse for a network of this order of complexity. Figure 3.16(a) shows the performance of the inference on the same network but for 60 s recording, sampled at 256 Hz. Note how both the inferred frequency of the first oscillator, and the estimation of the coupling parameters loses accuracy. However, when the complexity of the network is reduced and just 3 oscillators are coupled as shown in figure 3.16(b) (with same natural frequencies and coupling parameters as in Equation 3.36), the amount of information is sufficient to reach a more precise estimation.

3.4 Phase extraction

So far, simulations have been run starting from numerically generated phases to build synthetic time series (for the time-frequency representation of Section 3.1.5 and coherence discussions of Section 3.2.1) or to be used as input of the dynamical Bayesian inference for the estimation of cross-frequency coupling in Section 3.3. However, in real life, what is usually measured is the time series, not the phase evolution, and therefore the first problem one has to face when they wish to evaluate cross-frequency phase coupling is how to extract the phases themselves.

3.4.1 Filtering

Firstly, the frequency bands of interest need to be filtered out of the time series. The transfer function H of a N-order digital filter can be expressed in terms of transfer function coefficients $a_{1\ldots N+1}$ and $b_{1\ldots N+1}$ as

$$H(e^{i2\pi f}) = \frac{b_1 + b_2 e^{-i2\pi f} + b_3 e^{-2i2\pi f} + \cdots + b_N e^{-(N-1)i2\pi f}}{a_1 + a_2 e^{-i2\pi f} + a_3 e^{-2i2\pi f} + \cdots + a_N e^{-(N-1)i2\pi f}} \,. \tag{3.38}$$

One of the possible choices is the finite-impulse-response Butterworth filter(Butterworth, 1930).

The transfer function coefficients $a_{1\ldots N+1}$ and $b_{1\ldots N+1}$ for the Butterworth filter are computed by running the Matlab function `butter`. In order to obtain a band-pass filter with low (f_l) and high (f_h) cut-off frequencies, the non-dimensional frequencies used for the construction are f_l/f_N and f_h/f_N respectively, with f_N the Nyquist frequency. Given the coefficients, the function `filtfilt` performs zero-phase digital filtering by processing the input data in both the forward and reverse directions. This strategy allows one to obtain zero phase distortion in the filtered time-series. It is worth noting that the choice of the filter type is not fundamentally impacting the analysis, as long as particular care is taken to avoid phase distortion and overlapping between bands.

Figure 3.17 shows the magnitude frequency response of Butterworth filters centred around the EEG frequency bands introduced in Section 3.1.5. Different orders of the filter are shown by different colours as explained in the colour-bar.

The order of the filter needs to be adjusted to different frequencies of interest, as higher frequencies require a quicker roll-off at the cut-down frequency. On the other hand, the higher limit of the possible filter order is proportional to the frequency where it is centred. If the order is pushed beyond that limit, the filter looses the linear response in the pass-band, i.e. becomes unstable. One way to select the optimal order for a specific frequency band is to push the order till the filter becomes unstable, and then select the stable value of the previous step. Figure 3.17 on the left shows the example of the first instability of the delta band filter, when the order is pushed to 5 (black dotted line). Note how the order 5 is fine for higher frequency intervals. In particular, the selected orders for this case are 4 for delta, 5 for theta, 5 for alpha, 8 for beta, 12 for gamma bands.

It can be seen in Figure 3.17 how the frequency response in the band-passing intervals

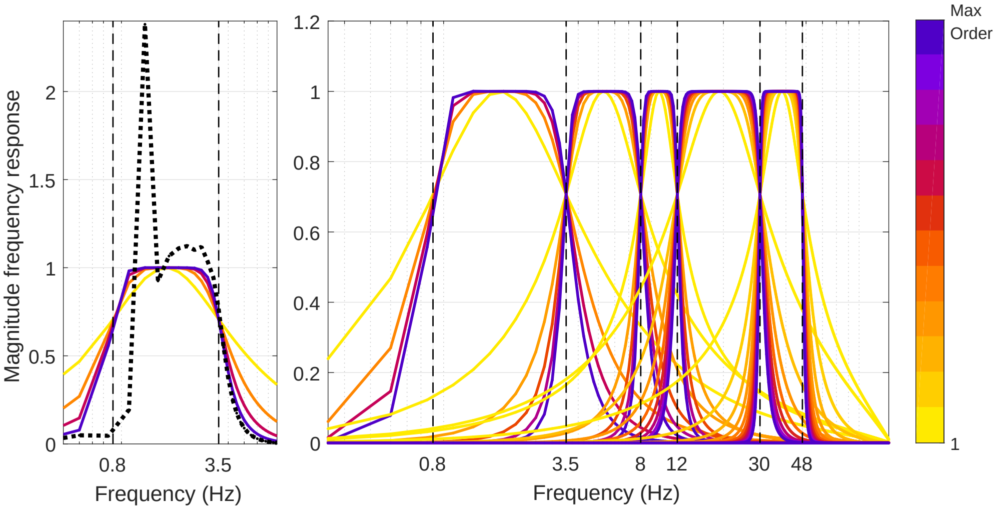

FIGURE 3.17: Magnitude frequency response for different orders of Butterworth filters, centred on the EEG bands of interest. Note how the cut-off slope becomes steeper with increasingly high orders. The order increses of 1 for each line plotted, according to the colormap. The maximum order corresponds to 4 for the delta and 12 for the gamma bands. On the left, as an example, it is shown that the filter for the δ band becoming unstable at order 5 (black dotted line).

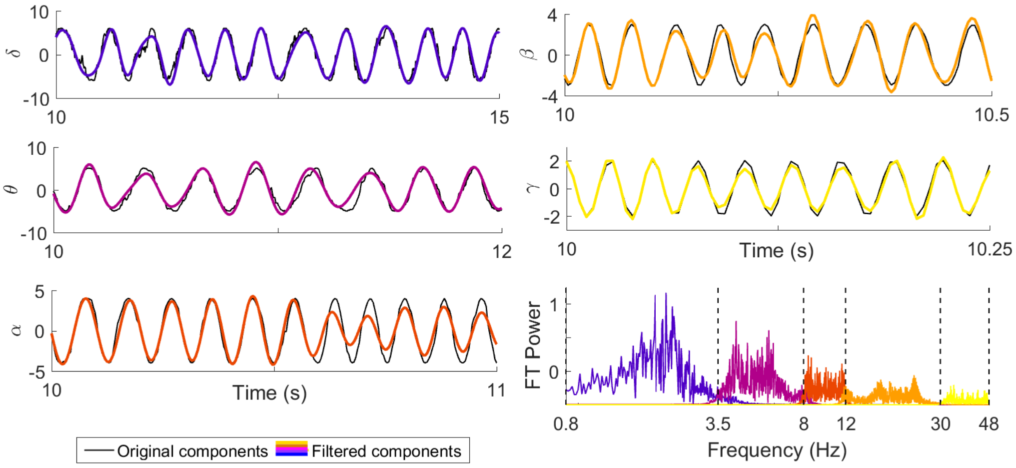

FIGURE 3.18: The performance of the selected filters when applied to the time series $s(t) = \sum_{i=1}^{5} s_i(t)$ built with Equations 3.9 and 3.10. Each filtered component is plotted with a coloured line over the corresponding numerically generated $s_i(t)$ (thin black lines). The length of the window is chosen to include around 10 periods of the oscillation of interest. Fourier transforms of each filtered bands are shown with same colours in the right-bottom panel.

stays constant around 1. This flat frequency response is an important feature of Butterworth filters, when compared to other filers like elliptic or Chebyshev which introduce ripples around the cut-off frequencies (Parks and McClellan, 1972). Moreover, being a zero-phase filter, Butterworth has the advantages of not introducing phase distortions in the filtered bands. This means that features in a filtered output appear exactly where they occur in the unfiltered signal, which is a crucial feature for the investigation of phase coupling. A downside of the Butterworth filter is overshooting at step-response for orders >1. However, when dealing with biomedical time-series, the occurrence of ’steps’ is rather unlikely, and this feature is not considered as a possible issue.

The performance of the selected filters when applied on the time series $s(t) = \sum_{i=1}^{5} s_i(t)$ built with Equations 3.9 and 3.10 are shown in Figure 3.18. Each filtered component is overlapped to the corresponding original numerically generated $s_i(t)$. The length of the window is choosen to include around 10 period of the oscillation of interest. Note how the filter succeeds in tracing back the original component –minus the noise– without introducing any phase-delay or major distortions of the oscillations.

During this preprocessing procedure, particular care must be taken to minimise the overlap between the spectra of the filtered time-series (Lehnertz et al., 2014): overlaps of consecutive frequency intervals would result in overestimating the corresponding phase-to-phase coupling. Spectra of the filtered bands are shown in the last panel of Figure 3.18. In this case, for example, the shared information due to the overlapping between alpha and beta bands' spectral content could cause over-estimation of the coupling between these two frequency bands. A possible way to do so is narrowing the band-passing frequency bands in order to set the cut-off frequencies apart.

With regard to the possible time-variability of the frequency content in the real time-series, the described filtering setting can extract it as long as it is limited into the corresponding cut-off values of each band.

3.4.2 Hilbert transform

Once the filtered time-series are obtained, the corresponding phase evolution can be extracted by computing the Hilbert transform $H(t)$ (Gabor, 1946). This linear transformation allows one to expand a time-series $s(t)$ into the complex plane, obtaining the analytical representation $u(t) = s(t) + H(t) = \Re[u(t)] + i\Im[u(t)] = A(t) \cdot e^{i\phi(t)}$ introduced in Section 3.1.1.

The Hilbert transform $H(t)$ of the time series $s(t)$ is given by the transformation

$$H(t) = -\frac{1}{\pi} \lim_{\epsilon \to 0} \int_{\epsilon}^{\infty} \frac{s(t+\tau) - s(t-\tau)}{\tau} d\tau \,, \tag{3.39}$$

which is equivalent to the convolution of $s(t)$ and $1/(\pi t)$. Because $\Im[u(t)] = H(t)$ and $\Re[u(t)] = s(t)$, it follows that amplitude and phase of the polar representation of the analytical form $u(t)$ can be computed as

$$\begin{aligned} A(t) &= |(s(t) + iH(t)| \\ \phi(t) &= \arg\big(s(t) + iH(t)\big) \,. \end{aligned} \tag{3.40}$$

Figure 3.19 on the left depicts in the complex plane the analytical representation $u(t)$ of a simulated time series built as $s(t) = t^2 \sin(2\pi t)$. The plot is achieved by plotting $s(t)$ against $H(t)$. On the right, the time evolutions of $s(t)$, $H(t)$, $A(t)$ and $\phi(t)$ are shown. Note how $A(t)$ constitutes the envelope of $s(t)$, and $\phi(t)$ defines the phase of $s(t)$. The values $\pm\pi$ in the phase corresponds to the lower point of each period of $s(t)$.

It can be also noted in Figure 3.19 how the first periods of $\phi(t)$ are not well defined. This is an artefact due to the border effect. To avoid affecting the further steps of the analysis, the beginning and end of the Hilbert transform are discarded from the data, shortening the data for a length of 4 periods of the slower oscillation of interest.

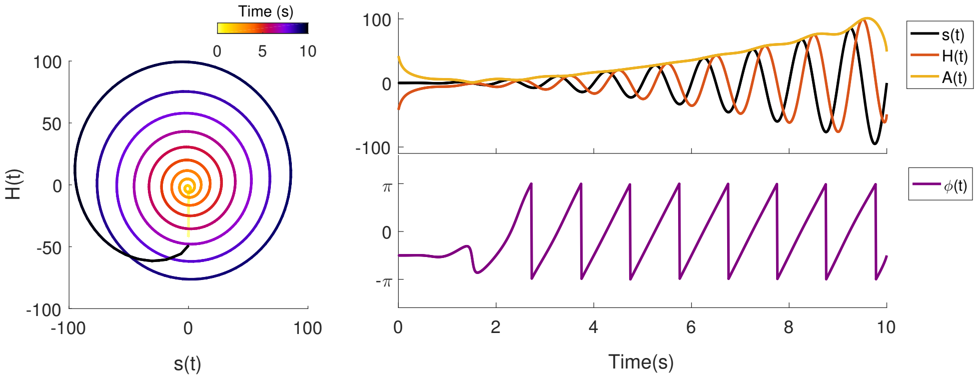

FIGURE 3.19: Analytic representation of the signal $s(t) = t^2 \sin(2\pi t)$ achieved with the Hilbert transform on the complex plane. Time series are plotted in black, and its Hilbert transform in orange. The envelope of the two is the module of the analytic representation. The phase $\phi(t)$, wrapped between $-\pi$ and π is the angle of the analytic representation $u(t)$.

3.4.3 Protophase to phase

The phase $\phi(t)$ extracted by means of the Hilbert transform should be monotonically increasing for a time series characterised by a dominant natural frequency and a small amount of noise. However, for its construction, it is not secured that $\phi(t)$ grows uniformly with the instantaneous frequency $\omega(t)$. As a matter of fact, it could contain a spurious part due to repeated non-linearities present in each period of the oscillation of interest which could mask the actual coupling functions. For this reason, $\phi(t)$ is usually called *protophase* (Kralemann et al., 2008). For noise-free systems, the *real* phase $\varphi(t)$ can be reconstructed so that it fulfils the relation $\dot{\varphi} = \omega$ with the transformation

$$\frac{d\varphi}{dt} = \omega \rightarrow \frac{d\varphi}{d\phi}\frac{d\phi}{dt} = \omega \rightarrow \frac{d\varphi}{d\phi} = \frac{\omega}{\dot{\phi}} \rightarrow \varphi = \int_0^{\phi} \frac{\omega}{\dot{\phi}} d\phi \, . \tag{3.41}$$

For noisy time series, one should average $\frac{\omega}{\dot{\phi}}$, obtaining

$$\frac{d\varphi}{d\phi} = \omega \langle \frac{dt}{d\phi} \rangle_{\phi} = \sigma(\phi) \ \rightarrow \varphi = \int_0^{\phi} \sigma(\phi) d\phi \, , \tag{3.42}$$

where $\sigma/2\pi$ is the probability density of ϕ and can be written as an integral along the trajectory (Kralemann et al., 2008).

By approximating $\sigma(\phi)$ with a k-order Fourier series $\sum_k S_p e^{ik\phi}$ with coefficients $S_p(k) = \frac{1}{N}\sum_t e^{-ik\phi(t)}$, the *real* phase $\varphi(t)$ can be obtained from the protophase $\phi(t)$ with the transformation $\varphi(t) = \phi(t) + 2\sum_k \Im[\frac{S_p(k)}{k}(e^{ik\phi(t)} - 1)]$, where N is the time series' number of points.

This transformation is particularly important when dealing with noisy data or with time-series having complicated waveforms. In the next section the effect of the transformation on band-pass filtered time-series will be evaluated and discussed.

3.4.4 Effect of phase extraction and filtering

In this section a numerical simulation has been run with two coupled oscillators resembling a delta-alpha bidirectional interaction:

$$\begin{cases} \dot{\phi}_1(t) & = 2\pi f_1(t) + c_{1:2} \sin\big(\phi_2(t)\big) + \xi_1(t) \\ \dot{\phi}_2(t) & = 2\pi f_2(t) + c_{2:1} \sin\big(\phi_1(t)\big) + \xi_2(t) \, , \end{cases} \tag{3.43}$$

with natural frequencies $f_1 = 1$ Hz, $f_2 = 8$ Hz, and $c_{1:2} = 5, \ c_{2:1} = 10$ and Gausian noise $\xi_1 = \xi_2$ with noise strength $D = 0.0002$. The phase extraction and filtering have

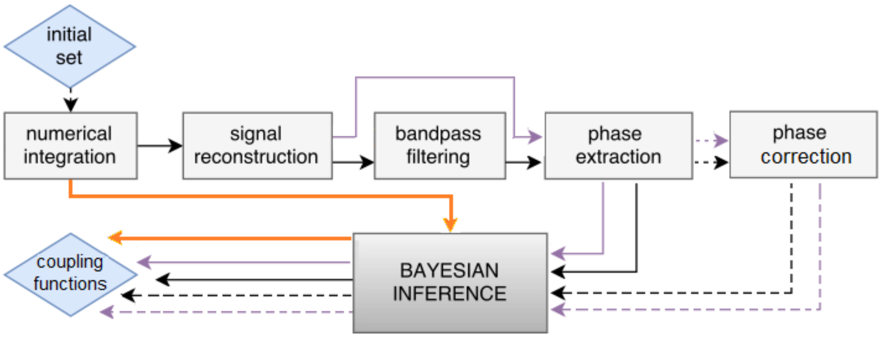

FIGURE 3.20: Diagram of computational steps from the initial set of parameter to the coupling functions for the 5 sets of phases: (i) numerical phases (orange path), (ii,iii) signal reconstructed from the numerical phases, Hilbert transformed (black solid path) and undergoing proto-phase to phase correction (black dashed path), (iv,v) signal reconstructed from the numerical phases, bandpassed, Hilbert transformed (purple path) and undergoing proto-phase to phase correction (purple dashed path).

been performed as explained in the Sections 3.4.1 and 3.4.2. In order to evaluate the specific effect of both steps, they have been applied separately to the numerical data as shown in the diagram of Figure 3.20.

First, the phase extraction using Hilbert transform has been applied to the numerically generated time series, and then the protophase-to-phase transformation has been performed.

Line plots in Figure 3.21 show a period of ϕ_1 and ϕ_2, with the numerical phases (black lines), the output of Hilbert transform (golden line) and of the transformation (purple line) vertically shifted for easier visual comparison. Note how, for the slower phase ϕ_1, the numerical output (black line) clearly contains nonlinearity due to the direct coupling $X_2 \rightarrow X_1$. The nonlinearities were still visible in the Hilbert transform applied to the reconstructed time series $s_1 = cos(\phi_1)$ (golden line), even if less defined. The output of the transformation (purple line) still showed some small indentations but was almost linear. The corresponding coupling functions on the first row of Figure 3.21 showed different morphology. The sinusoidal wave propagating along the ϕ_2 axes due to the direct coupling was clearly present in the form computed from numerical phases. The functions reconstructed from the proto-phases and the corrected phases had smaller amplitude and became more diagonal.

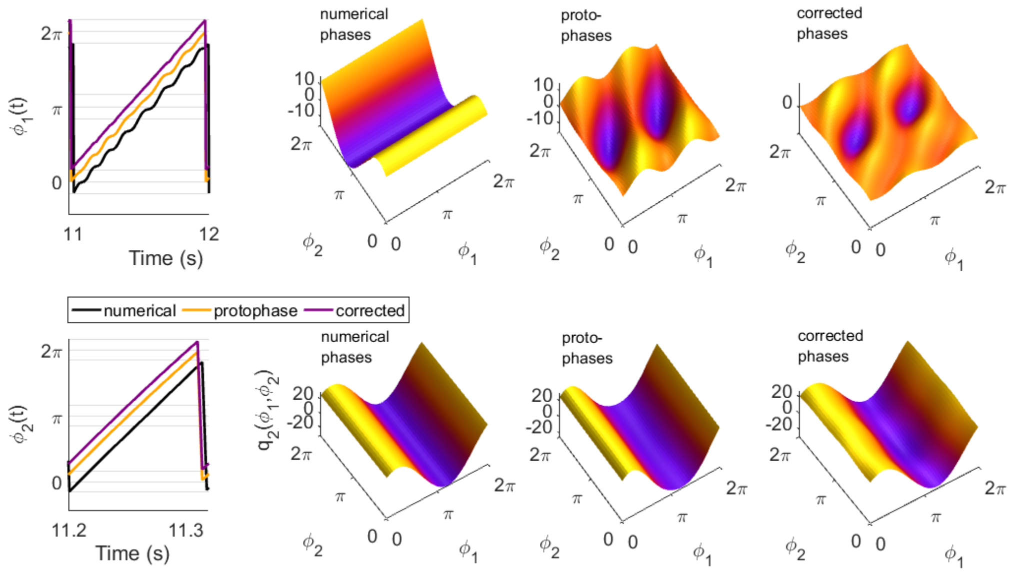

FIGURE 3.21: Effect of Hilbert transform and protophase-to-phase transformation on a bidirectionally coupled system of phase oscillators. One period of the numerical phases are shown in black, the proto-phases extracted with Hilbert transform in yellow, and the corrected protophase-to-phase in purple. A vertical shift is added for easier comparison. The coupling functions q_1 and q_2 are computed for the 3 sets of phases. Note how the shape of q_1 is lost after the phase extraction.

For the faster oscillator X_2 the effect of the phase extractions were far less marked. On the second row of Figure 3.21, despite the direct coupling $X_1 \rightarrow X_2$, the black line for the numerical phase evolution did not show evident nonlinearities. Therefore, phase extraction and protophase-to-phase transformation did not add any significant distortion to the numerical phase. Similarly, the forms of the coupling functions were qualitatively similar, with a slightly less sharp form in the function computed from the corrected phases. This effect could be due to a further –visually unnoticeable– linearisation of the phases introduced by the transformation.

A similar procedure has been followed in order to assess also the effects of filtering in a bidirectionally coupled system. The signals $s = \sum_{i=1}^{2} cos(\phi_i)$ has been decomposed in $\tilde{s}_1$ and $\tilde{s}_2$ by applying Butterworth filter as discussed in Section 3.4.1. The time-series $s_i = cos(\phi_i)$, with $i = 1, 2$ are plotted on the top panel in Figure 3.22 in orange lines, and the filtered oscillations are overlapped in thin purple lines. Note how in s_1 the effect of the coupling was marked in the orange line, but got smoothed out in the filtered signal.

On the contrary, the two lines almost overlapped for s_2, with the effect of the coupling still visible in the frequency modulation of the oscillation.

In Figure 3.22, one period of the phases and the corresponding coupling functions have been shown as in Figure 3.21. Note how the filtering step already linearised the protophase of ϕ_1 gold line), and therefore the transformation protophase-to-phase did not evidently modify it any further (purple line).

The effect of filtering is clear also in the coupling functions. The flat coupling functions q_1 for the proto-phases and corrected phases indicates that the coupling from the higher to the lower frequency oscillator was erased from the filtered time-series. On the contrary,

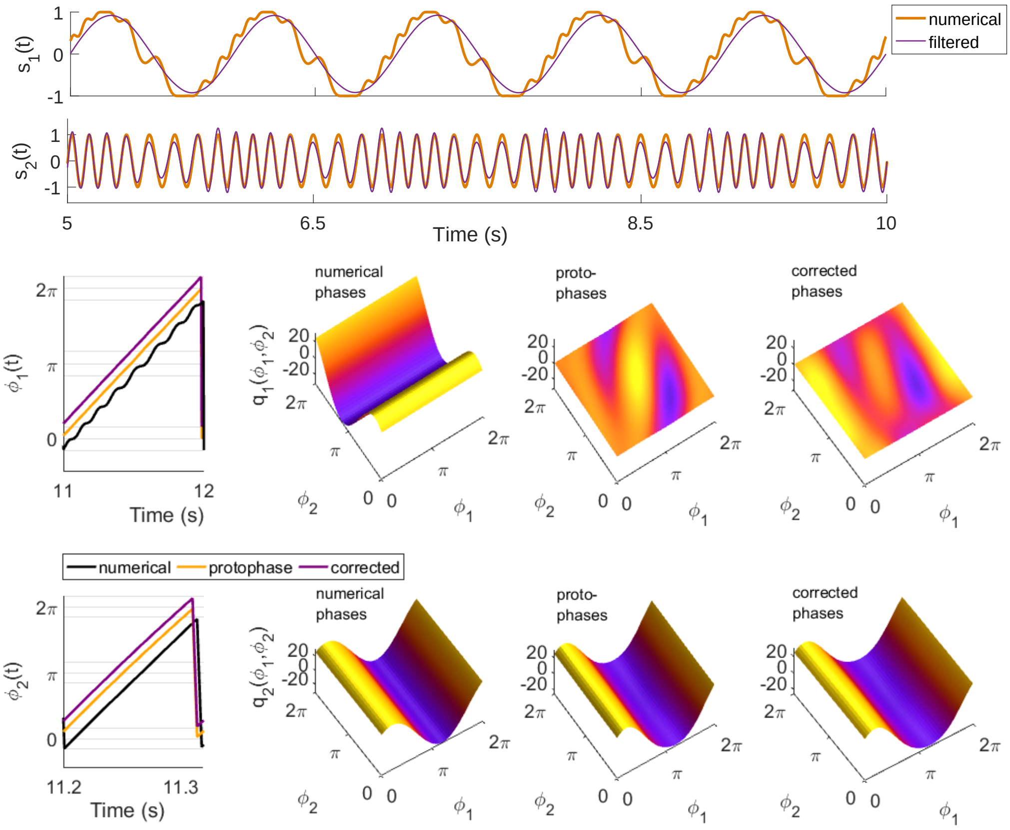

FIGURE 3.22: Effect of filtering on a bidirectionally coupled system of phase oscillators. The original time-series are plotted in orange lines, and the filtered oscillations are overlapped in thin purple lines. Below, one period of the numerical phases are shown in black, the proto-phases extracted with Hilbert transform from the filtered time-series in yellow, and the corresponding corrected protophase-to-phase in purple. A vertical shift is added for easier comparison. The coupling functions q_1 and q_2 are computed for the 3 sets of phases: note how the shape of q_1 is lost after the filtering is performed.

the form of the coupling function q_2 was again almost identical for the filtered and unfiltered cases. The protophase-to-phase step does not bring any substantial changes once filtering was performed upstream.

These examples highlighted how consideration upon bidirectional cross-frequency coupling from real data must take account of the preprocessing steps. The simulations run in this sections showed how the high-to-low coupling components, even if present, are likely to be cancelled by the filtering procedure. Also, the protophase-to-phase transformation was shown to be almost irrelevant when applied to narrow-band filtered time-series. For the sake of correctness, however, this step will be always undertaken in the upcoming calculations.

3.5 Surrogates analysis

In the current chapter, numerical simulations have been performed in order to illustrate the measures that will later be applied in the studies. However, when dealing with real data, usually only one realisation of the process is available. The inner parameters ruling the model are unknown, and they are what have to be estimated by the analysis. It is therefore not possible to vary those parameters and see how the system reacts.

Moreover, from the simulation introduced in this chapter, it emerged that even independent time series will generate non-zero values of coherence and coupling. The problem is then to determine a threshold above which a measure represents an actual dynamical property of the system and not a signature of noisy process arising by chance.

The idea is to generate, starting from the data, surrogate time series which preserve some features of the original data, but not the dynamical property that is to be measured (Breakspear and Terry, 2002, Schreiber and Schmitz, 2000, Theiler et al., 1992). The surrogates must therefore satisfy the null hypothesis which has to be tested. As an example, in this introduction, it will be assumed that the task is validating coupling measures. The null hypothesis would then be 'the time-series are uncoupled'. Therefore, the surrogate signals are constructed by destroying in the time series those relationships which make the null hypothesis false, while still preserving other statistics of the data, e.g. power spectra, amplitude, localised time evolution or others.

Once a number of surrogates is created, the measure is computed on each of them. From the distribution of the resultant values, which will be here called ζ, a threshold Z is marked, above which the measure from real data are considered valid.

But how many surrogates to compute and which threshold to choose? The latter depends on the confidence level one wants to achieve on the results of the testing. Conventionally, a confidence level of 95% is expressed as $(1-\alpha)$, with $\alpha = 0.05$. If $N = 100$ surrogates are generated, then the $(1-\alpha)N = 95^{th}$ value of the resultant distribution ζ is to be considered as the threshold Z. If the measure on real data exceeds Z, it can be claimed with $(1-\alpha)\cdot 100\% = 95\%$ confidence that data are inconsistent with the null hypothesis (e.g. the time series are coupled).

Such estimation of significance level is called *rank ordering*. In case of a Gaussian distribution of the results, the 95% threshold corresponds to the $mean{+}2\ standard\ deviations$ of ζ. However, surrogate distributions are not always Gaussian, therefore the non-parametric rank ordering has to be preferred when a test for normality fails, or is not performed.

For one-side testing (i.e. when just the upper threshold for ζ is considered) the minimum number of surrogates to generate is $K/\alpha - 1$, where K is some positive integer number depending on how spread ζ is (Schreiber and Schmitz, 2000). The threshold Z has to be picked as the Kth highest value of ζ. The previous example of 100 surrogates and $\alpha = 0.05$ reflects the case of $K = 5$. For compactly distributed ζ, it may be enough using $K = 1$. For $\alpha = 0.05$, this choice would require generating only 19 surrogates and then taking as significance level Z the maximum value of them.

Finally, it should be emphasized that surrogate testing is a tool to invalidate a null hypothesis (e.g. it can prove that the time series are NOT uncoupled, i.e. it can prove coupling).

However, if it fails to reject the null hypothesis, nothing can be said about it (e.g. a result below the threshold Z does not imply that the time series are uncoupled, i.e. it can not prove uncoupling).

In what follows, numerical examples will explore the performances of different surrogates technique in validating coupling parameters for numerical oscillators.

3.5.0.1 Surrogates for coupling

To search for significant coupling between oscillators, we need to generate surrogates in which there is no coupling. Three different types of surrogates are briefly introduced below, and their performance is tested on simulated data.

Cyclic phase permutation (CPP) surrogates

Cyclic phase permutation surrogates are surrogates acting on the phases. The time evolution of the phases is wrapped between $0 - 2\pi$, generating a sequence of slopes corresponding to distinct periods (growing from 0 to 2π). The initial and final incomplete periods are then discarded, and the rest are rearranged in a random order.

This procedure allows one to destroy the time dependence between two time-series, whilst preserving the within-phase dynamics of each of them. These surrogates are therefore very powerful in testing for interdependence between phase dynamics (Vejmelka and Paluš, 2008). As the dynamical Bayesian inference technique works directly with the phase of oscillators, cyclic phase permutation surrogates seem to be a promising choice (Stankovski et al., 2017b). Moreover, the calculation of CPP surrogates is very fast.

A downside of CPP surrogates is that, if used to test for phase coherence, they might fail to reject the null hypothesis if the time series involved are coherent by sharing a steady frequency. For the same reason, the CPP are able to validate the process of phase synchronization and distinguish it from simple coincidence of rhythms. (Mezeiová and Paluš, 2012, Vejmelka and Paluš, 2008)

Fourier transform (FT) surrogates

Fourier transform (FT) surrogates work by randomising the phase information in the original data while preserving the spectral amplitude. The phase randomization serves to preserve linear features, i.e. the power spectrum and autocorrelation, but should destroy any nonlinear behaviour. Therefore, the null hypothesis is *the data do not contain any nonlinear structure* (Schreiber and Schmitz, 2000). They are widely used, and computationally very cheap.

They are generated by calculating the Fourier transform $F(f)$ of the original time-series $s(t)$. Being $s(t)$ real, $F(f)$ is symmetrical, therefore the surrogates are generated by operating on the first half of it, $F_{1/2}(f)$. Namely, $F_{1/2}(f)$ is multiplied by $e^{i\tilde{\phi}}$, where $\tilde{\phi}$ is a sequence of random phases. This step generates $\tilde{F}_{1/2}(f)$. The second half of the transform is created by flipping horizontally the complex conjugate of $\tilde{F}_{1/2}(f)$. The final FT surrogate is the real part of the inverse Fourier transform of $\tilde{F}(f)$ (Schreiber and Schmitz, 2000).

In order to be generated correctly, $s(t)$ must contain an integer number of periods of oscillations. In real, noisy, wide spectra time series this can be approximated by truncating the series so that the last sample matches the value and the first derivative of the first. This preprocessing step shortens the data available, and is therefore one of the drawbacks of the FT surrogates.

Wavelet iterative amplitude adjusted Fourier transform (WIAAFT) surrogates

Wavelet iterative amplitude adjusted Fourier transform (WIAAFT) surrogates were also tested, as they are a more sophisticated and computationally very expensive technique capable of generating signals which look very similar to the original data (Keylock, 2006). Wavelet surrogates are based on the discrete Wavelet transform (DWT). Similarly to the FT surrogates, they rely on some manipulation of the DWT coefficients, and then on the use of the inverse Wavelet transformation to recover a time-series (Keylock, 2006). In particular, a number of FT surrogates is computed on the coefficients of each scale of the DWT. A further step is performed so that also the distribution of the amplitude of the surrogates matches the one of the original coefficients (Schreiber and Kantz, 2003). From the computed surrogates, the version which most closely matches the original coefficients is chosen by applying a least squares algorithm. Finally, the inverse DWT is computed to reconstruct the final surrogate time series.

The main feature of the WIAAFT surrogates is that they produce a time series which ‘looks like’ the original data in terms of its temporal evolution. This means that, in case of non-stationary behaviour of the data, the non-stationarieties in the time-evolution of the real series are reproduced in the same temporal locations in the surrogates too.

Comparison between the surrogate techniques

To simulate the coupled system, phase oscillators $X_1,\ X_2$ are generated by the usual system of stochastic differential equations as

$$\begin{cases} \dot{\phi}_1(t) & = 2\pi f_1(t) + c_{1:1}\ \sin(\phi_1(t)) + c_{1:2}\ \sin(\phi_2(t)) + \xi_1(t) \\ \dot{\phi}_2(t) & = 2\pi f_2(t) + c_{2:1}\ \sin(\phi_1(t)) + c_{2:2}\ \sin(\phi_2(t)) + \xi_2(t). \end{cases} \tag{3.44}$$

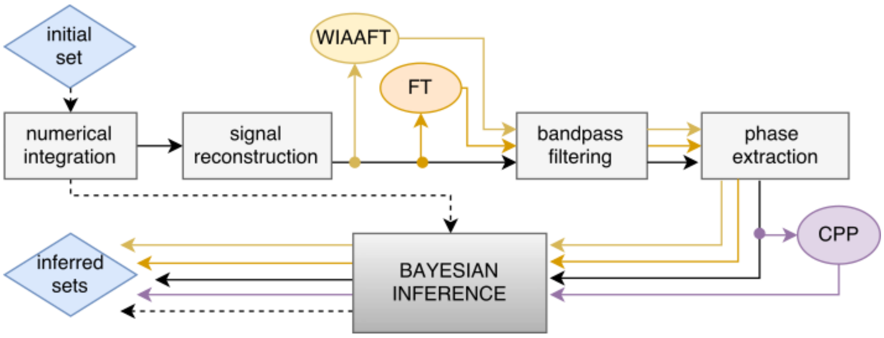

FIGURE 3.23: Diagram of computational steps from the initial set of parameter to the output of the inference for the 5 sets of phases: (i) numerical phases (dashed black path), (ii) signal reconstructed from the numerical phases (black solid path), (iii) WIAAFT surrogates (yellow path), (iv) FT surrogates (orange path) and (v) CPP surrogates (purple path). Boxes indicate the processing steps. Note that CPP surrogates are computed on a further level of the process than WIAAFT and FT surrogates

The frequencies were set as $f_1 = 1$ and $f_2 = 8$ Hz. The initial set of coupling parameters were set as $c_{1:1} = c_{2:2} = 0.2,\ c_{2:1} = C \cdot (1 + 0.3 \sin(2\pi 0.006t)),\ +c_{1:2} = 0$, with $C = [0,\ 0.6,\ 6]$. This produced a system with constant weak self couplings and a unidirectional time-varying coupling from the slower oscillator X_1 to the faster oscillator X_2.

Figure 3.23 illustrates the sequence of steps undertaken for the analysis, and highlights the point in the stream where surrogates are applied. The black-dashed path indicate the sequence of steps required to infer the coupling parameters from the numerically generated phases. As before, in order to simulate real time-series, $s_1(t)$ and $s_2(t)$ were created by applying the cosine function to the phases, and the final simulated signal was reconstructed as $s(t) = s_1(t) + s_2(t)$. The output of this step constitutes the input of the WIAAFT (yellow path) and FT surrogates (orange path). The components were then reconstructed from numerical, WIAAFT and FT time series by Butterworth bandpass filtering, and the phases recovered with Hilbert transform and protophase-to-phase transformation. The numerical output of this step (black solid path) constituted the input for the CPP surrogate (purple path). All the four sets of phases were then used as input of the dynamical Bayesian inference, and the 5 inferred sets of parameters were compared.

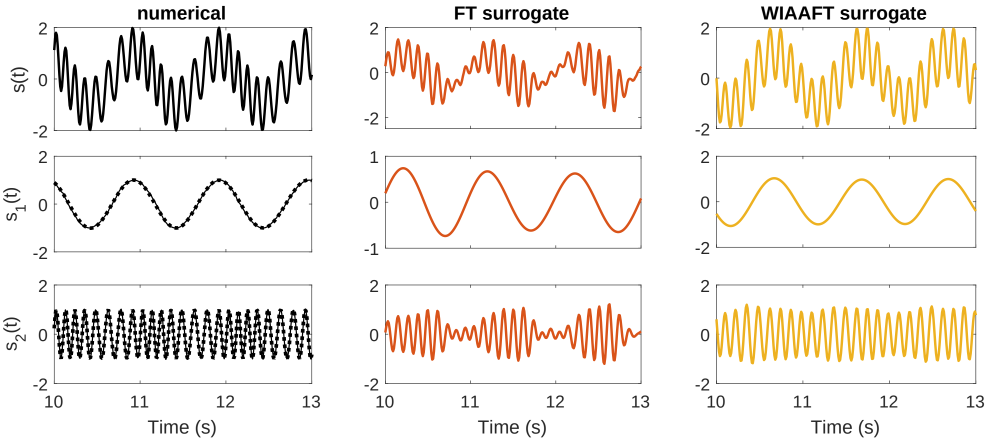

FIGURE 3.24: 2 s time windows of the time series $s(t)$ (top row), generated by $s_1(t)$ (middle row) and $s_2(t)$ (bottom row) for the system with strongest coupling ($\langle c_{2,1} \rangle = 6$). The original numerically generated time series are shown as solid black lines lines. The corresponding filtered oscillations are overlapped as dotted black lines. The surrogates of $s(t)$ are shown in orange for FT and yellow for the WIAAFT, with the corresponding bandpass filtered oscillations.

Figure 3.24 shows the time series resultant from the numerically generated phases in thin black lines and the ones recovered from the filtering procedure in dashed black lines. The surrogates generated from the original time series are shown in orange for FT and yellow for WIAAFT. Both methods aim to preserve the spectral content of the signal, and it can be seen in the bottom panels how the frequency modulation of s_2 is, in both surrogate cases, less evident. The coupling seems to be converted into a more complicated waveform with variable amplitude. This feature is not relevant for the dynamical Bayesian inference, which is based solely on the phase and independent of the amplitude.

Results of the dynamical Bayesian inference for the 5 sets of phases are shown in Figure 3.25. The numerical values of the coupling parameter are plotted with grey lines, the values inferred from the numerically generated phases are shown with solid black, and

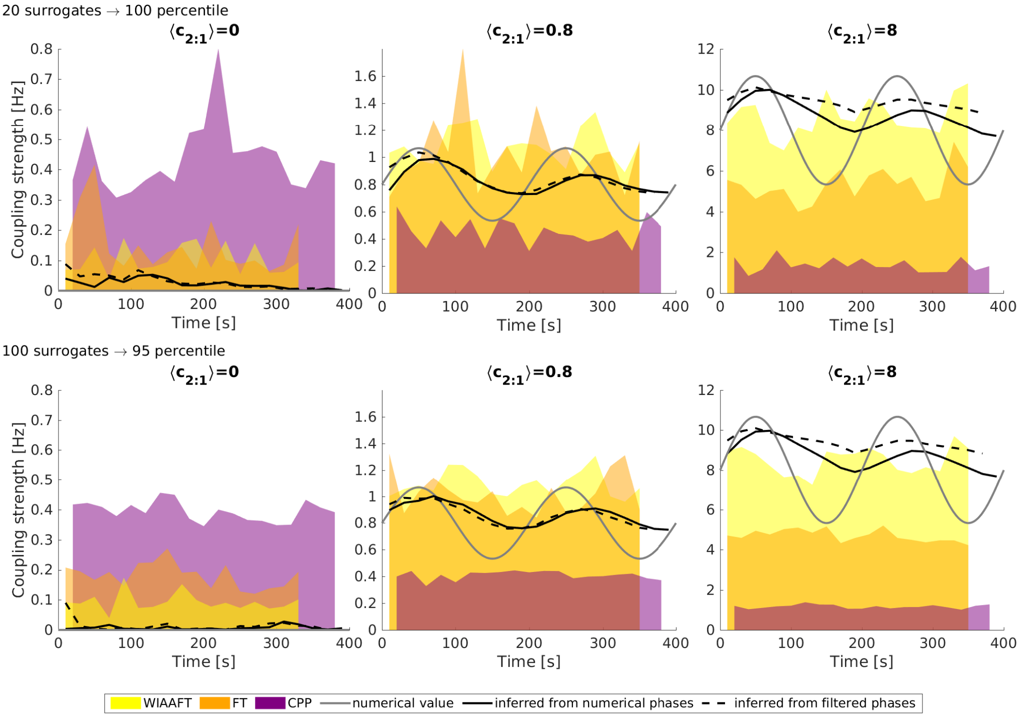

FIGURE 3.25: Results of the dynamical Bayesian inference for the 5 sets of phases shown with arrows in Figure 3.23: the numerical values of the coupling parameter (grey solid lines), the values inferred from the numerically generated phases (solid black lines), and from the filtered phases (dashed black lines). The surrogate thresholds are shaded with transparency in yellow for WIAAFT, orange for FT, and purple for CPP. The computation has been performed with both a set of 20 surrogates (100 percentile threshold) and with a set of 100 (95 percentile threshold). Each column of panels corresponds to a different values of $\langle c_{2,1} \rangle$, i.e. null, weak and strong direct coupling.

the valeus inferred from the filtered phases with dashed black lines. Surrogate thresholds are shaded with transparency in yellow for WIAAFT, orange for FT, and purple for CPP.

The computation has been performed with both a set of 20 surrogates by setting the threshold as the maximum value of the distribution (first row of Figure 3.25) and with a set of 100 surrogates, with the threshold at 95 percentile (second row). Each column of panels in the figure corresponds to a different values of $\langle c_{2,1} \rangle$, i.e. null, weak and strong direct coupling.

The comparison between vertically aligned panels shows how the thresholds are similar, with less variability between time windows when 100 surrogates are performed. The horizontal comparison allows one to evaluate the performance of the different surrogate techniques for different levels of coupling strength.

For the null direct coupling, numerical and filtered series assume a value very close to zero, lower than surrogate thresholds. In other words, all the 3 surrogate methods succeed to indicate that the inferred values does not correspond to an actual coupling.

For both weaker and stronger direct coupling, the inferred parameters for the numerical and filtered phases (black solid and dashed lines) not only resemble the set value (grey lines) of $\langle c_{2,1} \rangle$, but also correctly follow its time evolution. The performances of FT and WIAAFT surrogates are similar in the case of $\langle c_{2,1} \rangle = 0.8$, generating thresholds comparable the actual value of the coupling. For $\langle c_{2,1} \rangle = 8$, the FT succeed in validating the inferred coupling strength, while the WIAAFT still generate a value not lower than the actual coupling.

On the contrary, the CPP surrogates succeed in both cases to validate the inferred value of the coupling parameter, with a lower threshold and also a lower time-variability than the other techniques.

3.5.0.2 Conclusions about the surrogate techniques

For validating phase-coupling between oscillation, it is crucial to generate surrogates which fit the null hypothesis of being uncoupled. Among the surrogates here tested, the CPP techniques gave the most consistent results, validating (or invalidating) with more ample margins the cases in which coupling was present (or absent). They intuitively represent the perfect compromise between destroying the phase-coupling and maintaining the other features of the time series, as the overall time evolution is randomised whilst preserving the within-phase evolution.

It emerged from this investigation that the approach of FT surrogates, by preserving the spectra, could maintain traces of coupling in the reconstructed surrogates. Similarly, the approach of WIAAFT surrogates resulted too conservative in respect of the nonlinear features of the time-series, and was not appropriate for this specific application.

It should be mentioned that another possible technique is to compute inter-subjects surrogates, when data from more than one subject is available. They create a set of different realisations of similar processes by merging time-series from different subjects in the same condition. Independence between each of them is guaranteed by considering time-series from different individuals involved in the experiment. However, inferred coupling parameters are not completely independent of subject-specific features of the signals, in particular from the subject-specific natural frequencies. It will be seen when dealing with real data that the surrogate thresholds for coupling are strongly subject-dependent. Therefore, it seems more appropriate to test each subject with their own specific set of surrogates in order to validate whether a value of coupling is or not to be considered relevant.

The inter-subject surrogate technique is instead appropriate for the validation of phase-coherence, as the computation is performed point-by-point in the frequency space and therefore should be not biased on the subject-specific spectral distribution.

3.5.1 Statistical tests

In order to test for significant differences between distributions, two-sided Wilcoxon tests are applied to the data (Gibbons and Chakraborti, 2011). Wilcoxon tests are non-parametric, which is a fundamental feature when dealing with non-normal distributions, e.g. when the t-test is not suitable to be applied. These tests compare the median of the distributions by applying a ranking-based algorithm. The test's result is independent from the actual values of the distributions' points, and depend strictly on their ranking.

In case of unpaired distributions, the *Wilcoxon rank sum test* (also known as *Mann–Whitney U test*) was applied. In this version of the test, the sample points from both groups $g = 1 : 2$ are ranked and R_g for each group is calculated as the sum of the corresponding ranks. Calling n_g the number of samples for each group,

$$U_g = R_g - n_g(n_g + 1)/2 \; . \tag{3.45}$$

The smallest value between the two U_g is used to calculated the p-value, according to significance tables (Lowry, 2014).

For cases in which intersubject distributions on data referred to the same probe/combination of probes the paired version of the test (the *Wilcoxon sign rank test*) has been used. The test is performed by the ranking the absolute differences between the group values of each pair and by considering the sign of the difference. This means calculating the score

$$W = \sum_{i=1}^{N} [\mathrm{sgn}(x_{2,i} - x_{1,i}) \cdot R_i] \; , \tag{3.46}$$

where N are the number of pairs, and R the rank. Tables provide guidelines on the p-value of W as function of the sample size N (Lowry, 2014).

The significance value for rejecting the null hypothesis of equal medians is set as α=0.05.

Chapter 4

ASD features

Autistic Spectrum Disorder (ASD) is a neurodevelopemental condition affecting around 700,000 individuals in the UK: more than 1 in a 100 (Brugha et al., 2012). Currently, the diagnosis of this disorder is based on behavioural criteria: the evaluation score is based on the presence of impaired verbal communication, sensory dysfunctions and social interactions (Gotham et al., 2009). People in the spectrum often have a preference for unchanging and predictable situations, which they recreate by a pattern of repetitive behaviours and by keeping restricted, often very focused, fields of interests. Individuals with ASD can have great difficulties in dealing with social interactions, and in general with unstructured, unpredictable situations (Gomot and Wicker, 2012).

Being a spectrum, the disorder can manifest with extremely variable characteristics and degrees of severity. The spectra of people with ASD diagnosis range from non-verbal to high functioning individuals (Lord et al., 2000).

In the past, it has been theorised that ASD subjects could be defined as cases of 'extreme male brain'. The theory was first suggested by Hans Asperger in 1944, when he wrote: 'The autistic personality is an extreme variant of male intelligence. Even within the normal variation, we find typical sex differences in intelligence. In the autistic individual, the male pattern is exaggerated to the extreme' (Asperger, 1944).

The theory has been more formally revised in recent years by Baron-Cohen (Baron-Cohen, 2002). The author suggested to score the prevalence of male and females brain features in individuals according to their ability to ’systemising’ and ’empathising’, instead of the more classically applied gender classification based on verbal and spatial abilities. The male brain in this psychometric scale is found in those individuals in whom systemising is significantly better than empathising. The female brain is defined as the opposite profile. Using these definitions, the author suggests that autism could be considered as an extreme of the normal male profile.

The disorder is highly inheritable and spans in a wide range of severity. Being a spectrum ASD comprehends an extremely heterogeneous population, spamming from non-verbal to high functioning individuals. Studies of infants at high risk of autism have shown that characteristic social deficits in ASD can emerge in children as young as 1–2 years (Ozonoff et al., 2010). However, the current diagnosis process usually requires longer, with subjects on the ASD spectrum being diagnosed even in early adolescence.

4.1 Current diagnosis procedure

Despite the huge effort spent by the scientific community to explain and characterize genetic (De Rubeis et al., 2014, Ronemus et al., 2014) and neuroanatomical (Barnea-Goraly et al., 2004, Casanova et al., 2002) features of the disorder, the diagnosis procedure is currently still based on behavioural tests and interviews (Gotham et al., 2009).

The criteria taken into account in order to assess the presence of ASD are mainly the presence of impaired verbal communication, limited interest for social interactions and sensory dysfunctions. Some of the scales used are:

- Childhood Autism Rating Scale (CARS) (Ozonoff et al., 2005)
- Autism **Behavior** Checklist (ABC) (Oro et al., 2014)
- Autism Diagnostic **Observation** Schedule (ADOS) (Lord et al., 1989)

- Autism Diagnostic **Interview** (ADI)(Lord et al., 1994)
- Diagnostic and Statistical Manual of Mental Disorders (DSM-IV)(Spitzer and Williams, 1980)

4.2 From genetic to anatomical characterisation

Under a genetic point of view, a growing body of research suggests that ASD could be associated with changes in genes playing a role in synaptic brain functions (Berkel et al., 2010, Durand et al., 2007, Gilman et al., 2011).

Alterations in the genes coding for the protein Reelin is believed to affect the migration and formations of layers during cortical development (Fatemi et al., 2005). Also, deficiencies in GABA-receptor expression or function are likely involved in ASD (Rubenstein and Merzenich, 2003). A reduced activity of the inhibitory GABAergic activity could lead to hyperexcitability in neural networks. This lack of balance between excitatory and inhibitory signals is likely to be a cause of the typically impaired ability to ignore background stimuli or excessive sensorial input in ASD (Lord et al., 2000).

At a developmental stage, when pruning and synaptogenesis are most dynamically shaping the neural network, different genetic expression within synapses could play a crucial role in generating an alternative wiring. Specific neuroanatomical features are logical to follow, and recent findings claim that, from hundreds of genes linked with ASD, as few as 10 subgroups of anatomical features could be definable (Donovan and Basson, 2016).

Several studies reported brain enlargement has been observed in children with ASD (Amaral et al., 2008, Courchesne et al., 2001, Schumann et al., 2010). In particular, studies on retrospective head circumference and longitudinal brain volume studies of 2 years old at high risk of autism shed some light on the timing of this phenomena, linking also brain volume overgrowth with severity of the disorder (Hazlett et al., 2005).

More recently, the same authors focused on MRI scans of 6 and 12 months of age in order to detect features preceding the brain volume overgrowth. They found that hyper-expansion of the cortical surface area was found in infants who were later diagnosed with autism (Hazlett et al., 2017).

The overgrowth of cerebral cortex is in line with the hypothesis which describes the autism brain having an excessive number of mini-columns (Casanova et al., 2002). Such over-populated cortex might result in a local overconnectivity and a more sensitive activation process. This may play a role in the impairment of cognitive processes typical of ASD, as well as in the high co-morbidity of epilepsy and ASD (Tuchman and Rapin, 2002). The mini-columns hypothesis also suggested that the overgrowth of cortical cells could result in decreased pruning and reduced synaptogenesis (Marchetto et al., 2016), phenomena which both can led to a topologically different brain network.

A recent comparative study was performed on Autism Brain Imaging Data Exchange, including about 1000 participants aged 6–65 years (Haar et al., 2016). Thicker cortex was one of the anatomical features that can still be detected when comparing brains of ASD and CG adults, while other differences (such as the volumetric overgrowth of the brain which characterize the brain of ASD toddler) were found to be later on compensated for.

4.3 EEG results from literature

At a higher level of abstraction from genetics and cellular dynamics, it is a generally agreed that ASD can be pictured by maps of brain synchronisation patterns that are distinguishable from control groups, in an interplay of under- and over-connectivity (Belmonte et al., 2004, Wass, 2011).

The importance to involve objective measures in the diagnosis process is evident. In the last 15 years, several possible biomarkers of ASD from EEG signals have been identified

(Billeci et al., 2013, Gurau et al., 2017). Studies focused mainly on differences in functional connectivity and spectral power evaluated by time-frequency methods. Being such a diversity of condition, it is not surprising that the outcomes were not univocal.

In this section, a brief review of literature results is presented. Studies included in this list were chosen for analysing EEG of ASD young children in resting state, with measures like spectral power and coherence. For comparison, information on reference technique, age of the subjects, experimental design and method applied have been reported in this review, together with the main results.

4.3.1 Power

Investigations on spectral features of EEG from ASD children gave variable results. The information of the studies and outcomes are shown in Table 4.1.

4.3.1.1 Type of measures

Most of the studies investigated the spectral content of the EEG by applying Fourier transform on short epochs of the time-series, and by averaging the result. The exceptions were only two: one applied a method called 'multi-taper' (Thomson et al., 2000), which simulates multiple realisations of the same time series sample. The other applied the Welch transform, a modified version of the short time Fourier transform using window function on overlapping segments of data.

4.3.1.2 General outcomes

Results for the power investigations are not in complete agreement. From the corresponding columns in Table 4.1, it can be hypothesised that age of the subjects, reference channel, type of activity or resting state might have again played a role in generating the mixed outcomes. One should also bear in mind that inter- and intra-subjects variability are hypothesised to be a key-feature themselves (David et al., 2016).

Author Year	Reference	Age	Subjects number	Setting	Method	Result
Tierney et al. (2012)	CA-eyes	0.5-2 years	65 HRA 57 CG	Eyes open	FT	$\Downarrow$ all bands absolute power in HRA at 6 months
Pop-Jordanova et al. (2010)	NA	3-6 years	9 ASD intragroup	Attention tasks	FT	$\Uparrow$ δ $\Uparrow$ θ absolute power in F region
(Stroganova et al., 2007)	LE	4-6 years	40 ASD 40 CG	Visual attention	FT	$\Uparrow$ δ absolute power in Fp region
Lushchekina et al. (2012)	LE	4-7 years	27 ASD 24 CG	Eyes closed	FT	$\Downarrow$ θ and $\Uparrow$ γ absolute
Orekova et al. (2006)	LE	3-8 years	37 ASD	Visual attention	FT	$\Uparrow$ γ absolute power
Matlis et al. (2015)	BP	4–8 years	27 ASD 55 CG	Eyes open	MT	$\Downarrow$ α posterior/ anterior power ratio
Machado et al. (2015)	LE	4.5-8 years	11 ASD 14 CG	Eyes open	WP	$\Downarrow$ δ, θ PSD in the C region $\Downarrow$ β in P region, lateralised to the R
Cantor et al. (1986)	LE	5-9 years	11 ASD 13 CG	Eyes open	FT	$\Uparrow$ δ, $\Downarrow$ α absolute power
Coben et al. (2008)	LE	6-10 years	20 ASD 20 CG	Eyes closed	FT	$\Downarrow$ δ absolute power in F(L) region $\Uparrow$ β in Z region $\Uparrow$ θ in O(R) region
Sheikhani et al. (2009)	LE	6-11 years	11 ASD 17 CG	Eyes open	FT	$\Uparrow$ γ absolute power
Elhabashy et al. (2015)	LE	4-12 years	21 ASD 21 CG	Eyes open	FT	$\Uparrow$ δ and θ absolute power especially in F region
Chan et al. (2007)	LE	6-12 years	66 ASD 48 CG	Eyes open	FT	$\Uparrow$ δ, $\Downarrow$ α relative power

Table 4.1: Review of spectral power studies in ASD children, ordered by age of the participants (HRA=high risk of autism, BP= bipolar, LE=linked ears, PSD=power spectral density, P=parietal, Fp=prefrontal, F=frontal, C=central, O=occipital, L=left, R=right, Z=mid-line, MT=multitaper, WP=Welch periodogram).

	⇑ power in ASD	⇓ power in ASD
δ	absolute F (Pop-Jordanova et al., 2010) (Elhabashy et al., 2015) absolute Fp (Stroganova et al., 2007) absolute (Cantor et al., 1986) relative (Chan et al., 2007)	absolute C (Machado et al., 2015) absolute F L (Coben et al., 2008)
θ	absolute F (Pop-Jordanova et al., 2010) (Elhabashy et al., 2015) absolute O R (Coben et al., 2008)	absolute (Lushchekina et al., 2012) absolute C (Machado et al., 2015)
α		relative (Chan et al., 2007) posterior/anterior ratio (Matlis et al., 2015) absolute (Cantor et al., 1986)
β	absolute Z (Coben et al., 2008)	absolute P, R (Machado et al., 2015)
γ	absolute (Lushchekina et al., 2012) (Sheikhani et al., 2009) (Orekova et al., 2006)	

TABLE 4.2: Summary of outcome of coherence studies in ASD children, grouped by frequency bands (P=parietal, F=frontal, Fp=prefrontal, C=central, O=occipital, L=left, R=right, Z=midline).

However, for some frequency bands, the results are unanimous. Table 4.2 shows how, within the studies, absolute and relative power in the alpha band where never higher for the ASD group. On the contrary, gamma power never resulted lower for the ASD.

For the theta band, the results are mixed. However, the studies detecting higher power for the ASD had been conducted on older children, in respect to the studies showing a higher theta power for the CG. No obvious discriminant could be found for the mixed results obtained for the delta and beta bands.

4.4 Coherence

A recently reviewed substantial body of evidence (Gurau et al., 2017, Schwartz et al., 2016), which includes a study on a big population of children (Duffy and Als, 2012), suggests that analysing the coherence of EEG activity across the scalp could be a promising way to depict the inner neural circuitry which could be characteristic of the disorder. Nevertheless, details of the *typical* ASD-connectivity emerging from different studies are, once again, rarely converging to a unique picture.

However, this divergence should not be seen as contradictory: as for the spectral power investigations, different group age, experimental settings and analysing methods could have led to apparently contradictory coherence results.

4.4.1 Experimental diversity

EEG recordings for the coherence studies were performed under resting state conditions, with eyes either open or closed, during sleep or during task performance. The age of the subjects varied from few months to 12 years of age.

As for the power, also the choice of reference electrode was not consistent between coherence studies. Among all the choices, linked ears (LE) and common average (CA) where the most common. Few studies adopted current source density (CSD) reconstruction, bipolar montages, single ear, nose, right leg and linked mastoids references.

Author Year	Refe-rence	Age	Subjects number	Setting	Result
Keehn et al. (2015)	CA	6-12 months	11 HRA+ 30HRA- 46CG	View images of familiar or unfamiliar face	⇑ L lateralization of intra-hemispheric γ MSC at 12 months
Righi et al. (2014)	CA	6-12 months	26 CG 17HRA- 5HRA+	Listen to speech sounds	⇓ average γ LC at 12 months
Orekhova et al. (2014)	CA	12-17 months	26 CG 18HRA- 10HRA+	Watch social and non-social video	⇑ α PL over the F and C areas, in both video condition
Catarino et al. (2011)	Nose	29 months	11 ASD 15 CG	Object recognition	⇓ α and θ MSC
Domínguez et al. (2013)	CSD	2-5 years	72 ASD 31 CG	View emotional faces	⇑ IC in δ and θ over P region and in shortrange connections in L hemisphere in δ θ and α
Boersma et al. (2013)	RL	2-5 years	12 ASD 19 CG	Viewing pictures of cars and faces	⇑ global PL in high-α, β
Buckley et al. (2015)	LE	3-6 years	87 ASD 29CG	Eyes-open resting	⇑ MSC in deep sleep No difference in awake
Lushchekina et al. (2016)	LE	4-7 years	27 ASD 24 CG	Eyes closed	⇓ δ and θ MSC in F-P connections ⇓ α for F-T connections ⇑ β and γ MSC
Machado et al. (2015)	LE	4.5-8 years	11 ASD 14 CG	Eyes open	⇑ δ MSC L short-range ⇑ δ β, and γ MSC medium/long-range ⇑ interhemispheric short/ medium-range in P region
Coben et al. (2008)	LE	6-11 years	20 ASD 20 CG	Eyes closed	⇓ δ and θ MSC long-range for F-P connections and globally at short-range
Carson et al. (2014)	LM	8-11 years	19 ASD 13 CG	Eyes open, watch blank screen	⇓ α MSC in interhemispheric T-P and F regions
Elhabashy et al. (2015)	LE	4-12 years	21 ASD 21 CG	Eyes open	⇓ δ, θ, and α MSC intra-hemispheric ⇓ θ MSC interhemispheric over C/P/O regions ⇑ δ MSC interhemispheric over T regions

Author Year	Reference	Age	Subjects number	Setting	Result
Clarke et al. (2016)	LE	7-12 years	20 ASD 20 CG	Eyes closed	$\Downarrow$ α and β MSC in F short/ medium interhemispheric
Cantor et al. (1986)	LE	4-12 years	11 ASD 13 CG	Eyes open	$\Uparrow$ α and δ MSC inter-/ intra-hemospheric
Chan et al. (2011)	LE	4-12 years	11 ASD 13 CG	Object recognition	$\Uparrow$ θ MSC in F (L) region
Sheikhani et al. (2012)	LE	8-12 years	17 ASD 11 CG	Eyes open	$\Uparrow$ γ MSC between T and other brain regions $\Downarrow$ β MSC over T-P L regions
Duffy and Als (2012)	CSD	2-12 years	430 ASD 554 CG	Eyes open	$\Downarrow$ θ, α, β MSC short-range $\Uparrow$ δ and β MSC in medium/long-distance
Lazarev et al. (2015)	SE	6-16 years	14 ASD 16 CG	Eyes closed	No difference

TABLE 4.3: Review of coherence studies in ASD children, ordered by age of the participants (CSD=current source density, CA= common average, RL=right leg, LE=linked ears, LM=linked mastoids, SE=single ear, HRA+=autism developed from high risk situation, HRA-=autism not developed from high risk situation, MSC= magnitude square coherence, LC= linear coherence, PL=phase lag, IC=imaginary coherence, P=parietal, F=frontal, C=central, T=temporal, O=occipital, L=left).

As proved by several studies (Nunez et al., 1997, Qin et al., 2010, Yao et al., 2005), the choice of reference has a significant impact on the outcome especially in coherence studies. The linear transformation, by subtracting the reference time series from all the probes, inevitably reduces the coherence between electrodes containing similar information than the reference time series, while enhancing at the same time the impact of the opposite scenario.

In what follows, the different experimental settings from literature will be discussed. The results of the studies will then be compared in the light of the non-homogeneous experimental frameworks.

4.4.1.1 Coherence measures

Analogously to the power investigations, Table 4.3 reports the information and results of coherence studies on EEG of autistic children. Within the literature studies, the definition of *coherence* was not unique: even if most of them apply magnitude-squared coherence (MSC), few studies used other parameters like linear coherence (LC) (Righi et al., 2014), imaginary coherence (IC) (Domínguez et al., 2013) or phase lag (PL) (Boersma et al., 2013, Orekhova et al., 2014). Although all the methods provide a measure of the coherence of phase at different frequencies, there are some differences. The methods are briefly introduced below.

- MSC: It considers both magnitude of the spectral power and phase relationship. Given two signals $x_1(t)$ and $x_2(t)$ with time frequency representation $X_i(t, f)$ and $X_j(t, f)$, the cross spectrum at every frequency bin will be

  $$S_{ij}(f) = \langle X_i(t, f) X_j^*(t, f) \rangle_t \ . \tag{4.1}$$

  Based on this measure, the MSC is computed as (Bendat and Piersol, 1986)

  $$MSC_{ij}(f) = \frac{|S_{ij}(f)|^2}{|S_{ii}(f) S_{jj}(f)|} \ . \tag{4.2}$$

  It is similar to the Wavelet phase coherence (WPC) discussed in Section 3.2, defined as $WPC(f) = |\langle e^{i\Delta\phi(f,t)} \rangle_t|$, with $\Delta(\phi) = \phi_i - \phi_j$ (Mormann et al., 2000, Sheppard et al., 2012).

- PL: Based on the phases extracted by frequency transformations (like FT or WT), or on the Hilbert transform, it expresses the level of asymmetry of the instantaneous phase difference between two EEG signals. It is computed as $PL(f) = |\langle \text{sign}\big(\Delta\phi(f, t)\big) \rangle_t|$ (Stam et al., 2007). The asymmetry implies the presence of a time preserved, non-zero phase lag. Compared to the other measures of coherence, it has the advantage to be less affected by the influence of volume conduction and the choice of the reference electrodes (Boersma et al., 2013). On the other hand, symmetrical lags due to mutual interactions are discarded by this measure.

- LC: Based on discrete wavelet transform, it is an event-related measure of spectral correlation, computed on few-cycles-long time epochs (Delorme and Makeig, 2004). It allows one to detect whether an event triggers a phase locked response in a time series. It can be computed comparing time series from different trials, or on from different locations.
- IC: Instead of the coherence module of LC, it extracts the value of the phase difference (Nolte et al., 2004). A high value of IC can not be caused by a linear mixing of uncorrelated sources, and therefore is not sensitive to volume conduction effects (Stam et al., 2007). However, IC can not be interpreted as a measure of interaction, since it depends both on the strength of the coupling and the value of the phase difference.

4.4.1.2 General outcome

Although the outcomes of the studies are quite variable, some common thread can be found (summarised in Table 4.4).

Three studies detected for the delta band significantly lower fronto-parietal coherence in ASD for young children (Coben et al., 2008, Lushchekina et al., 2016). In the same band, shorter connections have been found stronger in the same age ASD group (Domínguez et al., 2013, Machado et al., 2015). Three studies found on the contrary higher coherence in delta band for long distance and/or inter-hemispheric connections, but all of them had been performed on a set of subjects including older children (Cantor et al., 1986, Duffy and Als, 2012, Elhabashy et al., 2015).

Similar pictures emerge for the theta band, with most of the studies detecting lower coherence for the ASD group in long distance connections (Catarino et al., 2011, Coben et al., 2008, Elhabashy et al., 2015, Lushchekina et al., 2016), and higher coherence for shorter links (Chan et al., 2011, Domínguez et al., 2013).

For alpha activity, the majority of the studies detected a lower coherence in the ASD group (Carson et al., 2014, Catarino et al., 2011, Clarke et al., 2016, Duffy and Als, 2012, Elhabashy et al., 2015, Lushchekina et al., 2016). However, the age of the participants could again have played a role in the different outcome: studies finding lower coherence within alpha oscillations in the CG had been mostly performed on younger children (Boersma et al., 2013, Domínguez et al., 2013, Orekhova et al., 2014).

Outcomes are quite consistent for the beta band. Across the different studies, it has been found that the coherence is higher in the ASD group both generally and in medium-long distance connections (Boersma et al., 2013, Duffy and Als, 2012, Lushchekina et al., 2016, Machado et al., 2015), while it is lower for shorter distances (Clarke et al., 2016, Duffy and Als, 2012, Sheikhani et al., 2012).

The gamma band again seems to generate almost unanimous outcome, with only one study (based on LC) detecting a lower coherence (Righi et al., 2014) and four studies reporting higher degrees of coherence in this band for the ASD group (Keehn et al., 2015, Lushchekina et al., 2016, Machado et al., 2015, Sheikhani et al., 2012).

To our knowledge, ASD brain connectivity has been described exclusively by detecting coherence within the same frequency range. However, the phase modulation acting from the slower wave to the faster is believed to play an important role in brain processes (Jensen and Colgin, 2007). To assess if this phenomenon is somehow impaired in ASD, cross frequency phase interactions in EEG data will be quantified in this work.

	$\Uparrow$ coherence in ASD	$\Downarrow$ coherence in ASD
δ	P short (Domínguez et al., 2013) short L (Machado et al., 2015) inter-H T (Elhabashy et al., 2015) inter-H, intra-H (Cantor et al., 1986) long-med (Duffy and Als, 2012)	F-P (Lushchekina et al., 2016) F-P long (Coben et al., 2008) intra-H (Elhabashy et al., 2015)
θ	P, short L (Domínguez et al., 2013) F L (Chan et al., 2011)	generally (Catarino et al., 2011) F-P (Lushchekina et al., 2016) F-P long (Coben et al., 2008) C-P-O inter-H (Elhabashy et al., 2015) short (Duffy and Als, 2012)
α	F,C (Orekhova et al., 2014) short L (Domínguez et al., 2013) generally (Boersma et al., 2013) inter-H and intra-H (Cantor et al., 1986)	generally (Catarino et al., 2011) F-T (Lushchekina et al., 2016) intra-H, T-P F inter-H (Carson et al., 2014) intra-H (Elhabashy et al., 2015) F short-med inter-H (Clarke et al., 2016) short (Duffy and Als, 2012)
β	generally (Boersma et al., 2013) (Lushchekina et al., 2016) med-long (Machado et al., 2015) (Duffy and Als, 2012)	F short-med inter-H (Clarke et al., 2016) T-P L (Sheikhani et al., 2012) short (Duffy and Als, 2012)
γ	intra-H L (Keehn et al., 2015) generally (Lushchekina et al., 2016) med-long (Machado et al., 2015) T-other regions (Sheikhani et al., 2012)	generally (Righi et al., 2014)

TABLE 4.4: Summary of outcome of coherence studies in ASD children, grouped by frequency bands (P=parietal, F=frontal, C=central, T=temporal, O=occipital, L=left, H=hemispheric).

Chapter 5

Application to ASD data

5.1 Participants

A total of 22 boys and 10 girls were recruited for this study within the Blackpool Teaching Hospitals. Inclusion criteria were:

- Clear diagnosis of ASD or normal development
- Age between 3 years 0 months and 5 years
- Parents able and willing to provide informed consent

Exclusion criteria were:

- Medications known to affect brain function
- Structural brain and chromosome abnormalities
- Uncertainty re-diagnosis or developmental progress
- First degree relative with ASD diagnosis (for neurotypical only)
- Epilepsy or undiagnosed seizure episodes

	Subject number	Age [months]	ADOS score	Hand Preference	Summary
ASD males	#1	42	19	ND	
	#2	45	19	ND	Age=50±6
	#4	50	19	Right	ADOS=17.6±3.5
	#10	56	11	ND	Right= 53.8%
	#13	50	22	ND	Left=7.7%
	#14	50	20	ND	ND=38.5%
	#15	52	20	Right	
	#17	47	21	ND	
	#18	56	13	Left	
	#19	43	19	ND	
	#24	58	16	Right	
	#36	46	18	Right	
	#39	58	12	Right	
CG males	#7	55	0	Right	
	#8	45	2	Right	Age=46±7
	#23	53	0	Right	ADOS=1±1
	#25	55	0	ND	Right=55.6%
	#26	44	2	ND	Left=0%
	#28	44	0	Right	ND=44.4%
	#29	47	1	Right	
	#31	36	2	ND	
	#33	36	2	ND	

TABLE 5.1: Summary of the male subjects' characteristics (ND=Not Determined)

Sbj#	Setting		Activity			State		
	On lap	On chair	No visible activity	Looking at a screen	Bubbles	Sleepy	Quiet	Some movements
#1	X		X			X		
#2	X				X			X
#4	X			X			X	
#10	X		X				X	
#13	X		X				X	
#14	X		X				X	
#15		X		X			X	
#17		X	X				X	
#18		X	X				X	
#19	X			X			X	
#24	X			X			X	
#36	X			X			X	
#39	X		X				X	
#7	X		X			X		
#8		X	X				X	
#23		X		X			X	
#25	X		X				X	
#26	X		X					X
#28	X		X				X	
#29	X		X				X	
#31	X		X					X
#33	X		X				X	

TABLE 5.2: Summary of male subjects's state during the selected time-window

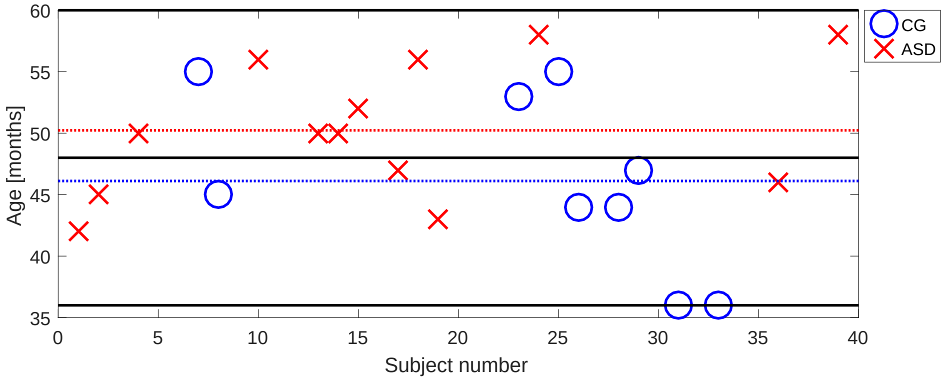

FIGURE 5.1: Age of the males subjects: ASD individuals are marked with the red crosses, and CG with blue circles. Black line mark the threshold of 3, 4, 5 years of age, and dashed lines show the average age for both groups (p-value=0.18).

	Subject number	Age [months]	ADOS score	Hand Preference	Summary
CG females	#5	38	0	Right	Age=46±7 ADOS=0±0 Right=55.6% Left=0% ND=44.4%
	#6	50	0	Right	
	#11	41	0	Left	
	#12	47	0	ND	
	#16	52	0	Right	
	#20	43	0	ND	
	#34	41	0	Right	
	#37	41	0	Right	
ASD females	#21	49	MIS	Right	
	#22	51	MIS	Left	

TABLE 5.3: Summary of the female subjects' characteristics (ND=Not Determined)

Sbj#	Setting		Activity			State		
	On lap	On chair	No visible activity	Looking at a screen	Bub-bles	Sleepy	Quiet	Some move-ments
#21	X			X			X	
#22	X			X			X	
#5	X		X					X
#6	X		X					X
#11		X	X					X
#12		X	X				X	
#16		X	X					X
#20		X	X					X
#34	X		X					X
#37	X		X				X	

TABLE 5.4: Summary of female subjects' state during the selected time-window

Informed consent was obtained from all subjects' parents, and the clinical trial was registered as UKCRN ID 14936.

Because of the rare incidence of ASD in females, it was not possible to recruit a sufficient number of ASD girls to either match the ratio of females in the control group or to perform separate comparisons by gender. Characteristics of male subjects are reported in Figure 5.1 and Table 5.1, and the experimental setting in Table 5.2. Corresponding summary has been made for the female subjects, in Tables 5.3 and 5.4.

Within the males, 13 subjects (aged 50±6 months) had a diagnosis of ASD (ADOS score 17.6±3.5). Mothers of 7/13 of the ASD children (38.5%) declared that no hand-preference emerged yet for their child, 5/13 declared a right-hand preference (53.8%), and 1/13 (7.7%) had left-hand preference. The control group was composed of 9 subjects (aged 46±7 months), selected for having no signs or familiar risk of autism (ADOS score 1±1). For the control group, 4/9 (44.4%) were still undecided about their hand preference, and 5/9 (55.6%) were right-handed.

5.1.1 Signal recording

EEG signals were recorded by using the Nicolet cEEG machine (Viasys Healthcare, USA). 19 probes -plus the reference and the ground channels- where placed on the children's scalps with the standard 10-20 montage (Fig.5.2). recordings were acquired at a sample frequency of 256 Hz. A video-footage of each acquisition was recorded by a camera fixed at a distance of 2 meters in front of the children. The recording sessions

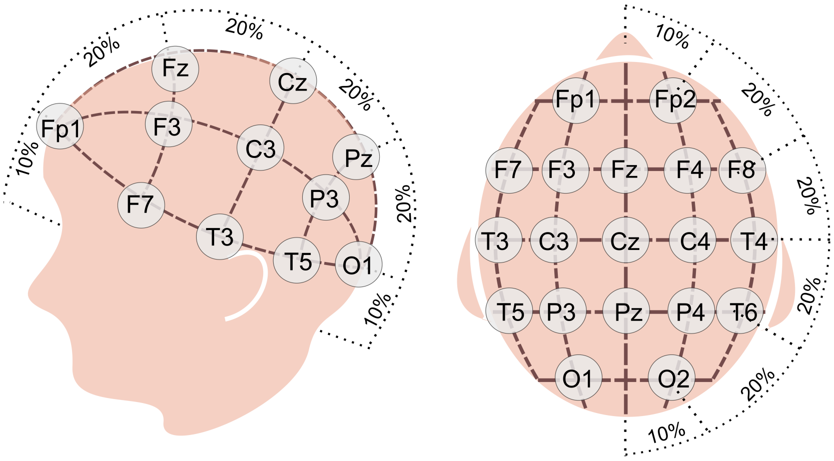

FIGURE 5.2: Side and top view of the 10-20 EEG standard montage.

lasted for around 20 minutes, with the children sit on a chair (or their stroller) or on their parent's lap.

Some children accepted the situation calmly, and needed no distraction for the whole length of the recording, while others showed signs of distress or drowsiness as a response to the unusual lack of activity and interactions. In order to keep them as relaxed as possible, the children were -when needed- entertained with a video played on a smartphone, or by the means of soap bubbles. A summary of the experimental settings for each subjects is shown in Table 5.2.

5.2 Preprocessing

The time series were visually inspected while simultaneously playing the video-recording of the experiment in order to identify the best continuous time-window of relaxed resting state containing as few artefacts as possible.

The best compromise between presence of artefacts due to movements of the subjects (never more that $5s$) and length of the signal was met by carefully selecting within the resting state epochs a time-window of 1 minute from all the recordings. An example of a selected time-window is shown in Figure 5.3. In the time series, the spikes are artefacts due to muscle activation (i.e. eye-movements and facial expressions). The bigger low frequency artefacts visible in F7 and F8 are possibly due to the movement of the cables.

The selected signals were then band-passed within the range of interest (0.8-48Hz). Any residual trends were removed by subtracting the 3rd order polynomial better fitting to the signals.

In order to preserve the original local features of the signals, it was chosen not to perform any manipulation in the shorter time domains, like de-spiking or linearising artefactual-looking epochs.

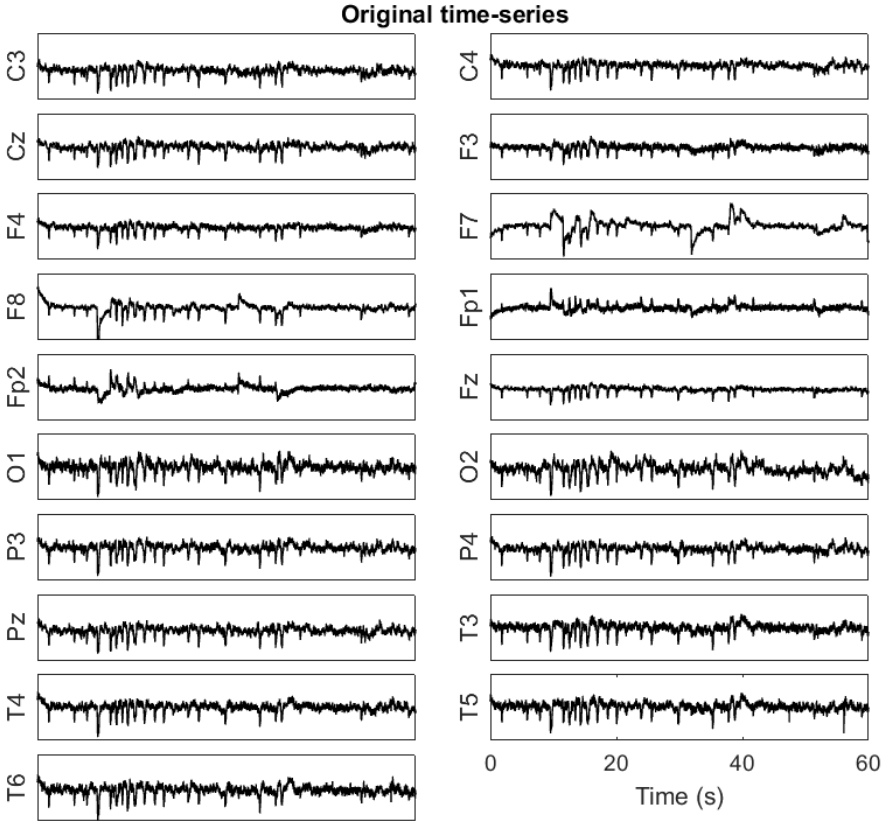

FIGURE 5.3: Example of a selected 1 min time window of all the probes from the data of a CG male.

5.3 Selection of frequency bands limits

After visualising the power spectra, it was noticed that the presence of the 5 classic frequency bands was not obvious in them. Moreover, it was not possible to trace a demarcation line between theta and alpha bands and between beta and gamma bands without crossing a peak in the spectra of some subject. Also, theta-alpha bands and beta-gamma bands showed uniform features between the two groups, as it will be shown in the next Sections.

For these reasons, it was decided to merge theta-alpha and beta-gamma in two unique bands. The frequency limits sets for the low frequency (LF), middle-range frequency (MF) and high frequency (HF) are shown in Table 5.5.

Band name	Lower limit (Hz)	Higher limit (Hz)
LF δ	0.8	3.5
MF $\theta - \alpha$	3.5	12
HF $\beta - \gamma$	12	48

TABLE 5.5: Limits for the EEG bands selected for this study

5.4 Summary of the methods

The methods discussed in Chapter 3 were applied in order to characterise the features and dynamics of the EEG time series. In particular, the measures were applied to the data and visualised as follows:

- The Wavelet transform (WT) of Equation 3.6 discussed in Section 3.1.4 was applied on the time series, with a central frequency of $f_0 = 2$.
    - The power spectra were obtained by averaging $|WT^2|$ along the time dimension. In the figures, shaded portions of the spectra indicates frequency bins for which the group distributions resulted significantly different.
    - In order to compare between subjects the ratio of each spectral component within the total spectral power, the relative power was also computed. The normalisation was performed so that the sum of all the frequency samples in a relative spectrum equals to 1.
    - Interval comparisons were performed by averaging the spectra within each band, for each subject. The resultant 19 values were used to generate an interpolated group-specific head-map for each frequency band. Similar head-maps were used to indicate the significance of differences between the groups, with discrete un-interpolated shades of blue and red indicating with a lighter colour a p-value<0.05 and with a darker colour p-value<0.01.

- The Wavelet phase coherence was computed for all the undirected pairs of probes, as discussed in Section 3.2. The average value within each interval was used for group-comparisons.
  - Fourier transform surrogates were used to validate each combination of probes, as discussed in Section 3.5.
  - Head-maps were used to indicate significant differences between the groups, with non-directional lines in two shades of blue and red indicating with a lighter colour a p-value<0.05 and with a darker colour p-value<0.01. Only comparisons with the higher value above the surrogate threshold are shown.
- Wilcoxon rank sum test or Wilcoxon sign rank test were used to evaluate the statistical significance, as explained in Section 3.5.1.

5.5 Measurement bias in the recordings

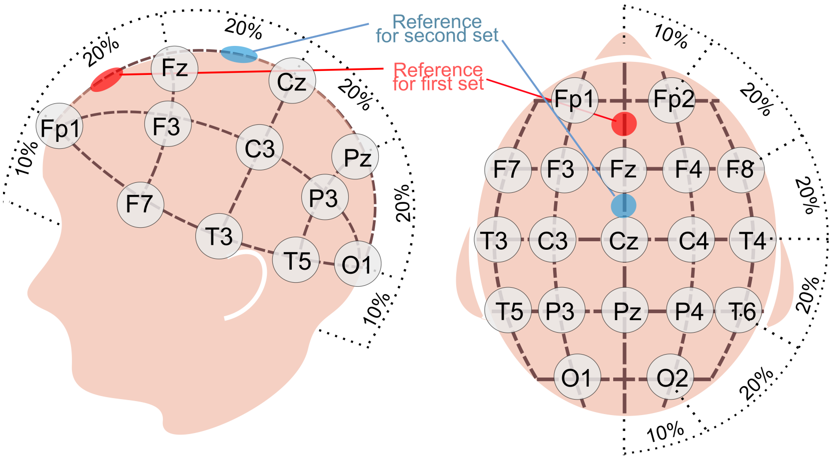

FIGURE 5.4: Side and top view of the 10-20 EEG standard montage, showing the accidentally different placements of the reference probe.

After the whole set of subjects underwent the recording, it was noticed that a strong correlation existed between the EEG features emerging from the dynamical characterisation of the time series and date of the experiment. Further investigations revealed that the EEGs were measured with two different positions for the reference probe: anteriorly (group 1) and posteriorly (group 2) of Fz. The difference between the settings is shown in Figure 5.4. The composition of the groups is reported in Table 5.6.

This inconsistency in the protocol introduced a bias in the brain dynamics investigations. Absolute power and wavelet phase coherence were the most clearly affected and therefore are discussed in this section.

How much this bias affected the results was obvious when applying the methods of power and coherence on mixed groups of subjects divided by the location of the reference. With these criteria, each group contained ASD, CG, males and females subjects. It was therefore unlikely that the significance of the outcome could reflect a real difference in brain dynamics of groups distinguished by anything else than the reference placement.

Figure 5.5 shows the result of this test. The significance for this comparison is spread across all the frequency spectrum and over the vast majority of probes (for power) and pairs of probes (for coherence).

It can be also noticed that both the absolute power and coherence were significantly lower in the areas closer to the reference electrode's position. In particular, group 1 had higher power and coherence centrally (further form the anterior position of the reference probe) and group 2 had higher power and coherence frontally (further form the central position of the reference probe).

This can be explained remembering that for unipolar electrodes referenced to the probe X, the times series V_A of the probe A is a voltage derived from the difference of electric potential energy E_A and E_X. For closer probes, the electric potential energy in each time sample is more likely to be more similar than for probes placed further away, and therefore the recorded voltage would be less informative. In particular, similar electrical activity which is collected both by the probe A and by the reference will be subtracted-out in the time series of probe A, resulting in lower absolute power and coherence between nearby probes.

Absolute power

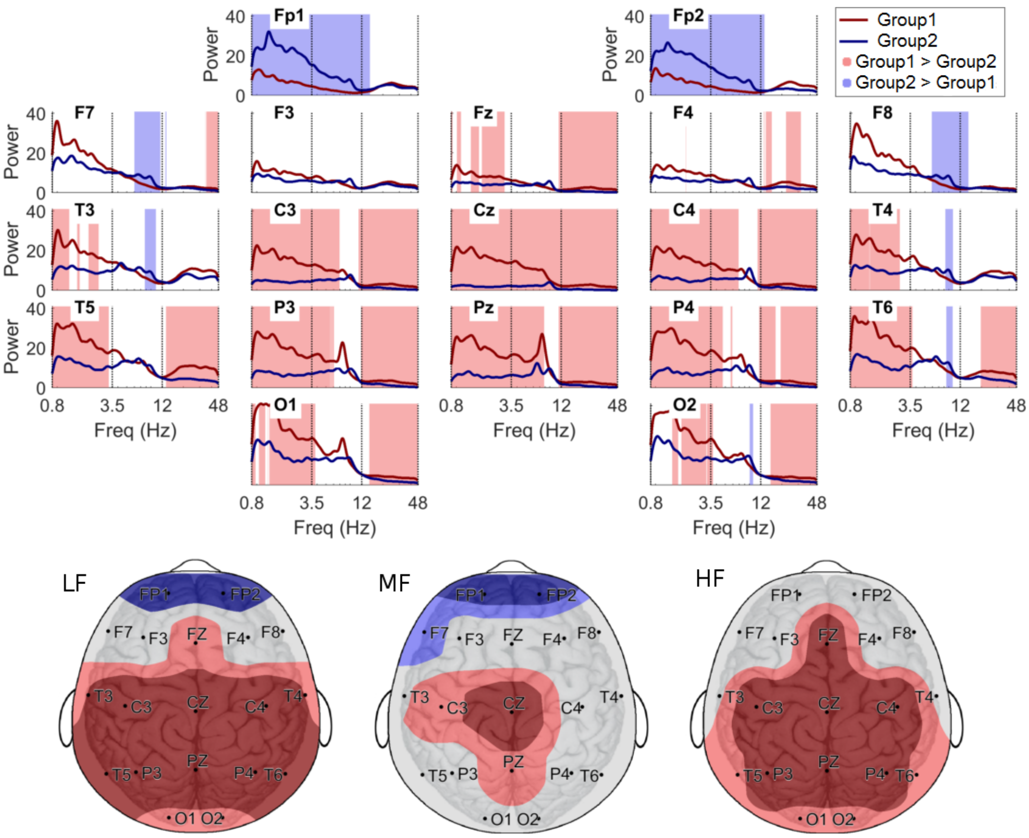

Phase coherence

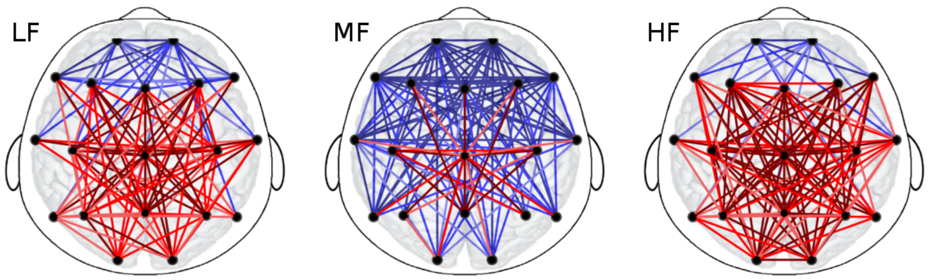

FIGURE 5.5: Significant differences in absolute power and coherence for LF, MF and HF bands for the recordings with different locations of the reference probe: red for group1 and blue for group 2. On heads, brighter colour indicate a p-value <0.05, while darker colour indicate a p-value <0.01. Note the extension of the significant differences, located further from the corresponding reference-placement.

	ASD males	CG males	ASD females	CG females
Group 1	10	2	0	6
Group 2	3	7	2	2

TABLE 5.6: Composition of the subgroups measured with different location of the reference probe

5.5.1 Normalisation strategies

In order to minimize the bias due to different placements of the reference probes from the recordings, power and coherence analysis has been performed on the data by subtracting different reference signals. Two re-referencing strategies has been tested: subtraction of the common average (CA) and of the apex electrode's signal (Cz).

The effect that different referencing choices cause to the analysis has already been briefly introduced in Section 2.1.5. Following the notation introduced therein, the CA re-referencing procedure on the probe A would generate from V_A a new time series V'_A by subtracting the time series V_{CA}. If A was referenced to X, and B to Y, this process should remove the dependence in V_A and V_B on the different positions of X and Y, because

$$\begin{aligned} V'_A &= V_A - V_{CA} = (V_A - V_X) - (1/N \sum V_i \; - V_X) = V_A - V_{CA} \\ V'_B &= V_B - V_{CA} = (V_B - V_Y) - (1/N \sum V_i \; - V_Y) = V_B - V_{CA} \; . \end{aligned} \tag{5.1}$$

Similar mechanism would apply when choosing to reference to Cz. This time a new time series V'_A would be produced by subtracting the time series V_{Cz}. This process should again remove the dependence in V_A and V_B on X and Y, because

$$\begin{aligned} V'_A &= V_A - V_{Cz} = (V_A - V_X) - (V_{Cz} - V_X) = V_A - V_{Cz} \\ V'_B &= V_B - V_{Cz} = (V_B - V_Y) - (V_{Cz} - V_Y) = V_B - V_{Cz} \; . \end{aligned} \tag{5.2}$$

Figure 5.6 shows the same time series from the CG male shown in Figure 5.3, after the re-referencing transformation. It can be noticed how the diffused muscle artefacts were attenuated by both techniques. It can also be noticed how the two linear transformations

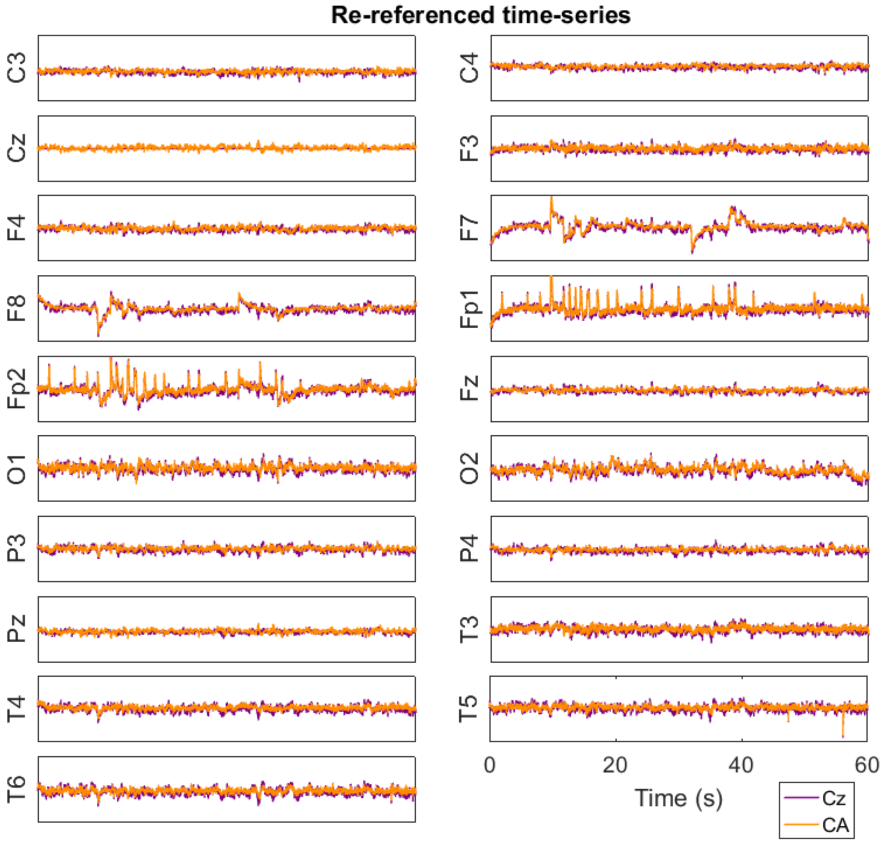

FIGURE 5.6: Selected 1-minute time window of all the probes from the time series of Figure 5.3, after the re-referencing. Note that the overlapped time series are similar in the overall time evolution, but not identical at a local scale.

generate, at the visible level similar results. However, the dynamical interactions will be affected by the choice, as discussed below.

5.5.2 Comparison of re-referencing to common average and to Cz

The performance of the two transformations in reducing the bias on power and coherence are here shown and commented. Neither of the re-referencing completely erases the differences for power and coherence between the groups. The remaining differences could be actually due to the different populations composing them. This is a realistic scenario, because (as shown in Table 5.6) data from 10 ASD males, 2 CG males, 6 CG females were acquired with the more anterior reference (group 1) and data from 3 ASD males, 2

ASD females, 7 CG males, 2 CG females were acquired with the more central reference (group 2).

5.5.2.1 Wavelet absolute power

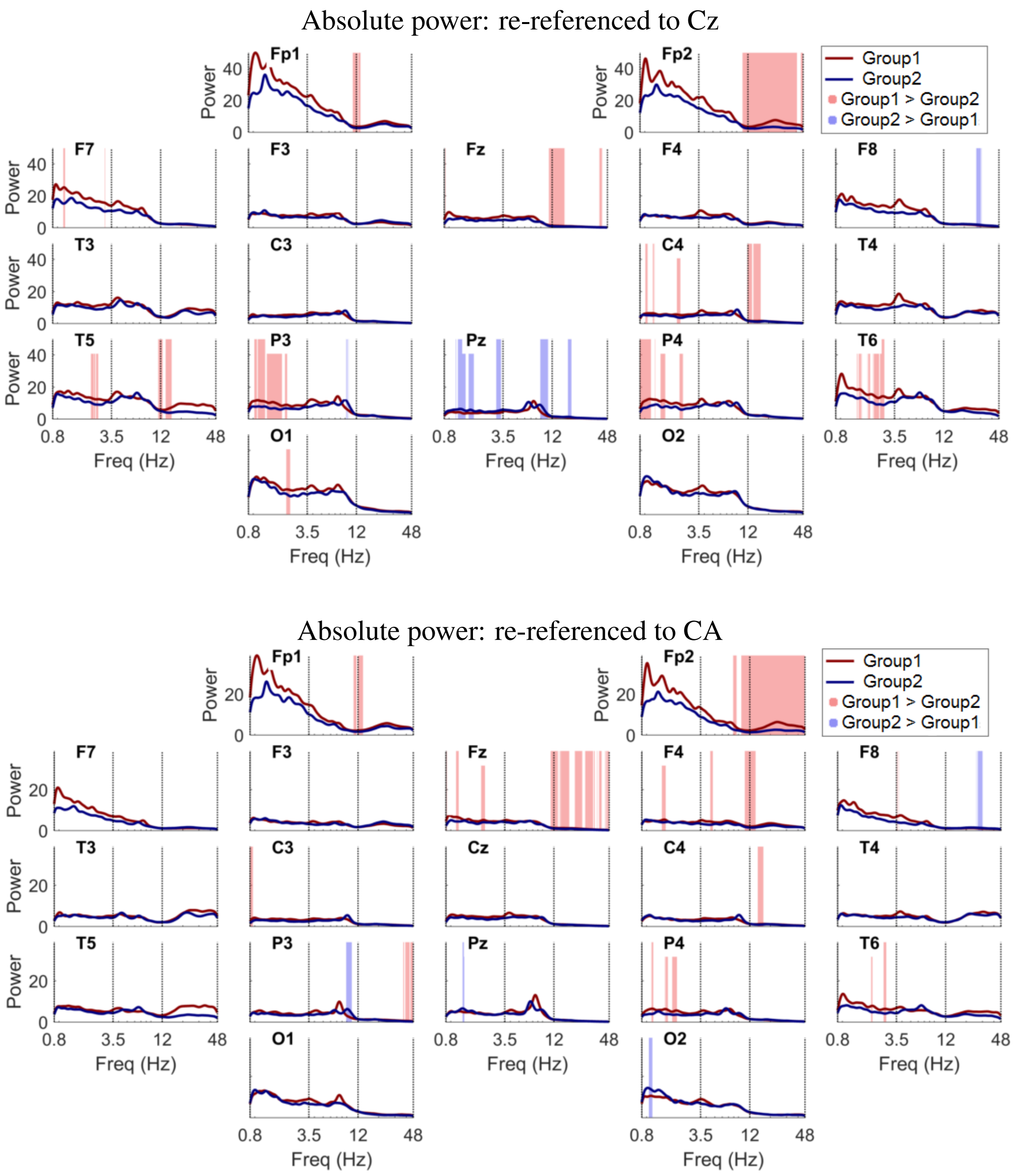

FIGURE 5.7: Performance of the re-referencing to Cz and CA in diminishing the measurement bias for absolute power. Panels show significant differences in absolute power spectra for the recordings grouped by different locations of the reference probe: red for group 1 and blue for group 2.


Residual significance for Cz

Residual significance for Cz and CA

FIGURE 5.8: Performance of the re-referencing to the probe Cz and CA in diminishing the measurement bias for absolute power. Significant differences for LF and HF bands for the recordings grouped by different locations of the reference probe: red for group1 and blue for group 2.

However, by comparing the absolute power panels of Figure 5.7 with Figure 5.5 it is evident that the significant differences between the group 1 and group 2 were heavily reduced after re-referencing the time series both to the CA or to Cz. Moreover, the trend of higher pre-frontal power for group 2 is inverted, suggesting that the features due to the subjects composing the groups overcame the effect of the bias after the re-referencing.

A summary for the residual absolute power differences between group 1 and group 2 is shown on the head-map in Figure 5.8. For both Cz and CA, the differences after re-referencing were found significantly higher on Fz and Fp1 for group 2 and on F8 for group 1.

The main difference between the re-referencing methods found in the absolute power resides at LF frequencies, with a residual significant group-difference in the parietal probes remaining only when re-referencing to Cz.

5.5.2.2 Wavelet phase coherence

For phase coherence, removing the CA from the time series did not seem to erase the reference bias as effectively as for the power spectra (first row of Figure 5.9). However, the number of significantly different pairs got still strongly reduced after the procedure.

Also, by comparing coherence maps in Figure 5.5 and 5.9, it emerges that the pattern of differences changed after the re-referencing to CA, with the appearance of LF fronto-posterior links for group 2 and MF and HF links involving the outer probes for group 1. This fact could again be due to the different composition of the groups, with majority of ASD males in group 1 and CG males in group 2 (Table 5.6).

Among the two strategies, re-referencing to Cz generated the lowest number of links with residual significance, as it can be seen by comparing rows in Figure 5.9. However, most of the links appearing significant after the Cz transformation were also detected after the CA re-referencing.

For LF and MF, higher frontal coherence was detected by both normalisations for group 1, with the main difference that the long-distance fronto-posterior coherences were not significant after Cz was removed.

Rereferenced to common average

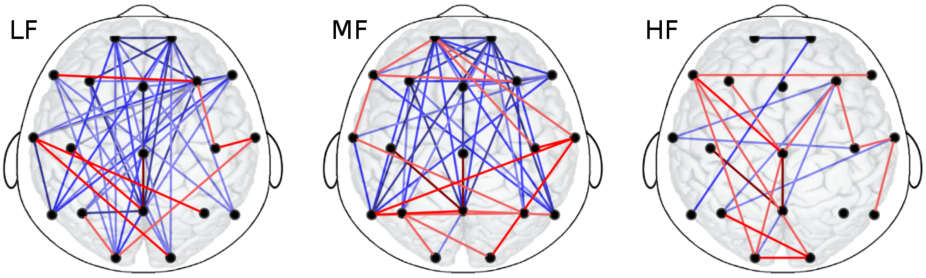

Rereferenced to the probe Cz

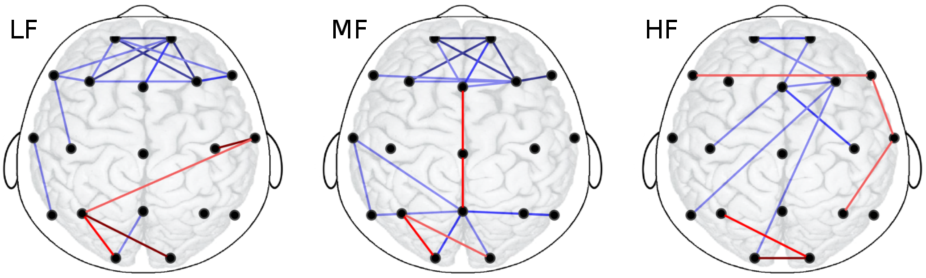

FIGURE 5.9: Performance of the re-referencing to the common average time series (top row) and to the probe Cz (bottom row) in diminishing the measurement bias for phase coherence. Significant differences for LF, MF and HF bands for the recordings grouped by different locations of the reference probe: red for group1 and blue for group 2.

This investigation highlighted how, while the local features of the time series (like power) do not seem to be heavily influenced, some non trivial effects can appear in the connectivity maps for different re-referencing choices.

In order to understand in more detail this phenomenon, the changes in coherences due to different re-referencing will be investigated here for individual subjects. The pair Fp1-Fz (which showed higher coherence for group 2 in the original time series) was chosen for

Original time series

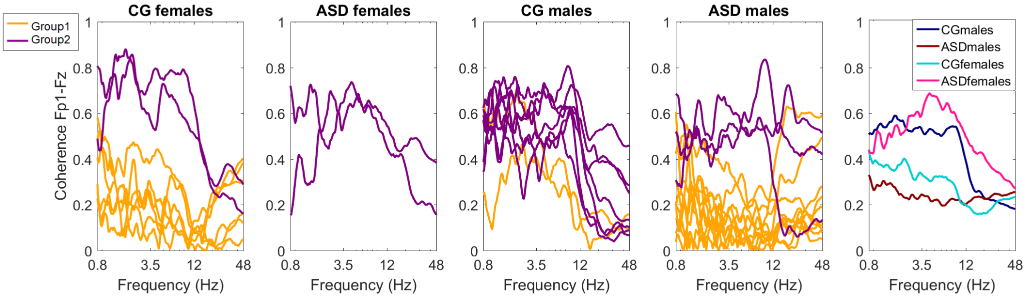

Re-referenced to Cz

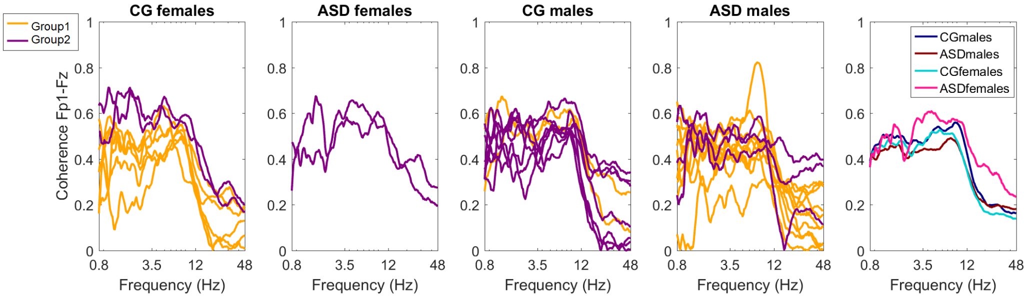

Re-referenced to CA

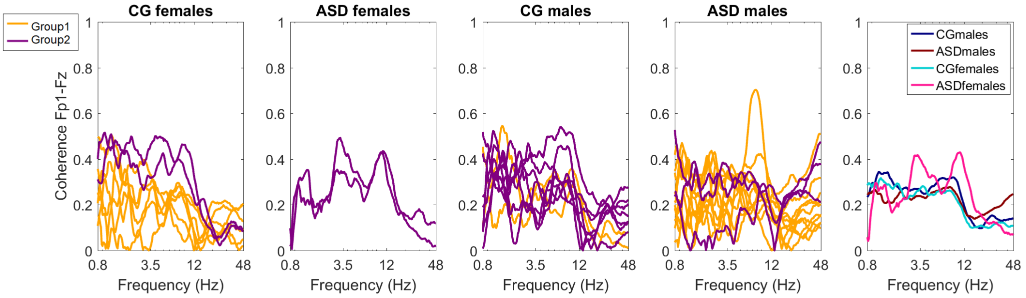

FIGURE 5.10: Effect of re-referencing on phase coherence between Fp1-Fz, for all the subjects, divided by group of belonging. Different reference positions are indicated by yellow and purple lines. Last panels on the right show the groups average. First row shows the original reference, the second row the Cz reference, and the last row the CA reference. Note how the yellow and purple subgroups of coherence are clearly separated in the original data and become less distinguishable after re-referencing.

the comparison.

In Figure 5.10, coherences from group 1 subjects are plotted in yellow and group 2 in purple. First row shows the original reference, the second row the Cz reference, and the last row the CA reference. For each row, different panels show different types of subjects (for gender and presence of autism). The last panels on the right show the group-averages.

It can be noted how the yellow and purple subgroups of coherences are clearly separated in each panel for the original data (first row), and became less distinguishable after re-referencing (second and third row). In particular, re-referencing to Cz (second row) generates generally higher coherences than the CA (third row), especially at lower frequencies.

The group averages on the right panels show how the initial bias due to prevalence of ASD males and CG females in group 1 and CG males and ASD females in group 2 was evened out by both re-referencing strategies, even if in a different fashion.

5.5.2.3 Conclusion about re-referencing

In the investigation performed on the effects of re-referencing, it emerged that the different approaches do not seem to introduce significant biases on the power content of the time series. On the contrary, the computation of phase coherence gives slightly different results according to the re-reference technique chosen.

The Cz normalisation seems to perform better in order to reduce the bias in phase coherence when compared to the CA (Figure 5.9). However, because of the high number of variables included in this situation (among which the different reference and different groups composition), it is hard to define what actually generates this difference.

Also, by using Cz as a reference, connectivity investigations are biased toward a specific location. By removing the CA, on the contrary, the effect of re-referencing is more uniformly distributed across all the probes. It is worth mentioning that, in any case, the distribution of re-referencing effect is still not perfectly uniform for the CA re-referencing, as probes with more consistent voltage contribute more to the average. Despite this, CA re-referencing is a widely applied technique in EEG studies (Table4.3).

In the light of these considerations, CA re-referencing was preferred over Cz, and applied for the comparisons performed on the time series for the ASD investigation.

5.6 Results for spectral power and phase coherence

The methods listed in Section 5.4 are now applied to compare data from ASD and CG males, re-referenced to the common average. In the following figures, blue colour indicates the CG and red the ASD group.

5.6.1 Power

An example of the time-frequency representation of the WT power is shown in Figure 5.11, for the complete multichannel recording of Figure 5.6. Each panel is placed on the corresponding probe-position on the head. For better visualisation the colormap was re-scaled for each panel.

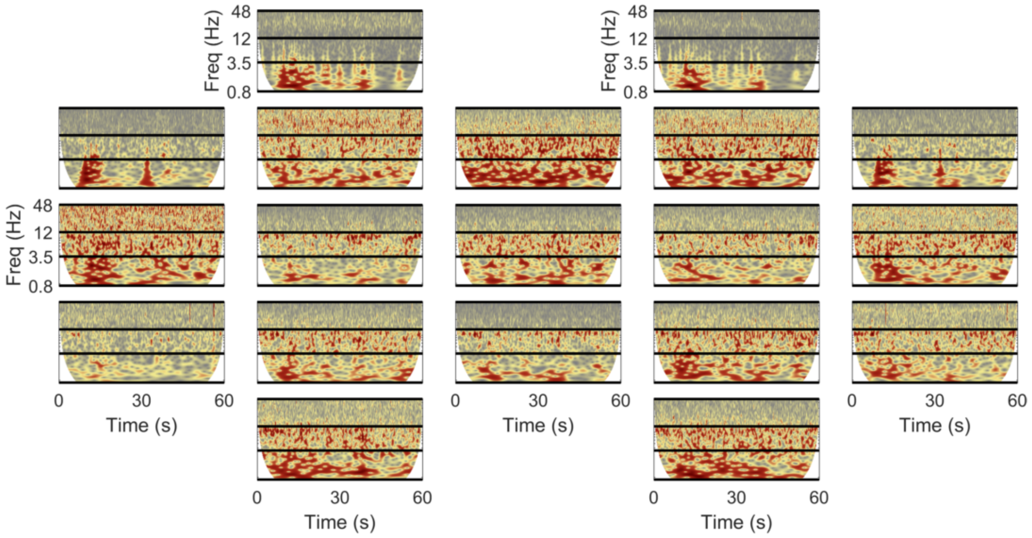

FIGURE 5.11: Example of time-frequency representation of the Wavelet power for the time series shown in Figure5.6. Each panel is placed on the corresponding probe position.

In the example shown in Figure 5.11, artefacts affected the LF content of the WT in the pre-frontal probes. Most likely, they are due to ocular movements like blinking. They occur every few seconds, and propagate also into the MF range. Despite this distorted distribution of the spectral content due to non-neuronal electrical activity, a ridge of HF neuronal activity is still visible for both probes.

The alpha wave (included in the MF range) was for this subject the brain activity that was sustained more constantly in time: the ridge corresponding to alpha activity emerged in most of the probes, especially around the visual cortex (electrodes O1 – O2 and P4 – P3). HF activity on the beta-gamma range was better distinguishable on the frontal electrodes, located over the association areas of the cortex.

The group-medians of the time-averaged WT absolute power are shown in Figure 5.12, with axes sharing the same vertical scale. For both groups, due to the ocular artefacts present across all the subjects, the pre-frontal probes displayed the higher absolute power on LF and MF bands. Also for both groups, the alpha band spectral peak was visible in most probes within the MF band. HF activity was more prevalent on the temporal channels.

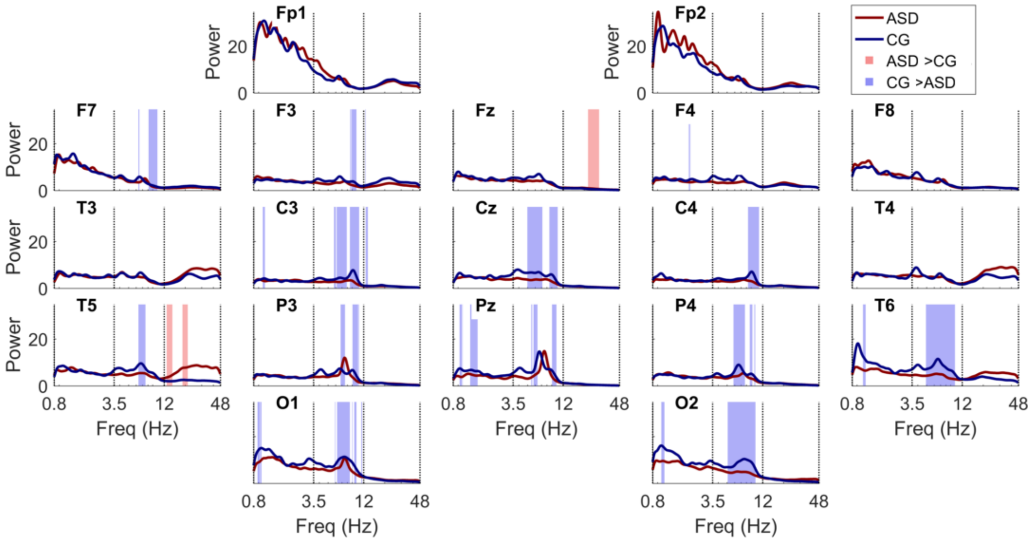

FIGURE 5.12: Absolute power group-median spectra shown over the probes location, compared between ASD (red) and CG (blue) groups. Significant results (p<0.05) are shown, when present, with blue shading indicating CG>ASD and red CG>ASD.

Almost no significance was found in the LF band, with some narrow-band exceptions of higher CG power in the posterior part of the head. Contiguous intervals within the MF band resulted significantly higher for the CG, in theta and alpha ranges for all the probes except for the anterior-temporal and pre-frontal probes. At HF, some narrow band where found higher for the ASD group, on Fz and T5.

The head-maps help depicting the spatial distribution of EEG spectral power. The maps

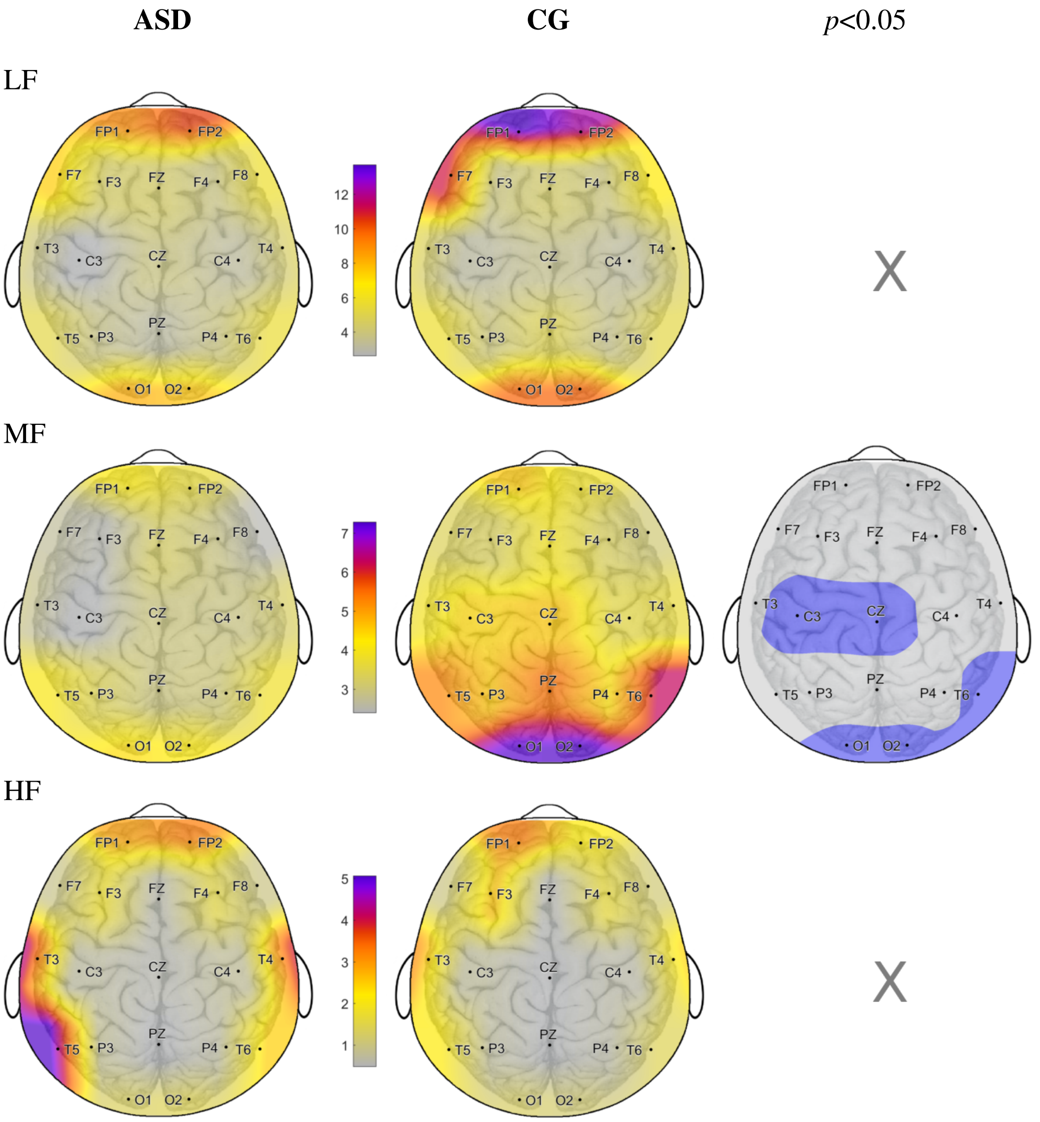

FIGURE 5.13: Results for the group-median absolute power over the probes distribution, compared for the 3 frequency bands, between ASD and CG subjects. Each band shares the same colormap for better comparison. On the right, significant results (p<0.05) are shown when present, with blue indicating CG>ASD and red CG>ASD.

are generated by spatially interpolating the band-average values measured underneath each probe.

Figure 5.13 summarises the absolute power results. In the first row, the LF content due to eye movements on the pre-frontal area was present for both groups. Also the visual cortex underneath the occipital probes generated LF content in the EEG, for both groups. No significance in group comparisons was found for this interval. On the contrary, some significant differences due to the higher alpha spectral peaks in the CG emerged from the MF band, with higher absolute power for multiple probes on the central and occipito-temporal areas. No significance was pictured by the HF comparison, although the ASD group generated an area of asymmetrically high power on the left temporal probes.

Outcomes were similar for the relative power, and are shown in Figure 5.14. The alpha spectral peak became more evident in this representation, and again it was mostly higher for the CG. Intervals within HF had significantly higher relative power for the ASD group on Fz, and on very narrow intervals within the LF band across the scalp.

For the relative power, significant differences emerged in each of the three bands by investigating the band-average content, as shown in Figure 5.13. A higher LF relative power

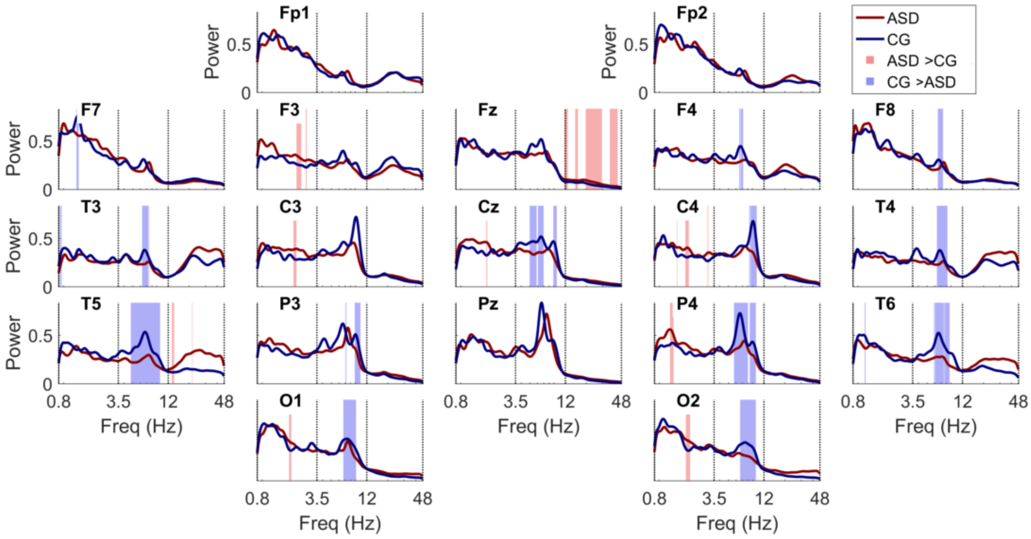

FIGURE 5.14: Relative power spectra shown over the probes location, compared between ASD (red) and CG (blue) groups. Significant results (p<0.05) are shown, when present, with blue shading indicating CG>ASD and red CG>ASD

was found for the ASD group on the central probes. On the contrary, the MF relative power was higher for the CG over the whole central area, extending to the posterior-temporal probes and to the lateral-parietal probes. For the HF band, only the Fz relative power resulted significantly different, i.e. higher in the ASD group. Again, some non-significant left asymmetry was present in this band for the ASD group.

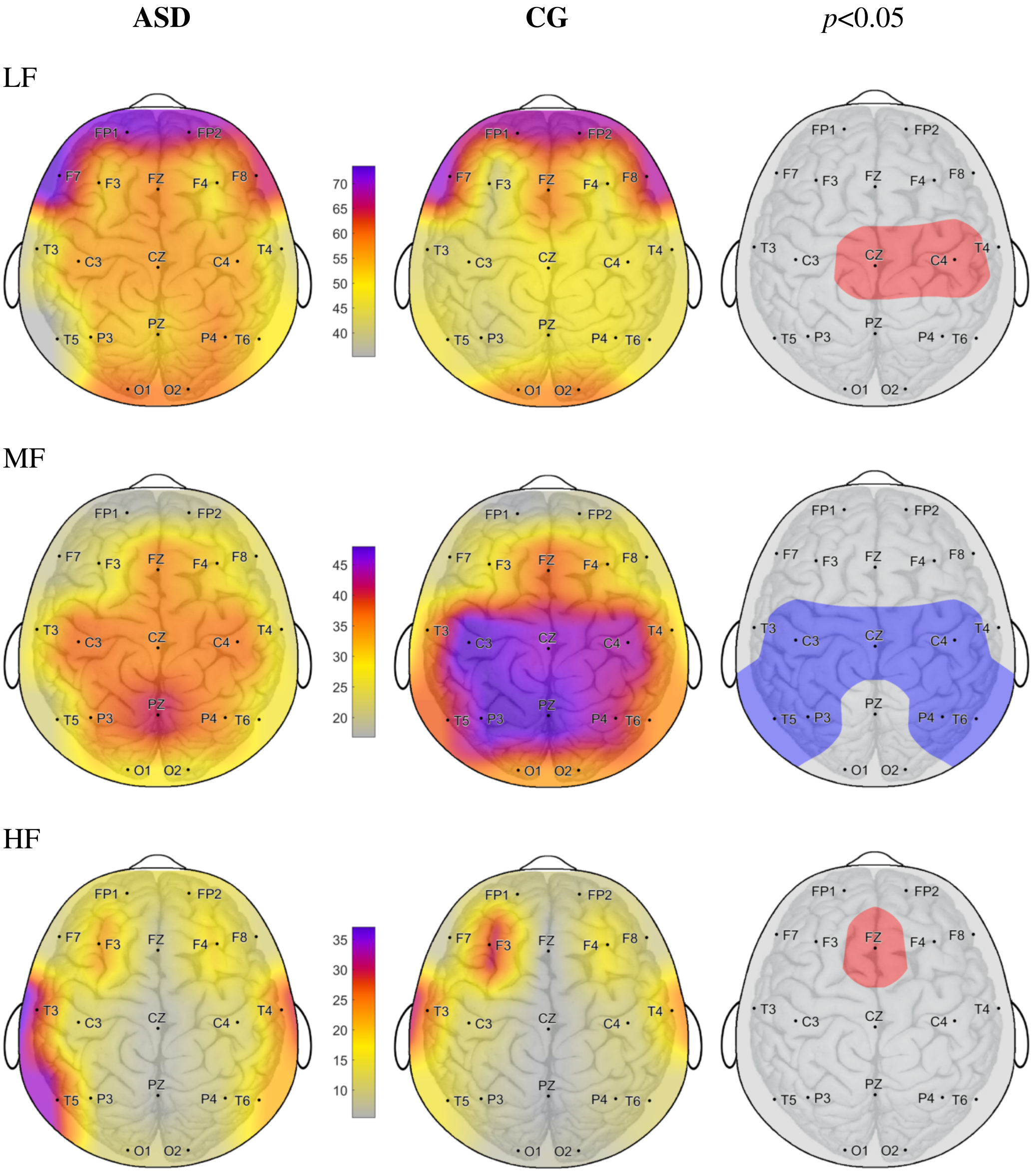

FIGURE 5.15: Results for the group-median relative power for time series re-referenced to the CA over the probes distribution, compared for the 3 frequency bands between ASD and CG subjects. Each band shares the same colormap for better comparison. On the right, significant results ($p<0.05$) are shown when present, with blue indicating CG>ASD and red CG>ASD.

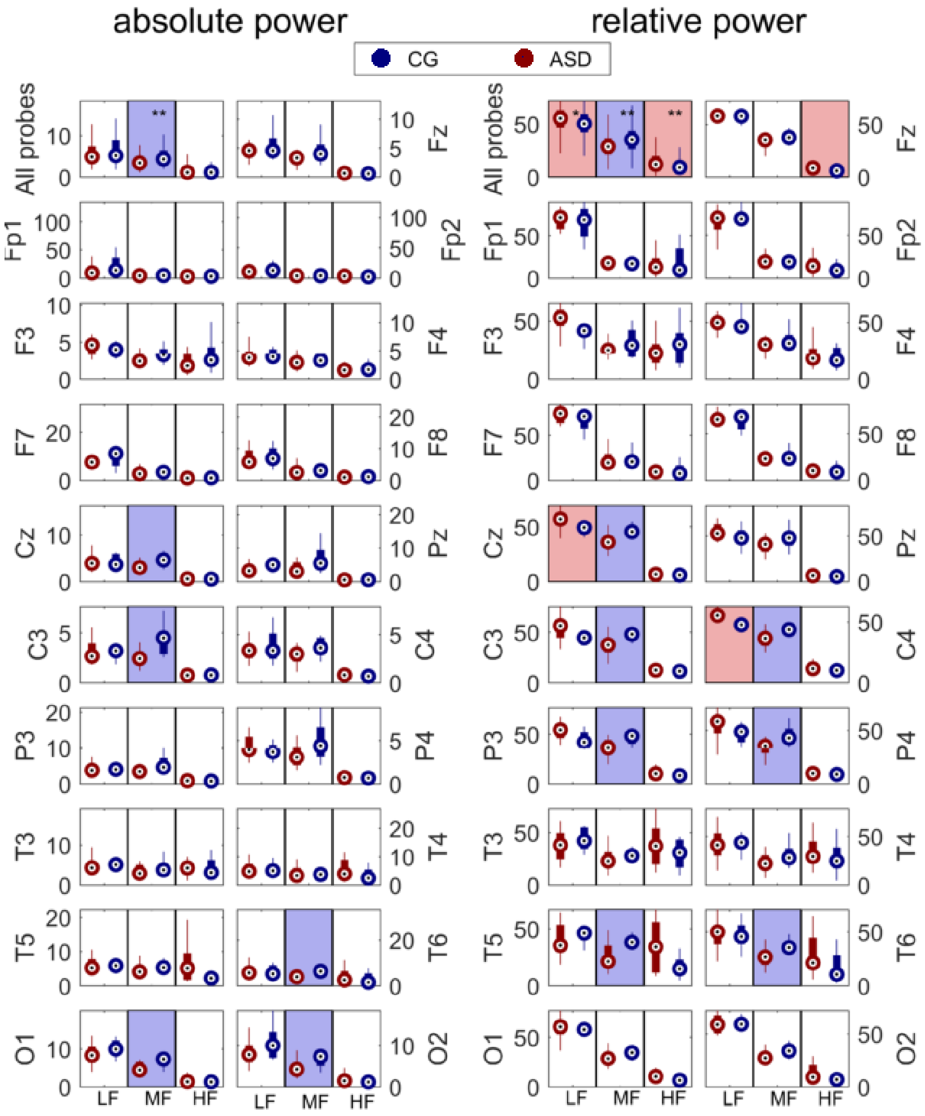

FIGURE 5.16: Box-plots for the absolute and relative power for time series re-referenced to the CA over the probes distribution, compared for the 3 frequency bands between ASD and CG subjects. Significant results (p<0.05) are shown when present, with blue indicating CG>ASD and red CG>ASD.

Box-plots in Figure 5.16 summarise the band-average results of both the absolute and relative power analysis. In the figure, shaded background indicates significantly different group distributions. By comparing absolute and relative power panels, it emerged that the pattern of differences was consistent across the two measures.

The relative power enhanced the differences especially at a global level (first panel), detecting significantly different distributions in all three frequency bands. In particular, LF and HF relative power was higher for the ASD subjects, while the MF was higher for the CG. For the probe-by-probe comparisons, only two occurrences of significance in the absolute power were lost in the relative power (O1 and O2 on the MF band).

From Figures 5.13 and 5.15, it emerged that some asymmetric distribution was present for the ASD group, especially at HF. As this result was also reported in the literature (Table 4.2), it was decided to investigate if any significant differences were present in the spectra of corresponding probes on the left and right side of the head, within the groups. In this case, the statistical test used was the Wilcoxon sign rank test, which allowed paired comparisons. No extended differences emerged from this investigation (Figure 5.17), with only some few-bins-wide power intervals within the LF and MF band which resulted higher in the left side of the head for the ASD group (marked with bright red for the sake of visibility).

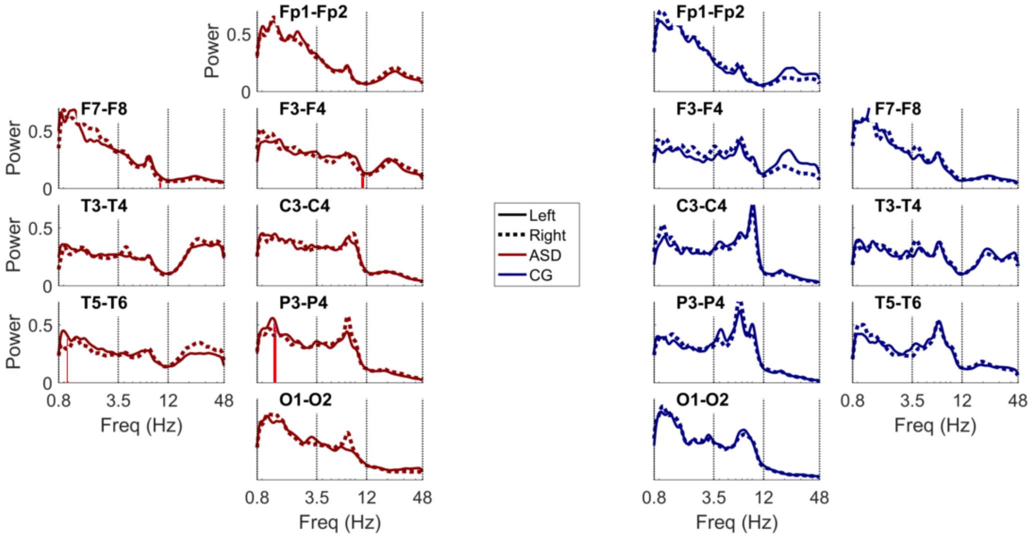

FIGURE 5.17: Comparison of the relative power spectra for longitudinally symmetrical probes for time series re-referenced to the CA, for ASD (red, on the left) and CG (blue, on the right) subjects, shown over the probes' location. No significant differences, i.e. significant asymmetry, emerged ($p<0.05$).

5.6.2 Phase coherence

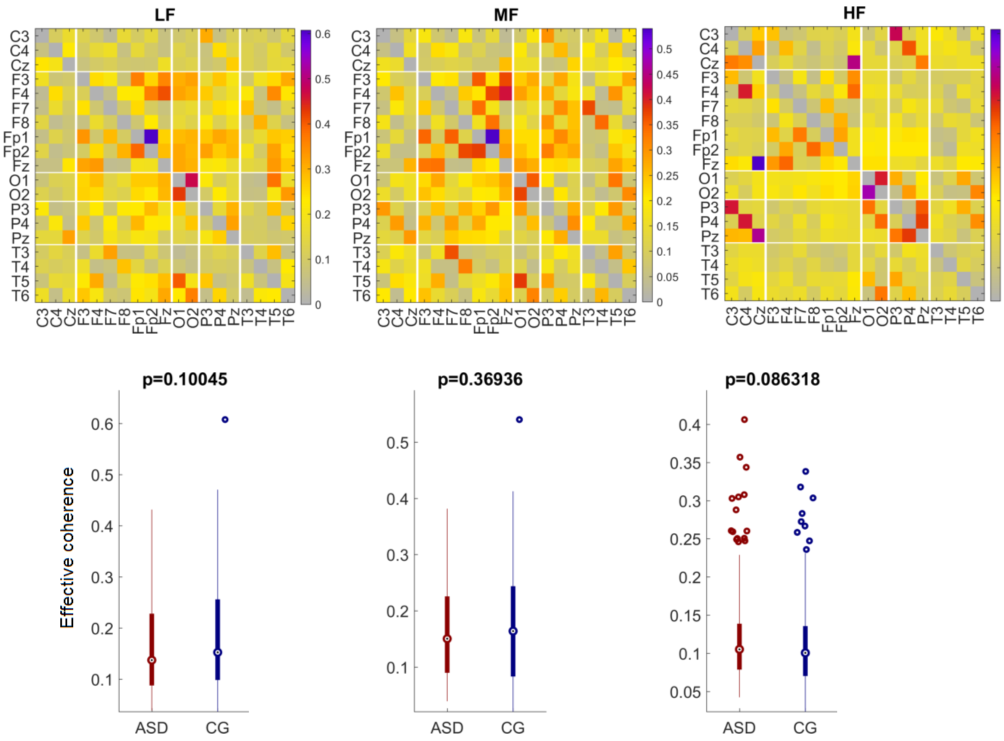

FIGURE 5.18: Values of group-average effective phase coherence for LF, MF and HF bands. The bottom-left left half of the matrices contain values for ASD group, and the top-right for CG. White lines divide brain areas (top). Box-plots for group comparison (bottom). Note how matrices are qualitatively symmetrical, ans no group difference emerges for the overall effective coherence.

By computing the Wavelet phase coherence, it was possible to investigate the spatial pattern of propagation of brain activity, i.e. functional connectivity, in each frequency interval.

Matrices mapping the group-average effective coherence values for each frequency band for all the undirected pairs of probes are shown on the top in Figure 5.18, with the same colormap. As the matrices are symmetrical for each group, ASD values are shown in the bottom-left halves, and CG in the top-right. Brain areas in the matrices are grouped by white lines.

The symmetrical aspect of the matrices suggests that the propagation of brain activity was generally similar between the ASD and CG groups, and some considerations can be drawn regardless of the group of belonging. For instance, by comparing the colour distributions within the matrices for different frequency ranges, it can be observed that in LF and MF the highest coherence was found in short-distance pairs within the occipital and pre-frontal and between occipito-temporal areas. Long-range high coherence was found in both LF and HF bands, for pairs linking frontal with occipital and parietal areas. For the HF band, on the contrary, the highest coherence values were found for short-distance links like Cz-Fz and O1-O2, but also for pairs within the frontal area and within and between posterior and central areas, tracing more centralised connectivity maps.

For the group comparison, plots in Figure 5.19 show the median time-average Wavelet phase coherence only for those pairs of probes generating significantly higher values for ASD (first row) and CG (second row). Each frequency band is considered separately, and shaded with the corresponding group's colour, for clarity. The figure shows also the thresholds for both FT (dark grey) and inter-subject (light grey) surrogates.

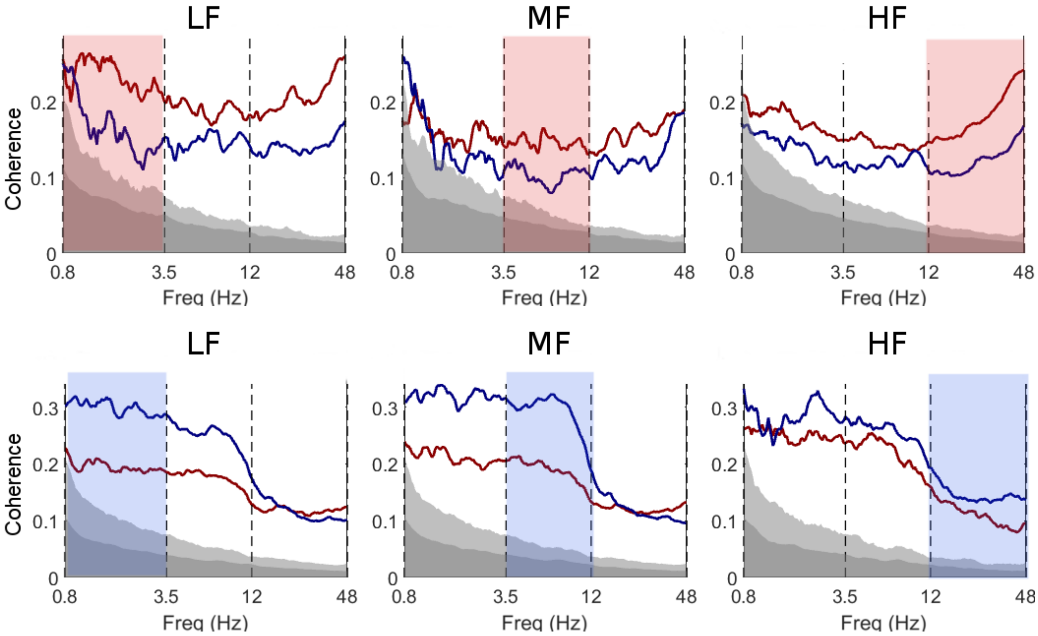

FIGURE 5.19: Group average frequency evolution of the phase coherence for links significantly different in the LF, MF and HF range, plotted over the corresponding intersubject (light grey) and FT (dark grey) surrogate thresholds. Blue and red shades highlight the band of interest. The top row indicates pairs for ASD >CG, and the bottom row CG >ASD.

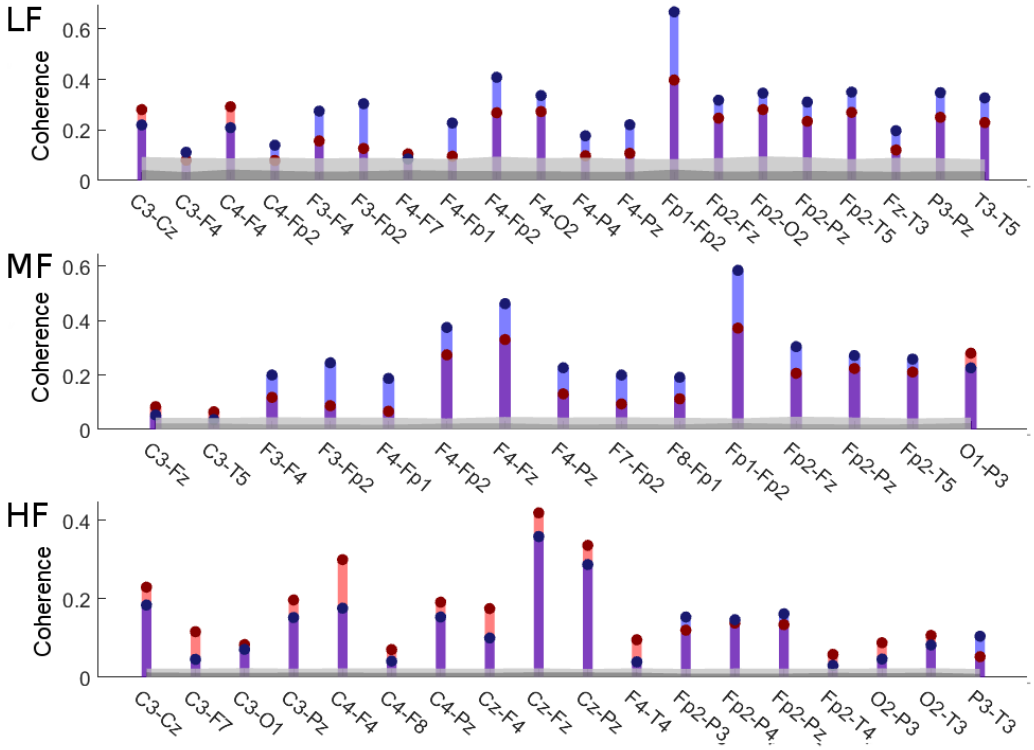

FIGURE 5.20: Actual values of the significantly different coherences for LF, MF and HF bands, plotted over the corresponding inter-subject (light grey) and FT (dark grey) surrogate thresholds.

The band-average values for phase coherence and surrogates for each of the significantly different pairs are shown in Figure 5.20. There, it can be seen that only three pairs generated higher phase coherence in the ASD group for both the LF and MF band. Also, out of these six values, three were very close to the surrogates threshold.

Most of the significantly different values, both in the LF and the MF range, were higher for the CG. In this case, the differences in coherence between the groups were more consistent, and further from the surrogate thresholds. The corresponding plots in Figure 5.19 for the two panels in the bottom row show how the blue curves stay a 0.1-step above the ASD red curves in the LF and HF coherence, for then becoming more overlapping in the HF range.

On the contrary, for the HF band, the majority of the significantly different values of coherence were higher for the ASD group, generating also the biggest differences from the

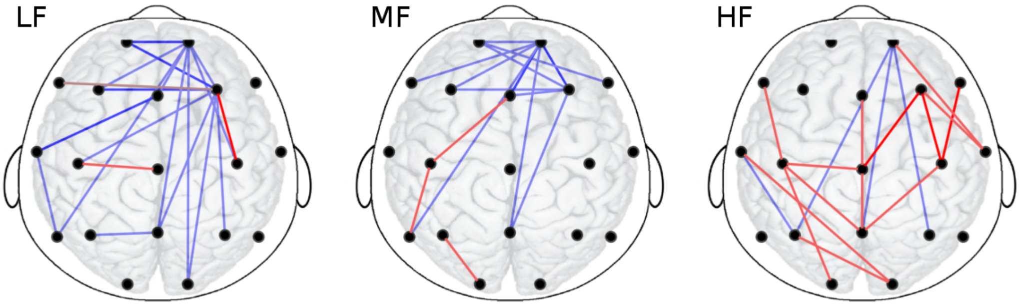

FIGURE 5.21: Pairs with significantly different phase coherence values for time series for LF, MF and HF bands, with blue indicating CG>ASD and red CG>ASD (p<0.05 in lighter and p<0.01 in darker colour)

CG values and from the surrogates (5.20). The corresponding plot on the top-right panel in Figure 5.19 reflects this difference, with the curves starting to go apart in correspondence of the HF range.

In order to evaluate the spatial distribution of the differences, the pairs of probes generating significantly different values of band-average between the groups are connected by lines on the head-maps in Figure 5.21, for each frequency bands. The intensity of the colour in the figure indicates the significance level.

By comparing the different topography of the connectivity maps for the LF range, it can be noticed that the long distance fronto-occipital and fronto-posterior links already discussed for Figure 5.18 generated higher coherence for the CG group.

Also the values of a cluster of short-distance pairs within the frontal and pre-frontal areas were higher for the CG in the LF band. These frontal links remained higher for the CG group in the MF band, but the significance disappear in the HF range. There, the majority of the significantly different coherences were higher for the ASD group and involved shorted links revolving around the central area of the scalp.

Figure 5.22 presents the values of coherence differences (Δ_{WPC}) between the CG and ASD group for the significant links, grouped on the horizontal axes by brain areas involved. Areas are ordered on the axes longitudinally from frontal to occipital. The colour of the dots indicates the frequency band (purple for LF, orange for MF and yellow for HF).

It is clear from this representation how the Δ_{WPC} between the groups in the LF and MF were higher for CG group in the frontal areas and decreasing toward the central one. On the contrary, for the HF band, the Δ_{WPC} were higher for the ASD group on the central area, decreasing toward both frontal and occipital zones.

On the top-right panel of Figure 5.22, similar graph groups the dots according to which brain sides they linked. This representation highlights how the inter-hemispheric coherences (L-R column) was mostly higher for the CG group in the LF and HF range. Also, for the CG, the intra-hemispheric links were preferentially located within the right side (R-M and R-R columns). For the ASD group, on the other hand, higher coherence was found between probes placed mostly within the same hemisphere or involving the middle-line.

On the bottom left panel of Figure 5.22 the dots are grouped by distance (in arbitrary units ranging from 0 to 10). Again, a trend could be be identified, with higher Δ_{WPC}

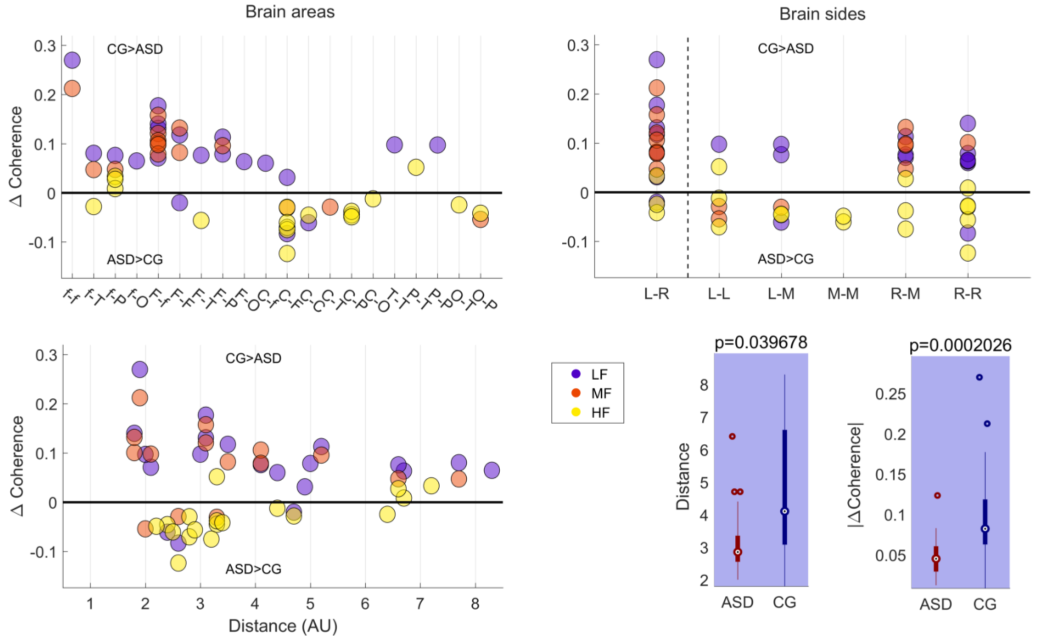

FIGURE 5.22: Values of the difference between ASD and CG median coherence, for significantly different pairs. Each dot corresponds to a line in Figure 5.21. Different colours indicate different frequency bands. Values are grouped by distance, brain sides and brain areas linked.

	Lower freq. limit (Hz)	Higher freq. limit (Hz)	Order of Butterworth filter
LF	0.8	3.4	4
MF	3.6	11.5	5
HF	12.5	48	10

TABLE 5.7: Filtering parameters for the EEG data
Note that the higher and lower frequency boundaries of consecutive bands are not exactly matching in order to minimize overlapping of the filtered content.

for short-range connections decreasing with the distance for both groups. For the CG, LF, MF and HF the dots were spread on the whole axes, while for the ASD group the significantly higher coherences were almost uniquely found between short-medium range connections. Few links with higher coherences for ASD were found also in the MF-HF ranges. However, those links generated very small Δ_{WPC}.

The bottom-right panel of Figure 5.22 shows the box-plot distributions of both the distance between the probes generating significantly different links, and of $|\Delta_{WPC}|$ for the significantly different pairs. A prevalence of longer distance links within the pairs having significantly different coherence emerged for CG (p<0.05). Also the absolute values of Δ_{WPC} were higher for the CG (p<0.0005).

5.7 Cross-frequency coupling comparison

The dynamical Bayesian inference (discussed in Section 3.3) was applied to in order to reconstruct and compare the phase coupling functions from the ASD and CG.

5.7.1 Summary of the methods

A brief summary of methods applied to reconstruct and assess the coupling functions is provided below.

- The time series were filtered as discussed in Section 3.4.1, with the parameters for each band indicated in Table 5.7.

- The Hilbert transform was applied to the filtered time series to obtain the corresponding collective neuronal phases. The protophase-to-phase transformation was also applied to the series, as discussed in Section 3.4.2. An example of filtered bands and extracted phase is shown (with the corresponding FT power spectra) in Figure 5.23.

- The dynamical Bayesian inference (Section3.3.3) was run to reconstruct the coupling for triplet of LF, MF and HF phases. For each directed combination of probes $A \to B$, the LF and MF phases from A were coupled with the HF phase from B. This design allowed to reconstruct how the low-to-high coupling acted and propagated over the brain network. Local coupling was also reconstructed by computing the inference with LF, MF and HF phases from the same probe.

- The coupling strength for each partial component of the LF, MF→HF coupling was calculated from the matrices of coupling coefficients, as explained in Section 3.3.4.1.

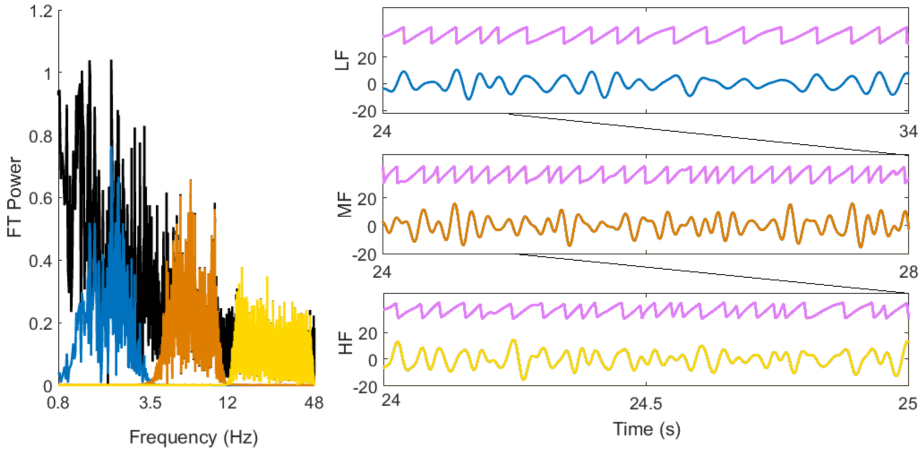

FIGURE 5.23: On the left, example of the Fourier spectra of the time series from the probe T6 from the time series of Figure 5.3 (black line) and of the corresponding filtered components (blue for LF, orange for MF, yellow for HF). On the right, time-windows of the filtered time series (in the same colour-scheme) and the corresponding extracted phases (in pink). Different lengths of the window shown: 10 s for LF, 4 s for MF, 1 s for HF.

  - Phase shuffling surrogates were computed for each inference (25 repetitions), and the maximum value of the strength generated by each individual, probes-specific surrogates distribution was used as a threshold to validate the corresponding real outcome for each investigated coupling component.
  - The results validated from the surrogates were analysed according to the following criteria: .
    - By considering, for each probes combination, which percentage of subjects from the ASD and CG groups had a value of the coupling strength higher than the corresponding surrogate threshold.
    - By considering the median effective value of the coupling strength (i.e. above the surrogates) for the ASD and CG.
- The form of the coupling functions for the LF, MF→HF coupling was reconstructed from the matrices of coupling coefficients, as explained in Section 3.3.2. Forms were investigated both for local and for spatially-propagated networks. Surrogate distributions were used to validate the results.
- Quantitative comparisons between the forms were performed by calculating both the polar similarity index, discussed in Section 3.3.4.2 and the similarity with average functions, in particular:
  - Intra-subject variability was assessed by computing the similarity between single forms and the subject-average.
  - Inter-subject variability was assessed by computing the similarity between single forms and the group-average.
- For group-comparisons of the distributions, the Wilcoxon sign-rank test is applied as explained in Section 3.5.1.

5.7.2 Coupling strength

The net and partial contributions to the coupling strength are here discussed.

5.7.2.1 Net coupling

The coupling coefficients inferred by the dynamical Bayesian technique were grouped in order to assess to total (net) strength of the LF, MF→HF coupling. In other words, all the coefficients corresponding to base functions of the type

$$\begin{aligned} &\sin(K_1\phi_{LF}(t) \pm K_2\phi_{MF}(t) \pm K_3\phi_{HF}(t)) \qquad \text{and} \\ &\cos(K_1\phi_{LF}(t) \pm K_2\phi_{MF}(t) \pm K_3\phi_{HF}(t)), \end{aligned} \tag{5.3}$$

with K_1, K_2, K_3 assuming values among 0, 1 and 2, are included in the Euclidian norm of Equation 3.33.

The head-maps in Figure 5.24 show the different prevalence of significant coupling in ASD and CG. Arrows link the probes for which the phase coupling between LF, MF (start) and HF (end) bands was higher than surrogates. Circles indicate locally significant coupling. Colour intensity codes for the actual percentage of subjects showing significance. For clarity, only values above the 15% thresholds are shown on these head-maps.

The box-plot on the top right panel in Figure 5.24 shows the distribution of values above the threshold. Low values of the median for the boxes indicates inter-subject variability for the phase coupling (many links with low percentage of subjects each). On the contrary, outliers on the top of the boxes appear when a high percentage of subjects had the strength of a specific link above the surrogates. On the second row, matrices show the complete distribution of these values (with no threshold).

Panels in both rows indicates how ASD and CG resulted to have different patterns of phase coupling modulating the HF activity. In particular, ASD subjects showed a prevalence of significant coupling starting from the mid-line (probe Pz), while for the CG the significant interactions were mostly happening on the outer areas of the head-map (temporal, occipital and side frontal probes).

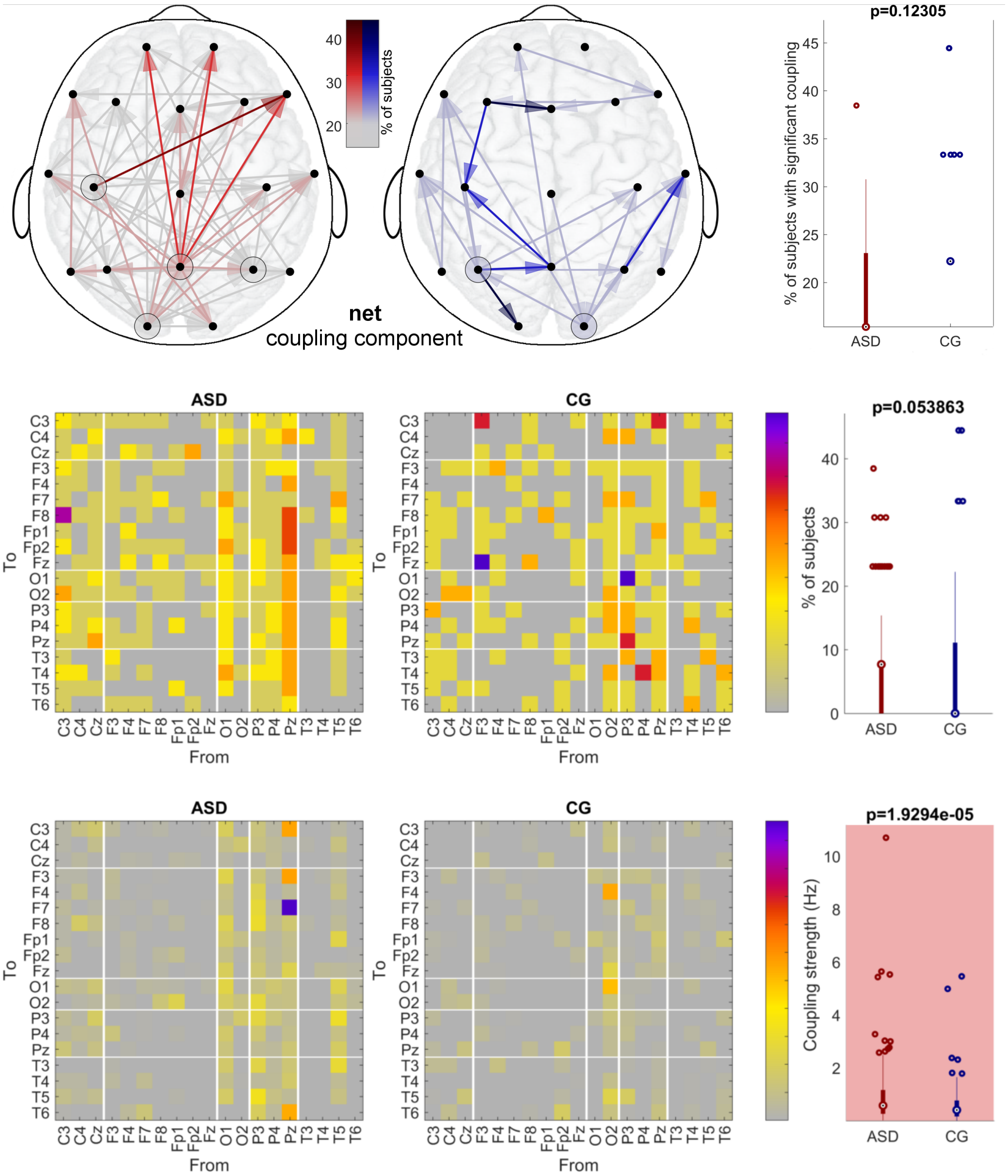

FIGURE 5.24: On the top, head-maps for the phase coupling for CG (blue) and ASD (red) groups for the net coupling are shown: arrows link the probes for which the phase coupling between LF and/or MF (start) and HF (end) bands was higher than surrogates. Circles indicate locally significant coupling. Colour intensity codes for the actual percentage. For clarity, values above the 15% threshold are shown. The box-plot on the top-right summarises the content of the head-maps. Matrix-maps and corresponding box-plot on the second row show the complete distribution for the percentage values. On the third row, values of effective coupling strength are shown for each pair (significantly higher for the ASD group).

In this case, two links (F3→Fz and P3→O1) were significant for almost 45% of the CG subjects, while only C3→F8 was significant for more than 35% of the subjects in the ASD group. Also the more consistent number of links having a low-value of percentage in the diagrams indicate that the ASD group had higher inter-subject variability in the net coupling. In general, the complete distribution of percentages was not significantly different between the groups (p>0.05 in the box-plot on the middle-right), indicating that albeit being more variable, the overall amount of significantly coupled links was not lower for the ASD group.

On the bottom of Figure 5.24, matrix-maps show the actual values of effective coupling strength (above the individual surrogates) for each pair. In this case, the comparison resulted significant, with the ASD group summing up in a higher value than the CG (p<0.001). The columns corresponding to the posterior and occipital areas were the most populated for the ASD group in the matrices of both rows indicating common sources of coupling generating from those areas.

5.7.2.2 Direct LF→HF coupling

By isolating the coefficients related to the base functions involved in partial contribution to the coupling like

$$\begin{aligned} &\sin(K\phi_{LF}(t)) \qquad \text{and} \\ &\cos(K\phi_{LF}(t)), \end{aligned} \tag{5.4}$$

with K assuming values among 1 and 2, it was possible to assess the specific contributions to the overall coupling due to the direct modulation of LF to HF (simulated in Figure 3.11).

Head-maps in Figure 5.25 show a high prevalence of this type of coupling for both groups. The threshold for visualisation was here put to 30%. No evident pattern emerged from

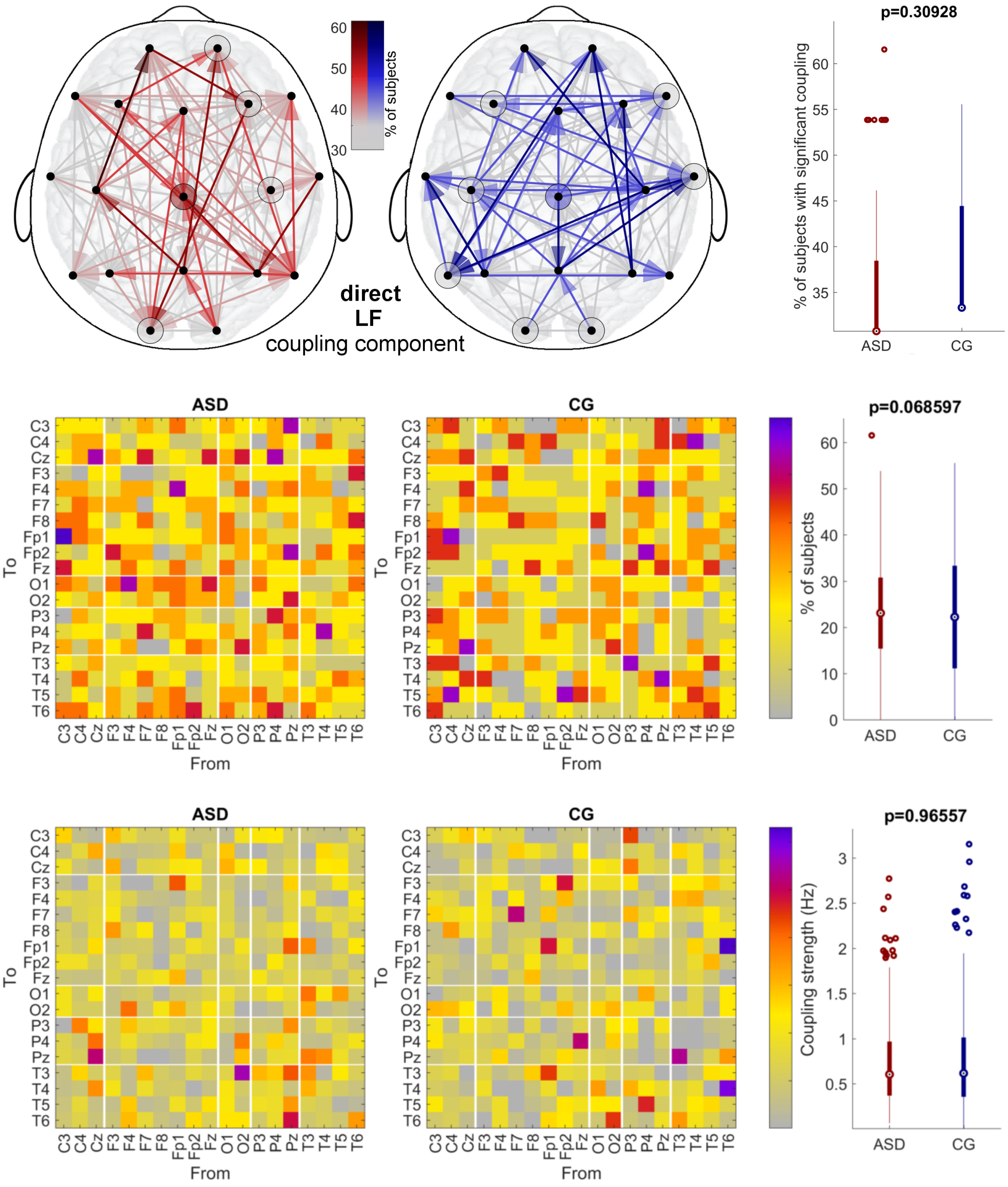

FIGURE 5.25: On the top, head-maps for the phase coupling for CG (blue) and ASD (red) groups for the LF→HF coupling are shown: arrows link the probes for which the phase coupling between LF (start) and HF (end) bands was higher than surrogates. Circles indicate locally significant coupling. Colour intensity codes for the actual percentage. For clarity, values above the 30% threshold are shown. The box-plot on the top-right summarises the content of the head-maps. Matrix-maps and corresponding box-plot on the second row show the complete distribution for the percentage values. On the third row, values of effective coupling strength are shown for each pair.

the maps, except for a cluster of high values directed from central to temporal and to pre-frontal areas in the CG (visible in both the head-maps and in the corresponding matrix-map on the second row).

The actual values of the effective strength in the bottom row also did not indicate any evident trend. Interestingly, the columns corresponding to the coupling from the central area in CG did not include any high value of effective strength, which were high in the matrix of significant percentages. This means that the significant couplings mentioned above did not correspond to particularly high values of effective strength. Box-plots in Figure 5.25 confirmed that no overall difference was found between the groups in both cases.

5.7.2.3 Direct MF→HF coupling

The coefficients modulating base functions like

$$\begin{aligned} &\sin(K_1\phi_{MF}(t)) \qquad \text{and} \\ &\cos(K\phi_{MF}(t)), \end{aligned} \tag{5.5}$$

with K assuming values among 1 and 2, describe the direct coupling acting from the MF to the HF.

The head-maps and matrices in Figure 5.26 indicate a substantial inter-subject variability, especially for ASD. A significantly lower distribution of percentage of subjects above the 15% threshold was found for the ASD group (p<0.01, in the box-plot). On the contrary, some general patterns valid across the subjects can be recognised for the CG. For examples, the matrix on the second row highlights how a high percentage of subjects had significant coupling starting from the temporal areas, in particular from the probe T4. Also, more than 30% of the subjects had significant T3→Fp1 and T3→Fp2 partial coupling.

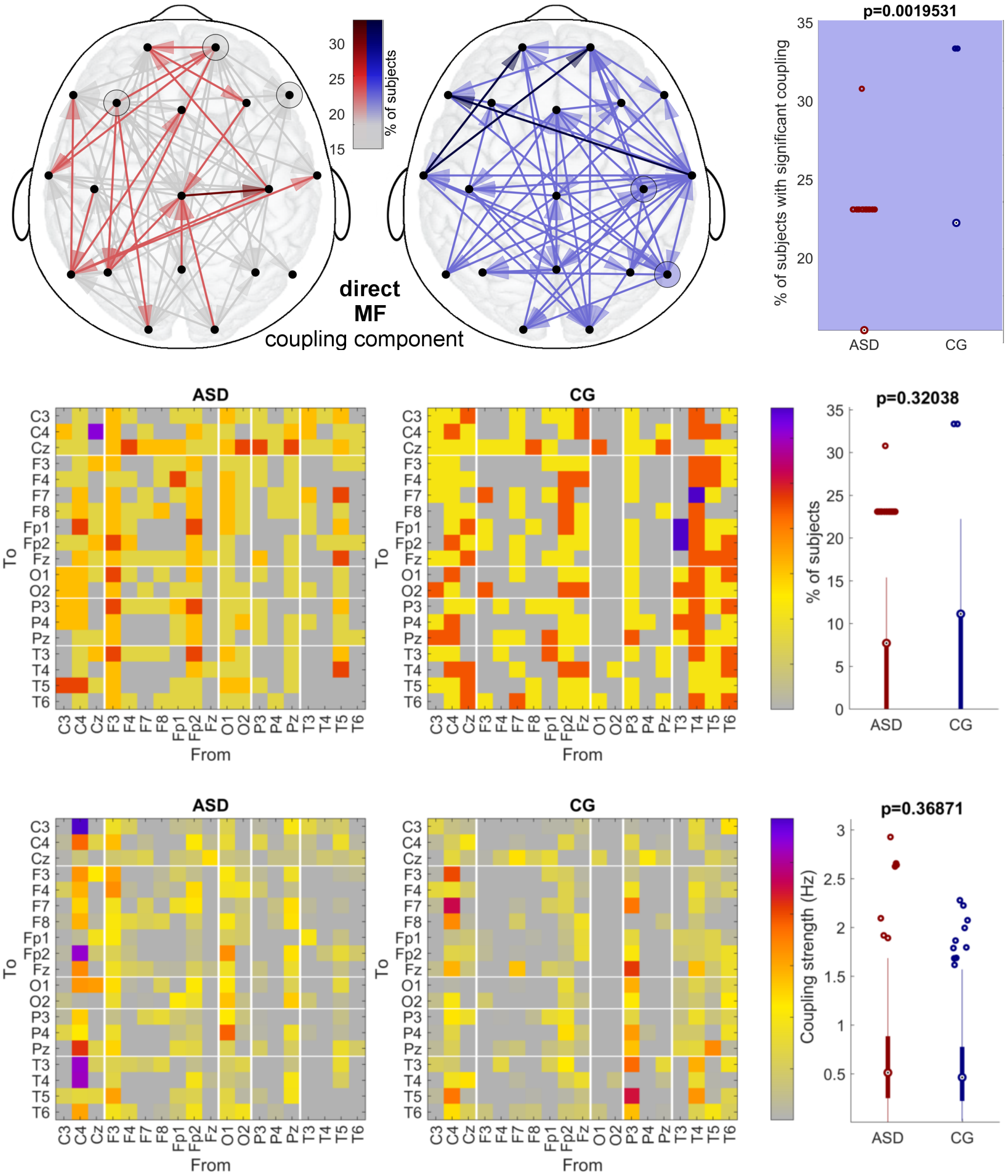

FIGURE 5.26: On the top, head-maps for the phase coupling for CG (blue) and ASD (red) groups for the MF→HF coupling are shown: arrows link the probes for which the phase coupling between MF (start) and HF (end) bands was higher than surrogates. Circles indicate locally significant coupling. Colour intensity codes for the actual percentage. For clarity, values above the 15% threshold are shown. The box-plot on the top-right summarises the content of the head-maps (significantly higher for the CG). Matrix-maps and corresponding box-plot on the second row show the complete distribution for the percentage values. On the third row, values of effective coupling strength are shown for each pair.

No overall difference between the percentages was found between the groups (box-plot on the middle row), indicating that the higher variability in the ASD group compensated for the lower percentages found.

With regards to the effective strength, the matrices on the bottom row of Figure 5.26 clearly indicate a prevalence of coupling exerted from the probe C4 for ASD subjects and from P3 and C4 for the CG. Also, the columns corresponding to the coupling from the occipital probes were virtually empty for the CG and more densely populated for the ASD group, both for the percentage of subjects and for the effective strength.

5.7.2.4 Direct LM, MF→HF coupling

A very high inter-subject variability was also found in the coupling component due to the combined effect of LF and MF activity, i.e. relative to base functions like

$$\begin{aligned} &\sin(K_1\phi_{LF}(t) \pm K_2\phi_{MF}(t)) \qquad \text{and} \\ &\cos(K_1\phi_{LF}(t) \pm K_2\phi_{MF}(t)), \end{aligned} \tag{5.6}$$

with K_1, K_2 assuming values among 1 and 2.

Head-maps of Figure 5.27 show a very diffused pattern of coupling for both groups. However, the CG had few links which were significant for almost 60% of the subjects. Among them, the highest were from T4 and T5 to P4. Such popular connections were not present in the ASD group, which presented once again a more pronounced inter-subjects variability.

For the effective strength, two high values were found for the ASD group or the links Fp1→O2 and Fp2→O1.

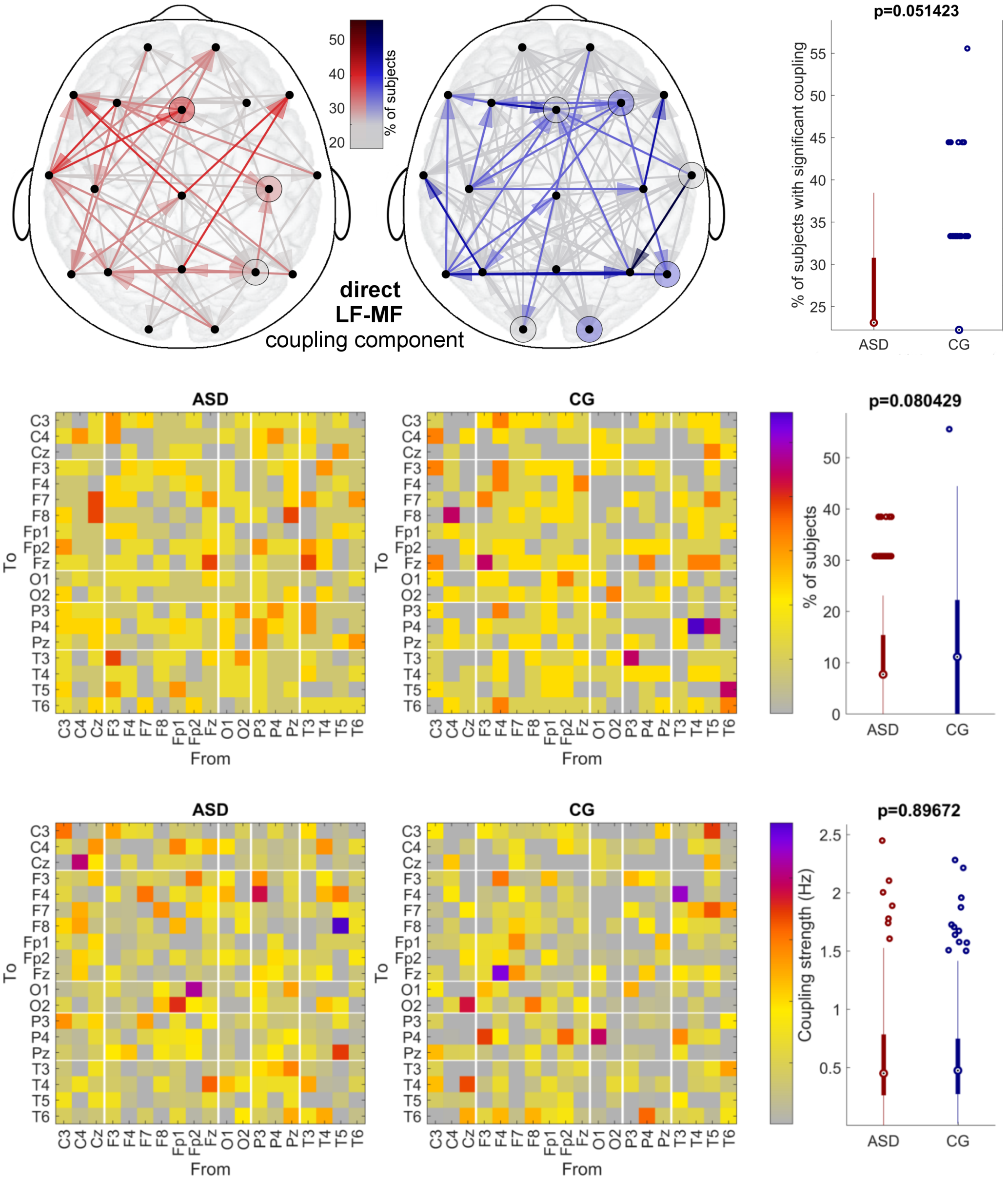

FIGURE 5.27:

On the top, head-maps for the phase coupling for CG (blue) and ASD (red) groups for the LF, MF→HF coupling are shown: arrows link the probes for which the phase coupling between LF, MF (start) and HF (end) bands was higher than surrogates. Circles indicate locally significant coupling. Colour intensity codes for the actual percentage. For clarity, values above the 15% threshold are shown. The box-plot on the top-right summarises the content of the head-maps. Matrix-maps and corresponding box-plot on the second row show the complete distribution for the percentage values. On the third row, values of effective coupling strength are shown for each pair.

5.7.3 Form of the coupling functions

The coupling coefficients inferred by the dynamical Bayesian technique, corresponding to coupling functions like

$$\begin{aligned} &\sin(K_1\phi_{LF}(t) \pm K_2\phi_{MF}(t)) \qquad \text{and} \\ &\cos(K_1\phi_{LF}(t) \pm K_2\phi_{MF}(t)), \end{aligned} \tag{5.7}$$

with K_1, K_2 assuming values among 0, 1 and 2, were used to reconstruct the form of the coupling function LF, MF→HF for each pair of probes, for each subject.

To do so, as explained in Section 3.3.1, the coefficients were multiplied by their corresponding base functions, on the bi-variate $\phi_{LF} - \phi_{MF}$ space. The form of the resultant three-dimensional function integrates the information carried by the coefficients, and give an insight into the mechanism underlying the coupling beyond its strength.

To allow quantitative comparisons between the forms, the polar similarity index is computed for the four main direction of coupling showed in Figure 3.13.

5.7.3.1 Form of the local coupling functions

For each subject, 19·19 coupling functions are computed. Investigating the local coupling reduces the number to 19 for each subject, allowing to visualise their forms on the corresponding probe location. To do so, the coupling mechanisms within each probe is evaluated by considering only the interactions LF, MF→HF, with the phases $\phi_{LF}, \phi_{MF}, \phi_{HF}$ extracted from the same probe.

Figure 5.28 shows in red and blue colormap the forms of the local coupling functions for ASD and CG, on the corresponding probe position. Group-average forms from the surrogates time series are also shown – in grey– for both groups. The forms from the figure express complex interactions between the phases, with no visually distinguishable predominance of any of the 'deterministic' forms shown in Figure 3.13.

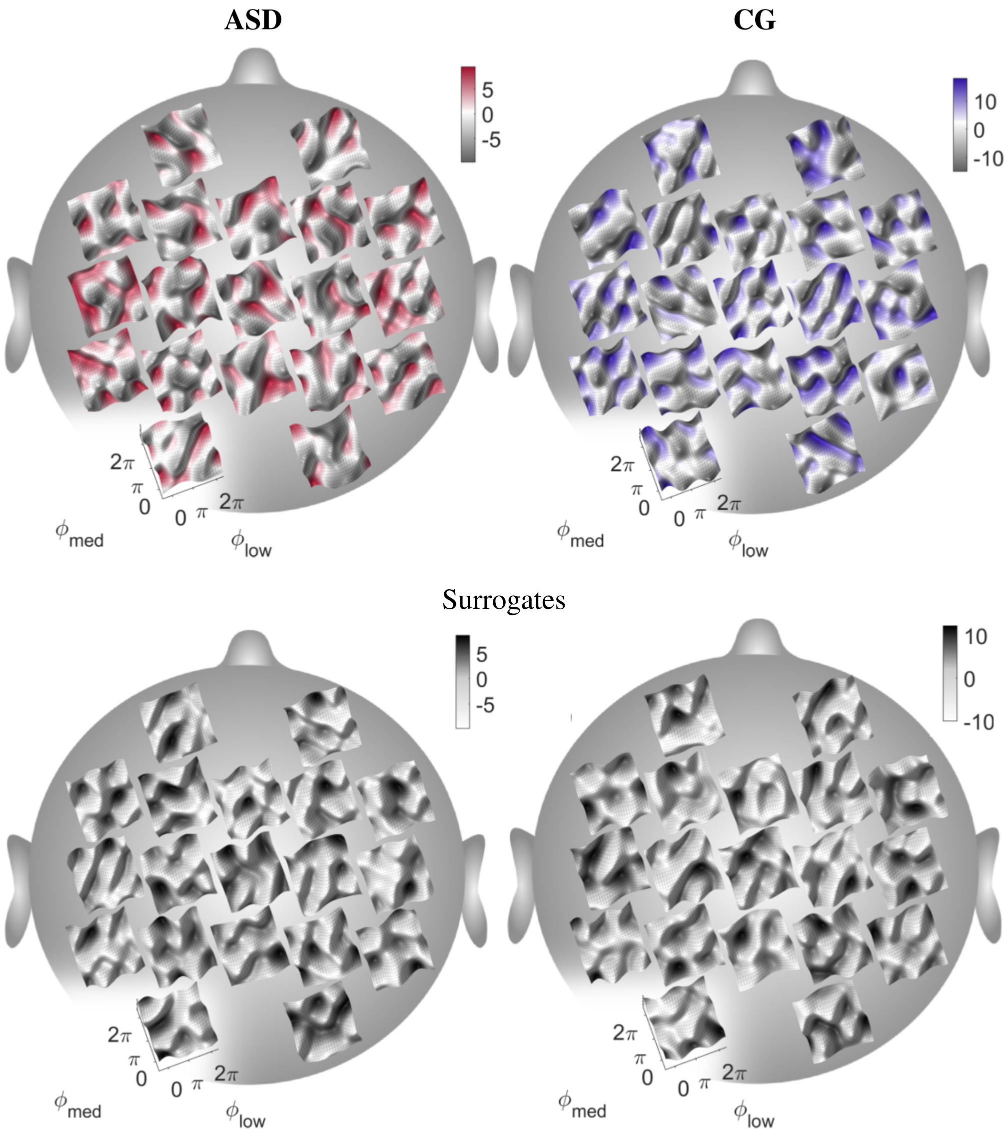

FIGURE 5.28: Forms of the group-average coupling functions, on the corresponding probe position. Red colormap indicates ASD group, blue CG, and gray colormap indicate the group-average forms from the surrogates time series for each group.

The computation of the polar similarity index helps in summarising the morphological information of such functions, by computing the similarity between them and the four numerical forms shown at the bottom of Figure 5.29. The numerical forms develop in the directions parallel to the ϕ_{LF} axes (p_1, in blue), parallel to the ϕ_{MF} axes (p_2, in red), and along the two diagonals (d_1 in pink and d_2 in black).

In terms of the meaning of the numerical forms, it is important to remember that the direction p_1 is associated with the direct coupling $LF \rightarrow HF$, the direction p_2 is with

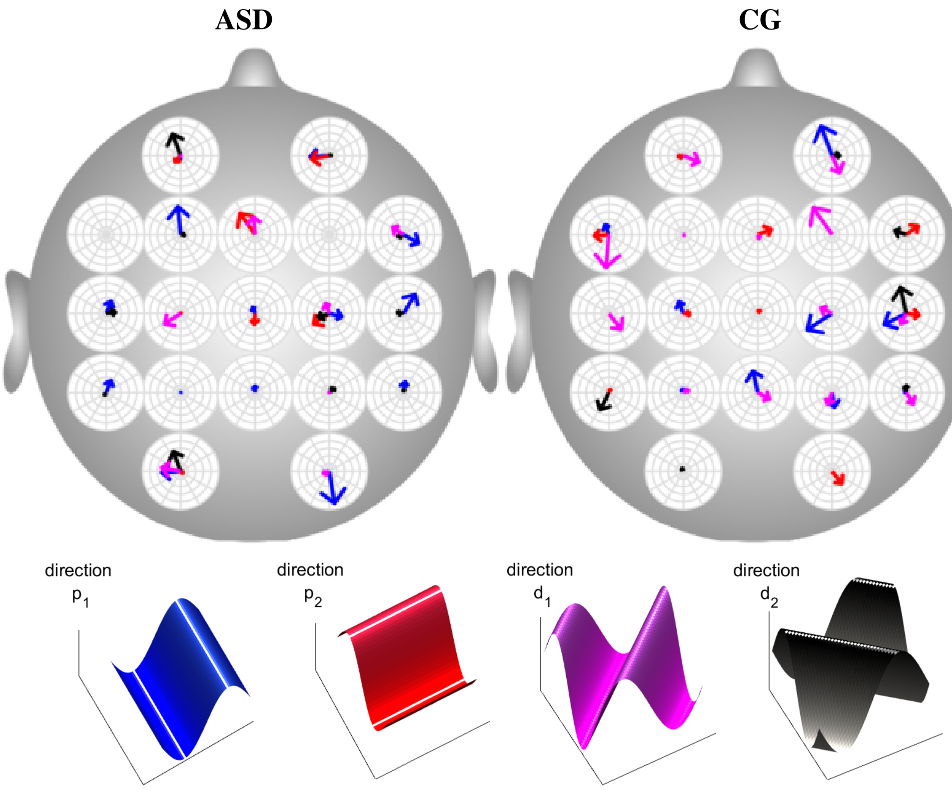

FIGURE 5.29: Polar similarity indices of the group-average coupling functions, on the corresponding probe position. The colour of the arrow indicated the direction of coupling tested with the numerical forms, shown below. Values above the corresponding surrogate polar similarity are shown. For better visualisation the scale of the polar-plots is [0 0.5].

the direct coupling $MF \rightarrow HF$, and the directions d_1 and d_2 with the $LF, MF \rightarrow HF$ couplings.

Values of the similarity index corresponding to each of the directions are plotted in the polar planes on the head-maps at the top of Figure 5.29, for both ASD and CG group. The module of the surrogate similarity was subtracted from the real result, in order to show only the effective similarity.

The plot highlights how in both groups the module of the similarity for the direction p_1 (blue arrows) survived the surrogates test for most of the probes, while, on the contrary, p_2 (red arrows) was less present. Effective similarity for direction d_1 and d_2 emerged more frequently for the CG.

5.7.4 Form of the spatially distributed coupling functions

Similarly to what has been done for the coupling strength, results from each direction of similarity were investigated both in terms of how many subjects provided a value higher than surrogates, and of the actual values.

Direction p_1

Results for the direction p_1 are shown in Figure 5.30. The head-maps on the top indicate that, for most pairs of probes, the form of the similarity to p_1 was higher than the surrogates in more than 70% of the subjects, with a case of 100% for the CG. In particular, it emerged that the HF activity in the occipital area received very frequently a modulation from more anterior LF waves. Pz→ O2 was one of the most popular links for the ASD group. For the CG the most common links were C4→O1 and Pz→O2.

No significant difference between the groups emerged both from the links shown on the heads, and for the complete distribution shown in the second-row matrices. Also the median values of effective similarity to p_1 were not significantly different between the groups.

It is worth noting that, for the CG, high values of effective similarity were found in the posterior part of the head, within and between the temporal, parietal and occipital areas.

Direction p_2

Outcomes of the similarity with the numerical p_2 are reported in Figure 5.31. In this case, less subjects showed a value higher than the surrogates, with a maximum around 90% and more scarcely populated head-maps. A preferential posterior-to-anterior direction of coupling emerged for the CG, with F3 and T3 receiving several incoming arrows in more than 80% of the subjects. Also the prefrontal area received very frequently a modulation from long distance probes in the CG. In the case of the ASD group, the posterior-to-anterior preferential direction was less obvious and counterbalanced for example by Cz being modulated by anterior sources.

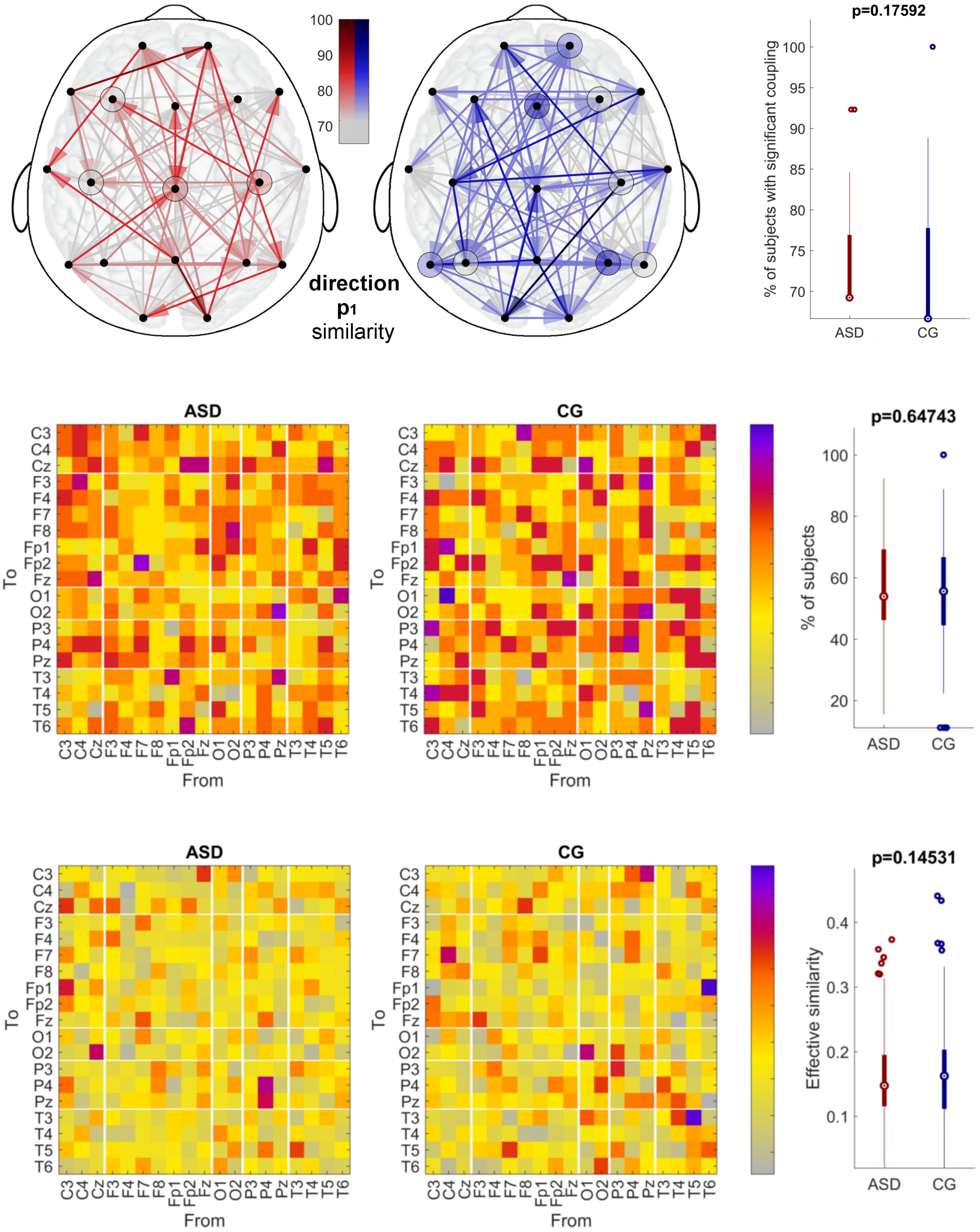

FIGURE 5.30: Head-maps for the polar similarity of the CG (blue) and ASD (red) coupling functions with the form p_1, describing the LF→HF coupling. Arrows link the probes for which the similarity was higher than surrogates and circles indicate locally significant coupling. Colour intensity codes for the actual percentage. For clarity, only value above the 65% threshold are shown. The box-plot on the top-right summarises the content of the head-maps. Matrix-maps and box-plot on the second row show the complete distribution for the percentage values. Matrix-maps and box-plot in the third row show the distribution of the effective similarity for each pair.

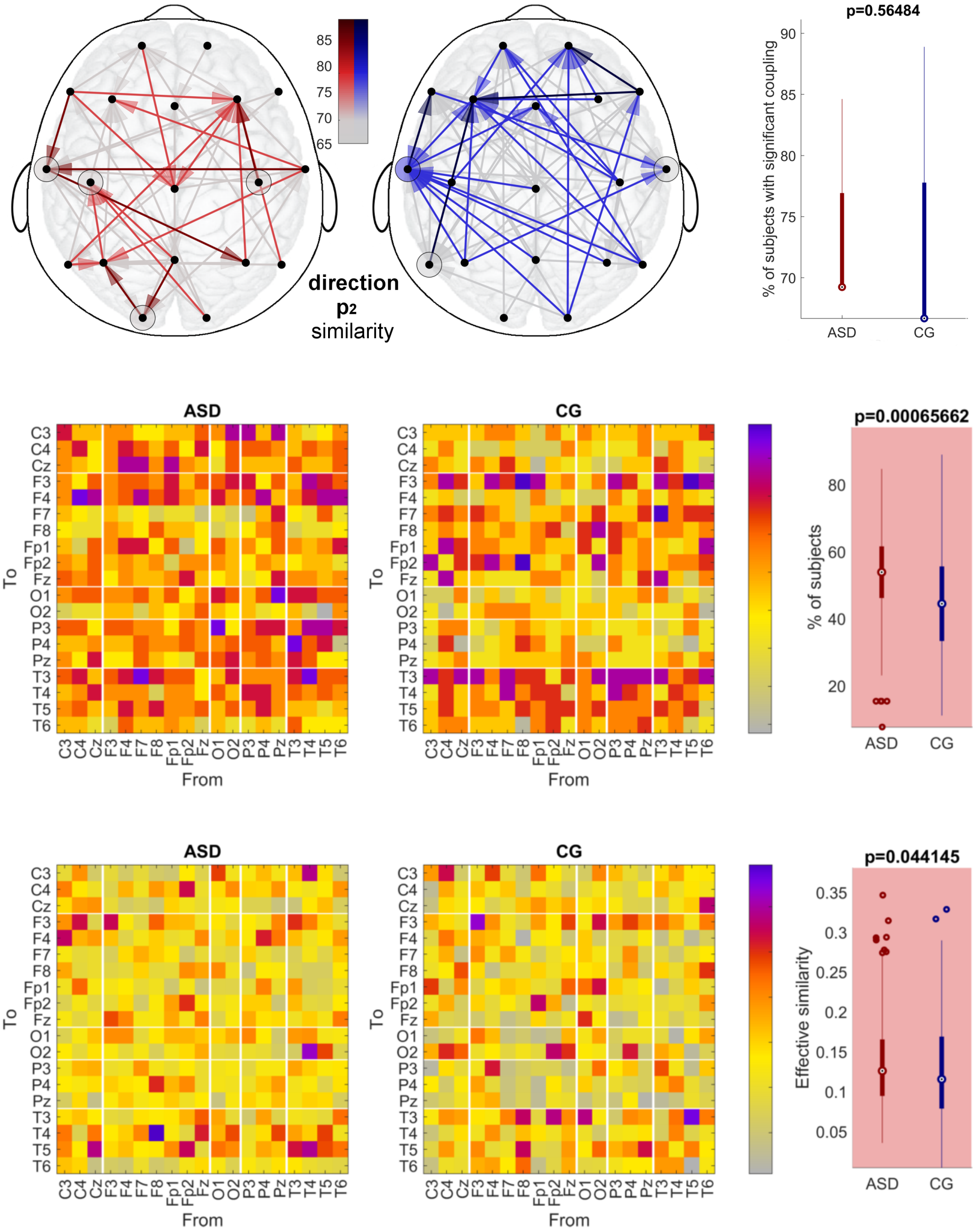

FIGURE 5.31: Head-maps for the polar similarity of the CG (blue) and ASD (red) coupling functions with the form p_2, describing the MF→HF coupling. Arrows link the probes for which the similarity was higher than surrogates and circles indicate locally significant coupling. Colour intensity codes for the actual percentage. For clarity, only value above the 65% threshold are shown. The box-plot on the top-right summarises the content of the head-maps. Matrix-maps and box-plot on the second row show the complete distribution for the percentage values (significantly higher for the ASD group). Matrix-maps and box-plot in the third row show the distribution of the effective similarity for each pair (significantly higher for the ASD group).

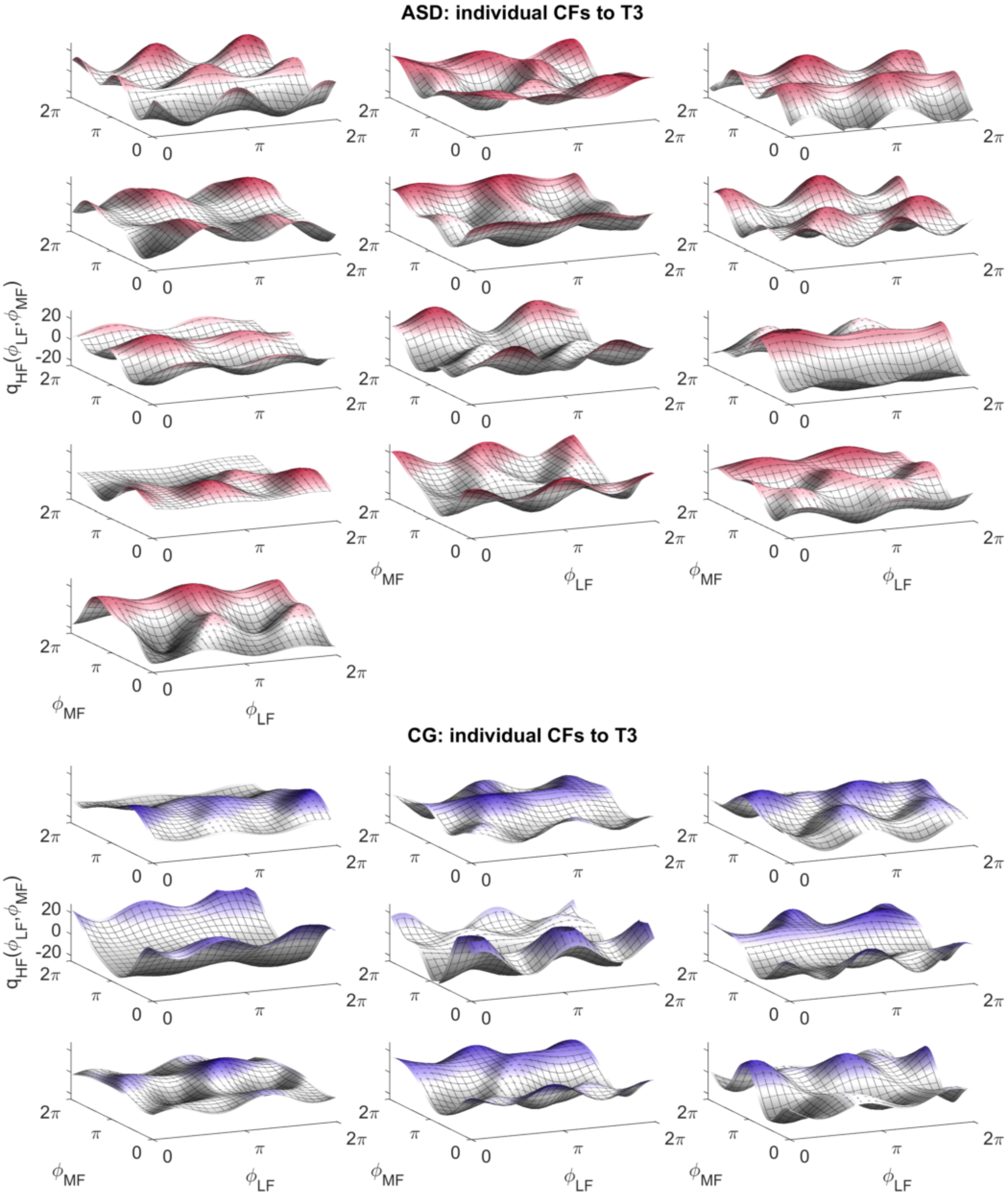

FIGURE 5.32: Individual average-coupling-functions directed to the probe T3 for the CG. The probe T3 was chosen for generating high values of effective similarity with p_2 for a consistent percentage of subjects. Note how the sinusoidal form develops consistently along ϕ_{MF} with smaller perturbations along ϕ_{LF}, especially for the CG.

Matrix-maps and box-plot in the middle row of Figure 5.31 indicate how the overall percentage of subjects with a effective value of p_2-similarity was higher for the ASD group (p<0.001). ASD subjects showed a more spread distribution of significant links for around 50% of the subjects, especially for the ones directed to the central, occipital and parietal areas.

Also the values of effective similarity to p_2 were slightly higher for the ASD group, as shown in the last row of panels in Figure 5.31. In particular, high values were found for connections toward T4 and T5 in the ASD group, and T3 and F3 for the CG. The latter outcome overlaps with results discussed for the percentage of subjects shown in the panel above.

This particular case was investigated more deeply, as an example, by visualising for each subject the average forms of the coupling functions acting on the probe T3, shown in Figure 5.32.

In most of the functions, the dominant feature emerging from the form was indeed the p_2 component, with the sinusoidal shape along ϕ_{MF} propagating relatively unchanged along the ϕ_{LF} axes. This was true especially for the CG. In the case of the ASD group, this propagation was more often interrupted by some contributions from ϕ_{LF}.

Direction d_1

Figure 5.33 shows the results from the investigation about the similarity to the diagonal form d_1. For the ASD, Pz and P4 often received modulation from the pre-frontal probes. In the CG, C4 and Cz seemed to modulate the HF content of both temporal and frontal probes. The only significant difference found between the groups was in the effective similarity, with clusters of high values for couplings within the frontal area and from the central and frontal to the temporal area in the CG.

Direction d_2

Results for the second diagonal direction of similarity d_2 are represented in Figure 5.34. No significant difference was found for this comparison between ASD and CG. The head-maps and matrices of percentage showed how, for both groups, frontal and temporal probes frequently received incoming modulation from diffused areas. For the CG, the modulation was coming especially from occipital and parietal probes.

Results for the effective similarity showed that, for the CG, high values were found in links directed to the probe C4 and on short distances on local links in temporal and frontal areas.

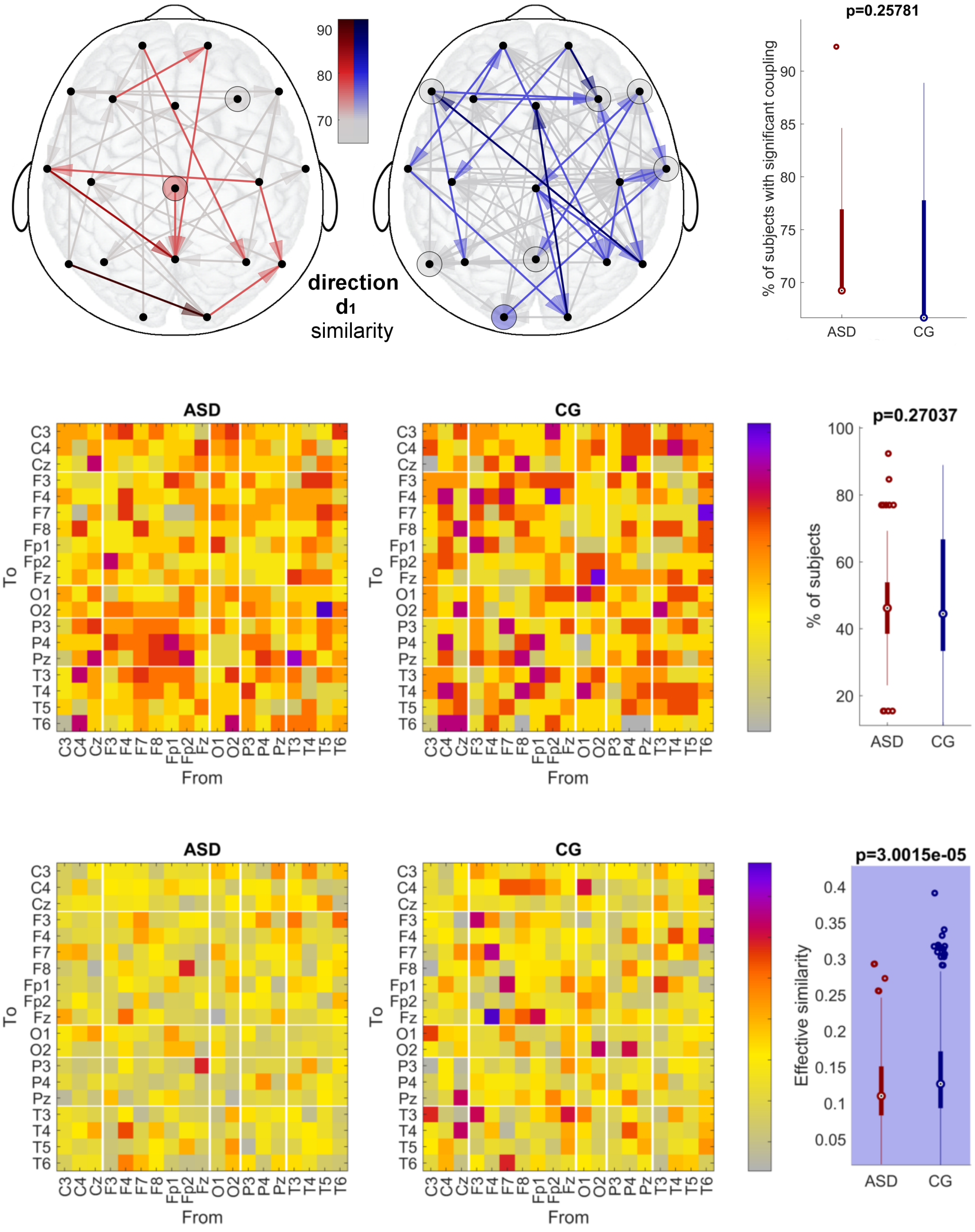

FIGURE 5.33: Head-maps for the polar similarity of the CG (blue) and ASD (red) coupling functions with the form d_1, describing the diffusive LF, MF→HF coupling. Arrows link the probes for which the similarity was higher than surrogates and circles indicate locally significant coupling. Colour intensity codes for the actual percentage. For clarity, only value above the 65% threshold are shown. The box-plot on the top-right summarises the content of the head-maps. Matrix-maps and box-plot on the second row show the complete distributions for the percentage values. Matrix-maps and box-plot in the third row show the distributions of the effective similarity for each pair (significantly higher for CG).

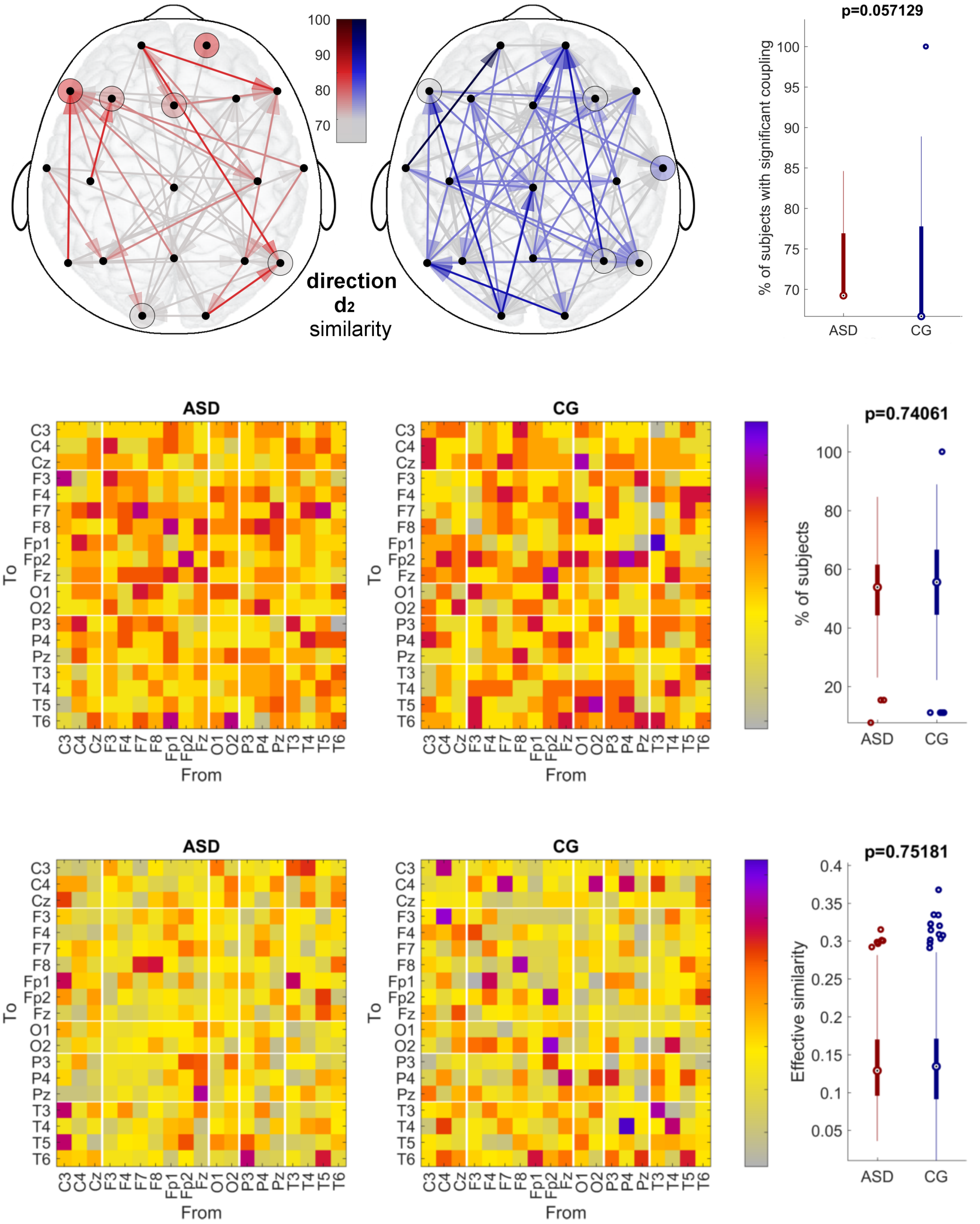

FIGURE 5.34: Head-maps for the polar similarity of the CG (blue) and ASD (red) coupling functions with the form d_1, describing the additive LF, MF→HF coupling. Arrows link the probes for which the similarity was higher than surrogates and circles indicate locally significant coupling. Colour intensity codes for the actual percentage. For clarity, only value above the 65% threshold are shown. The box-plot on the top-right summarises the content of the head-maps. Matrix-maps and box-plot on the second row show the complete distributions for the percentage values. Matrix-maps and box-plot in the third row show the distributions of the effective similarity for each pair.

5.7.4.1 Intra-subject variability

In order to evaluate the intra-subject variability of the form of the coupling functions, all the forms for each subject were compared with the subject's average form by applying the similarity measure based on 2-dimensional correlation between two forms. Therefore, high values of this similarity indicate lower intra-subject variability.

Forms in Figure 5.35 explain the meaning of this type of similarity. On the left, the intra-subject average coupling functions are shown for one CG and one ASD subject. On the right, the forms generating, respectively, the highest and the lowest values of the similarity are shown. The polar plots on the corners summarise the morphological features of form of the functions.

For the case selected for the CG on the top panels of Figure 5.35, the forms do not have any obvious preferential component, as it is indicated by the small arrows in the polar

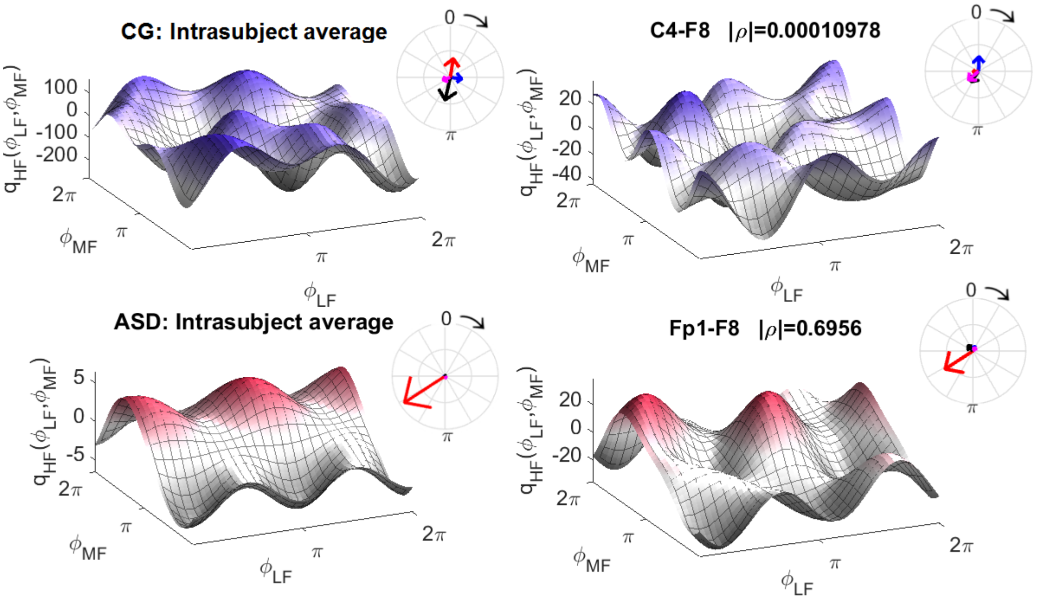

FIGURE 5.35: In the left column, two example of two intra-subjects coupling functions are shown. In the right column, the forms generating respectively the lowest and highest intra-subjects similarity indices are presented. On the side of each coupling function, the polar plots show the similarity indices describing its form.

plots. Also, corresponding arrows between the average and the C4→F8 form have different modules and phases. The resultant similarity value is very small ($|\rho| = 0.00001$).

On the contrary, in the case shown for the ASD subject on the bottom panels of Figure 5.35, the forms generated a similarity of $|\rho| = 0.7$. The resemblance is clear by qualitatively observing the forms, with the p_2 as prevalent component and a smaller second-order modulation along ϕ_{LF}. The polar plot quantifies this resemblance, by indicating for both forms a p_2 arrow with modules significantly bigger than the others, and similar phases.

Figure 5.36 shows the group-average values of the intra-subject similarity, for each combination of probes. The overall value was not significantly different between the groups. For both ASD and CG, the highest similarities emerged grouped by rows, i.e. in functions directed to a specific probe.

In particular, for both groups, interactions acting on F3 seemed to be the most similar to the group average. P4 also contained high values of intra-subject similarity for both groups. The group maps were different with regards to the C4 and T5 rows, which contained, respectively, high values only for the ASD and for the CG.

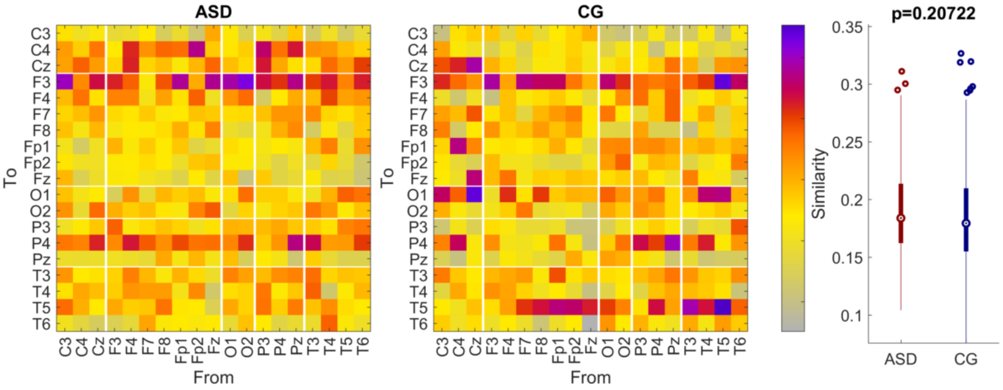

FIGURE 5.36: Intra-subject variability of the form of the coupling function, evaluated as group average similarity between each coupling functions and the subject's average. Martix-maps show the values of intra-subject similarity, and the box-plot their distributions.

5.7.4.2 Inter-subject variability

Similar procedure allowed to quantify the inter-subject variability within the groups. This time, the average form was calculated between coupling functions from corresponding pairs of probes, in each group. The similarity was then computed for each pair between individual subject's form and the group average.

Results of this computation are shown if Figure 5.37. Significant difference between the groups emerged from the matrices, as shown in the box-plot on the side. In particular, the ASD group resulted having a much lower inter-subject similarity of the coupling functions, i.e. higher variability spread across all the pairs.

The highest values of inter-subject similarity were found in links within the central area of the ASD group, for the link T4→P4, and generally for the frontal to parietal and temporal to parietal zones.

The most and the least variable inter-subjects average coupling functions are shown in Figure 5.38. The most variable inter-subject coupling function was the T4→T3 for the ASD group, shown on the left, in red. It generated a $|\rho| < 0.2$. The polar plots underneath it are divided for each direction of similarity, showing with an arrow the index of the visualised function, and with dots the indices relative to the individual subjects' forms

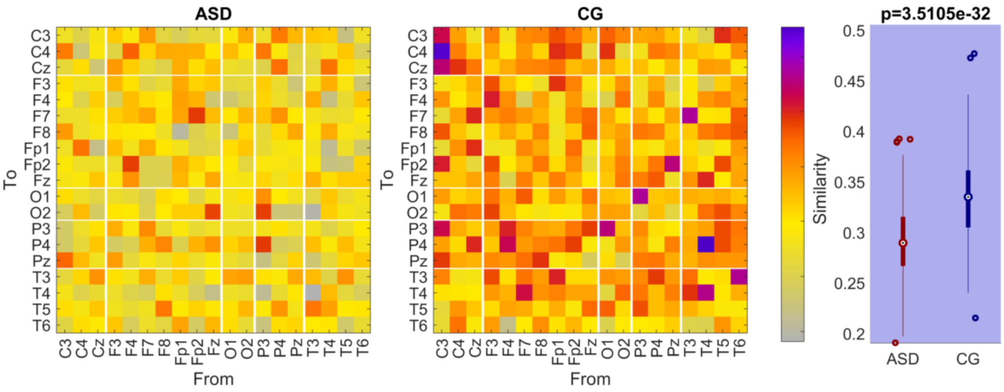

FIGURE 5.37: Inter-subject variability of the form of the coupling function, evaluated as group average similarity between each coupling function and the corresponding group's average. Martix-maps show the values of inter-subject similarity, and the box-plot their distributions, resulting significantly higher for the CG group.

(generating the shown average). The biggest arrows emerged for the d_1 direction, consistently with the qualitative aspect of the form having a slightly preferential component along the ϕ_{MF} axes. The scattered dots around the arrow explains both the inter-subject variability and the not obvious form of the shown function, which generated as average of very different forms, hence the high inter-subject variability.

On the right, the case with the highest similarity $|\rho| > 0.45$ is shown, which corresponds to the pair of probes C3→C4 from the CG. The form has an evident preferential component along the ϕ_{LF} axes, which is depicted by the long blue arrow in the d_1 polar plot. The dots in this case are clustered around a specific phase in the polar plane of each similarity direction: this indicates that the average form (shown) originates from a distribution of functions having similar morphological features, hence the low inter-subject variability.

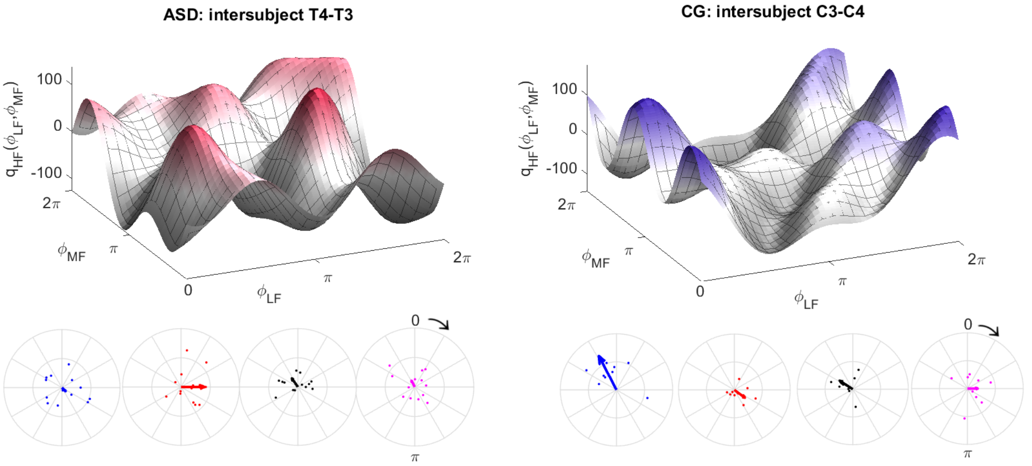

FIGURE 5.38: Example of two group-average coupling functions generating respectively the lowest and highest inter-subjects similarity indices. On the bottom, the polar plots show the similarity indices describing the form of the individual coupling function (with dots) and of the inter-subject's form shown on the top (with arrow). Note how coherent dots distributions generated the form with higher inter-subject similarity.

Chapter 6

Discussion

The outcomes of the comparison of brain dynamics between ASD and CG are here summarised, in order to discuss the possible meaning of the identified discriminants as biomarkers for ASD.

6.1 Power

Power results can be summarised as follows:

- Generally, the power was higher for the ASD group in the LF and HF range, and for the CG in the MF range.
- Relative power provided a better discrimination between the groups than the absolute power.
- Higher absolute power for CG in the MF was found on the occipital probes.
- CG showed higher relative MF power on central, parietal and temporal areas.
- ASD had higher relative power for the LF band on central areas and for HF on Fz.

These outcomes are in line with what has been reviewed in Section 4.3.1 about literature results for resting state EEG features in autistic children.

For the LF band, even if no specific probe generated higher delta power, the overall power was higher for ASD in the LF interval. Higher LF power – in the delta range – was also detected by several other studies (Cantor et al., 1986, Chan et al., 2007, Clarke et al., 2016, Elhabashy et al., 2015, Pop-Jordanova et al., 2010, Stroganova et al., 2007). For the MF bands, outcomes of this work showed higher power for the CG in the MF band. Studies gave mixed results for the theta band, but found generally lower alpha band (Cantor et al., 1986, Chan et al., 2007, Matlis et al., 2015). For the HF band, the higher power of the ASD group confirmed literature findings for the beta-gamma bands (Coben et al., 2008, Orekova et al., 2006, Lushchekina et al., 2012, Sheikhani et al., 2009).

As suggested (Wang et al., 2013), the origin of this different distribution of power could reside in neurochemical abnormalities within synaptic receptors. This could be the case because power in HF and LF bands is believed to be modulated by the inhibitory circuitry within the pyramidal cells (Tierney et al., 2012). As discussed in Section 4.2, genes coding for GABA receptors appear to be different in ASD, contributing to increased neuronal excitability, particularly during development (Ma et al., 2005). Impairment of the same GABAergic inhibition was also linked to the HF activity emerging during epileptic seizures (Wendling et al., 2002).

GABAergic activity has also been suggested to play a role in generating the power in the alpha band (within the MF range) by active inhibition (Jensen and Mazaheri, 2010). This processes, contributing to the 'idling' effect (Klimesch et al., 2007) of alpha, are involved in the top-down control of sensorimotor responses, which include the ability to adjust the behaviour according to the environmental contest. For the alpha band, an increased power is believed to be connected with an attentive restful state, and ability to concentrate despite stimuli coming from a distracting environment (Klimesch et al., 2007, Sauseng et al., 2005). The detected lower power in the MF could therefore be linked with some ASD behavioural features.

The lower MF power in temporal and posterior areas could be also explained by the more densely packed minicolumnar structure (Casanova et al., 2002), preventing the GABAergic interneurons from propagating a proper idling effect.

6.2 Coherence

The main points emerging from the coherence investigation are:

- Generally, HF activity was coherent at shorter distances, while LF and MF activity were found more coherent across longer distances.
- ASD and CG showed an opposite trend in having preferentially more short-distance HF coherence and more long-distance LF and MF coherence.
- The CG showed a relevant number of higher inter-hemispheric coherences for the LF and MF ranges, while the ASD group had higher intra-hemispheric HF coherence.
- For the CG, the coherence was higher especially for the frontal-prefrontal links, while the ASD group had more coherent links between the centro-frontal zones.

With regards to the distance, the most agreed traditional theory based on fMRI studies depicts the autistic brain with a pattern of under-connectivity between distant brain region, and over-connectivity between more proximal areas (Belmonte et al., 2004, Courchesne and Pierce, 2005, Just et al., 2004). However, recent studies did not find any relation between the distance of the probes generating coherent links and the presence of ASD, showing a more variate and complex scenario (Duffy and Als, 2012, Mohammad-Rezazadeh et al., 2016). Coherence results presented in this work are in agreement with the traditional approach, detecting significant group differences in the length of coherent links.

Results presented in this study also indicated for ASD a strong pattern of diminished coherence within the prefrontal-temporal lobes in the LF and MF, counterpoised to a higher coherence between frontal, parietal and central area of the scalp for the HF ranges. The under-connectivity of MF in the frontal areas (where processing of sensorial functions like hearing is located) could signify an impairment on the 'idling-effect' of alpha for ASD, contributing to the reduced ability of an ASD individual to cope with noisy environmental inputs.

According to the *theory of minicolums* (Casanova et al., 2002), in autism the development and interconnections between GABAergic interneuron could be disrupted by the densely packed cortical cellular structure, especially in the prefrontal and temporal areas. In line with this theory, those areas showed a lower phase coherence in LF and MF frequency range in ASD, potentially reflecting impaired connectivity for the GABAergic interneurons.

On the other hand, the higher centro-frontal and centro-occipital HF range coherence of the ASD group, partially overlapping with an increasing in the power, may reflect structural hyper-connectivity. This increased synchronisation of the HF activity is also in line with the mini-columns theory, and with the early over-growth of brain matter reported in children with ASD (Billeci et al., 2013). This hypothesis of over-synchronisation in the HF range could also be an explaination for the >40% co-morbidity of epilepsy with autism (Palmen et al., 2004).

Finally, inter-hemispheric coherence appeared to be reduced in ASD when compared to the CG. On the contrary, ASD showed a more extended intra-hemispheric coherence. A recent fMRI study comparing males and females' brain functional connectivity (Ingalhalikar et al., 2014) showed similar differences for males and females brains, respectively. According to this representation of males and females brain features, what emerged from this work is in agreement with the 'extreme male brain' theory of the autistic brain (Baron-Cohen, 2002).

6.3 Coupling functions

The investigations of phase-to-phase coupling brought the following results:

- LF→HF component: no overall significant differences were found in strength and similarity.
- MF→HF effective coupling strength was detected in a significantly higher percentages of subjects for CG.
- p_2 similarity was significantly higher both in percentage of subjects and effective values for ASD.
- d_1 similarity had significantly higher values for CG.
- Net HF had significantly higher values for ASD.
- Significantly higher inter-subject variability was found for ASD group.

The cross-frequency coupling investigation performed in this study sheds for the first time light on the differences between the effective connectivity in ASD and CG young children.

The analysis of strength and similarity of the coupling allowed us to evaluate two complementary types of information. The strength quantified the amount of cross-frequency modulation by linearly combining the inferred coefficients, averaged in time. On the other hand, investigations on the forms allowed to assesses the combined modulation mechanism generated by the collective effect of the single coefficients and their base functions.

In other words, the strength is linked to the amplitude of the coupling function, while the form of it is related to the mechanism of the coupling. Therefore, a high value of coupling strength could generate a surrogate-looking form of the coupling function in which the mechanism of the interaction is unclear. On the contrary, a low value of strength could lead to a small-amplitude coupling function describing a clear, albeit weak, coupling mechanism.

Within the triplet LF, MF→HF, the most interesting results were given by the partial component MF→HF. This includes the well known theta→gamma coupling, summarised in

Section 2.1.7. In this interaction, the slower theta wave travelling from different functional networks is believed to integrate the information coded by gamma in HF local networks across longer distances and periods of time (Jensen and Colgin, 2007).

Theta-gamma phase-to-power coupling was detected during memory tasks (Schack et al., 2002), in electrocortigrams of epileptic patients during cognitive tasks (Canolty et al., 2006), on the hippocampus during a working memory task (Axmacher et al., 2010), during visual tasks (Voytek et al., 2010).

It follows that a weaker coupling from theta band (in the MF) could lead to a brain network in which the HF activity propagates on medium-long distances in a different, less controlled way. Results of this investigation showed that most of the CG subjects shared a specific subset of links in which MF→HF coupling strength was above the surrogate threshold. The overall percentage of subjects with effective coupling strength for MF→HF was not different between the groups, with the ASD subjects presenting more variable maps.

Under a topological point of view, the ASD group had MF→HF coupling acting prevalently on the HF of the central probes, while for the ASD group the direction was opposite (MF from Cz modulating the HF in the periphery). This difference could indicate the preferential direction of information flow in the cortico-thalamic circuitry (Alexander, 1986).

By observing the matrices of the effective coupling strength for MF, it emerges how, preferentially, high values are grouped in columns. This could indicate how, especially for the CG, the source of MF acts as a 'coupling mean' travelling through the network and integrating the clusters of HF activity along the way. Rows of high values in the coupling strength's matrix, like for the Cz probe for the ASD in the MF→HF coupling, indicates a less physically meaningful coupling generating from mixed sources and directed to the same target. This difference in the prevalent direction between ASD and CG was found also in the LF→HF coupling-maps, both for strength and similarity.

However, the forms of the coupling functions have been found to be significantly more similar to the p_2 numerical form (associated with MF→HF) for the ASD group. The significance indicates the presence of the mechanism for the MF→HF coupling in the ASD group, which nevertheless transmits weaker interactions than in the CG. Again, a mixed map of periphery-to-central links emerged from the ASD group when compared to a more homogeneous posterior-to-anterior CG map defining a clear direction for the propagation of the coupling.

With regards to the net HF coupling, encompassing all the coupling coefficients defining the triplet LF, MF→HF, the head maps for the coupling strength described a fundamental difference between the groups. Parietal and occipital probes acted as starting points for long distance connections for the ASD group, while the CG map was characterised by shorter distance links developing around the periphery of the head. The effective values of the strength were significantly higher for the ASD group.

This result is apparently in contradiction with what shown and discussed for the partial LF→HF, MF→HF and LF, MF→HF components of the coupling. However, one should bear in mind that those partial components, which carry the most physically meaningful parts of the interaction, are not the only ones generating the total coupling. Other components contain the self-dynamics HF→HF and the common LF, HF→HF, MF, HF→HF and MF, LF, HF→HF components are included in the net coupling strength.

Because of the filtering and the proto-phase-to-phase transformations, self dynamics should not emerge from the analysis. Residual traces of self-dynamics could be due to a small overlapping in the spectral content of the MF and HF filtered bands, and therefore should not carry a relevant physical meaning. This should not have influenced investigations on the form of the coupling, as the similarity analysis presented in this work does not include dependences on ϕ_{HF}: the investigated forms are uniquely a function of ϕ_{LF} and ϕ_{MF}.

Other interesting outcomes of the coupling investigation regarded the intra- and inter-subject variability. It emerged that, within each subject, the forms of the coupling exerted on the probe F3 were generally the most similar to the group average. P4 followed for the ASD group, and T5 for the CG. The probe F3 is also a frequent target of the MF→HF coupling. This result highlights once again how the MF→HF component is of central importance for the investigated brain dynamics. No statistical difference emerged for intra-subject variability of the coupling functions, indicating that ASD does not either enhance or reduce the propagation of similar coupling mechanisms within the brain network.

On the contrary, ASD seemed to be associated with a higher inter-subject variability of the coupling function, when compared to the CG. Among the CG, it is worth noting that the most similar function detected between the subjects was the T4→P4, which was also found similar to the numerical forms in a considerable percentage of subjects for all the 4 investigated directions (p_1, p_2, d_1 and d_2). This suggests that the most common features of coupling functions underlie a specific mechanism and not a surrogate-like form.

The higher in inter-subject variability for ASD was the most significant difference found in this study, with a overall 5% lower similarity to the group average for the ASD group (p=$3{\cdot}10^{-32}$). This result remarks how the variability between individuals can be considered as a feature of ASD. The spectral nature of the disorder and the many different ways in which it manifests might play a role in such variability. As it has been recently suggested (David et al., 2016), that inter- and intra-subjects variability could be a key-feature of ASD even between individuals belonging to similar areas of the spectrum.

Chapter 7

Conclusions

In conclusion, the methods applied allowed us to describe in detail the different brain dynamics associated with the presence of ASD in young children.

The outcome of the analysis confirmed previous results for power and coherence investigations in EEG of young children, with the novelty of applying wavelet-based methods for both.

The main advantage in the power investigation introduced by the wavelet transform is the logarithmic resolution of the frequency axes, which fits the spectral distribution of the EEG signal well. Moreover, the adjustment of the central frequency allows to optimally set the compromise between time and frequency resolution.

For the coherence analysis, the wavelet transform allows once again to work on logarithmically distributed frequency steps, and to consider the evolution of the phases in time. Also, the phase-defined coherence excludes effects due to the amplitude of the time-series which are not completely excluded in more commonly applied techniques like the magnitude squared coherence.

In this work, cross-frequency phase coupling has been evaluated for the first time from the EEG of ASD and CG children. The brain has been modelled as a multidimensional network of coupled phase oscillators subject to noise, whose time-variable coupling parameters were inferred by means of the dynamical Bayesian inference.

The reconstructed coupling functions bring a novel perspective to neuroscience by providing unique insight into the effective connectivity from EEG signals. Moreover, the polar similarity index that has been specifically developed here allows one to describe the form of the functions in quantitative detail. The comparisons of LF, MF→HF phase coupling functions in the ASD and CG demonstrate how neural coupling functions can be reconstructed from spatially distributed sources, and what benefits and possibilities are introduced by their assessment. In principle, the method can equally be applied to the time series created by any pair of coupled oscillatory processes (Stankovski et al., 2015, 2017b, Ticcinelli et al., 2017).

In summary, the analysis disclosed the following main results for the ASD – CG comparison. Power investigations detected higher neuronal synchronisation for the ASD group in the LF and HF range, and for the CG in the MF range. Functional connectivity assessed with wavelet phase coherence disclosed patterns of higher coherence for ASD in short distance HF connections on the central area of the scalp, which could be linked to the over-synchronised activity of local ensembles of neurons, reflected also in the high HF power on the same areas in the ASD. The higher coherence on longer LF connections in CG was on the contrary not linked with the emergence of higher power, and could have reflected more the propagation of coherent waves between different networks than the neuronal synchronisation within local neuronal ensembles. For the CG, short-range coherence was higher especially for the frontal-prefrontal links in LF and MF bands, suggesting a cognitive function of the coherent links.

Coupling functions allowed to study the effective connectivity. The MF→HF component of the coupling disclosed topological network differences in the frequency-range including the well known theta-gamma modulation. A higher percentage of subjects with significant coupling strength in the CG was counterpoised to a more deterministic form of the coupling function in the ASD group, suggesting an impairment in the amount of effective modulation performed more than a lack of pathways for it. Also higher inter-subject variability emerged from the comparison of forms of the coupling functions in the ASD group, in line with the theory of autism as an idiosyncratic brain (David et al., 2016, Hahamy et al., 2015). Especially for the CG, LF and MF modulation were found to travel from the sources through the network on preferential directions (often posterior-to-anterior), while the ASD displayed more variable and often peripheric-to-central patterns. This difference suggested the presence of a less structured theta-to-gamma coupling, which would be in line with the cognitive features of ASD.

7.1 Personal contribution

For the preparation of this PhD thesis, an introductory research on brain anatomical and functional features has been undertaken, followed by a research on the meaning and origin of the brain waves recorded in the EEG.

Bibliographical research on the current knowledge about brain features and EEG dynamics in children with ASD has been performed and summarised.

Numerical simulations have been performed in order to fully understand the mechanisms behind each method of analysis applied for the characterisation of the brain dynamics, including the surrogate techniques. The relevant parameters of each method have been tuned to achieve an optimal application to this specific investigation. The methods of wavelet phase coherence and dynamical Bayesian inference developed by the group have been applied for the first time to a all-to-all multidimensional network (having 19 nodes).

For the Bayesian inference, the numerical program for the method has been generalised in order to encompass any number of oscillators, and its performance on networks with different orders has been numerically evaluated.

The polar similarity index has been developed to allow quantitative comparisons of the form of the coupling, and its usefulness has been proven within the investigation.

Analysis of effective coupling in the EEG of ASD children has been performed for the first time, and the results have been interpreted under the light of what is known about brain dynamics and ASD.

7.2 Limitations

The greatest care has been taken in order to pre-process the data in the most suitable way before performing the analysis.

However, the bias in the data discussed in Section 5.5 might still have played a role in enhancing the differences detected by the methods applied. Because of the unfortunate mixed composition of the same-reference groups reported in Table 5.6, it was not possible to perform any statistical comparison between sets which were reference-wise homogeneous.

Also, the different strategies undertaken by the EEG technicians in order to keep the children still and quiet (letting them look at a screen, or listen to the parent's voice) might have influenced the brain activity of each subjects.

Finally, the limited number of subjects involved, especially in the CG, limits the statistical validity of the outcomes.

Despite these limitations, the procedure followed for this investigation has been thoroughly developed, and led to promising preliminary outcomes. For these reasons, the publication of the results outside of this thesis is in plan only after additional data are collected.

Also, few methodological limitations should be mentioned.

When studying brain connectivity from EEG, one should bear in mind that volume conduction on the scalp affects measures of functional connectivity. In order to reduce this effect, several models have been proposed to reconstruct the source time-series. However, a more dense array of EEG probe than the one used in this study (e.g. 128 channels) is recommended in order to apply such techniques. However, this type of artefacts are likely to affect the measures of coherence in similar fashion between the groups, and therefore comparative results should still be reliable.

In the applied methods, a set of parameters must be chosen, which inevitably inserts some degrees of subjectivity in the measures. Among them:

- The choice of the re-referencing system.
- For the Wavelet transform, the choice of the type of Wavelet and of the central frequency f_0.
- For the filtering, the type and shape of the filter, and the bands definition.
- For the dynamical Bayesian inference, the length of the window used for each cycle of the computation and the propagation constant.

No golden standard exists for the optimal extraction of phases from a time-series with complex spectral content. In this case, a compromise between the identification of consistent bands of activity and the width of such bands has been undertaken. However, the division in wider frequency bands leads to a less precise extraction of the phase evolution with the Hilbert transform.

7.3 Further developments

The validity of the presented results is planned to be verified in the near future by applying the procedure developed for the drawing of this thesis to a more consistent cohort of data.

Confirming the presented results –or disclosing different ones– would allow one to select the best discriminants among the differences emerged, and to finalise the algorithm providing a biomarker for ASD from EEG time series.

Under a methodological point of view, some improvement could be performed in the steps preceeding the application of the dynamical Bayesian inference. For example the limits of the frequency bands could be customised for each participant, allowing the use of narrower bands centred on the most prevalent frequencies. Also, a systematic way to evaluate the quality of the phase extraction could be implemented.

The applied methods are suitable to be extended in many ways. Among them, for example, the dynamical Bayesian inference could be modified in order to reconstruct also the amplitude coupling.

Appendix A

Brain structure

A.1 Structure

In order to better understand what is the physical structure underlying the EEG signal, a brief introduction on the human brain and its main parts (Figure A.1), is here provided. When not otherwise indicated, the anatomical and functional notions reported in this section have been extracted from Kandel's *Principles of Neural Science* (Kandel et al., 2000), (Chapters 1-2,4).

The cerebellum

Located occipitally, this structure has been known to play a fundamental role in the coordination and precision of movements, but also in other cognitive functions (Middleton and Strick, 2000). It is connected to the cortex through circuits involving the inner structures of the brain (basal ganglia).

The thalamus

The thalamus is a large mass of gray matter into the inner brain. It allows interactions between the cortex, sensorial organs and subcortical structures. In particular, each sensory system (except for the olfactory) is associated with a specific nucleus of the thalamus,

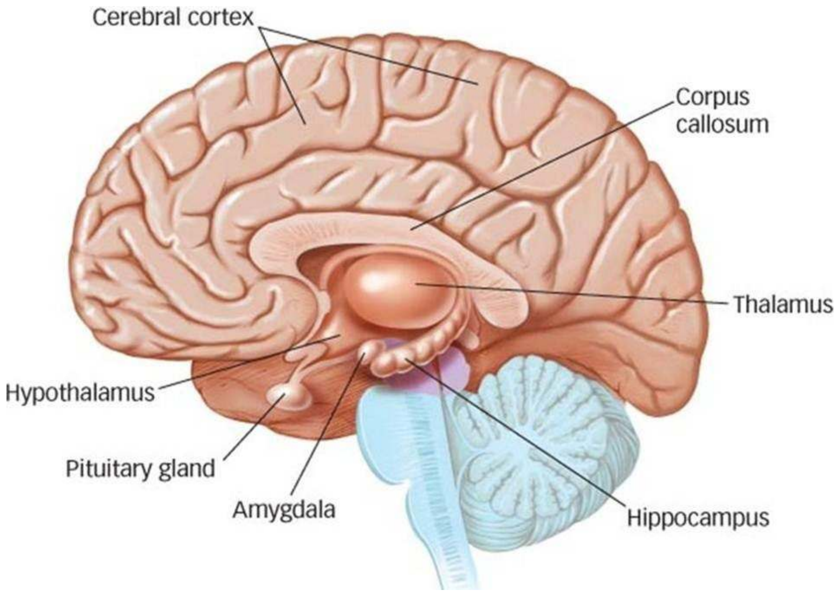

FIGURE A.1: An anatomical illustration of the human brain, longitudinal view (Public domain figure).

which is at its turn connected to the specific areas of the cortex via thalamocortical fibers. For example, the visual information captured by the retina is sent to the latero-cingulate nucleus of the thalamus, which is then connected to the visual cortex where the information is processed.

Thalamocortical fibers extending from the thalamus reach the cortex at different layers. Connections are usually reciprocal, forming thalamo-cortico-thalamic circuits. These loops form the functional units responsible to parallel processing of different types of information (Alexander, 1986, Parent and Hazrati, 1995) constantly happening in the brain.

A.1.1 The Cortex

The cerebral cortex is the outer and largest part of the human brain. The most outer layers of the cortex mostly contain bodies, dendrites and axonal termination of neurons, forming what is called *grey matter* in counter-position to the deepest layer, the *white matter* composed by the axons. The ratio surface/volume of the cortex is very high, thanks to the multiple folds generating ridges (gyri) and a grooves (sulci). This layout allows to generate several functionally differentiated areas in a relatively restricted volume. The modular functionality of the cortex is provided both by this differentiation of areas and by a layered cellular structure. The connectivity of cortical neurons both on short and long distance develops within the cortex layers.

The cortex is divided in two hemispheres, connected in the mid-line at the longitudinal fissure by the corpus callosum, composed by the neuronal axons and their myelinic outlayers. According the the number of layers that compose it, the cortex also can be divided into neocortex, where most of he high order brain functions take place (6 layers) and the allocortex, responsible to process information coming from the olfactory system (4 layers).

A.1.1.1 Layers

Each layer of the cortex is characterised by specific neuronal cell types. Cortical cells can be connected both between cortical regions or with subcortical regions. Neuronal pathways in the cortex can therefore be either direct, or passing from other structures, like the thalamus.

Within the neocortex, six main layers can be distinguished, from the outer (pial surface) to inner part (white matter):

- Layer I contains glial cells, dendrites of pyramidal neurons and horizontal axons.
- Layer II, contains small pyramidal neurons.
- Layer III, contains small and medium-size pyramidal neurons. Layers I through III are the main target of inter-hemispheric cortical connections.
- Layer IV, contains different types of stellated and pyramidal neurons. This layer is the principal target of thalamocortical fibres and intra-hemispheric cortical connections.

- Layer V, contains large pyramidal neurons whose axons are connected to subcortical structures.
- Layer VI, contains few large pyramidal neurons and many small spindle-like neurons. It sends efferent fibres to the thalamus, establishing a reciprocal interconnection between the cortex and the thalamus.

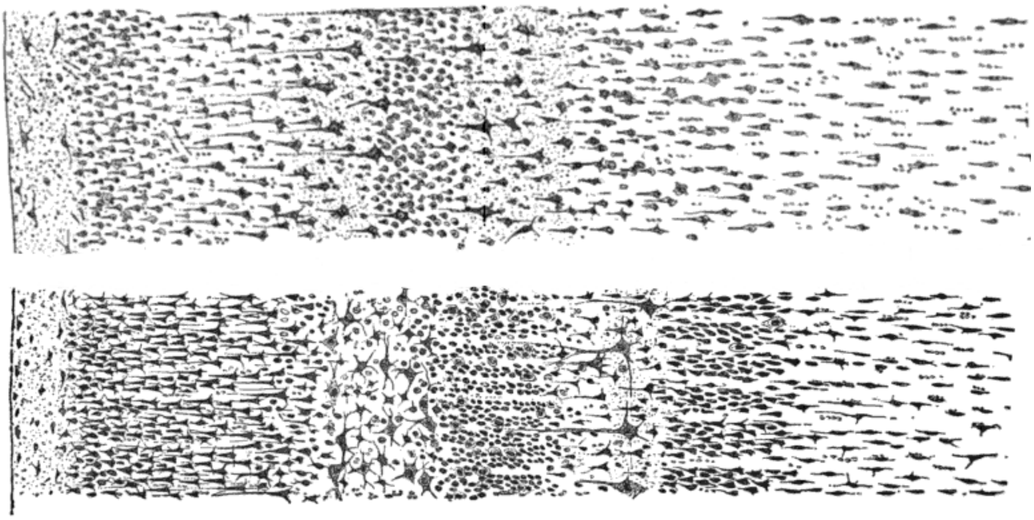

FIGURE A.2: Drawings of cortical lamination by Santiago Ramon y Cajal, with the surface of the cortex at the left. Top: slice of visual cortex of a human adult. Bottom: slice of motor cortex of a human adult (Public domain figure).

Information processing within each layer is determined by different temporal dynamics. A study on the visual cortex of rats showed for example that layers II/III generate a slower 2 Hz oscillation while a fast 10–15 Hz rhythm can be observed in layer V (Sun and Dan, 2009).

A.1.1.2 Minicolumns

Cortical microcircuits developing perpendicularly to the neocortical surface form the minicolumns. These groups of 80-100 neurons are believed to constitute the unit of the extensively complex brain network.

The cells in the mid-layer of the columns are the target of thalamic inputs, which can propagates both toward the surface and toward the inner brain. This type of connectivity reduces the time delay needed for all the cells from a specific area to respond to a stimulus (Jones, 2000). Complex dynamics of inhibitory and excitatory responses modulate the propagation of the action potential. The stimulus propagates both within a column and between different columns linked by pyramidal dendrites and interneurons. Different areas of the brain are characterised by minicolumns with specific horizontal layers. This specialisation of individual columns increases the selectivity for propagation and processing of information.

A different organisation within the layers of the minicolumns is believed to be connected with autism and schizophrenia (Casanova et al., 2002). It is still not clear however if the different morphology of minicolumns is a cause or a consequence of the disorders.

A.1.1.3 Areas

The cortex is traditionally divided into areas according to the function which is fulfilled, i.e. sensory, motor, and associative.

The sensory areas receive and process information coming from sensory organs. If the sensorial inputs are transmitted by the thalamus, the targeted areas go under the name of primary sensory areas. They are involved in vision, hearing and touch.

The motor areas are responsible both for coordinating voluntary movements in space, and of deciding which voluntary movements to perform according to higher-order processing.

The association areas are the parts of the cerebral cortex that are not involved in sensory and motor functions. They allow interactions with the environment by providing abstract thinking, memory and language abilities. Within the association areas, the parietal, temporal, and occipital lobes are believed to integrate motor and sensory input with memory information. The frontal lobe is believed to be involved in action planning and abstract thoughts. The association areas are organised as distributed networks, connecting different areas of the cortex. Association networks do not work in isolation, but are coupled in a complex system of hierarchical relationships, interactions and competition (Yeo et al., 2011).

A.2 Cellular level

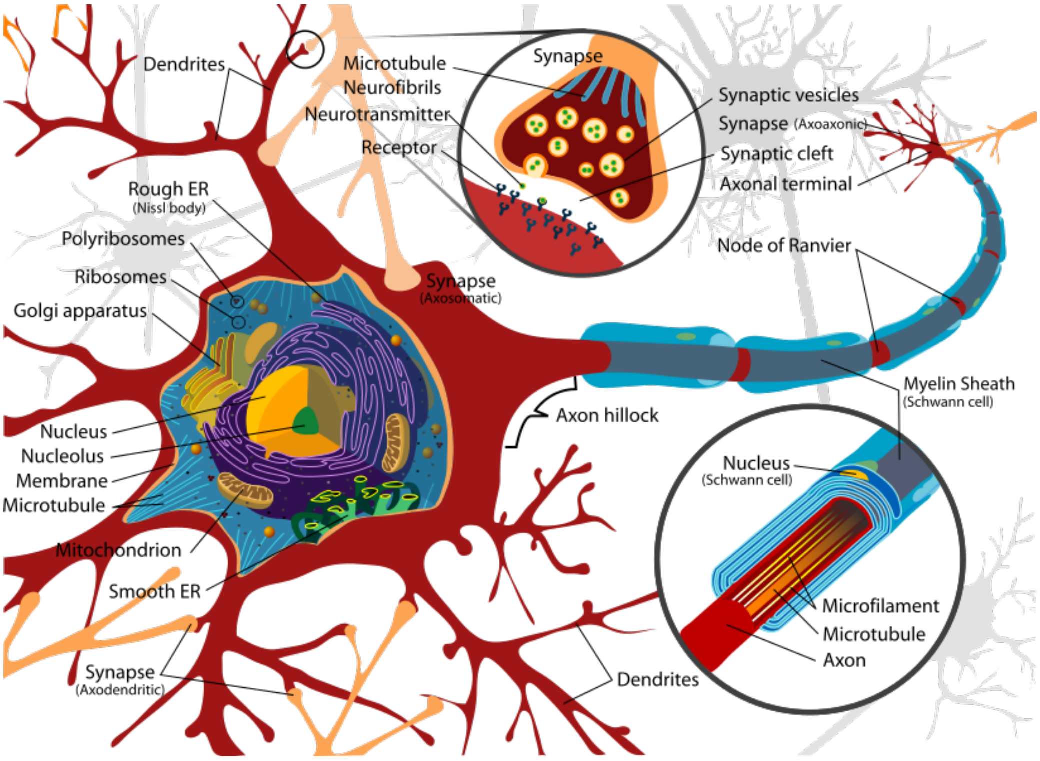

FIGURE A.3: Schematic illustration of the different parts of a neuron (Public domain figure).

The units of cerebral functions are complex cells called neurons (Figure A.3). A neuron is composed by a cellular body (soma) from which the dendrite protrudes, and an axon which terminates with synapses. Dendrites are thin branch-like structures hundreds of μm long, ending with receptors. The axon is a prolongation of the soma covered by a myelinic insulation, and travels for a distance so that its synapses can reach other cells. Axonal synapses of a neuron connect with dendritic receptors of another, allowing pathways for the electrochemical signal to travel into the network. The human brain is composed by about 100 billion cells connected in a complex network, with an estimated number of 200 trillion connections between them.

Neurons are electrically excitable cells. They maintain voltage gradients by means of the interaction between ion pumps and channels placed within their membranes. Ions such as sodium, potassium, chloride, and calcium kept with different concentrations inside and outside of the cell give rise to the cross-membrane voltage.

The signal is transmitted from a cell to another basing on a *all-or-none* mechanism. If the cross-membrane voltage reaches a specific threshold, an electrochemical pulse is generated. From the soma, this *action potential* travels along the axon till it reaches the axonal terminals. There, at the pre-synaptic terminal, the pre-synaptic neuron releases neurotransmitters, which may bind to the receptors of the post-synaptic neuron.

Synaptic signals can have both positive or negative charge, and therefore be either excitatory or inhibitory. The excitatory and inhibitory contributions reaching a neuron sum up into the soma. If the net effect is inhibitory, the neuron will be in a state further from its threshold potential, therefore less likely to fire. If the net effect is excitatory, the potential will be closer to the threshold and neuron will be more likely to fire. According to the type of expressed receptors, synapses can be prevalently excitatory (Type I) or inhibitory (Type II). Type I are typically located within the dendrites, while Type II are usually found on the cell body. To promote signal propagation, the surface of excitatory synapse is larger than their inhibitory counterparts.

Neurotransmitters can be synthesised in the cell body or in the axon, and are then stored into vesicles in the axon terminal. Released neurotransmitters can either be metabolised by specific enzymes, or enter again the axon terminal. More than 100 neurotransmitters have been identified. In human brains, glutamic acid, or glutamate, is the main excitatory neurotransmitter, while gamma-Aminobutyric acid (GABA) is the main inhibitory neurotransmitter.

Different types of neurons exist in the human brain. Among them, pyramidal cells are the primary excitatory units of the cerebral cortex. The complexity of pyramidal cells increases from posterior to anterior brain regions (Elston, 2003), with the pre-frontal cells implicated in cognitive ability. Basket cells are inhibitory GABAergic interneurons, found throughout different regions of the cortex and cerebellum. Spindles cells are large cells permitting fast information processing, and are found exclusively in specific regions of the cortex. Neurons linking the input (sensory) with the output (motor) functions of the brain are called interneurons (Markram et al., 2004). Local interneurons are characterised by short axons. They connect nearby neurons to transmit information locally. Relay interneurons have long axons and connect circuits of neurons in different regions of the brain. In the human brain, approximately 20% of neurons are interneurons. They are primarily inhibitory, and use the neurotransmitters GABA or glycine.

The brain also contains diverse non-neuronal cells: the glial cells. Among them, oligodendrocytes provide support and insulation to axons; Astrocytes perform many functions, including extra-provision of glucose to neurons and regulation between neural activity and blood flow (Parri and Crunelli, 2003); Microglia provide the main form of active immune defense in the brain.

The blood–brain barrier is formed by a layer of brain endothelial cells that line the cerebral capillary bed. Coupled with neurons and astrocytes, it controls the osmotic passage of water and gases and selective transport of substances like glucose and aminoacids from the vascular system into the brain (Abbott et al., 2006).

Appendix B

EEG glossary

In 1974 a first glossary of EEG terminology was published by International Federation of Societies for Electroencephalography and Clinical Neurophysiology (IFSECN). A second updated version came out in 1999, but the definition of bands did not change across the two publications. Some key-terms are reported below:

- *Rhythm:* EEG activity consisting of waves of approximately constant period.
- *Wave:* Any change of the potential difference between pairs of electrodes in EEG recording.
- *Band:* Portion of EEG frequency spectrum, i.e. delta, theta, alpha, beta bands.
- *Delta:* Frequency band under 4 Hz. Comment: for practical purposes lower frequency limit is 0.5 Hz, as DC potential differences are not monitored in conventional EEGs.
- *Theta:* Rhythm with a frequency of 4 to under 8 Hz.
- *Alpha:* Rhythm at 8-13 Hz occurring during wakefulness over the posterior regions of the head, generally with maximum amplitudes over the occipital areas. Amplitude varies but is mostly below 50 mV in the adult. Best seen with the eyes closed

and during physical relaxation and relative mental inactivity. Blocked or attenuated by attention, especially visual, and mental effort.

- *Beta:* in general: any EEG rhythm between 14 and 40 Hz. Most characteristically: a rhythm from 14 to 40 Hz recorded over the fronto-central regions of the head during wakefulness. Amplitude of fronto-central beta rhythm varies but is mostly below 30 mV. Blocking or attenuation by contralateral movement or tactile stimulation is especially obvious in electrocorticograms. Other beta rhythms are most prominent in other locations or are diffuse.
- *Gamma:* Frequency band above 40 Hz.

Bibliography

N. J. Abbott, L. Rönnbäck, and E. Hansson. Astrocyte–endothelial interactions at the blood–brain barrier. *Nature Reviews Neuroscience*, 7(1):41–53, 2006.

S. Achard, R. Salvador, B. Whitcher, J. Suckling, and E. D. Bullmore. A resilient, low-frequency, small-world human brain functional network with highly connected association cortical hubs. *Journal of Neuroscience*, 26(1):63–72, 2006.

A. Aertsen, G. Gerstein, M. Habib, and G. Palm. Dynamics of neuronal firing correlation: modulation of" effective connectivity". *Journal of Neurophysiology*, 61(5):900–917, 1989.

G. Alexander. Parallel Organization of Functionally Segregated Circuits Linking Basal Ganglia and Cortex. *Annual Review of Neuroscience*, 9(1):357–381, 1986.

D. G. Amaral, C. M. Schumann, and C. W. Nordahl. Neuroanatomy of autism. *Trends in Neuroscience*, 31(3):137–145, 2008.

F. Amzica and M. Steriade. Electrophysiological correlates of sleep delta waves. *Electroencephalography and Clinical Neurophysiology*, 107(2):69–83, 1998.

R. G. Andrzejak, K. Lehnertz, F. Mormann, C. Rieke, P. David, and C. E. Elger. Indications of nonlinear deterministic and finite-dimensional structures in time series of brain electrical activity: Dependence on recording region and brain state. *Physical Review E*, 64(6), 2001.

H. Asperger. Die „autistischen psychopathen” im kindesalter. *European Archives of Psychiatry and Clinical Neuroscience*, 117(1):76–136, 1944.

N. Axmacher, M. M. Henseler, O. Jensen, I. Weinreich, C. E. Elger, and J. Fell. Cross-frequency coupling supports multi-item working memory in the human hippocampus. *Proceedings of the National Academy of Sciences USA*, 107(7):3228–3233, 2010.

A. Bailey, A. Le Couteur, I. Gottesman, P. Bolton, E. Simonoff, E. Yuzda, and M. Rutter. Autism as a strongly genetic disorder: evidence from a british twin study. *Psychological Medicine*, 25(1):63–77, 1995.

N. Barnea-Goraly, H. Kwon, V. Menon, S. Eliez, L. Lotspeich, and A. L. Reiss. White matter structure in autism: preliminary evidence from diffusion tensor imaging. *Biological Psychiatry*, 55(3):323–326, 2004.

Baron-Cohen. The extreme male brain theory of autism. *Trends in Cognitive Sciences*, 6 (6):248–254, 2002.

E. Başar, C. Başar-Eroglu, S. Karakaş, and M. Schürmann. Gamma, alpha, delta, and theta oscillations govern cognitive processes. *International Journal of Psychophysiology*, 39(2):241–248, 2001.

T. Bayes. An essay towards solving a problem in the doctrine of chances. *Philosophical Transactions of the Royal Society of London*, 53:370–418, 1763.

M. K. Belmonte, G. Allen, A. Beckel-Mitchener, L. M. Boulanger, R. a. Carper, and S. J. Webb. Autism and abnormal development of brain connectivity. *The Journal of Neuroscience*, 24(42):9228–9231, 2004.

J. S. Bendat and A. G. Piersol. Random data analysis and measurement techniques. *J. Wiley Interscience*, pages 134–135, 1986.

H. Berger. Ueber das Elektroenkephalogramm des Menschen. *Archiv Fur Psychiatrie Und Nervenkrankheiten*, 87:527–570, 1929.

H. Berger. Über das elektrenkephalogramm des menschen. *Archiv Fur Psychiatrie Und Nervenkrankheiten*, 94(1):16–60, 1931.

H. Berger. Über das elektrenkephalogramm des menschen. *Archiv Fur Psychiatrie Und Nervenkrankheiten*, 108(3):407–431, 1938.

S. Berkel, C. R. Marshall, B. Weiss, J. Howe, R. Roeth, U. Moog, V. Endris, W. Roberts, P. Szatmari, D. Pinto, M. Bonin, A. Riess, H. Engels, R. Sprengel, S. W. Scherer, and G. A. Rappold. Mutations in the SHANK2 synaptic scaffolding gene in autism spectrum disorder and mental retardation. *Nature Genetics*, 42(6):489–491, 2010.

L. Billeci, F. Sicca, K. Maharatna, F. Apicella, A. Narzisi, G. Campatelli, S. Calderoni, G. Pioggia, and F. Muratori. On the application of quantitative EEG for characterizing autistic brain: a systematic review. *Frontiers in Human Neuroscience*, 7:442, 2013.

M. Boersma, D. J. Smit, H. de Bie, G. C. M. Van Baal, D. I. Boomsma, E. J. de Geus, H. A. Delemarre-van de Waal, and C. J. Stam. Network analysis of resting state eeg in the developing young brain: structure comes with maturation. *Human Brain Mapping*, 32(3):413–425, 2011.

M. Boersma, C. Kemner, M. A. de Reus, G. Collin, T. M. Snijders, D. Hofman, J. K. Buitelaar, C. J. Stam, and M. P. van den Heuvel. Disrupted functional brain networks in autistic toddlers. *Brain Connectivity*, 3(1):41–9, 2013.

W. Bosl, A. Tierney, H. Tager-Flusberg, and C. Nelson. EEG complexity as a biomarker for autism spectrum disorder risk *BMC Medicine*, 9:18, 2011.

M. Breakspear and J. Terry. Detection and description of non-linear interdependence in normal multichannel human eeg data. *Clinical Neurophysiology*, 113(5):735–753, 2002.

A. Brovelli, M. Ding, A. Ledberg, Y. Chen, R. Nakamura, and S. L. Bressler. Beta oscillations in a large-scale sensorimotor cortical network: directional influences revealed by granger causality. *Proceedings of the National Academy of Sciences of the United States of America*, 101(26):9849–9854, 2004.

T. Brugha, S. Cooper, S. McManus, S. Purdon, J. Smith, F. Scott, N. Spiers, and F. Tryer. Estimating the prevalence of Autism Spectrum Conditions in adults: extending the 2007 adult psychiatric morbidity survey. *The NHS Information Centre for Health and Social Care*, pages 1–31, 2012.

A. Bruns, R. Eckhorn, H. Jokeit, and A. Ebner. Amplitude envelope correlation detects coupling among incoherent brain signals. *Neuroreport*, 11(7):1509–1514, 2000.

A. W. Buckley, R. Scott, A. Tyler, J. M. Mahoney, A. Thurm, C. Farmer, S. Swedo, S. A. Burroughs, and G. L. Holmes. State-dependent differences in functional connectivity in young children with autism spectrum disorder. *EBioMedicine*, 2(12):1905–1915, 2015.

S. Butterworth. On the theory of filter amplifiers. *Wireless Engineer*, 7(6):536–541, 1930.

G. Buzsáki. Theta rhythm of navigation: link between path integration and landmark navigation, episodic and semantic memory. *Hippocampus*, 15(7):827–840, 2005.

G. Buzsáki. *Rhythms of the Brain*. Oxford University Press, Oxford, 2006.

G. Buzsáki. Neural syntax: cell assemblies, synapsembles, and readers. *Neuron*, 68(3): 362–385, 2010.

G. Buzsáki and A. Draguhn. Neuronal oscillations in cortical networks. *Science*, 304: 1926–1929, 2004.

G. Buzsáki and X.-J. Wang. Mechanisms of Gamma Oscillations. *Annual Review of Neuroscience*, (35):203–225, 2012.

R. T. Canolty, E. Edwards, S. S. Dalal, M. Soltani, S. S. Nagarajan, H. E. Kirsch, M. S. Berger, N. M. Barbaro, and R. T. Knight. High gamma power is phase-locked to theta oscillations in human neocortex. *Science*, 313(5793):1626–1628, 2006.

D. S. Cantor, R. W. Thatcher, M. Hrybyk, and H. Kaye. Computerized EEG analyses of autistic children. *Journal of Autism and Developmental Disorders*, 16(2):169–187, 1986.

A. M. Carson, N. M. Salowitz, R. A. Scheidt, B. K. Dolan, and A. V. Van Hecke. Electroencephalogram coherence in children with and without autism spectrum disorders: decreased interhemispheric connectivity in autism. *Autism Research*, 7(3):334–343, 2014.

M. F. Casanova, D. P. Buxhoeveden, A. E. Switala, and E. Roy. Minicolumnar pathology in autism. *Neurology*, 58(3):428–432, 2002.

A. Catarino, O. Churches, S. Baron-Cohen, A. Andrade, and H. Ring. Atypical eeg complexity in autism spectrum conditions: a multiscale entropy analysis. *Clinical neurophysiology*, 122(12):2375–2383, 2011.

R. Caton. Electrical currents of the brain. *The Journal of Nervous and Mental Disease*, 2 (4):610, 1875.

A. S. Chan, S. L. Sze, and M.-C. Cheung. Quantitative electroencephalographic profiles for children with autistic spectrum disorder. *Neuropsychology*, 21(1):74–81, 2007.

A. S. Chan, Y. M. Y. Han, S. L. Sze, M.-c. Cheung, W. W.-m. Leung, R. C. K. Chan, and C. Y. To. Disordered connectivity associated with memory deficits in children with autism spectrum disorders. *Research in Autism Spectrum Disorders*, 5:237–245, 2011.

A. R. Clarke, R. J. Barry, A. Indraratna, F. E. Dupuy, R. McCarthy, and M. Selikowitz. EEG activity in children with Asperger's Syndrome. *Clinical Neurophysiology*, 127 (1):442–451, 2016.

P. Clemson, G. Lancaster, and A. Stefanovska. Reconstructing time-dependent dynamics. *Proceedings of IEEE*, 104(2):223–241, 2016.

R. Coben, A. R. Clarke, W. Hudspeth, and R. J. Barry. EEG power and coherence in autistic spectrum disorder. *Clinical Neurophysiology*, 119:1002–1009, 2008.

H. W. Cole and W. J. Ray. Eeg correlates of emotional tasks related to attentional demands. *International Journal of Psychophysiology*, 3(1):33–41, 1985.

E. Courchesne and K. Pierce. Brain overgrowth in autism during a critical time in development: Implications for frontal pyramidal neuron and interneuron development and connectivity. *International Journal of Developmental Neuroscience*, 23(2-3 SPEC. ISS.):153–170, 2005.

E. Courchesne, C. Karns, H. Davis, R. Ziccardi, R. Carper, Z. Tigue, H. Chisum, P. Moses, K. Pierce, C. Lord, et al. Unusual brain growth patterns in early life in patients with autistic disorder an mri study. *Neurology*, 57(2):245–254, 2001.

I. Daubechies. The wavelet transform, time-frequency localization and signal analysis. *IEEE Transactions on Information Theory*, 36(5):961–1005, 1990.

N. David, T. R. Schneider, I. Peiker, R. Al-Jawahiri, A. K. Engel, and E. Milne. Variability of cortical oscillation patterns: A possible endophenotype in autism spectrum disorders? *Neuroscience and Biobehavioral Reviews*, 71:590–600, 2016.

F. P. De Lange, O. Jensen, M. Bauer, and I. Toni. Interactions between posterior gamma and frontal alpha/beta oscillations during imagined actions. *Frontiers in Human Neuroscience*, 2, 2008.

S. De Rubeis, X. He, A. P. Goldberg, C. S. Poultney, K. Samocha, A. Ercument Cicek, Y. Kou, L. Liu, M. Fromer, S. Walker, T. Singh, L. Klei, J. Kosmicki, S.-C. Fu, B. Aleksic, M. Biscaldi, P. F. Bolton, J. M. Brownfeld, J. Cai, N. G. Campbell, A. Carracedo, M. H. Chahrour, A. G. Chiocchetti, H. Coon, E. L. Crawford, L. Crooks, S. R. Curran, G. Dawson, E. Duketis, B. A. Fernandez, L. Gallagher, E. Geller, S. J. Guter, R. Sean Hill, I. Ionita-Laza, P. Jimenez Gonzalez, H. Kilpinen, S. M. Klauck, A. Kolevzon, I. Lee, J. Lei, T. Lehtimäki, C.-F. Lin, A. Ma'ayan, C. R. Marshall, A. L. McInnes, B. Neale, M. J. Owen, N. Ozaki, M. Parellada, J. R. Parr, S. Purcell, K. Puura, D. Rajagopalan, K. Rehnström, A. Reichenberg, A. Sabo, M. Sachse, S. J. Sanders, C. Schafer, M. Schulte-Rüther, D. Skuse, C. Stevens, P. Szatmari, K. Tammimies, O. Valladares, A. Voran, L.-S. Wang, L. A. Weiss, A. Jeremy Willsey, T. W. Yu, R. K. C. Yuen, E. H. Cook, C. M. Freitag, M. Gill, C. M. Hultman, T. Lehner,

A. Palotie, G. D. Schellenberg, P. Sklar, M. W. State, J. S. Sutcliffe, C. A. Walsh, S. W. Scherer, M. E. Zwick, J. C. Barrett, D. J. Cutler, K. Roeder, B. Devlin, M. J. Daly, and J. D. Buxbaum. Supple: Synaptic, transcriptional and chromatin genes disrupted in autism. *Nature*, 515(7526):209–215, 2014.

G. Deco, V. K. Jirsa, P. a. Robinson, M. Breakspear, and K. Friston. The dynamic brain: From spiking neurons to neural masses and cortical fields. *PLoS Computational Biology*, 4(8), 2008.

A. Delorme and S. Makeig. Eeglab: an open source toolbox for analysis of single-trial eeg dynamics including independent component analysis. *Journal of Neuroscience Methods*, 134(1):9–21, 2004.

R. E. Dolmetsch, R. S. Lewis, C. C. Goodnow, and J. I. Healy. Differential activation of transcription factors induced by Ca^{2+} response amplitude and duration. *Nature*, 386: 855–858, 1997.

L. G. Domínguez, J. Stieben, J. L. P. Velázquez, and S. Shanker. The imaginary part of coherency in autism: differences in cortical functional connectivity in preschool children. *PLoS One*, 8(10):e75941, 2013.

J. F. Donges, Y. Zou, N. Marwan, and J. Kurths. The backbone of the climate network. *EPL*, 87(4):48007, 2009.

A. P. A. Donovan and M. A. Basson. The neuroanatomy of autism - a developmental perspective. *Journal of Anatomy*, 44:4–15, 2016.

F. H. Duffy and H. Als. A stable pattern of EEG spectral coherence distinguishes children with autism from neuro-typical controls - a large case control study. *BMC Medicine*, 10(1):64, 2012.

A. Duggento, T. Stankovski, P. V. E. McClintock, and A. Stefanovska. Dynamical Bayesian inference of time-evolving interactions: From a pair of coupled oscillators to networks of oscillators. *Physical Review E*, 86:061126, 2012.

C. M. Durand, C. Betancur, T. M. Boeckers, J. Bockmann, P. Chaste, F. Fauchereau, G. Nygren, M. Rastam, I. C. Gillberg, H. Anckarsäter, E. Sponheim, H. Goubran-Botros, R. Delorme, N. Chabane, M.-C. Mouren-Simeoni, P. de Mas, E. Bieth, B. Rogé, D. Héron, L. Burglen, C. Gillberg, M. Leboyer, T. Bourgeron, I. Carina, H. Anckarsäter, E. Sponheim, H. Goubran-Botros, R. Delorme, N. Chabane, P. D. Mas, E. Bieth, B. Rogé, D. Héron, L. Burglen, C. Gillberg, I. C. Gillberg, H. Anckarsäter, E. Sponheim, H. Goubran-Botros, R. Delorme, N. Chabane, M.-C. Mouren-Simeoni, P. de Mas, E. Bieth, B. Rogé, D. Héron, L. Burglen, C. Gillberg, M. Leboyer, and T. Bourgeron. Mutations in the gene encoding the synaptic scaffolding protein SHANK3 are associated with autism spectrum disorders. *Nature Genetics*, 39(1):25–27, 2007.

M. E. E. Orekova, T. Stroganova, G. Nygren, I. Posikera, C. Gillberg. High frequency activuty in ongoing EEG from young children with autism: A two sample study. *Clinical Neurophysiology*, 117:217–218, 2006.

H. Elhabashy, O. Raafat, L. Afifi, H. Raafat, K. Abdullah, et al. Quantitative eeg in autistic children. *The Egyptian Journal of Neurology, Psychiatry and Neurosurgery*, 52(3):176, 2015.

G. N. Elston. Cortex, cognition and the cell: new insights into the pyramidal neuron and prefrontal function. *Cerebral Cortex*, 13(11):1124–1138, 2003.

A. K. Engel and P. Fries. Beta-band oscillations—signalling the status quo? *Current Opinion in Neurobiology*, 20(2):156–165, 2010.

A. K. Engel, P. Fries, and W. Singer. Dynamic predictions: oscillations and synchrony in top-down processing. *Nature Reviews Neuroscience*, 2(10):704–716, 2001.

L. Faes, D. Marinazzo, F. Jurysta, and G. Nollo. Linear and non-linear brain–heart and brain–brain interactions during sleep. *Physiological Measurement*, 36(4):683–698, 2015.

S. H. Fatemi, A. V. Snow, J. M. Stary, M. Araghi-Niknam, T. J. Reutiman, S. Lee, A. I. Brooks, and D. A. Pearce. Reelin signaling is impaired in autism. *Biological Psychiatry*, 57(7):777–787, 2005.

B. Feige, K. Scheffler, F. Esposito, D. S. Francesco, J. Hennig, and E. Seifritz. Cortical and subcortical correlates of electrocephalographic alpha rhythm modulation. *Journal of Neurophysiology*, 93:2864–2872, 2004.

M. Ferrari and V. Quaresima. A brief review on the history of human functional near-infrared spectroscopy (fnirs) development and fields of application. *Neuroimage*, 63 (2):921–935, 2012.

J. Fourier. *Analytical theory of heat, by M. Fourier*. At Firmin Didot, p, 1822.

K. Friston, R. Moran, and A. K. Seth. Analysing connectivity with Granger causality and dynamic causal modelling. *Current Opinion in Neurobiology*, 23(2):172–178, 2013.

K. J. Friston. Functional and effective connectivity: a review. *Brain Connectivity*, 1(1): 13–36, 2011.

K. J. Friston, A. P. Holmes, C. Price, C. Büchel, and K. Worsley. Multisubject fmri studies and conjunction analyses. *Neuroimage*, 10(4):385–396, 1999.

K. J. Friston, L. Harrison, and W. Penny. Dynamic causal modelling. *Neuroimage*, 19(4): 1273–1302, 2003.

D. Gabor. Theory of communication. *Journal of IEEE*, 93:429–457, 1946.

J. D. Gibbons and S. Chakraborti. Nonparametric statistical inference. In *International Encyclopedia of Statistical Science*, pages 977–979. Springer, 2011.

S. R. Gilman, I. Iossifov, D. Levy, M. Ronemus, M. Wigler, and D. Vitkup. Rare De Novo Variants Associated with Autism Implicate a Large Functional Network of Genes Involved in Formation and Function of Synapses. *Neuron*, 70(5):898–907, 2011.

R. I. Goldman, J. M. Stern, J. Engel Jr, and M. S. Cohen. Simultaneous eeg and fmri of the alpha rhythm. *Neuroreport*, 13(18):2487, 2002.

M. Gomot and B. Wicker. A challenging, unpredictable world for people with autism spectrum disorder. *International Journal of Psychophysiology*, 83(2):240–247, 2012.

K. Gotham, A. Pickles, and C. Lord. Standardizing ados scores for a measure of severity in autism spectrum disorders. *Journal of Autism and Developmental Disorders*, 39(5): 693–705, 2009.

C. W. Granger. Investigating causal relations by econometric models and cross-spectral methods. *Econometrica*, pages 424–438, 1969.

O. Gurau, W. J. Bosl, and C. R. Newton. How useful is electroencephalography in the diagnosis of autism spectrum disorders and the delineation of subtypes: A systematic review. *Frontiers in Psychiatry*, 8, 2017.

S. Haar, S. Berman, M. Behrmann, and I. Dinstein. Anatomical Abnormalities in Autism? *Cerebral Cortex*, 26(4):1440–1452, 2016.

D. Hagemann, E. Naumann, and J. F. Thayer. The quest for the eeg reference revisited: A glance from brain asymmetry research. *Psychophysiology*, 38(5):847–857, 2001.

A. Hahamy, M. Behrmann, and R. Malach. The idiosyncratic brain: distortion of spontaneous connectivity patterns in autism spectrum disorder. *Nature Neuroscience*, 18(2): 302–309, 2015.

H. C. Hazlett, M. Poe, G. Gerig, R. G. Smith, J. Provenzale, A. Ross, J. Gilmore, and J. Piven. Magnetic resonance imaging and head circumference study of brain size in autism: birth through age 2 years. *Archives of General Psychiatry*, 62(12):1366–1376, 2005.

H. C. Hazlett, H. Gu, B. C. Munsell, S. H. Kim, M. Styner, J. J. Wolff, J. T. Elison, M. R. Swanson, H. Zhu, K. N. Botteron, D. L. Collins, J. N. Constantino, S. R. Dager, A. M. Estes, A. C. Evans, V. S. Fonov, G. Gerig, P. Kostopoulos, R. C. McKinstry, J. Pandey,

S. Paterson, J. R. Pruett, R. T. Schultz, D. W. Shaw, L. Zwaigenbaum, J. Piven, J. Piven, H. C. Hazlett, C. Chappell, S. R. Dager, A. M. Estes, D. W. Shaw, K. N. Botteron, R. C. McKinstry, J. N. Constantino, J. R. Pruett Jr, R. T. Schultz, S. Paterson, L. Zwaigenbaum, J. T. Elison, J. J. Wolff, A. C. Evans, D. L. Collins, G. B. Pike, V. S. Fonov, P. Kostopoulos, S. Das, G. Gerig, M. Styner, and C. H. Gu. Early brain development in infants at high risk for autism spectrum disorder. *Nature*, 542(7641):348–351, 2017.

S. Hu, M. Stead, Q. Dai, and G. A. Worrell. On the recording reference contribution to eeg correlation, phase synchorony, and coherence. *IEEE Transactions on Systems, Man, and Cybernetics, Part B (Cybernetics)*, 40(5):1294–1304, 2010.

W. J. Hudspeth and K. H. Pribram. Psychophysiological indices of cerebral maturation. *International Journal of Psychophysiology*, 12(1):19–29, 1992.

C. Huygens. Horologium oscillatorium sive de motu pendulorum. *Muguet*, 1673.

D. Iatsenko, A. Bernjak, T. Stankovski, Y. Shiogai, P. J. Owen-Lynch, P. B. M. Clarkson, P. V. E. McClintock, and A. Stefanovska. Evolution of cardio-respiratory interactions with age. *Philosophical Transactions of the Royal Society of London*, 371(1997): 20110622, 2013.

D. Iatsenko, P. V. McClintock, and A. Stefanovska. Linear and synchrosqueezed time–frequency representations revisited: Overview, standards of use, resolution, reconstruction, concentration, and algorithms. *Digital Signal Processing*, 42:1–26, 2015.

M. Ingalhalikar, A. Smith, D. Parker, T. D. Satterthwaite, M. A. Elliott, K. Ruparel, H. Hakonarson, R. C. R. E. R. C. R. E. Gur, R. C. R. E. R. C. R. E. Gur, and R. Verma. Sex differences in the structural connectome of the human brain. *Proceedings of the National Academy of Sciences of the United States of America*, 111(2):823–828, 2014.

J. R. Isler, P. G. Grieve, D. Czernochowski, R. I. Stark, and D. Friedman. Cross-frequency phase coupling of brain rhythms during the orienting response. *Brain Research*, 1232: 163–172, 2008.

H. H. Jasper and H. L. Andrews. Electro-encephalography: Iii. normal differentiation of occipital and precentral regions in man. *Archives of Neurology & Psychiatry*, 39(1): 96–115, 1938.

O. Jensen and L. L. Colgin. Cross-frequency coupling between neuronal oscillations. *Trends Cognit. Sci.*, 11(7):267–269, 2007.

O. Jensen and A. Mazaheri. Shaping functional architecture by oscillatory alpha activity: gating by inhibition. *Frontiers in Human Neuroscience*, 4, 2010.

O. Jensen and C. D. Tesche. Frontal theta activity in humans increases with memory load in a working memory task. *European Journal of Neuroscience*, 15(8):1395–1399, 2002.

V. Jirsa and V. Müller. Cross-frequency coupling in real and virtual brain networks. *Frontiers in Computational Neuroscience*, 7:78, 2013.

E. G. Jones. Microcolumns in the cerebral cortex. *Proceedings of the National Academy of Sciences*, 97(10):5019–5021, 2000.

M. A. Just, V. L. Cherkassky, T. a. Keller, and N. J. Minshew. Cortical activation and synchronization during sentence comprehension in high-functioning autism: Evidence of underconnectivity. *Brain*, 127:1811–1821, 2004.

E. R. Kandel, J. H. Schwartz, T. M. Jessell, S. A. Siegelbaum, A. J. Hudspeth, et al. *Principles of Neural Science*, volume 4. McGraw-hill New York, 2000.

B. Keehn, V. Vogel-Farley, H. Tager-Flusberg, and C. A. Nelson. Atypical hemispheric specialization for faces in infants at risk for autism spectrum disorder. *Autism Research*, 8(2):187–198, 2015.

C. J. Keylock. Constrained surrogate time series with preservation of the mean and variance structure. *Physical Review E - Statistical, Nonlinear, and Soft Matter Physics*, 73 (3):2–5, 2006.

S. Khan, A. Gramfort, N. R. Shetty, M. G. Kitzbichler, S. Ganesan, J. M. Moran, S. M. Lee, J. D. E. Gabrieli, H. B. Tager-Flusberg, R. M. Joseph, M. R. Herbert, M. S. Hämäläinen, and T. Kenet. Local and long-range functional connectivity is reduced in concert in autism spectrum disorders. *Proceedings of the National Academy of Sciences of the United States of America*, 110(8):3107–3112, 2013.

I. Z. Kiss, Y. Zhai, and J. L. Hudson. Predicting mutual entrainment of oscillators with experiment-based phase models. *Physical Review Letters*, 94:248301, Jun 2005.

W. Klimesch. EEG alpha and theta oscillations reflect cognitive and memory performance: a review and analysis. *Brain Research Reviews*, 29(2):169–195, 1999.

W. Klimesch, P. Sauseng, and S. Hanslmayr. EEG alpha oscillations: the inhibition–timing hypothesis. *Brain Research Reviews*, 53(1):63–88, 2007.

B. Kralemann, L. Cimponeriu, M. Rosenblum, A. Pikovsky, and R. Mrowka. Phase dynamics of coupled oscillators reconstructed from data. *Physical Review E*, 77(6, Part 2):066205, 2008.

B. Kralemann, A. Pikovsky, and M. Rosenblum. Reconstructing phase dynamics of oscillator networks. *Chaos*, 21:025104, 2011.

B. Kralemann, M. Frühwirth, A. Pikovsky, M. Rosenblum, T. Kenner, J. Schaefer, and M. Moser. In vivo cardiac phase response curve elucidates human respiratory heart rate variability. *Nature Communications*, 4:2418, 2013.

Y. Kuramoto. *Chemical Oscillations, Waves, and Turbulence*. Springer-Verlag, Berlin, 1984.

J.-P. Lachaux, N. George, C. Tallon-Baudry, J. Martinerie, L. Hugueville, L. Minotti, P. Kahane, and B. Renault. The many faces of the gamma band response to complex visual stimuli. *Neuroimage*, 25(2):491–501, 2005.

H. Laufs, A. Kleinschmidt, A. Beyerle, E. Eger, A. Salek-Haddadi, C. Preibisch, and K. Krakow. EEG-correlated fMRI of human alpha activity. *NeuroImage*, 19(4):1463–1476, 2003.

V. V. Lazarev, A. Pontes, A. A. Mitrofanov, et al. Reduced interhemispheric connectivity in childhood autism detected by electroencephalographic photic driving coherence. *Journal of Autism and Developmental Disorders*, 45(2):537–547, 2015.

K. Lehnertz and C. Elger. Spatio-temporal dynamics of the primary epileptogenic area in temporal lobe epilepsy characterized by neuronal complexity loss. *Electroencephalography and Clinical Neurophysiology*, 95(2):108–117, 1995.

K. Lehnertz, G. Ansmann, S. Bialonski, H. Dickten, C. Geier, and S. Porz. Evolving networks in the human epileptic brain. *Physica D*, 267:7–15, 2014.

R. R. Llinás. The intrinsic electrophysiological properties of mammalian neurons: insights into central nervous system function. *Science*, 242(4886):1654–1664, 1988.

R. R. Llinas, A. A. Grace, and Y. Yarom. In vitro neurons in mammalian cortical layer 4 exhibit intrinsic oscillatory activity in the 10-to 50-hz frequency range. *Proceedings of the National Academy of Sciences*, 88(3):897–901, 1991.

C. Lord, M. Rutter, S. Goode, J. Heemsbergen, H. Jordan, L. Mawhood, and E. Schopler. Austism diagnostic observation schedule: A standardized observation of communicative and social behavior. *Journal of Autism and Developmental Disorders*, 19(2):185–212, 1989.

C. Lord, M. Rutter, and A. Le Couteur. Autism diagnostic interview-revised: a revised version of a diagnostic interview for caregivers of individuals with possible pervasive developmental disorders. *Journal of Autism and Developmental Disorders*, 24(5):659–685, 1994.

C. Lord, S. Risi, L. Lambrecht, E. H. Cook, B. L. Leventhal, P. C. DiLavore, A. Pickles, and M. Rutter. The autism diagnostic observation schedule—generic: A standard measure of social and communication deficits associated with the spectrum of autism. *Journal of Autism and Developmental Disorders*, 30(3):205–223, 2000.

R. Lowry. Concepts and applications of inferential statistics. 2014.

E. Lushchekina, O. Y. Khaerdinova, V. Y. Novototskii-Vlasov, V. Lushchekin, and V. Strelets. Synchronization of eeg rhythms in baseline conditions and during counting in children with autism spectrum disorders. *Neuroscience and Behavioral Physiology*, 46(4):382, 2016.

E. A. Lushchekina, E. D. Podreznaya, V. S. Lushchekin, and V. B. Strelets. A comparative EEG study in normal and autistic children. *Neuroscience and Behavioral Physiology*, 42(3):236–243, 2012.

D. Q. Ma, P. L. Whitehead, M. M. Menold, E. R. Martin, A. E. Ashley-Koch, H. Mei, M. D. Ritchie, G. R. Delong, R. K. Abramson, H. H. Wright, M. L. Cuccaro, J. P. Hussman, J. R. Gilbert, and M. A. Pericak-Vance. Identification of significant association and gene-gene interaction of GABA receptor subunit genes in autism. *The American Journal of Human Genetics*, 77(3):377–388, 2005.

C. Machado, M. Estévez, G. Leisman, R. Melillo, R. Rodríguez, P. DeFina, A. Hernández, J. Pérez-Nellar, R. Naranjo, M. Chinchilla, et al. Qeeg spectral and coherence assessment of autistic children in three different experimental conditions. *Journal of Autism and Developmental Disorders*, 45(2):406–424, 2015.

D. Mantini, M. G. G. Perrucci, C. Del Gratta, G. L. L. Romani, M. Corbetta, D. Gratta, R. C., G.l, M. Corbetta, C. Del Gratta, G. L. L. Romani, M. Corbetta, D. Gratta, R. C., G.l, M. Corbetta, C. Del Gratta, G. L. L. Romani, G. C. Del, G. L. L. Romani, and M. Corbetta. Electrophysiological signatures of resting state networks in the human brain. *Proceedings of the National Academy of Sciences of the United States of America*, 104(32):13170–13175, 2007.

M. C. Marchetto, H. Belinson, Y. Tian, B. C. Freitas, C. Fu, K. Vadodaria, P. Beltrao-Braga, C. A. Trujillo, A. P. Mendes, K. Padmanabhan, et al. Altered proliferation and networks in neural cells derived from idiopathic autistic individuals. *Molecular Psychiatry*, 2016.

D. Marinazzo, M. Pellicoro, and S. Stramaglia. Kernel method for nonlinear granger causality. *Physical Review Letters*, 100(14):144103, 2008.

D. Marinazzo, W. Liao, H. Chen, and S. Stramaglia. Nonlinear connectivity by granger causality. *Neuroimage*, 58(2):330–338, 2011.

H. Markram, M. Toledo-Rodriguez, Y. Wang, A. Gupta, G. Silberberg, and C. Wu. Interneurons of the neocortical inhibitory system. *Nature Reviews Neuroscience*, 5(10): 793, 2004.

P. J. Marshall, Y. Bar-Haim, and N. A. Fox. Development of the eeg from 5 months to 4 years of age. *Clinical Neurophysiology*, 113(8):1199–1208, 2002.

S. Matlis, K. Boric, C. J. Chu, and M. A. Kramer. Robust disruptions in electroencephalogram cortical oscillations and large-scale functional networks in autism. *BMC Neurology*, 15(1):97, 2015.

D. J. McFarland, L. a. Miner, T. M. Vaughan, and J. R. Wolpaw. Mu and beta rhythm topographies during motor imagery and actual movements. *Brain Topography*, 12(3): 177–186, 2000.

K. Mezeiová and M. Paluš. Comparison of coherence and phase synchronization of the human sleep electroencephalogram. *Clinical Neurophysiology*, 123(9):1821–1830, 2012.

C. M. Michel and M. M. Murray. Towards the utilization of eeg as a brain imaging tool. *Neuroimage*, 61(2):371–385, 2012.

F. A. Middleton and P. L. Strick. Basal ganglia and cerebellar loops: Motor and cognitive circuits. *Brain Research Reviews*, 31(2-3):236–250, 2000.

W. H. Miltner, C. Braun, M. Arnold, H. Witte, and E. Taub. Coherence of gamma-band EEG activity as a basis for associative learning. *Nature*, 397(6718):434–436, 1999.

R. E. Mirollo and S. H. Strogatz. Synchronization of pulse-coupled biological oscillators. *SIAM Journal on Applied Mathematics*, 50(6):1645–1662, 1990.

J. Miyazaki and S. Kinoshita. Determination of a coupling function in multicoupled oscillators. *Physical Review Letters*, 96:194101, May 2006.

I. Mohammad-Rezazadeh, J. Frohlich, S. K. Loo, and S. S. Jeste. Brain Connectivity in Autism Spectrum Disorder. *Current Opinion in Neurology*, 29(2):137–147, 2016.

F. Mormann, K. Lehnertz, P. David, and C. E. Elger. Mean phase coherence as a measure for phase synchronization and its application to the EEG of epilepsy patients. *Physica D: Nonlinear Phenomena*, 144(3):358–369, 2000.

M. M. Müller, T. Gruber, and A. Keil. Modulation of induced gamma band activity in the human eeg by attention and visual information processing. *International Journal of Psychophysiology*, 38(3):283–299, 2000.

M. Murias, S. J. Webb, J. Greenson, and G. Dawson. Resting state cortical connectivity reflected in eeg coherence in individuals with autism. *Biological Psychiatry*, 62(3): 270–273, 2007.

E. Niedermeyer and F. L. da Silva. *Electroencephalography: basic principles, clinical applications, and related fields*. Lippincott Williams & Wilkins, 2005.

G. Nolte, O. Bai, L. Wheaton, Z. Mari, S. Vorbach, and M. Hallett. Identifying true brain interaction from EEG data using the imaginary part of coherency. *Clinical Neurophysiology*, 115(10):2292–2307, 2004.

P. L. Nunez, R. Srinivasan, A. F. Westdorp, R. S. Wijesinghe, D. M. Tucker, R. B. Silberstein, and P. J. Cadusch. Eeg coherency: I: statistics, reference electrode, volume conduction, laplacians, cortical imaging, and interpretation at multiple scales. *Electroencephalography and Clinical Neurophysiology*, 103(5):499–515, 1997.

E. V. Orekhova, T. A. Stroganova, G. Nygren, M. M. Tsetlin, I. N. Posikera, C. Gillberg, and M. Elam. Excess of High Frequency Electroencephalogram Oscillations in Boys with Autism. *Biological Psychiatry*, 62(9):1022–1029, 2007.

E. V. Orekhova, M. Elsabbagh, E. J. Jones, G. Dawson, T. Charman, and M. H. Johnson. Eeg hyper-connectivity in high-risk infants is associated with later autism. *Journal of Neurodevelopmental Disorders*, 6(1):40, 2014.

A. B. Oro, M. E. Navarro-Calvillo, and C. Esmer. Autistic behavior checklist (abc) and its applications. In *Comprehensive Guide to Autism*, pages 2787–2798. Springer, 2014.

S. Ozonoff, B. L. Goodlin-Jones, and M. Solomon. Evidence-based assessment of autism spectrum disorders in children and adolescents. *Journal of Clinical Child and Adolescent Psychology*, 34(3):523–540, 2005.

S. Ozonoff, A.-M. Iosif, F. Baguio, I. C. Cook, M. M. Hill, T. Hutman, S. J. Rogers, A. Rozga, S. Sangha, M. Sigman, et al. A prospective study of the emergence of early behavioral signs of autism. *Journal of the American Academy of Child & Adolescent Psychiatry*, 49(3):256–266, 2010.

S. J. Palmen, H. van Engeland, P. R. Hof, and C. Schmitz. Neuropathological findings in autism. *Brain*, 127(12):2572–2583, 2004.

A. Parent and L. N. Hazrati. Functional anatomy of the basal ganglia. *Revista de Neurologia*, 25 Suppl 2:S121–S128, 1995.

T. Parks and J. McClellan. Chebyshev approximation for nonrecursive digital filters with linear phase. *IEEE Transactions on Circuit Theory*, 19(2):189–194, 1972.

R. Parri and V. Crunelli. An astrocyte bridge from synapse to blood flow. *Nature Neuroscience*, 6(1):5–6, 2003.

W. D. Penny, V. Litvak, L. Fuentemilla, E. Duzel, and K. Friston. Dynamic causal models for phase coupling. *Journal of Neuroscience Methods*, 183(1):19–30, 2009.

G. Pfurtscheller and A. Aranibar. Event-related cortical desynchronization detected by power measurements of scalp eeg. *Electroencephalography and Clinical Neurophysiology*, 42(6):817–826, 1977.

A. Pikovsky, M. Rosenblum, and J. Kurths. *Synchronization – A Universal Concept in Nonlinear Sciences*. Cambridge University Press, Cambridge, 2001.

N. Pop-Jordanova, T. Zorcec, A. Demerdzieva, and Z. Gucev. QEEG characteristics and spectrum weighted frequency for children diagnosed as autistic spectrum disorder. *Nonlinear Biomedical Physics*, 4:4, 2010.

Y. Qin, P. Xu, and D. Yao. A comparative study of different references for eeg default mode network: the use of the infinity reference. *Clinical Neurophysiology*, 121(12): 1981–1991, 2010.

G. Righi, A. L. Tierney, H. Tager-Flusberg, and C. A. Nelson. Functional connectivity in the first year of life in infants at risk for autism spectrum disorder: An EEG study. *PLoS ONE*, 9(8):1–8, 2014.

E. Rodriguez, N. George, J. P. Lachaux, J. Martinerie, B. Renault, and F. J. Varela. Perception's shadow: long distance synchronization of human brain activity. *Nature*, 397 (6718):430–433, 1999.

M. Ronemus, I. Iossifov, D. Levy, and M. Wigler. The role of de novo mutations in the genetics of autism spectrum disorders. *Nature Reviews Genetics*, 15(2):133–141, 2014.

M. G. Rosenblum and A. S. Pikovsky. Detecting direction of coupling in interacting oscillators. *Physical Review E*, 64(4):045202, 2001.

M. G. Rosenblum, L. Cimponeriu, A. Bezerianos, A. Patzak, and R. Mrowka. Identification of coupling direction: Application to cardiorespiratory interaction. *Physical Review E*, 65(4):041909, 2002.

J. L. R. Rubenstein and M. M. Merzenich. Model of autism: increased ratio of excitation/inhibition in key neural systems. *Genes, Brain, and Behavior*, 2:255–267, 2003.

P. Sauseng, W. Klimesch, W. Stadler, M. Schabus, M. Doppelmayr, S. Hanslmayr, W. R. Gruber, and N. Birbaumer. A shift of visual spatial attention is selectively associated with human eeg alpha activity. *European Journal of Neuroscience*, 22(11):2917–2926, 2005.

B. Schack, N. Vath, H. Petsche, H.-G. Geissler, and E. Möller. Phase-coupling of theta–gamma eeg rhythms during short-term memory processing. *International Journal of Psychophysiology*, 44(2):143–163, 2002.

T. Schreiber and H. Kantz. Predictability of complex dynamical systems. In *Observing and Predicting Chaotic Signals*. Springer, New York, 2003.

T. Schreiber and A. Schmitz. Surrogate time series. *Physica D*, 142(3-4):346–382, 2000.

C. M. Schumann, C. S. Bloss, C. C. Barnes, G. M. Wideman, R. A. Carper, N. Akshoomoff, K. Pierce, D. Hagler, N. Schork, C. Lord, et al. Longitudinal magnetic resonance imaging study of cortical development through early childhood in autism. *Journal of Neuroscience*, 30(12):4419–4427, 2010.

S. Schwartz, R. Kessler, T. Gaughan, and A. W. Buckley. EEG Coherence Patterns in Autism: An Updated Review. *Pediatric Neurology*, 2016.

A. Sheikhani, H. Behnam, M. Noroozian, M. R. Mohammadi, and M. Mohammadi. Abnormalities of quantitative electroencephalography in children with Asperger disorder in various conditions. *Research in Autism Spectrum Disorders*, 3(2):538–546, 2009.

A. Sheikhani, H. Behnam, M. R. Mohammadi, M. Noroozian, and M. Mohamamadi. Detection of abnormalities for diagnosing of children with autism disorders using of quantitative electroencephalography analysis. *Journal of Medical Systems*, 36:957–963, 2012.

L. W. Sheppard, A. Stefanovska, and P. V. E. McClintock. Detecting the harmonics of oscillations with time-variable frequencies. *Physical Review E*, 83:016206, 2011.

L. W. Sheppard, A. Stefanovska, and P. V. E. McClintock. Testing for time-localised coherence in bivariate data. *Physical Review E*, 85:046205, 2012.

V. N. Smelyanskiy, D. G. Luchinsky, A. Stefanovska, and P. V. E. McClintock. Inference of a nonlinear stochastic model of the cardiorespiratory interaction. *Physical Review Letters*, 94(9):098101, 2005.

R. L. Spitzer and J. B. Williams. Diagnostic and statistical manual of mental disorders. In *American Psychiatric Association*. Citeseer, 1980.

C. J. Stam, G. Nolte, and A. Daffertshofer. Phase lag index: Assessment of functional connectivity from multi channel EEG and MEG with diminished bias from common sources. *Human Brain Mapping*, 28(11):1178–1193, 2007.

T. Stankovski. Time-varying coupling functions: Dynamical inference and cause of synchronization transitions. *Physical Review E*, 95(2):022206, 2017.

T. Stankovski, A. Duggento, P. V. E. McClintock, and A. Stefanovska. Inference of time-evolving coupled dynamical systems in the presence of noise. *Physical Review Letters*, 109:024101, 2012.

T. Stankovski, A. Duggento, P. V. E. McClintock, and A. Stefanovska. A tutorial on time-evolving dynamical Bayesian inference. *European Physical Journal – Special Topics*, 223(13):2685–2703, 2014a.

T. Stankovski, P. V. E. McClintock, and A. Stefanovska. Coupling functions enable secure communications. *Physical Review X*, 4:011026, 2014b.

T. Stankovski, V. Ticcinelli, P. V. E. McClintock, and A. Stefanovska. Coupling functions in networks of oscillators. *New Journal of Physics*, 17(3):035002, 2015.

T. Stankovski, T. Pereira, P. V. E. McClintock, and A. Stefanovska. Coupling functions: Universal insights into dynamical interaction mechanisms. *Reviews of Modern Physics*,89(4):045001/, 2017b.

T. Stankovski, V. Ticcinelli, P. V. E. McClintock, and A. Stefanovska. Neural cross-frequency coupling functions. *Frontiers in Systems Neuroscience*, 11(33): 10.3389/fnsys.2017.00033, 2017b.

A. Stefanovska, M. Bračič, and H. D. Kvernmo. Wavelet analysis of oscillations in the peripheral blood circulation measured by laser Doppler technique. *IEEE Transactions on Biomedical Engineering*, 46(10):1230–1239, 1999.

M. Steriade. Impact of network activities on neuronal properties in corticothalamic systems. *Journal of Neurophysiology*, 86(1):1–39, 2001.

T. A. Stroganova, E. V. Orekhova, and I. N. Posikera. Eeg alpha rhythm in infants. *Clinical Neurophysiology*, 110(6):997–1012, 1999.

T. A. Stroganova, G. Nygren, M. M. Tsetlin, I. N. Posikera, C. Gillberg, M. Elam, and E. V. Orekhova. Abnormal EEG lateralization in boys with autism. *Clinical Neurophysiology*, 118:1842–1854, 2007.

S. H. Strogatz. Exploring complex networks. *Nature*, 410:268–276, 2001.

W. Sun and Y. Dan. Layer-specific network oscillation and spatiotemporal receptive field in the visual cortex. *Proceedings of the National Academy of Sciences*, 106(42):17986–17991, 2009.

Y. F. Suprunenko, P. T. Clemson, and A. Stefanovska. Chronotaxic systems: A new class of self-sustained nonautonomous oscillators. *Physical Review Letters*, 111(2):024101, 2013.

C. Tallon-Baudry and O. Bertrand. Oscillatory gamma activity in humans and its role in object representation. *Trends in Cognitive Sciences*, 3(4):151–162, 1999.

C. Tesche and J. Karhu. Theta oscillations index human hippocampal activation during a working memory task. *Proceedings of the National Academy of Sciences*, 97(2): 919–924, 2000.

J. Theiler, S. Eubank, A. Longtin, B. Galdrikian, and J. Farmer. Testing for nonlinearity in time series: the method of surrogate data. *Physica D*, 58(1–4):77–94, 1992.

D. J. Thomson et al. Multitaper analysis of nonstationary and nonlinear time series data. *Nonlinear and Nonstationary Signal Processing*, pages 317–394, 2000.

V. Ticcinelli, T. Stankovski, D. Iatsenko, A. Bernjak, A. E. Bradbury, A. R. Gallagher, P. Clarkson, P. V. McClintock, and A. Stefanovska. Coherence and coupling functions reveal microvascular impairment in treated hypertension. *Frontiers in Physiology*, 8: 749, 2017.

A. L. Tierney, L. Gabard-Durnam, V. Vogel-Farley, H. Tager-Flusberg, and C. a. Nelson. Developmental trajectories of resting eeg power: An endophenotype of autism spectrum disorder. *PLoS ONE*, 7(6), 2012.

I. T. Tokuda, S. Jain, I. Z. Kiss, and J. L. Hudson. Inferring phase equations from multivariate time series. *Physical Review Letters*, 99:064101, Aug 2007.

A. B. Tort, R. Komorowski, H. Eichenbaum, and N. Kopell. Measuring phase-amplitude coupling between neuronal oscillations of different frequencies. *Journal of Neurophysiology*, 104(2):1195–1210, 2010.

R. Tuchman and I. Rapin. Epilepsy in autism. *The Lancet Neurology*, 1(6):352–358, 2002.

D. C. Van Essen, K. Ugurbil, E. Auerbach, D. Barch, T. Behrens, R. Bucholz, A. Chang, L. Chen, M. Corbetta, S. W. Curtiss, et al. The human connectome project: a data acquisition perspective. *Neuroimage*, 62(4):2222–2231, 2012.

F. Varela, J.-P. Lachaux, E. Rodriguez, and J. Martinerie. The brainweb: phase synchronization and large-scale integration. *Nature Reviews Neuroscience*, 2(4):229–239, 2001.

M. Vejmelka and M. Paluš. Inferring the directionality of coupling with conditional mutual information. *Physical Review E*, 77(2):026214, 2008.

R. Vicente, M. Wibral, M. Lindner, and G. Pipa. Transfer entropy—a model-free measure of effective connectivity for the neurosciences. *Journal of Computational Neuroscience*, 30(1):45–67, 2011.

A. von Stein, C. Chiang, and P. Konig. Top-down processing mediated by interareal synchronization. *Proceedings of the National Academy of Sciences*, 97(26):14748–14753, 2000.

B. Voytek, R. T. Canolty, A. Shestyuk, N. E. Crone, J. Parvizi, and R. T. Knight. Shifts in gamma phase–amplitude coupling frequency from theta to alpha over posterior cortex during visual tasks. *Frontiers in Human Neuroscience*, 4:Art. No. 191, 2010.

W. G. Walter. The location of cerebral tumours by electro-encephalography. *The Lancet*, 228(5893):305–308, 1936.

J. Wang, J. Barstein, L. E. Ethridge, M. W. Mosconi, Y. Takarae, and J. A. Sweeney. Resting state EEG abnormalities in autism spectrum disorders. *Journal of Neurodevelopmental Disorders*, 5(1):24, 2013.

X.-J. Wang. Neurophysiological and Computational Principles of Cortical Rhythms in Cognition. *Physiological Reviews*, 90(3):1195–1268, 2010.

S. Wass. Brain and Cognition Distortions and disconnections : Disrupted brain connectivity in autism. *Brain and Cognition*, 75(1):18–28, 2011.

F. Wendling, F. Bartolomei, J. J. Bellanger, and P. Chauvel. Epileptic fast activity can be explained by a model of impaired GABAergic dendritic inhibition. *European Journal of Neuroscience*, 15(9):1499–1508, 2002.

A. T. Winfree. Biological rhythms and the behavior of populations of coupled oscillators. *Journal of Theoretical Biology*, 16(1):15, 1967.

D. Yao, L. Wang, R. Oostenveld, K. D. Nielsen, L. Arendt-Nielsen, and A. C. Chen. A comparative study of different references for eeg spectral mapping: the issue of the neutral reference and the use of the infinity reference. *Physiological Measurement*, 26 (3):173, 2005.

B. T. Yeo, F. M. Krienen, J. Sepulcre, M. R. Sabuncu, D. Lashkari, M. Hollinshead, J. L. Roffman, J. W. Smoller, L. Zollei, J. R. Polimeni, B. Fischl, H. Liu, and R. L. Buckner. The organization of the human cerebral cortex estimated by intrinsic functional connectivity. *Journal of Neurophysiology*, 106:1125–1165, 2011.